UNIVERSITY OF CAPE TOWN

MASTERS THESIS

# Investigating the sensitivity of one-dimensional turbulence schemes in the sub-Antarctic Southern Ocean

*Author:*
Kirodh BOODHRAJ

*Supervisor:*
Dr. Jacoba E. SMIT
Assoc/Prof. Marcello VICHI

*A thesis submitted in fulfillment of the requirements*
*for the degree of Masters*

*in the*

Department of Oceanography

January 30, 2018

University of Cape Town

The copyright of this thesis vests in the author. No quotation from it or information derived from it is to be published without full acknowledgement of the source. The thesis is to be used for private study or non-commercial research purposes only.

Published by the University of Cape Town (UCT) in terms of the non-exclusive license granted to UCT by the author.

University of Cape Town

# Declaration of Authorship

I, Kirodh BOODHRAJ, declare that this thesis titled, “Investigating the sensitivity of one-dimensional turbulence schemes in the sub-Antarctic Southern Ocean” and the work presented in it are my own. I confirm that:

- This work was done wholly or mainly while in candidature for a research degree at this University.
- Where any part of this thesis has previously been submitted for a degree or any other qualification at this University or any other institution, this has been clearly stated.
- Where I have consulted the published work of others, this is always clearly attributed.
- Where I have quoted from the work of others, the source is always given. With the exception of such quotations, this thesis is entirely my own work.
- I have acknowledged all main sources of help.
- Where the thesis is based on work done by myself jointly with others, I have made clear exactly what was done by others and what I have contributed myself.

Signed: Signed by candidate

Date: January 30, 2018

*"Hare Rama Hare Rama*
*Rama Rama Hare Hare*

*Hare Krishna Hare Krishna*
*Krishna Krishna Hare Hare"*

Maha Mantra

UNIVERSITY OF CAPE TOWN

# *Abstract*

Faculty of Science
Department of Oceanography

Masters

### **Investigating the sensitivity of one-dimensional turbulence schemes in the sub-Antarctic Southern Ocean**

by Kirodh BOODHRAJ

The sub-Antarctic Zone (SAZ) is a zone of vigorous vertical mixing in the Southern Ocean where it is difficult to obtain data for model validation on the turbulence conditions. In this study, a one-dimensional configuration from the Nucleus for the European Modelling of the Ocean (NEMO) model was implemented in order to determine the sensitivity and turbulence response of an idealized SAZ water column. Various turbulence scheme parameterizations that are available for ocean models were tested. Furthermore, the number of vertical levels were varied in order to ascertain the sensitivity of the grid. The forcing data were obtained from various reanalyses (ERA-Interim, NASA, NCEP and JRA55) and were likewise tested. Different turbulence diagnostics and univariate indicators were chosen to ascertain the turbulence response and to analyse the energetics of the water column. It was found that using different reanalyses produced different tracer (salinity and temperature) results. Even though the results varied considerably, very high correlations were found for the potential energy anomaly between reanalyses and insignificant correlations were found for the other indicators. This suggested that it was a valuable descriptor which captured the buoyancy fluxes and wind stress information and can be efficiently used to assess the vertical turbulent state with data such as ARGO profiles. It was further found that for a single reanalysis, the turbulence schemes had produced similar results (with small variability and not to the extent as changing the reanalysis) for the turbulence diagnostics and univariate indicators. An important finding of an entrapped warm water parcel beneath cooler waters was found in simulation outputs as well as ARGO validation data. For realistic conditions observed from the ARGO floats, as the season progressed, there were no more instances of a warm water parcel. There was no reason however, to why there should not have been eddies passing by the region. In simulations, the warm water parcel persisted throughout the season for simulated data, likely causing the early stratification that affects ocean models in the SAZ. The stratification was found to have an approximate one month early onset observed from comparing the ARGO data profiles to simulated profiles. The Brunt Väisälä frequency, potential energy anomaly as well as the buoyancy flux were analysed and these diagnostics indicated that an approximate one month early stratification was found during November. It was likely that this false stratification signal may have influenced the summer stratification leading to a poor representation of the Mixed Layer Depth (MLD) and various other indicators. It was found that during the austral winter months, the model simulated comparable MLD's to the ARGO float data as well as the Winter Cruise data (obtained from the *SA Agulhas II*), capturing the winter dynamics well.

# *Acknowledgements*

My deepest and warm gratitude goes to my parents (Suresh and Jaishree Boodhraj) and sister (Shaheri Boodhraj) for the moral support through the period of my Masters studies. My eternal thanks to both my competent supervisors (Assoc/Prof. Marcello Vichi and Dr. Jacoba E. "Kobie" Smit) without whom I would not be engaging in this beautiful field of study. Also for their inspiration and unlimited enthusiasm over the past two years. I am looking forward to carrying on these productive collaborations in the future. Furthermore to the support, help and knowledge they have transferred unto me. Many thanks goes to Dr. Onno Ubbink and Dr. Kobie Smit for initially helping me to seek out a supervisor for my Masters from the surrounding universities.

I also am grateful to all my extended family and friends (James Burns, Jenny Pan, Jan-Louis Schlebusch, Sudhama, Rags, Sonu, Toulouse de Vos-Fÿfer, Melise Steyn, Bafana Gweba, Michael Hart-Davis, Michael and Herman) who stood by my side and kept me company through tedious times. All at the weekly garden sessions with Phillip, Indren, Odi, Corine, Stewart and Dominique must be given credit for balancing my life style during this Masters. Special acknowledgement goes to the Vaishnavas (Hari Vilasa Dasa, Premananda Kirtana Dasa, Gopi Jivana Dasa, Godruma das, Jako, Axl, Joubert, Cronje, Robbi, Roland, Parv and Oom Robert) and Vaishnavis (Nilacala dasi, Kamalasita dasi, Lusi, Tara, Tasmin, Corine, Naledi and Tannie Tianni) of the local Hare Krishna Ashram for keeping my spiritual life and health in order. If anything went smoothly or roughly during my masters, it was because of Ett.

I acknowledge Chris Mahlati for the innumerable pieces of masters advice and comments given to me. Dr. Fine Wilms is acknowledged for the valuable help on sorting minor but difficult Ubuntu errors. Jeffrey Baloyi is acknowledged for his initial help and general advice of turbulence scheme modelling at the beginning of my Masters. I acknowledge Gert Wessels who suggested using splines solving the problem of data interpolation to the NEMO grid structure from the WOA data. Acknowledgement goes to Björn Backeberg for his kind help in helping me navigate through the introductory phase of my Masters. He gave me great tips on oceanographic phenomenon and how NetCDF files work and various other bits of oceanographic information. Many thanks to Louisa van der Merwe for the countless motivations and advice which were a great pick-me-up when things seemed down in these last two years.

Acknowledgement is given to all organizations which provided the data as well as all software used in this study. UCT is acknowledged for providing me with the academic environment and framework in order to do a Masters. The CSIR is acknowledged for the studentship funding program that I was part of which made it possible to pursue this Masters degree. Dr. Francois Engelbrecht is also acknowledged due to the partial VRESM funding which contributed to my masters as well as the valuable knowledge obtained from the VRESM project meetings.

This work is partly based on the research supported by the National Research Foundation through the SANAP grant SNA14072880912 given to Prof. M. Vichi. Lastly, acknowledgement goes to the *SA Agulhas II* for the wonderful voyage aboard her to the Marginal Ice Zone of Antarctica and all the wonderful people I had met onboard. I learned very valuable oceanographic skills which was made possible by my supervisors.

# Contents

# List of Figures

# List of Tables

# List of Abbreviations

| | |
|---|---|
| **AAIW** | Antarctic Intermediate Waters |
| **AASW** | Antarctic Surface Water |
| **ACC** | Antarctic Circumpolar Current |
| **ARGO** | Array for Real-time Geostrophic Oceanography |
| **ASF** | Antarctic Slope Front |
| **BVF** | Brunt Väisälä Frequency |
| **CCI** | Climate Change Initiative |
| **CFD** | Computational Fluid Dynamics |
| **CSW** | Continental Shelf Water |
| **CTD** | Conductivity, Temperature and Depth |
| **ECMWF** | European Centre for Medium-Range Weather Forecasts |
| **ESA** | European Space Agency |
| **E-W** | East-West |
| **GEBCO** | General Bathymetric Chart of the Oceans |
| **GFD** | Geophysical Fluid Dynamics |
| **GFDL** | Geophysical Fluid Dynamics Laboratory |
| **GLS** | Generic Length Scale |
| **GOTM** | General Ocean Turbulence Model |
| **HYCOM** | Hybrid Coordinate Ocean Model |
| **ITS** | International Temperature Scale |
| **JMA** | Japanese Meteorological Agency |
| **MITgcm** | MIT global circulation model |
| **MLD** | Mixed Layer Depth |
| **MOM** | Modular Ocean Model |
| **M-Y** | Mellor-Yamada |
| **NASA** | National Aeronautics and Space Administration |
| **NCEP** | National Centres for Environmental Prediction |
| **NEMO** | Nucleus for the European Modelling of the Ocean |
| **NOAA** | National Oceanic and Atmospheric Administration |
| **NP** | Northern Pacific |
| **N-S** | North-South |
| **PDE** | Partial Differential Equation |
| **PEA** | Potential Energy Anomaly |
| **POP** | Parallel Ocean Program |
| **PZ** | Polar Zone |
| **QNSE** | Quasi-Normal Scale Elimination |
| **ROMS** | Regional Ocean Modelling System |
| **RMSE** | Root Mean Square Error |
| **SACCF** | Southern Antarctic Circumpolar Front |
| **SAF** | sub-Antarctic Front |
| **SAMW** | sub-Antarctic Mode Waters |
| **SASW** | Sub-Antarctic Surface Water |
| **SAZ** | sub-Antarctic Zone |
| **SB** | Southern Boundary |
| **SCM** | Single Column Model |
| **SO** | Southern Ocean |

| | |
|---|---|
| **SOCCO** | Southern Ocean Carbon and Climate Observatory |
| **STF** | Sub-Tropical Front |
| **STSW** | Sub-Tropical Surface Water |
| **TEOS** | Thermodynamic Equation Of State |
| **TKE** | Turbulent Kinetic Energy |
| **WC_CTD** | Winter Cruise Conductivity, Temperature and Depth |
| **WOA** | World Ocean Atlas |

# List of Symbols

| | | |
|---|---|---|
| $f$ | Coriolis parameter | $\mathrm{rad\,s^{-1}}$ |
| $g$ | gravitational acceleration | $9.8\ \mathrm{m\,s^{-2}}$ |
| $\hat{i}, \hat{j}\ (x, y)$ | horizontal coordinates | |
| $\hat{k}\ (z)$ | vertical coordinate | |
| $k$ | turbulent kinetic energy (turbulence schemes) | $\mathrm{m^2\,s^{-2}}$ |
| k | vertical index (grids) | |
| $l_\varepsilon, l_K, l_u, l_d$ | TKE length scales | m |
| $p$ | pressure | Pa |
| $t$ | time | s |
| $u, v, w$ | velocity components corresponding to $\hat{i}, \hat{j}, \hat{k}$ | $\mathrm{m\,s^{-1}}$ |
| $B$ | buoyancy flux | $\mathrm{m^2\,s^{-3}}$ |
| $C_p$ | specific heat capacity | $\mathrm{J\,K^{-1}}$ |
| $\vec{D}^{\vec{U}}$, $D^S$ and $D^T$ | small parameterization terms | $\mathrm{m\,s^{-2}}$, $\mathrm{PSU\,s^{-1}}$, $\mathrm{^\circ C\,s^{-1}}$ |
| $E_f$ | evaporation flux | $\mathrm{kg\,m^{-2}}$ |
| $\vec{F}^{\vec{U}}$, $F^S$ and $F^T$ | surface forcing terms | $\mathrm{m\,s^{-2}}$, $\mathrm{PSU\,s^{-1}}$, $\mathrm{^\circ C\,s^{-1}}$ |
| $I$ | irradiance | $\mathrm{W\,m^{-2}}$ |
| $K$ | vertical diffusivity | $\mathrm{m^2\,s^{-1}}$ |
| $K_e$ | turbulent thermal diffusivity | $\mathrm{m^2\,s^{-1}}$ |
| $K_h$ | horizontal diffusivity | $\mathrm{m^2\,s^{-1}}$ |
| $M$ | shear frequency | $\mathrm{s^{-1}}$ |
| $N$ | Brunt Väisälä frequency | $\mathrm{s^{-1}}$ |
| $P_f$ | precipitation flux | $\mathrm{kg\,m^{-2}}$ |
| $Pr_{tr}$ | Prandtl number | |
| $Q$ | upward heat flux | $\mathrm{W\,m^{-2}}$ |
| $R$ | correlation coefficient | |
| $Ri$ | Richardson number | |
| $S$ | salinity | $\mathrm{g\,kg^{-1}}$ or PSU |
| $S_A$ | absolute salinity | $\mathrm{g\,kg^{-1}}$ |
| $T$ | temperature | K |
| $\vec{U}$ | velocity vector | $\mathrm{m\,s^{-1}}$ |
| $\vec{U}_h$ | horizontal velocity vector | $\mathrm{m\,s^{-1}}$ |
| $\alpha$ | thermal expansion coefficient | $\mathrm{^\circ C^{-1}}$ |
| $\beta$ | salinity contraction coefficient | $\mathrm{PSU^{-1}}$ |
| $\varepsilon$ | turbulent dissipation rate | $\mathrm{m^2\,s^{-3}}$ |
| $\eta$ | free surface elevation | m |
| $\nu$ | vertical viscosity | $\mathrm{m^2\,s^{-1}}$ |
| $\nu_b, K_b$ | background viscosity and diffusivity respectively | $\mathrm{m^2\,s^{-1}}$ |
| $\nu_h$ | horizontal viscosity | $\mathrm{m^2\,s^{-1}}$ |
| $\phi$ | potential energy anomaly | $\mathrm{J\,m^{-3}}$ |
| $\dfrac{d\phi}{dt}$ | time derivative of potential energy anomaly | $\mathrm{J\,m^{-3}\,s^{-1}}$ |
| $\rho_0$ | reference density | $10^3\ \mathrm{kg\,m^{-3}}$ |
| $\rho$ | in situ density | $\mathrm{kg\,m^{-3}}$ |
| $\sigma_k, \sigma$ | Schmidt numbers | |

| | | |
|---|---|---|
| $\tau$ | wind stress magnitude | $\mathrm{N\,m^{-2}}$ |
| $\Theta$ | potential temperature | $^{\circ}\mathrm{C}$ |
| $\vec{\Omega}$ | earth angular frequency vector | $\mathrm{rad\,s^{-1}}$ |
| $\nabla$ | vector differential operator | |
| $\nabla_h$ | horizontal vector differential operator | |

*Dedicated firstly to God, secondly to my parents whom I am forever grateful for and lastly to all my extended family and friends whom have seen me grow during this time.*

# Chapter 1

# Introduction

## 1.1 Problem statement

### 1.1.1 Background of this study

The Southern Ocean (SO) is a unique ocean that exhibits a plethora of physical processes. There is great interest surrounding the SO due its interconnectivity with the three major oceans (Atlantic, Indian and Pacific) of the world. The region which forms the interface between these major oceans is known as the sub-Antarctic Zone or SAZ. The SAZ surrounds the outer boarders of the SO. The SO is not bounded by a Western or Eastern boundary (continental plateaux) and forms a strong unbounded ocean current referred to as the Antarctic Circumpolar Current (ACC) (Talley et al., 2011a). The closed current and atmospheric conditions present at those latitudes enhances physical processes such as eddies and the divergence of turbulent momentum and tracer fluxes (or turbulent mixing).

It is a challenge to model the physical processes of the ocean for various reasons. Firstly, the length scales of the ocean vary considerably with respect to the horizontal (O(100 $\mathrm{km}$)) and vertical (O(5 $\mathrm{km}$)) directions (Bernard et al., 2006; Mercator, 2008). This has consequences on the effect of momentum and heat transfers on the system at various scales. Ocean models today separate the two length scales into a horizontal component and vertical component for efficient computation purposes. Secondly, limited computation power exists for simulating a very high resolution run of the governing equations of the ocean (known as the Primitive equations). Thirdly, the natural state of the ocean is a chaotic system (Thorpe, 2007). This makes it a very challenging system to model or predict. These are a few constraints which limit the ocean models in various aspects.

Due to the nature of the SO, vertical processes have a profound effect on the momentum and energy transfers taking place within the SO. For this study, only the divergence of turbulent momentum and tracer fluxes are considered and other vertical or horizontal processes are ignored. The physical process which induces the divergence of turbulent momentum and tracer fluxes is known as ocean turbulence. There are two main categories of turbulence inducing mechanisms for the oceans, namely external and internal processes (Thorpe, 2007). External processes include wind generated waves via wind stress, downward convection due to surface cooling and hydrothermal plumes found along oceanic ridges. Internal processes include breaking of internal waves (waves set up between inhomogeneous layers within the ocean), diapycnal mixing (mixing between oceanic layers of inhomogeneous properties) and double diffusion (stronger salinity contributions to density than the temperature) (Hibiya et al., 2002). The internal and external processes used in study consist mainly of wind stress and internal wave breaking.

The current method to resolve the vertical divergence of turbulent momentum and tracer fluxes in computational models is to use a turbulence scheme parameterization (Wilcox, 1988; Rodi, 1987; Blanke and Delecluse, 1993; Burchard and Bolding, 2001; Mellor and Yamada, 1982; Pacanowski and Philander, 1981) as the mathematics of turbulence is a natural framework of representing homogenization of fluid properties via the divergence of turbulent momentum and tracer fluxes. There are many turbulence schemes available in physical oceanography, namely $k-\varepsilon$, $k-\omega$, Mellor-Yamada (M-Y or k-kl), Generic, TKE0, TKE10, TKE30, Pacanowski/Philander and many more. This study explores and interprets the resulting energetics of various turbulence schemes to model the divergence of turbulent momentum and tracer fluxes within a vertical water column. Energetics refers to how energy, available from an external source other than the ocean (for example wind shear), is distributed and dissipated by the various turbulence mechanisms (internal and external processes) present (Thorpe, 2007). The simplest technique to determine which turbulence scheme is suitable for the region of interest is to use a Single Column Model (SCM) to model a one-dimensional water column in the ocean. A water column is simply an entire depth profile at a single point (specific latitude and longitude) in the ocean.

SCM's have been used extensively as a precursor before running more complex three dimensional ocean models (Optis and Monahan, 2017). They consist of modelling the time evolution of tracer properties of a single vertical column in the ocean at a specific location. Vertical turbulence schemes and other vertical processes can easily be parameterized into a SCM as they are flexible in incorporating these processes. Results are obtained almost immediately due to the low computational cost of these models. SCM's are also considered the "first generation ocean models" as they were surprisingly successful in simulating many sectors of the ocean (Gaspar, 1988).

Focussing on the vertical processes, Reffray et al. (2015) used the Nucleus for the European Modelling of the Ocean (NEMO) model to implement a SCM. They carried out a study on determining the mixing sensitivity of a water column located in the Northern Pacific ocean. After comparing various turbulence closure scheme parameterizations from their simulations, they validated these using data from ocean station *PAPA* (NOAA, 2016) in order to determine which turbulence scheme performed the best. They had chosen their study location in the Northern Pacific region because ocean station *PAPA* was located there. This serves as the motivation for this study to determine the turbulent response and vertical mixing sensitivity of a water column located in the SO.

The SAZ lies between the expanse of warm Sub-Tropical waters and the surrounding waters of the Antarctic continent. The SAZ is located between the Sub-Tropical Front (STF) and sub-Antarctic Front (SAF) which circumnavigate the Antarctic continent (Talley et al., 2011b). It also provides a 'window' to ocean-atmosphere interactions such as the formation of high oxygen sub-Antarctic Mode Waters (SAMW). Due to the multiple processes (horizontally and vertically) occurring in the SAZ region, it is intrinsically a three-dimensional system. It is however, an informative exercise to understand a one-dimensional model representation before attempting to fully understand a three dimensional model. In most ocean models, the seasonal dynamics for the SAZ region show a bias (Huang et al., 2014; Sallée et al., 2013), particularly for the vertical dynamics. This shows that the vertical dynamics needs attention in ocean models. This provides a good means to test a vertical one-dimensional ocean model in order to ascertain whether it performs well or not. Furthermore, this will help create a better understanding of the ocean model involved.

The SAZ region is very important for nutrient cycling and the biogeochemistry that links the SO to the other major oceans. For example, this region is a very large sink for global carbon dioxide and various other gases (Mongwe et al., 2016). Much effort has gone into modelling the nutrient cycles, but it is still poorly understood (Mongwe et al., 2016; McKiver et al., 2015). It is noted by McKiver et al. (2015) that the ocean physics firstly needs to be resolved to an acceptable accuracy before a biogeochemistry computational model would produce satisfactory results.

Turbulent mixing in the ocean can be approached in various ways, namely by deducing results from the large scale motion of the ocean, by gathering observations and by gaining an accurate understanding of the processes involved via mathematical framework (Gregg, 1987). The late 1960's was the start of ocean data collection and before then, inferences from large scale motion was used. There was a severe lack of understanding regarding the fundamental oceanic processes involved as well as in their coupling. Much work has been done since, although, currently the problem of loosely coupled physical models and sparse observations persists. There are generally sparse measurements in the SO and various observations indicate the presence of large turbulence and strong patchy turbulent areas governed by atmospheric forcing as well as bottom topography (Thompson et al., 2007). Leading validation data comes from Array for Real-time Geostrophic Oceanography (ARGO) floats (ARGO, 2017) which are left to drift (at the ocean's mercy) and collect salinity, temperature an other data profiles of the upper ocean. In this study ARGO data are used to validate the SCM implemented in the SO.

### 1.1.2 Research gap

The study carried out by Reffray et al. (2015) had focussed on a single location in the Northern Pacific Ocean. They did not extend their study to other oceanic locations using the one-dimensional model configuration they implemented in NEMO. This study extends the use of the model configuration by applying an adapted version of the model configuration to a location other than the Northern Pacific ocean. The current study location is located in the SAZ region off the coast of South Africa of the SO.

In their simulations, Reffray et al. (2015) had used 31 and 75 vertical levels in their grid configuration. The research gap here entails increasing the vertical grid resolution by increasing the number of vertical levels. This study has included 51, 101 and 151 (in addition to 31 and 75) vertical levels for the SO simulations. Important emphasis was placed on results obtained using 101 vertical levels due to the evermore increasing computational power available.

Of the many turbulence schemes that are provided in NEMO, the use of the Pacanowski/Philander scheme was not tested on the one-dimensional model implemented by Reffray et al. (2015). This is one research gap that is addressed in this study.

ERA-Interim was the only reanalysis which was implemented with this model and there is scope to evaluate the use of various other reanalyses (JRA55, NASA and NCEP) in combination with the various turbulence schemes.

## 1.2 Research objectives and important questions

The main research objectives is to:

1. Understand the various vertical turbulence schemes that are available in the oceanographic field and their implementation to one-dimensional models.
2. Implement the one-dimensional model (created by Reffray et al. (2015)) to the SAZ region off the coast of South Africa in the SO.
3. Examine the resulting output and energetic measures when using various combinations of reanalyses and turbulence schemes.
4. Determine which portions of the seasonal dynamics can be captured by a one-dimensional model.

Considering the research objectives above, this study provides a basis to pose some important questions grouped below.

(1) Turbulence closure scheme parameterizations:
- Based on the various means by which the turbulence closure schemes were derived, would changing the turbulence scheme produce similar tracer results as the previous results? Is it possible that there would be a high variability of the results?

(2) Reanalyses data:
- Since the data assimilation process of reanalyses are different, will the use of one reanalysis produce different results compared to using another reanalyses?

- Are there any turbulence diagnostics or univariate indicators that remain invariant under a change of reanalysis data?

(3) Validation data:
- How well will the observed ARGO float and Winter Cruise data temperature profile data compare with the simulation outputs?

- How is the representation of the timing of summer stratification and other seasonal dynamics dependent on the numerical parameterizations?

## 1.3 Hypothesis and approach

The hypothesis is that a SCM (one-dimensional model) can capture a relevant portion of the seasonal dynamics (stratification and deep turbulent mixing).

The approach taken will be to adapt the one-dimensional configuration created by Reffray et al. (2015) in order to implement it for the SO. The various turbulence diagnostics and indicators will then be analysed to determine the turbulence response and the sensitivity to vertical turbulent mixing of the water column.

Only turbulence schemes provided with NEMO will be considered in this study. This study is limited to the upper oceanic layers due to the overwhelming effect of turbulence in this region (Gaspar, 1988) which results from the atmospheric forcings (namely the lower ocean can be neglected).

ARGO data will be used to validate the simulation output and determine whether the seasonal dynamics are accurately captured.

## 1.4 Overview of chapters

As mentioned above, a SCM configuration will be developed in order to determine the turbulence response and other water column properties examined via the tracers (salinity and temperature). The energetics will be computed and analysed. The outline in the form of a flow diagram is shown in Fig. 1.1. ARGO validation data will be used in order to compare simulation output to observed temperature profiles.

This study is broken down into the following chapters and appendixes:

Chapter 2 provides a literature review that gives an extensive background to contextualize the study.

Chapter 3 describes the methodology used in determining the turbulence response of the SCM developed for the SO as well as the turbulence diagnostics and univariate indicators used in analysing the energetics of the model. A diagram of all simulations performed and their particular details are explained.

Chapter 4 presents the results obtained from running the simulations described in Chapter 3. The simulation outputs are validated against ARGO float and Winter Cruise temperature profile data. Furthermore, the energetics are analysed through the various turbulence diagnostics and univariate

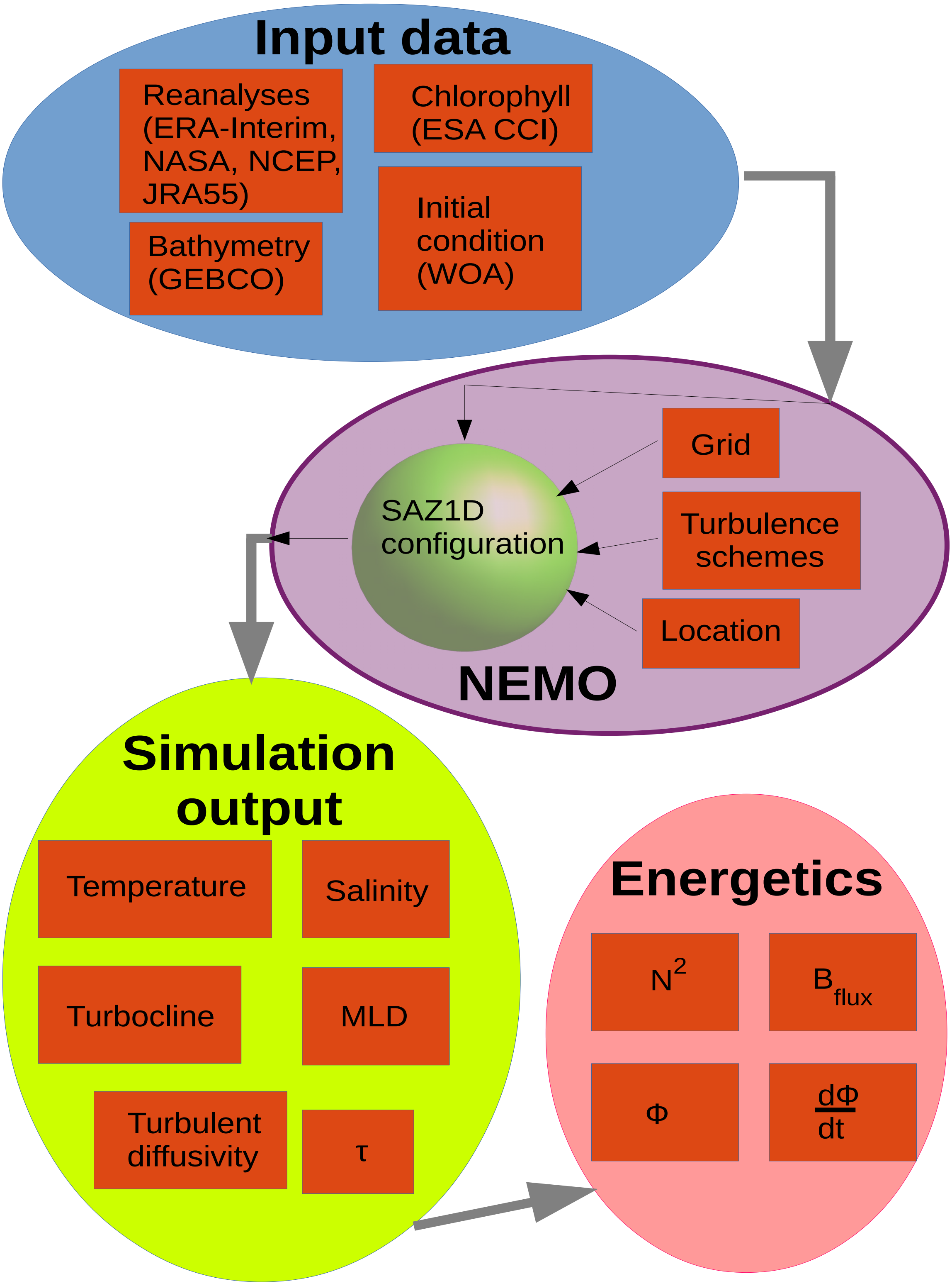

FIGURE 1.1: Flow diagram of the various steps carried out in this study. The input data are first processed for compatibility with NEMO's data formats and are fed into the model. Within NEMO, the grid, location and vertical turbulence scheme are specified. The output variables after running a simulation are used to calculate the energetics or turbulence diagnostics and univariate indicators.

indicators. Lastly, the correlations between reanalyses and turbulence schemes are presented.

Chapter 5 gives a summary of the results presented from Chapter 4. Secondly, a discussion on various viewpoints and ideas from the previous chapter that needed clarity is presented. Other researchers' work was compared to various ideas pertaining to the results of this study. Lastly, the study implications and future research are given at the end.

Chapter 6 concludes the study.

Appendix A shows the derivation of the mass balance equations for the Primitive model equations. This appendix derives the continuity equation that is used in ocean models.

Appendix B describes all technical details behind the creation of the SAZ1D configuration in NEMO. Details for the compilation and running of simulations using SAZ1D are detailed. The required data (boundary and initial conditions) needed for operating SAZ1D are explained. The C1D_PAPA configuration (created by Reffray et al. (2015)) is also included and explained in this appendix.

Appendix C presents the technical details, software and procedures used in order to process the raw reanalyses data obtained from their respective online databases. The entire procedure and processing scripts are provided for reproducibility purposes. The raw initial condition data processing particulars are also provided in this appendix.

Appendix D gives the supplementary correlation tables that are referred to in Chapter 4 providing extra information and insight into the results obtained in this study.

Appendix E provides supplementary results for temperature and salinity for the interested reader.

This study does not cover the following related aspects:

1. Use of various other reanalyses other than the ERA-Interim (Dee et al., 2011), NASA (NASA, 2017), NCEP (Kanamitsu et al., 2017) and JRA55 (JRA55, 2017) products to force simulations performed in this study.
2. Use of the double diffusive mixing or tidal mixing vertical process parameterizations.
3. Use of any other turbulence scheme (such as kpp) other than the $k-\varepsilon$ (Rodi, 1987), $k-\omega$ (Wilcox, 1988), M-Y (k-kl) (Mellor and Yamada, 1982), Generic (Burchard and Bolding, 2001), TKE family (Blanke and Delecluse, 1993) and Pacanowski/Philander (Pacanowski and Philander, 1981).
4. A full grid and result analysis from choosing different vertical levels and spacings for the grid structure.
5. Implementation of various stability functions which parameterize the turbulent viscosity and diffusivity in the Generic Length Scale (GLS) family of turbulence closure schemes.

# Chapter 2

# Literature

## 2.1 Introduction

Turbulence in the ocean is a predominating physical process involved in the transfer and distribution of momentum and energy (Thorpe, 2007). ’Process’ in this context implies a physical (spatio-temporal) event involving the transfer of energy from one scale to another or from one part of the ocean to another. There are various mechanisms inducing ocean turbulence as illustrated in Fig. 2.1 (GFDL, 2017). A large group of oceanic organisms thrive as a consequence of turbulent waters due to entrainment of nutrient rich waters (Peters and Marrasé, 2000). The principal turbulence inducing mechanisms discussed in this study include wind stress, radiation, precipitation and evaporation which form part of external sources of turbulence (Thorpe, 2007). The primary concern of this chapter is establishing previous work performed in the field of using turbulence schemes to model vertical mixing in the ocean. In recent years, there has been an increasing interest in modelling the vertical structure of the oceans for understanding phenomena that have a strong vertical component (Reffray et al., 2015, and references therein). The governing equations (called the Primitive equations) and assumptions for vertical processes in the ocean are reviewed and explained in this chapter. In order to resolve the Primitive equations, presented in Section 2.3.1, different numerical models can be used. Each model differs in the discretization and numerical implementation, however, the underlying equations remain unchanged. NEMO was chosen for this study as explained in Section 2.3.3. The chapter begins with the area of focus used in this study, namely the Southern Ocean.

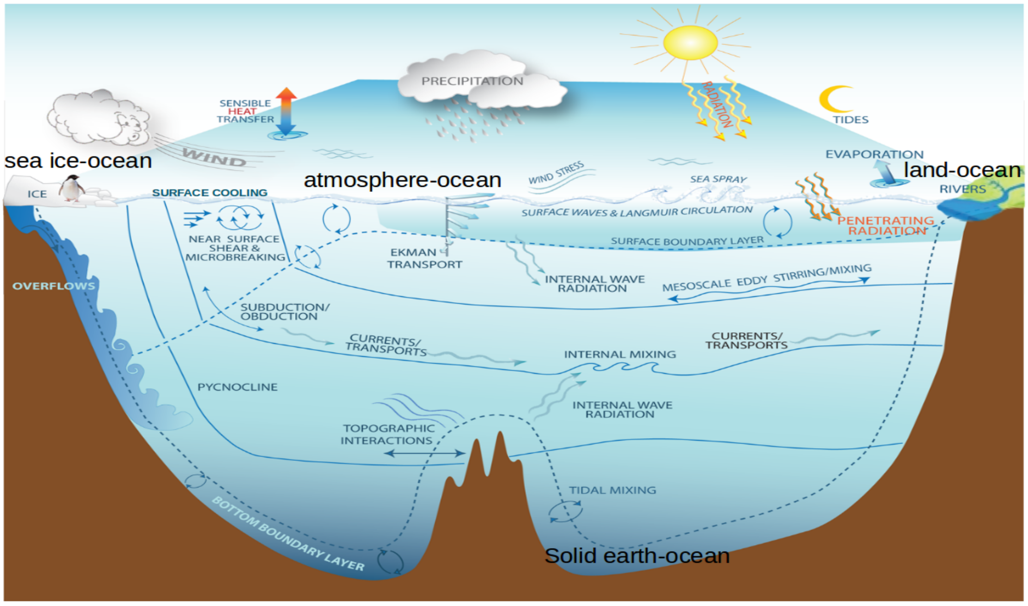

FIGURE 2.1: Various turbulence inducing mechanisms in the ocean as adapted from GFDL (2017). The boundary conditions (solid earth, sea-ice, atmosphere and land) used for a typical ocean domain are displayed at their location of influence.

## 2.2 Turbulent nature of the Southern Ocean

Within the Southern Ocean (SO), various fronts and zones are present (see Fig. 2.2). The outer boarders of the SO is boarded by the sub-Antarctic Zone (SAZ), boarded by the Sub-Tropical Front (STF) and sub-Antarctic Front (SAF). Closer to the Antarctic continent, the Polar Frontal zone and Antarctic zone (bordered the Polar Zone (PZ) and Southern Antarctic Circumpolar Front (SACCF)) are found respectively. Closer to the Antarctic shelf the Southern Boundary (SB) and the Antarctic Slope Front (ASF). Circumnavigating Antarctica is the Antarctic Circumpolar Current (ACC) forming a closed loop implying no eastern or western boundaries hinder the flow, as is the case with other major ocean currents (Talley et al., 2011a). The ACC is mainly driven by the westerly winds (Allison et al., 2010) imparting momentum to the waters via the wind stress. A cross section is shown in Fig. 2.3. This leads to deep and dense bottom waters and large water transport with all major oceans across the SAZ (Talley et al., 2011a). There are also large vertical exchanges of momentum and energy between the layers spanning the ACC. These properties in general causes the SO to manifest as being more turbulent in comparison to the other major oceans (Sheen et al., 2013). The turbulent nature is further intensified due to oceanic ridges steering the current. A number of researchers have reported the higher turbulence aspect of the SO (St. Laurent et al., 2012; Garabato et al., 2016) through measurements of turbulent kinetic energy dissipation, which suggested higher mixing rates in various areas of the ACC.

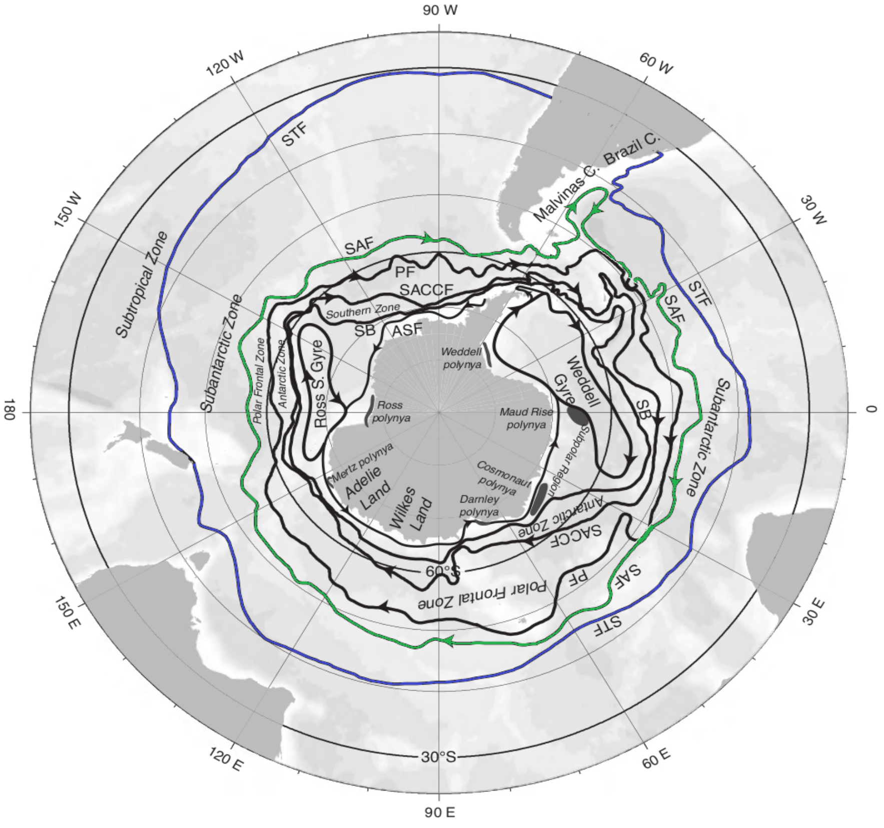

FIGURE 2.2: The various atmospheric fronts and oceanic zones of the Southern Ocean. Adapted from Talley et al. (2011a).

The Southern Ocean can be sectioned into three major vertical layers according to Monin et al. (1978), namely an upper mixed layer, intermediate layer where turbulence occurs sporadically and a bottom layer. These layers are generally separated by density stratification which effectively separates turbulence characteristics within each layer. There are two main categories inducing turbulence in the oceans, namely external and internal processes (Thorpe, 2007; Turner, 1973). External processes include tidal or wave induced flows (namely moon driven), downward convection due to surface

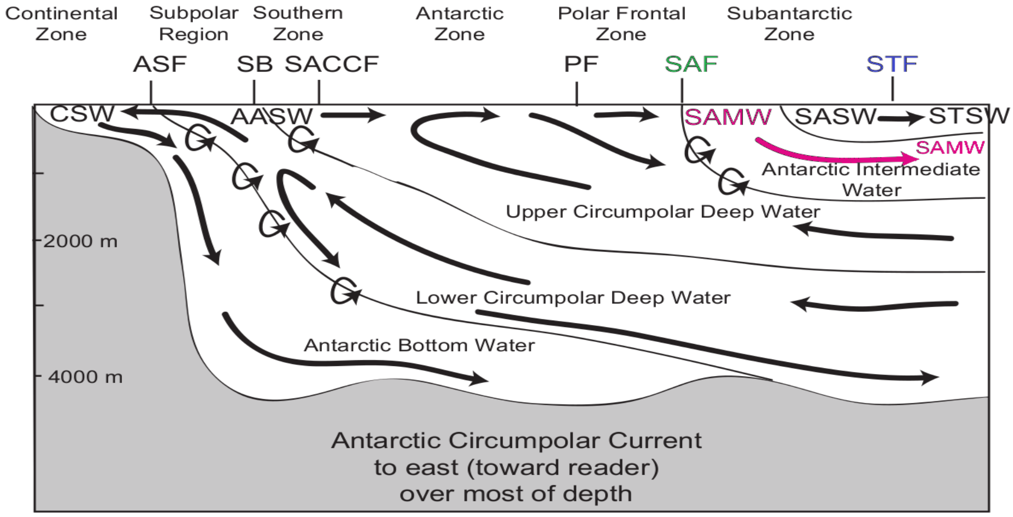

FIGURE 2.3: A typical cross section of the Southern Ocean showing the various circulation patterns. Close to the Antarctic shelf the Continental Shelf Waters (CSW) and Antarctic Surface Waters (AASW) are found. Within the SAZ the Sub-Antarctic Surface Water (SASW) moves northward becoming the Sub-Tropical Surface Water (STSW). Adapted from Talley et al. (2011a).

cooling, hydrothermal plumes and wind generated waves. Internal processes include breaking of internal waves leading to diapycnal mixing (namely vertical mixing across diapycnals) and double diffusion. These processes are not isolated and more than one process may be observed during a single time period and location. Turbulence in the stratified ocean occurs in localized regions due to energy and momentum distributions leading to unstable patches (Thorpe, 2007) which is highly influenced by the bottom topography. Occasionally after turbulent activity has homogenized the fluid, small scale changes in temperatures and salinity are found and referred to as fossil turbulence (Leung and Gibson, 2004). These turbulence inducing mechanisms occur in the SO.

The SAZ features as an important interface for atmosphere-ocean interactions. It is here that sub-Antarctic Mode Waters (SAMW) is formed (see Fig. 2.3) which are vertically well mixed and oxygen rich waters that ventilate the upper SO (Sallée et al., 2008; Rintoul and Trull, 2001). Furthermore, the Antarctic Intermediate Waters (AAIW), recognizable from low salinity and depleted oxygen, intrude into the SAZ. These waters form many interfaces for turbulent events to occur. Unfortunately, not much is known on the physical processes in the SAZ, making it an area of wide interest (Rintoul and Trull, 2001). This region is an important interface for biogeochemical cycling of carbon and nutrients (Mongwe et al., 2016) between the tropical waters of the three leading oceans (Atlantic, Indian and Pacific sectors) and the ACC.

The SO is subjected to strong wind forcing and mesoscale eddy production. Zonal intensities are stronger in the SO due to the ACC. Due to these extreme conditions, it is not easy to determine if current subgrid scale parameterizations and numerical techniques are sufficient for modelling the SO (Thompson et al., 2007). Many (for example Thompson et al., 2007; Ito and Marshall, 2008) have described the uncertainty in the literature regarding isopycnal mixing mechanisms and their relation to obtaining accurate values of global mixing.

Much progress has been made in the recent 50 years in gathering turbulence measurements from the oceans. This is achieved by deploying air-foil probes with thermistors measuring the small scale turbulence and dissipation of turbulent kinetic energy (Thorpe, 2007). Theoretically the dissipation can be determined via length scales in Monin-Obhukov and Kolmogorov theories (Foken, 2006; Kolmogorov, 1941).

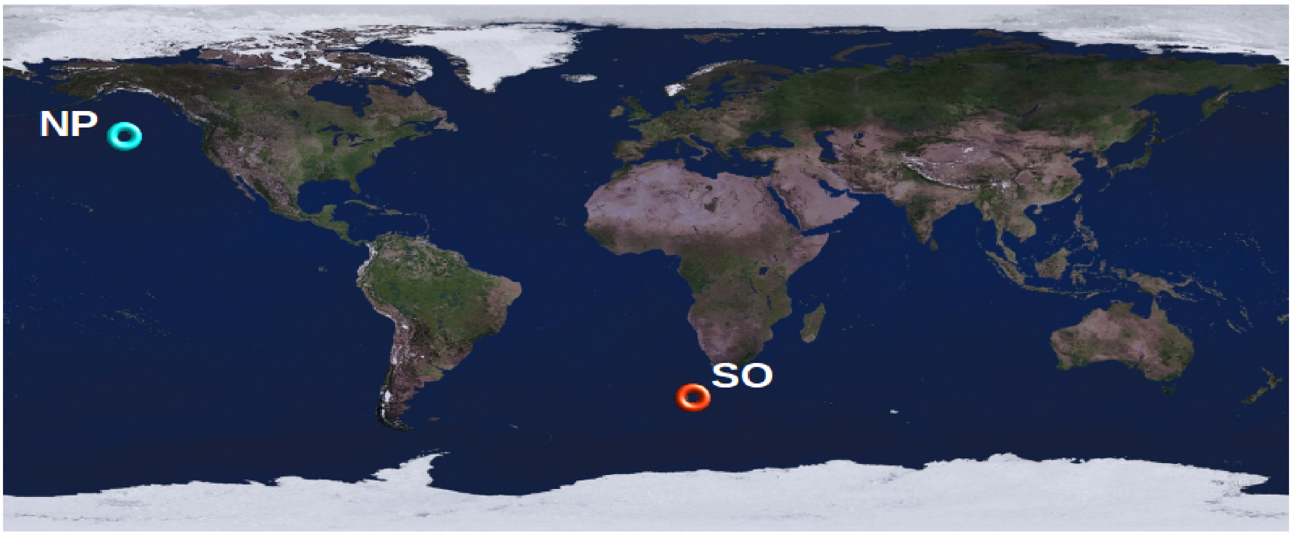

FIGURE 2.4: The approximate locations in the Northern Pacific (**NP**) (50.1°N, 144.9°W) and **SO** (47°S, 4.5°E) where simulations were performed for this study.

Extensive lab testing were performed to simulate the turbulence in the ocean. For example, Kato and Phillips (1969) attempted to quantify the turbulence dependence in an experiment under lab conditions containing an annulus shaped tank layered with various concentrations of saline water. The stress applied at the surface (via a rotating mechanism) resulted in mean horizontal shear causing entrainment (erosion) of denser waters below. Rapid mixing within the turbulent layer yielded an upper homogeneous fluid. The density gradient between the turbulent layer and stratified fluid below steepened as the turbulent layer deepened. Consequently, entrainment was hindered and internal waves were set up (Kato and Phillips, 1969).

The locations chosen for this study can be found in the SO south-west of South Africa. The approximate areas of study are shown in Fig. 2.4. The Northern Pacific (NP) location was chosen primarily due to Reffray et al. (2015) who used this location for their study. They had used this location for training purposes because Ocean station *PAPA* (NOAA, 2016) is moored there. Ocean station *PAPA* provided valuable validation data for their simulations (in order to compare various vertical turbulence schemes). The SO location was chosen due to the more turbulent nature of the waters (St. Laurent et al., 2012; Garabato et al., 2016) and furthermore because the location is in the southern hemisphere, where a study of comparing different vertical turbulence schemes in NEMO has not been performed previously.

## 2.3 Ocean Models

All ocean models use the Primitive equations (Griffies and Adcroft, 2013; Blanke and Delecluse, 1993) as the governing (base) equations. The Primitive equations originate from the Navier-Stokes equations (Navier, 1823) applied to a rotating sphere. They constitute the equations of motion for a global ocean system. The Primitive equations are presented as well as further simplifying assumptions which were applied to obtain the governing equations describing one-dimensional vertical processes.

Due to the complexity of the Primitive equation, existing methods for solving them are carried out computationally via discretization. The first computational ocean general circulation model was created at the Geophysical Fluid Dynamics Laboratory (GFDL) by Bryan (1969) which employed the z-coordinate system grid (see Gent (2011)). Many computational models currently exist such as the Modular Ocean Model (MOM) (GFDL, 2016), Parallel Ocean Program (POP) (Smith et al., 2010), Hybrid Coordinate Ocean Model (HYCOM) (HYCOM, 2016), MITgcm (Adcroft et al., 2016), Regional Ocean Modelling System (ROMS) (Robertson, 2007) and the Nucleus for the Modelling of the Ocean

(NEMO) (Madec, 2008).

Boundary conditions are required in conjunction with the Primitive equations. Four classes of boundary conditions (Madec, 2008) need to be specified, namely the land-ocean, solid earth-ocean, sea ice-ocean and atmosphere-ocean interface shown in Fig. 2.1. The land-ocean interface specifies fresh water flux from river runoff which mainly affect salinity concentrations. The solid earth-ocean boundary specifies geothermal heat and small salt fluxes. These heat and salt fluxes are normally negligible and are ignored. The sea ice-ocean boundary concerns the exchange of heat, salt and momentum near the poles where the physics of colder waters dominate. The atmosphere-ocean boundary (or surface forcings) is at the heart of understanding the affect of turbulence on the vertical structure of the ocean for this study. This boundary is key for the insertion of fresh water fluxes through precipitation or loss of water through evaporation. Thermal and wind stress (energy and momentum flux contributors respectively) are also specified on this boundary, having an effect on the vertical stratification structure. The shape of the ocean surface is also specified on this boundary. This study assumes the "rigid lid" model which is a flat ocean surface (Madec, 2008). This section will formulate the one-dimensional vertical form of the Primitive equations as well as describe the grid and boundary conditions pertaining to ocean models.

### 2.3.1 Primitive equations and governing equations describing vertical processes in the ocean

The full Primitive equations presented using the orthogonal Cartesian basis best serves the purpose of understanding the equations. The unit (basis) vectors in the Cartesian system are given by $\vec{i} = [1,0,0]$, $\vec{j} = [0,1,0]$, $\vec{k} = [0,0,1]$ referred to as the x-,y-,z-directions respectively. The velocity vector can be written as

$$\vec{U} = [u,v,w] = [u,v,0] + [0,0,w] = \vec{U}_h + w\vec{k}, \tag{2.1}$$

where $u,\ v,\ w$ are the velocity components and $\vec{U}_h$ denotes the horizontal velocity component.

In theory, flow variables can generally be decomposed into a mean and fluctuating part, i.e. $x = \overline{X} + x'$ where x represents a generic variable. In this study all quantities involving an apostrophe, "′", will refer to the fluctuating part of that variable decomposition. The fluctuating part has the property that its average yields 0, i.e. $\overline{x'} = 0$. In the derivation of the Primitive equations and various turbulence schemes (discussed in the below sections) there are products of fluctuating parts of variables (for example $x'y'$ where $y$ is another generic variable). The average of products of fluctuating parts of variables (known as the Reynolds average) does not necessarily yield 0.

The Primitive equations are a result of the Reynolds averaging procedure. The Reynold stresses contribute the viscous term in Eqns. 2.18-2.20 and is parameterized as

$$\overline{U_i'w'} = -\nu\frac{\partial U_i}{\partial z}. \tag{2.2}$$

The turbulent tracer fluxes are also parameterized in terms of the diffusivity and are given by

$$\overline{T'w'} = -K\frac{\partial T}{\partial z}, \tag{2.3}$$

$$\overline{S'w'} = -K\frac{\partial S}{\partial z}, \tag{2.4}$$

where $U_i$ are the horizontal velocity components, $\nu$ the turbulent viscosity and $K$ the turbulent diffusivity. For brevity, the Primitive equations are presented and only certain parts are derived below.

The **horizontal momentum** equations are given by

$$\frac{\partial \vec{U}_h}{\partial t} = -\left[\left(\nabla_h \times \vec{U}\right) \times \vec{U} + \frac{1}{2}\nabla_h\left(\vec{U}^2\right)\right]_h - f\vec{k} \times \vec{U}_h - \frac{1}{\rho_0}\nabla_h p + \vec{F}^{\vec{U}}, \tag{2.5}$$

where

$$\vec{F}^U(\vec{U}_h) = \frac{\partial}{\partial z}\left(\nu \frac{\partial \vec{U}_h}{\partial z}\right) + \nu_h[\nabla_h(\nabla \cdot \vec{U}_h) - \nabla \times (\nabla_h \times \vec{U}_h)], \tag{2.6}$$

with $\nabla_h = \left[\frac{\partial}{\partial x}, \frac{\partial}{\partial y}, 0\right]$ being the horizontal nabla operator.

The **vertical momentum** equation is given by

$$\frac{\partial p}{\partial z} = -\rho g. \tag{2.7}$$

The **conservation of mass** equation is given by

$$\nabla \cdot \vec{U} = 0. \tag{2.8}$$

The **tracer equations** for salinity and temperature are given by

$$\frac{\partial T}{\partial t} = -\vec{U} \cdot \nabla T + D^T + F^T, \tag{2.9}$$

$$\frac{\partial S}{\partial t} = -\vec{U} \cdot \nabla S + D^S, \tag{2.10}$$

where

$$F^T = \frac{1}{\rho_0 C_p}\frac{\partial I}{\partial z}, \tag{2.11}$$

$$F^S = E_f - P_f, \tag{2.12}$$

$$D^T = \frac{\partial}{\partial z}\left(K\frac{\partial T}{\partial z}\right) + \nabla_h \cdot (K_h \nabla_h T), \tag{2.13}$$

$$D^S = \frac{\partial}{\partial z}\left(K\frac{\partial S}{\partial z}\right) + \nabla_h \cdot (K_h \nabla_h S). \tag{2.14}$$

The heat fluxes are incorporated in Eqn. 2.9 via the irradiance term (Eqn. 2.11). The non-penetrative heat flux includes the sum of the latent, sensible, longwave and sea-ice heat fluxes. The penetrative heat flux is the solar flux.

The **equation of state** is a non-linear function of $T$, $S$ and $p$ that takes the functional form

$$\rho = \rho(T, S, p), \tag{2.15}$$

where t is time, $f = \vec{\Omega} \cdot \vec{k}$ the Coriolis parameter, $\vec{\Omega}$ the earth's angular frequency vector, $\rho_0 = 10^3\ \mathrm{kg\,m^{-3}}$ the reference density, $g = 9.8\ \mathrm{m\,s^{-2}}$ the gravitational acceleration, $\rho$ the *in situ* density, S the salinity, T the temperature, z the vertical coordinate, p the pressure, I the irradiance, $C_p$ the specific heat capacity, $\nu_h$ denotes the horizontal viscosity, $\nu$ the vertical viscosity, $K_h$ the horizontal diffusivity, $K$ the vertical diffusivity, $E_f$ the evaporation surface flux, $P_f$ the precipitation surface flux. $F^S$ is the surface forcing terms for the salinity tracer equation (Eqn. 2.10). $F^T$ describes the change of irradiance with depth. $D^S$ and $D^T$ are parameterizations for small scale physics (or diffusion terms) including momentum, salinity and temperature effects. The interested reader can refer to Appendix A for the derivation of the momentum and mass balances.

The following assumptions (Madec, 2008) were applied to the Navier-Stokes equations to derive the Primitive equations (Eqns. 2.5-2.15):

1. Spherical earth approximation
2. Thin shell approximation
3. Boussinesq approximation
4. Hydrostatic approximation
5. Incompressibility approximation

The assumptions are shown in Fig. 2.5. The spherical earth approximation assumes the earth is spherical. This assumption allows the use of the well developed mathematical operations on spheres. The thin shell approximation assumes the ratio of the depth of the ocean to the radius of the earth is minuscule, i.e. $\frac{z_{max\ depth\ of\ ocean}}{r_{earth}} \approx 0$, implying any terms involving this ratio can be ignored. The Boussinesq approximation was assumed in obtaining the vertical momentum equation (Eqn. 2.7). This assumption assumes density changes have no effect on the flow except for producing buoyancy forces (COMSOL, 2017), i.e. the upward pressure force and the downward gravitational force at a certain depth in the ocean are balanced. The hydrostatic approximation has important implications, namely vertical convection, i.e. density-driven vertical movement of water parcels is absent. Due to the absence of dynamical vertical convection, artificial mixing methods have to be employed such as a turbulence scheme. This assumption is a key aspect of this study. The hydrostatic assumption also implies that the density must remain stable, i.e. monotonously increasing with depth without any heavy waters on top of lighter waters. If heavy waters are found above lighter waters, prescribed vertical mixing takes effect for density stabilization. Lastly, the incompressibility constraint forces the total derivative of density of the fluid (ocean water in this case) to be 0. This has the consequence that the density is only affected by the advection of salinity and temperature and not due to volumetric changes of the fluid itself. This assumption affects the mass balance equation (Appendix A) for a compressible fluid.

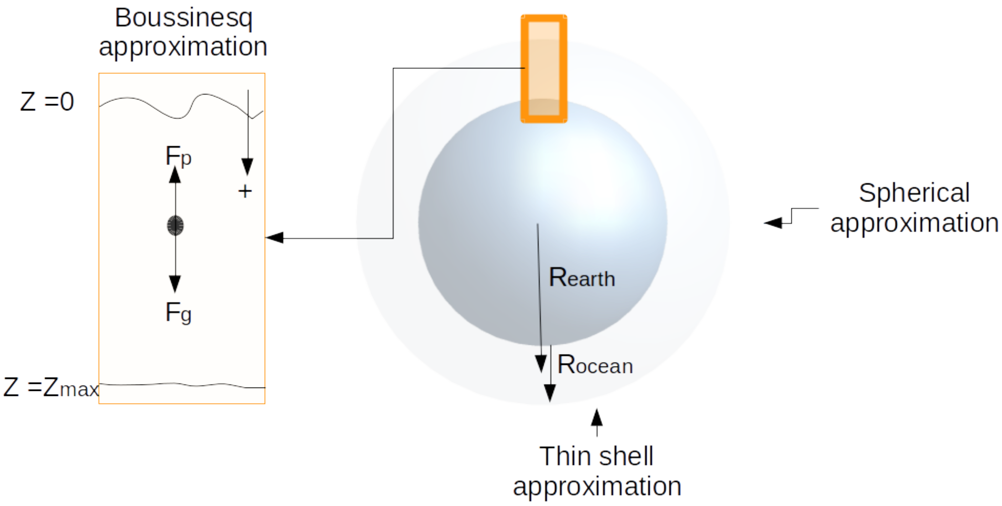

FIGURE 2.5: Depiction of assumptions applied to the Navier-Stokes equations for a rotating sphere in deriving the Primitive equations. The spherical approximation assumes a spherical earth, the thin shell approximation assumes the ocean depth to earth radius ratio is 0 and the Boussinesq approximation assumes no vertical transport, i.e. pressure force balances gravitational force. The positive direction is downwards from the surface to bottom.

$$\frac{\partial \rho(t)}{\partial t} - \nabla \cdot (\rho(t)\vec{U}) = 0. \tag{2.16}$$

Using the assumption that the total derivative of $\rho$ is 0, Eqn. 2.16 becomes

$$\frac{\partial \rho}{\partial t} - \rho \nabla \cdot (\vec{U}) = 0,$$

which simplifies to Eqn. 2.8.

The tracer equations (Eqns. 2.9-2.10) are essential for solving the Primitive equations because temperature and salinity are physical properties of the oceans that can be measured and validated against. The equations are constructed from source/sink, convective ($\vec{U} \cdot \nabla_h T$) and diffusive terms (Eqns. 2.13 and 2.14). The convective term transports the tracer throughout the domain of interest and the diffusive term spreads the quantity. A variety of tracer variables can be included into the model, namely carbon dioxide, nutrients, plankton, oil, salt, temperature, etc (Smith et al., 2016). Temperature and salinity are the only tracers used in this study.

### 2.3.2 One-dimensional form of Primitive equations

The Primitive equations were adapted to model a single vertical water column. This entailed singling out the vertical change $\left(\frac{\partial}{\partial z}\right)$ terms and discarding horizontal gradient terms, i.e. $\nabla_h = \vec{0}$. Note that a few horizontal gradient terms may still need to be present in order to parameterize certain oceanic phenomenon such as tides and the effect of eddies moving in the horizontal. In this study however, these phenomenon are not parameterized. These simplifications imply Eqn. 2.8 becomes

$$-\frac{\partial u}{\partial x} - \frac{\partial v}{\partial y} = \frac{\partial w}{\partial z},$$

$$\implies -\nabla_h \cdot \vec{U} = \frac{\partial w}{\partial z},$$

$$\implies \frac{\partial w}{\partial z} = 0 \implies w = \text{ constant} = 0, \tag{2.17}$$

where the constant is arbitrary and is set to 0. This has the implication that the vertical velocity throughout the water column is 0 (although diffusion effects are still present causing dissipation of energy and momentum through the column). On finer examination of the tracer equations (Eqns. 2.9 and 2.10), the terms $-\vec{U} \cdot \nabla T$ and $-\vec{U} \cdot \nabla S$ can be decomposed into the horizontal and vertical component, i.e. $-\vec{U} \cdot \nabla_h T + w\frac{\partial T}{\partial z}$ (and similar equation segment for salinity) which is simply 0 from using Eqn. 2.17. Applying the simplifying assumptions ($\nabla_h = \vec{0}$ and $w = 0$) on Eqns. 2.5, 2.9 and 2.10 yields

$$\boxed{\frac{\partial \vec{U}_h}{\partial t} = -f\vec{k} \times \vec{U}_h + \frac{\partial}{\partial z}\left(\nu \frac{\partial \vec{U}_h}{\partial z}\right)}, \tag{2.18}$$

$$\boxed{\frac{\partial T}{\partial t} = \frac{\partial}{\partial z}\left(K\frac{\partial T}{\partial z}\right) + \frac{1}{\rho_0 C_p}\frac{\partial I}{\partial z}}, \tag{2.19}$$

$$\boxed{\frac{\partial S}{\partial t} = \frac{\partial}{\partial z}\left(K\frac{\partial S}{\partial z}\right) + E_f - P_f}. \tag{2.20}$$

Eqns. 2.18-2.20 are the one-dimensional form of the Primitive equations used for this study. Although the horizontal processes were filtered out, they can still be parameterized (Optis and Monahan, 2017). In this study however, all horizontal processes are ignored.

### 2.3.3 Nucleus for the European Modelling of the Ocean (NEMO)

The Nucleus for European Modelling of the Ocean (NEMO) is an oceanographic computational modelling program used to model a variety of phenomena in the ocean. NEMO is used in many current models for ocean forecasting and predictability (Tonani et al., 2015) and is also capable of handling biogeochemistry, sea-ice and tracer capabilities (Madec, 2008; Gehlen et al., 2015). NEMO is an integral component of data assimilation in operational oceanography (Martin et al., 2015). NEMO includes test cases (preconfigured configurations) which can be tailored and adapted according to the users needs. It falls under the public CeCILL license (CeCILL, 2017), meaning the source code is freely available for use.

NEMO was chosen for this study due to its powerful capabilities and predefined configurations that were used for modelling one-dimensional vertical processes (Reffray et al., 2015). NEMO has also been widely used for modelling the SO (Biastoch et al., 2008).

### 2.3.4 Grids

Most ocean modelling software uses an Arakawa C grid (Arakawa and Lamb, 1977) for the domain (horizontal and vertical). The grid members (A, B, C, D or E Arakawa grid) differ due to the arrangement of model variables on the staggered grids. NEMO uses the C grid because the variables are conveniently staggered for efficient computation of the discretized Primitive equations (see Madec (2008)) and allowing the incorporation of no-slip boundaries, i.e. zero velocity at the boundary (HYCOM, 2016; Adcroft et al., 2016; Robertson, 2007; Madec, 2008). Grid resolutions in the vertical and horizontal differ considerably in scale because the vertical span of the ocean is deepest at 11 $\mathrm{km}$ whereas the horizontal spans hundreds of kilometres. This is noted from global ocean model configurations run by other research groups (Marsland et al., 2003; Bernard et al., 2006; Dutay et al., 2002; Mercator, 2008) having a vertical resolution of O(1-900 $\mathrm{m}$) and horizontal resolution of O(1/12-4°)≈O(10-400 $\mathrm{km}$).

The sections above have discussed the model, boundary conditions and grid, however these alone cannot account for the vertical mixing. A turbulence closure scheme is needed in conjunction to the model for closing the equations as well as to parameterizing the vertical turbulent viscosity and diffusivity.

## 2.4 Categories of vertical turbulence schemes

Many attempts have been made to represent the various turbulence inducing phenomenon into parameterizations useful for modelling them.

The major component of turbulence modelling is to accurately parameterize the oceanic vertical exchanges and mixing processes. This is done by determining turbulent viscosity and turbulent diffusivity values (Versteeg and Malalasekera, 2007; Namin et al., 2017). As seen in Section 2.3.1, these variables were shown as $\nu_h$, $\nu$ (horizontal and vertical viscosity respectively), $K_h$ and $K$ (horizontal and vertical diffusivity respectively). $K$ and $\nu$ will be referred to as the diffusivity and viscosity respectively henceforth. Turbulence schemes attempt to determine the turbulent coefficients, $K$ and $\nu$, as accurate as possible through various prognostic equations (excluding the Pacanowski/Philander scheme outlined below) with limiting constraints from the type of scheme. In many cases, these coefficients are arbitrarily selected to be constant or adjusted to conform to agreement with observed data (Gregg, 1987).

Most models resolve turbulence due to shear instabilities, whereas other sources of turbulence generation such as diapycnal mixing or tidal mixing need to be parameterized (Gregg, 1987). NEMO comes with a range of turbulence schemes that can be applied to simulate the vertical mixing in a water column. The turbulence schemes considered for this study are the $k-\varepsilon$ (Rodi, 1987), $k-\omega$ (Wilcox, 1988), Mellor-Yamada (M-Y or k-kl) (Mellor and Yamada, 1982), Turbulent Kinetic Energy (TKE) (Blanke and Delecluse, 1993), Generic (Umlauf and Burchard, 2003) and Pacanowski/Philander (Pacanowski and Philander, 1981) schemes. A good comparison between the $k-\varepsilon$, M-Y, Generic and $k-\omega$ schemes is given by Warner et al. (2005). In regards to the operation in NEMO, only one turbulence scheme may be used per simulation.

Diffusivity measures the strength of diffusion in a fluid pertaining to a specific property, e.g. mass diffusivity, thermal diffusivity or turbulent diffusivity. The diffusivity coefficients originate from the parameterization of the Reynolds stresses and turbulent tracer fluxes (shown in Eqns. 2.2-2.3).

There are various forms of diffusivities for example, molecular diffusivity is a physical process in fluids, describing the thermal conduction and momentum transfer between molecules. After the diffusion process has occurred, it cannot be completely reversed. The vertical turbulent eddy diffusivity ($K$ and herewith referred to as diffusivity) is a prognostic model variable (see Sections 2.4.2 and 2.4.3 below) that is an effective measure of local turbulence strength in the spatial domain. Higher diffusivities imply higher turbulence in the local region. The diffusivity's underlying effect is the smoothing or reducing of steep gradients in temperature, salinity and momentum. This is easily understood in the situation where there is a lower temperature water parcel above a higher temperature parcel, i.e. there is an overturning in the water column. The lower temperature parcel tends to sink interacting with the higher temperature parcel. The diapycnal mixing process allows for heat exchange between parcels thereby shallowing the gradients to the extent of the diffusivity value. The turbulent diffusivity is not a physical property and was created as a convenient means to serve as the proportionality coefficient between Reynolds stresses and diffusion terms. The effects of molecular diffusion is significantly smaller (O($10^{-6}$ $\mathrm{m}^2\,\mathrm{s}^{-1}$)) than the turbulent diffusivity, which dominates in turbulent regions and is generally larger (by a few orders of magnitude). Generally in the deep ocean interior, molecular diffusivity dominates due to low turbulence levels.

The diffusion term contains a divergence of gradient term and when positive, the quantity is diffused into the water column. It is possible to have negative diffusivities locally, as momentum or thermal build-up is possible. This will not cause any long term instabilities or errors. A global negative diffusivity however, will cause inaccurate results due to momentum and energy concentrating locally. It is preferable to have positive momentum diffusion (downwards) within the vertical column even though locally the momentum diffusion may be negative (Gent and Mcwilliams, 1990).

The turbulent Prandtl number is defined by

$$Pr_{tr} = \frac{\nu}{K}. \tag{2.21}$$

Each turbulent closure scheme computes the diffusivity and viscosity separately. The Prandtl number however, can be considered to be approximately constant (with minor variations) and can to a degree be treated as an invariant (Kawamura et al., 1999). This implies it is not necessary to perform rigid analysis on $\nu$ as an analysis on $K$ will suffice. This approach was used in the results section (Chapter 4).

All turbulence schemes (with exception of the Pacanowski/Philander scheme) outlined in the following subsections use local prognostic variables (for example length scales) for parameterizing the diffusivity and viscosity (Li et al., 2001). According to Mellor and Yamada (1982), the dependence on a single length scale variable is a considerable disadvantage for turbulence schemes as length scales are based on empirical measurements.

Turbulence schemes have a turbulent kinetic energy variable ($k$) that describes the amount of energy available for turbulence in the system. In advanced schemes an additional parameter $\varepsilon$ is introduced, referred to as the turbulent dissipation which describes the dissipation of $k$. The evolution of $k$ and $\varepsilon$ are governed by separate transport equations containing time evolution, diffusion, convection and forcing terms.

The overview of turbulence schemes begins with the Pacanowski/Philander scheme which is included in the Richardson number based schemes, i.e. simplest schemes. Following, are the TKE family of schemes and lastly the Generic Length Scale (GLS) family of schemes are addressed.

### 2.4.1 Richardson number based turbulence schemes: Pacanowski/Philander scheme

Prior schemes to the Pacanowski/Philander scheme (Pacanowski and Philander, 1981) used very crude techniques for parameterizing the vertical diffusivity and viscosity, i.e. only constant values for turbulent viscosity and diffusivity were used (Cummins, 1991). This turbulence scheme had improved results drastically to prior techniques and is occasionally still used today however, it has been outdated due to better schemes. The Pacanowski/Philander scheme is based on a parameterization through the Richardson number (the ratio of buoyancy to shear effects of the fluid in focus). The Richardson number ($Ri$) used by Pacanowski and Philander (1981) takes the form

$$Ri = \frac{N^2}{\left(\dfrac{du}{dz}\right)^2 + \left(\dfrac{dv}{dz}\right)^2}, \tag{2.22}$$

where $N$ is the Brunt Väisälä frequency (fully explained in Section 3.5.1). Use of the Richardson number to parameterize the viscosity and diffusivity coefficients yields

$$\nu = \frac{\nu_0}{(1 + \alpha Ri)^n} + \nu_b, \tag{2.23}$$

$$K = \frac{\nu}{(1 + \alpha Ri)} + K_b, \tag{2.24}$$

where $\nu_b$ and $K_b$ are background eddy viscosity and diffusivity respectively and $\alpha$ (not to be confused with the thermal expansion coefficient), $\nu_0$ and $n$ are adjustable parameters. Pacanowski and Philander (1981), who mainly focussed on the equatorial region, found that $\nu_0$, $\alpha$ and $n$ had the property of increasing/decreasing the shear and speed of the simulated equatorial jet. They also found that with careful parameter selection of $\nu_0,\ n,\ \alpha,\ \nu_b$ and $K_b$ a mixed layer (see Fig. 3.12) could be achieved in simulations.

Li et al. (2001) highlights the advantages and shortcomings of the Pacanowski/Philander scheme. The main advantage is that there is minimal computational cost in employing this scheme, i.e. this scheme is very efficient. Turbulence measurements carried out by Peters et al. (1988) found that the Pacanowski/Philander scheme underestimates the mixing at low $Ri$ while overestimates the mixing at high $Ri$ (Li et al., 2001). It has also been reported by Stammer et al. (1996) that the Pacanowski/Philander scheme performs unsatisfactorily in the extra tropics. In the Mediterranean however, the Pacanowski/Philander scheme performs satisfactorily as shown by Lovato et al. (2013) and Oddo et al. (2009).

In NEMO, the Pacanowski/Philander scheme can be located under the Richardson number based schemes section and is not named the Pacanowski/Philander scheme specifically (see Appendix B).

### 2.4.2 Turbulent Kinetic Energy (TKE) family of turbulence schemes (TKE0, TKE10 and TKE30)

The class of turbulence schemes, known as the TKE family, are fundamentally different to Richardson number based schemes which are algebraic. TKE schemes are known to be a 1.5 equation scheme involving a prognostic equation for $k$. The equations for the TKE turbulence closure scheme were originally developed by Gaspar (1988). Blanke and Delecluse (1993) implemented the TKE scheme in a computational model for the equatorial Atlantic ocean. The full set of equations for the TKE scheme used by Blanke and Delecluse (1993) are presented here. The turbulent kinetic energy variable is defined as

$$k = \frac{1}{2}\left(\overline{u'^2} + \overline{v'^2} + \overline{w'^2}\right). \tag{2.25}$$

The prognostic equation and budget for the time evolution of $k$ is governed by

$$\frac{\partial k}{\partial t} = -\frac{\partial\left(\overline{kw'} + \rho_0^{-1}\overline{p'w'}\right)}{\partial z} - \overline{\vec{u}'_h w'} \cdot \frac{\partial \vec{U}_h}{\partial z} + \overline{b'w'} - \varepsilon, \tag{2.26}$$

where $b' = g\rho_0^{-1}\rho'$ is the buoyancy and $\varepsilon$ is the turbulence dissipation rate. The vertical turbulent fluxes are parameterized using the vertical diffusivity and viscosity according to

$$-\overline{\vec{u}'_h w'} = \nu \frac{\partial \vec{U}_h}{\partial z}, \tag{2.27}$$

and

$$-\overline{b'w'} = -g\rho_0^{-1}K\frac{\partial \rho}{\partial z} = KN^2. \tag{2.28}$$

The introduction of an extra non-constant mixing coefficient $K_e$ (turbulent thermal diffusivity) is needed to incorporate the turbulent and pressure effects being expressed as a diffusion process

$$-\left(\overline{kw'} + \rho_0^{-1}\overline{p'w'}\right) = K_e\frac{\partial k}{\partial z} = 0. \tag{2.29}$$

The terms in Eqn. 2.29 are parameterized for theory closure but is actually 0. The $\overline{kw'}$ is the product of a mean and fluctuating quantity. The mean value is a constant rendering this term a fluctuating quantity. Due to the Reynolds averaging procedure this is clearly 0. The second term, $\overline{p'w'}$, involves the pressure fluctuation which is 0 because there is no pressure change (fluctuation) for a fixed depth in the ocean model.

$K$, $\nu$ and $\varepsilon$ are parameterized by defining a characteristic dissipation length ($l_\varepsilon$) and a characteristic mixing length ($l_K$) (Blanke and Delecluse, 1993), given by

$$K = \frac{\nu}{P_r}, \tag{2.30}$$

$$\nu = C_K l_K k^{1/2}, \tag{2.31}$$

$$\varepsilon = C_\varepsilon k^{3/2} l_\varepsilon^{-1}, \tag{2.32}$$

where $C_\varepsilon$ and $C_K$ are model constants and $P_r$ is the turbulent Prandtl number (defined as the ratio of the momentum diffusivity to the turbulent thermal diffusivity) (Tominaga and Stathopoulos, 2007). For convenience, two master length scales ($l_u$ and $l_d$) are chosen to indicate upward or downward conversions of TKE into potential energy defined through the integral equations

$$g\rho_0^{-1}\int_{z_0}^{z_0+l_u(z_0)}[\rho(z_0)-\rho(z)]dz = k(z_0), \tag{2.33}$$

$$g\rho_0^{-1}\int_{z_0-l_d(z_0)}^{z_0}[\rho(z)-\rho(z_0)]dz = k(z_0), \tag{2.34}$$

where $z_0$ is a user defined reference level. $l_K$ and $l_\varepsilon$ are further parameterized by $l_u$ and $l_d$ and are given by

$$l_K(z_0) = min[l_u(z_0), l_d(z_0)], \tag{2.35}$$

$$l_\varepsilon(z_0) = [l_u(z_0)l_d(z_0)]^{1/2}. \tag{2.36}$$

After substitution of the various parameterizations, Eqn. 2.26 becomes

$$\frac{\partial k}{\partial t} = \nu M^2 - KN^2 - \varepsilon, \tag{2.37}$$

where $M^2 = \frac{\partial \vec{U}_h}{\partial z}\cdot\frac{\partial \vec{U}_h}{\partial z} = \left(\frac{\partial u}{\partial z}\right)^2 + \left(\frac{\partial v}{\partial z}\right)^2$ is known as the shear frequency. For a high shear frequency term, the turbulent viscosity and diffusivity are enhanced leading to higher turbulence due to shear. Similarly for a large stratification (term with large positive $N$) the turbulence is suppressed. In the case however, where $N$ becomes negative (namely unstable stratification), turbulence is enhanced, i.e. $-KN^2$ becomes a turbulent kinetic energy production term (Soontiens and Allen, 2017).

Effectively, the TKE schemes calculates the amount of turbulent kinetic energy, dissipation of turbulent kinetic energy generated and a turbulent length scale, which are related according to the equations above, in order to determine coefficients for turbulent diffusivity and viscosity used in the one-dimensional form of the Primitive equations (Eqns. 2.18-2.20).

NEMO has three options in the family of TKE schemes, namely TKE0, TKE10 and TKE30. The 0, 10 and 30 are associated with the length scales $l_u$ and $l_d$. Turbulent kinetic energy is injected at 0 $\mathrm{m}$, 10 $\mathrm{m}$ or 30 $\mathrm{m}$ below the Mixed Layer Depth (MLD). Advantages of these schemes include the cheap cost, absence of a wall function (needed by particular schemes to deal with turbulent impenetrable boundaries) (Blanke and Delecluse, 1993) as well as the unconditional stability of the schemes due to being implicit. Regarding the operation in NEMO, the TKE0, TKE10 and TKE30 turbulence schemes fall under the same TKE category (Appendix B).

### 2.4.3 Generic Length Scale (GLS) family of turbulence schemes (Generic, $k-\varepsilon$, $k-\omega$ and Mellor-Yamada (M-Y))

The Generic Length Scale (GLS) family of schemes are a further improvement compared to the TKE schemes in the sense that there is a prognostic equation for the dissipation of turbulent kinetic energy ($\varepsilon$). The first systematic study for the creation of a general framework for 2.5 equation schemes were successfully carried out by Umlauf and Burchard (2003). They identified a 2.5 equation scheme with variable user defined parameters that when chosen correctly, recover the $k-\varepsilon$, $k-\omega$, M-Y (k-kl) and other schemes not mentioned in this study. The advantage (and convenience) of this framework is that a comparison of the schemes can be carried out using the same numerical discretization (Soontiens and Allen, 2017). These set of schemes contain a prognostic equation for $k$ and a generic variable $\psi$. A new scheme was introduced through this framework, termed the Generic scheme by Umlauf and Burchard (2003). The equations are outlined below beginning with the prognostic transport equation for turbulent kinetic energy

$$\frac{\partial k}{\partial t} + \vec{U} \cdot \nabla k = D_k + \nu M^2 - K N^2 - \varepsilon, \tag{2.38}$$

where $\vec{U}$ is the velocity, $D_k$ the turbulent and viscous transport (or diffusion) term, $M^2$ (shear frequency) and $N^2$ (buoyancy or Brunt Väisälä frequency) the turbulent kinetic energy production terms due to shear and buoyancy effects respectively. The diffusion term is given by

$$D_k = \frac{\partial}{\partial z}\left(\frac{\nu}{\sigma_k}\frac{\partial k}{\partial z}\right), \tag{2.39}$$

where $\sigma_k$ is a constant Schmidt number (the ratio of the viscosity to mass diffusivity) (Tominaga and Stathopoulos, 2007). The dissipation, $\varepsilon$, is parameterized through a generic variable (or turbulent quantity), $\psi$, introduced by Umlauf and Burchard (2003) and is given by

$$\varepsilon = (C_\mu^0)^{3+(p/n)} k^{3/2+(m/n)} \psi^{-1/n}, \tag{2.40}$$

where $C_\mu^0$, $m$, $n$ and $p$ are model constants. The generic variable (or turbulent quantity) $\psi$ can also be written in terms of the length scale $l$ and is given by

$$\psi = (C_\mu^0)^p k^m l^n \tag{2.41}$$

where $\psi$ is an invertible function of both $k$ and $l$. The prognostic transport equation governing the turbulent quantity $\psi$ is given by

$$\frac{\partial \psi}{\partial t} + \vec{U} \cdot \nabla \psi = D_\psi + \frac{\psi}{k}\left(C_{\psi 1} \nu M^2 - C_{\psi 3} K N^2 - C_{\psi 2} \varepsilon\right), \tag{2.42}$$

where $C_{\psi 1}$, $C_{\psi 2}$ and $C_{\psi 3}$ are model constants and $D$ represents the diffusion term given by

$$D_\psi = \frac{\partial}{\partial z}\left(\frac{\nu}{\sigma}\frac{\partial \psi}{\partial z}\right), \tag{2.43}$$

where $\sigma_\psi$ is a constant Schmidt number. The diffusivity and viscosity is parameterized as follows

$$\nu = C_\mu \sqrt{k} l \quad \text{and} \quad K = C_\mu' \sqrt{k} l, \tag{2.44}$$

where $C_\mu$ and $C_\mu'$ are known as stability functions. This study uses Canuto A stability functions (Canuto et al., 2001) because Reffray et al. (2015) points out that Burchard and Bolding (2001) found Canuto A functions yielded better results than other stability functions. In summary, the transport equations take the final form

$$\frac{\partial k}{\partial t} + \vec{U} \cdot \nabla k = \frac{\partial}{\partial z}\left(\frac{\nu}{\sigma_k}\frac{\partial k}{\partial z}\right) + \nu M^2 - K N^2 - \varepsilon, \tag{2.45}$$

$$\frac{\partial \psi}{\partial t} + \vec{U} \cdot \nabla \psi = \frac{\partial}{\partial z}\left(\frac{\nu}{\sigma}\frac{\partial \psi}{\partial z}\right) + \frac{\psi}{k}\left(C_{\psi 1} \nu M^2 - C_{\psi 3} K N^2 - C_{\psi 2} \varepsilon\right). \tag{2.46}$$

Using Eqns. 2.40, 2.41, 2.45 and 2.46, it is possible to recover the $k-\varepsilon$, $k-\omega$ and M-Y schemes by specifying correct values for model constants: $p, n, m, C_{\psi 1}, C_{\psi 2}, C_{\psi 3}$ and Schmidt numbers: $\sigma_k, \sigma_\psi$. Umlauf and Burchard (2003) had created their Generic scheme by specifying unique values for the model constants and Schmidt numbers. They had found values for the model constants from various test cases performed. The corresponding parameter values for each turbulence scheme are displayed in Table 2.1. Note the Mellor-Yamada scheme depends on a wall function ($F_{wall}$) whereas the $k-\varepsilon$, $k-\omega$ and Generic schemes do not. This can be viewed as a limitation for the Mellor-Yamada scheme as extra computation is involved.

TABLE 2.1: Model constants and Schmidt number values defining the various turbulence schemes in the Generic equations framework of Umlauf and Burchard (2003). $F_{wall}$ represents the wall function needed for the Mellor-Yamada scheme to operate. The values for $C_{\psi3}$ can be varied depending on the mixed layer depth dynamics of the ocean model (Umlauf and Burchard, 2003). The values used in the NEMO model are all 1 and are shown below.

| Constants and Schmidt number variables | M-Y (k-kl) | $k-\varepsilon$ | $k-\omega$ | Generic |
|---|---|---|---|---|
| p | 0 | 3 | -1 | 0 |
| m | 1 | 1.5 | 0.5 | 1 |
| n | 1 | -1 | -1 | -0.67 |
| $C_{\psi1}$ | 0.9 | 1.44 | 0.555 | 1 |
| $C_{\psi2}$ | 0.5 $F_{wall}$ | 1.92 | 0.833 | 1.22 |
| $C_{\psi3}$ | 1 | 1 | 1 | 1 |
| $\sigma_k$ | 1.96 | 1 | 2 | 0.8 |
| $\sigma$ | 1.96 | 1.2 | 2 | 1.07 |

Effectively, the GLS set of schemes calculates the generated amount of turbulent kinetic energy and the dissipation of turbulent kinetic energy (from the respective prognostic equations) in order to determine coefficients for turbulent diffusivity and viscosity utilized in the one-dimensional form of the Primitive equations (Eqns. 2.18-2.20) (Walsh et al., 2017). The Generic framework is a powerful formulation which neatly unified seemingly unrelated turbulence schemes. These turbulence closure scheme parameterizations were originally implemented in the public General Ocean Turbulence Model (GOTM) and is now fully incorporated in NEMO.[1]

### 2.4.4 Alternative turbulence schemes

Various other turbulence schemes are provided in NEMO, namely double diffusive mixing parameterization, tidal mixing parameterization, new tidal mixing parameterization and K-Profile Parameterization (Madec, 2008). Turbulence schemes not incorporated in NEMO include Yonsei University Scheme or YSU, Quasi-Normal Scale Elimination (QNSE) and various others (Optis and Monahan, 2017). These schemes were not implemented and do not fall within the scope of the current study.

## 2.5 Importance of Reffray et al. (2015) work in relation to this study

Reffray et al. (2015) had carried out a study of simulating a one-dimensional water column in order to determine the turbulence response. They implemented the vertically reduced Primitive equations (Eqns. 2.18-2.20) into NEMO to create a configuration named C1D_PAPA for simulating the water column. Their study was located at 50.1°N, 144.9°W in the NP shown in Fig. 2.4. The time period of focus was the annum 15 June 2010 - 14 June 2011. The simulations consisted of implementing different turbulence closure schemes ($k-\varepsilon$, M-Y, $k-\omega$, Generic, TKE0, TKE10 and TKE30) to investigate the dynamics of the upper water column. Reffray et al. (2015) had not implemented the Pacanowski/Philander scheme (or any other) in their study. Further simulations included combinations between time steps of 360 s, 1200 s and 3600 s as well as 75 and 31 vertical grid levels.

The temperature and salinity results that they had found were validated using data obtained from ocean buoy station *PAPA* (NOAA, 2016). The Root Mean Square Errors (RMSE) were also calculated. From their study, they concluded that $k-\varepsilon$ scheme performed the best compared to the other turbulence schemes tested. The $k-\varepsilon$ scheme results produced the least bias (simulated result subtract validation data) and lowest RMSE values from the validation process.

---

[1] http://www.gotm.net

Further details on their method are presented in the following Chapter (Chapter 3) because this study builds upon their work. A turbulence response and mixing sensitivity analysis will be carried out using the same turbulence schemes Reffray et al. (2015) had used with the addition of the Pacanowski/Philander turbulence scheme. The schemes will be applied to a one-dimensional model for a location in the SO.

## 2.6 Summary of literature

This chapter has provided an overview of the Primitive equations which forms the basis of any ocean model. The associated fundamental assumptions used in reducing the full set of Primitive equations to a one-dimensional form (vertical direction only) were shown. The vertical component of the Primitive equations were derived using these assumptions and were deemed useful for testing the dynamics of vertical processes. Various turbulence closure scheme parameterizations (Pacanowski/Philander , TKE, $k - \varepsilon$, $k - \omega$, M-Y and Generic) used in this study were briefly discussed. The following chapter outlines the methodology which applies the work done by Reffray et al. (2015) in order to model a one-dimensional water column in the SAZ region of the Southern Ocean.

# Chapter 3

# Methods

## 3.1 Introduction

This chapter describes the methodology and process used in order to obtain a NEMO configuration to model the turbulence response and mixing sensitivity of a water column in the sub-Antarctic Zone (SAZ). The advantages, disadvantages, obtaining and processing of input data (namely boundary conditions consisting of reanalyses data and initial conditions consisting of temperature and salinity profiles) are given here. Validation data used in this study are also presented. The methodology begins by explaining the techniques Reffray et al. (2015) had used in their study and how these were adapted and tailored for the Southern Ocean (SO) simulations. This chapter further presents all simulations performed as well as the analysis techniques, univariate indicators and turbulence diagnostics used for the analysis of results.

## 3.2 Research design

This section introduces the technical details of the C1D_PAPA configuration used by Reffray et al. (2015). C1D_PAPA forms the base structure for the SAZ1D configuration. Later in this section the SAZ1D configuration is introduced and the modification of C1D_PAPA to SAZ1D (core section of the methodology) is detailed. The locations pertaining to the C1D_PAPA and SAZ1D configurations are in the Northern Pacific (NP) (50.1°N, 144.9°W) and SO (47°S, 4.5°E) respectively and the approximate locations are shown in Fig. 2.4.

### 3.2.1 One-dimensional fluid configuration in the Northern Pacific (C1D_PAPA )

C1D_PAPA is currently a standard configuration within NEMO (Madec, 2008). The C1D_PAPA configuration is composed of the horizontal and vertical grid (used to achieve one-dimensionality), number of vertical levels, spacing between vertical levels, initial conditions, boundary conditions, turbulence scheme options and general parameter selection. The details of the C1D_PAPA configuration is presented in the below subsections.

#### 3.2.1.1 Horizontal and vertical grid structure

The grid selection and structure plays an important role for turbulence modelling. Most ocean modelling software uses an Arakawa grid (Arakawa and Lamb, 1977) for the domain (horizontal and vertical). The grid members (Arakawa A, B, C, D or E grid) differ due to the arrangement of variables on the staggered grids. NEMO in general, uses the Arakawa C grid because of the conveniently staggered variables for efficient computation of the discretized Primitive equations (discrete form of Eqns. 2.18-2.20) and allowing the incorporation of no-slip boundaries, i.e. zero velocity at the boundary (HYCOM, 2016; Adcroft et al., 2016; Robertson, 2007; Madec, 2008). Grid resolutions in the vertical and horizontal differ considerably in scale because the vertical span of the ocean is deepest at 11 km whereas the horizontal spans hundreds of kilometres. This is noted from global ocean model configurations run by other research groups (Marsland et al., 2003; Bernard et al., 2006; Dutay et al., 2002; Mercator, 2008) having a vertical resolution of O(1-900 m) and horizontal resolution of O(1/12-4°)≈O(10-400 km). The vertical staggered grid is essential for this study and is shown in Fig. 3.1.

Reffray et al. (2015) had performed many one-dimensional simulations using a vertical grid for testing the turbulence response of a water column located in the NP. They stated that for *"purely numerical reasons, the Arakawa A grid is used"* because all quantities (vector and scalar) are calculated at the same grid point, i.e. there is no staggering of grids. In general, a one-dimensional grid would consist of a line of grid points. Due to NEMO's grid structure conventions however, a three dimensional grid had to be used for operation. This implied the use of a minimal three dimensional grid structure which consisted of a $3 \times 3$ horizontal grid, i.e nine nodes per horizontal level. The horizontal resolution is $0.1^{\circ}$ in the zonal and meridional directions. The vertical grid is unbounded and can have as many levels between the surface (0 m) and bathymetry, i.e. the maximum depth at the location. The overall grid has nine columns arranged in a square lattice formation using z-level coordinates as shown in Fig. 3.1.

The one-dimensionality must now be addressed as a three dimensional grid is being used. The concept of making all horizontal gradients zero (see Section 2.3.2) is used to obtain the one-dimensionality needed. This means all scalar and vector quantities per vertical layer on all nine nodes are identical. In other words, scalar and vector quantities vary per vertical level but not per horizontal level. Note that this implies that phenomenon affecting horizontal dynamics are not accounted for.

The model is a rigid-lid model implying $w = 0$ at the surface, removal of kinematic and dynamic effects of small displacements of the surface and suppression of surface gravity-inertial waves (Bryan, 1969). The bottom level is embedded into the ocean bed, i.e. the salinity and temperature values are forced to be 0. The reason is to enforce the no-slip boundary condition and to prevent downwards false convection.

#### 3.2.1.2 Number of vertical levels and vertical spacing between grid levels

The number of vertical levels can be specified by the user and is unbounded. The number of vertical levels are constrained to fit between the surface and bathymetry for the specified location. The NP location bathymetry is 4200 m (GEBCO, 2016).

The number of vertical levels and their distribution are important for resolving the upper dynamics in the water column for this study. Regarding recent ocean simulations in the scientific community, the minimum vertical levels used is approximately 30 (Marsland et al., 2003; Bernard et al., 2006; Dutay et al., 2002; Mercator, 2008). Any number of vertical levels chosen below 30 has a high probability of producing poor results due to the coarse upper resolution. The highest number of vertical levels found to be physically achievable in (global models) is 130 (Marsland et al., 2003; Bernard et al., 2006; Dutay et al., 2002; Mercator, 2008) and any number of vertical levels larger than 130 is too expensive and time consuming to consider. Taking into consideration these number of levels (30 and 130) as limiting constraints, 31, 51, 75 (default value for the C1D_PAPA configuration), 101 and 151 vertical levels were chosen to carry out the simulations (see Fig. 3.3). The *ORCA2* grid configuration (Madec, 2008) which provides parameters for the generation of a 31 vertical level grid was also employed. The *ORCA2* grid configuration has 10 m spacings near the surface and a bathymetry value of 5000 m.

Due to the fact that the bottom vertical level is embedded into the ground, used by NEMO's grid structure (see Fig. 3.1), odd numbered levels were chosen. Overall, this implied that the number of vertical levels that could be used was an even number, i.e. one level less. This meant that when simulating, the useful number of vertical levels used were 30, 50, 74, 100 and 150. An even number of levels is used for convenience as the numerics and data processing are made simpler. 151 vertical levels was used in the simulations for examining the turbulence response of the turbulence schemes under very fine grids for two reasons, namely the simulations are not time intensive for

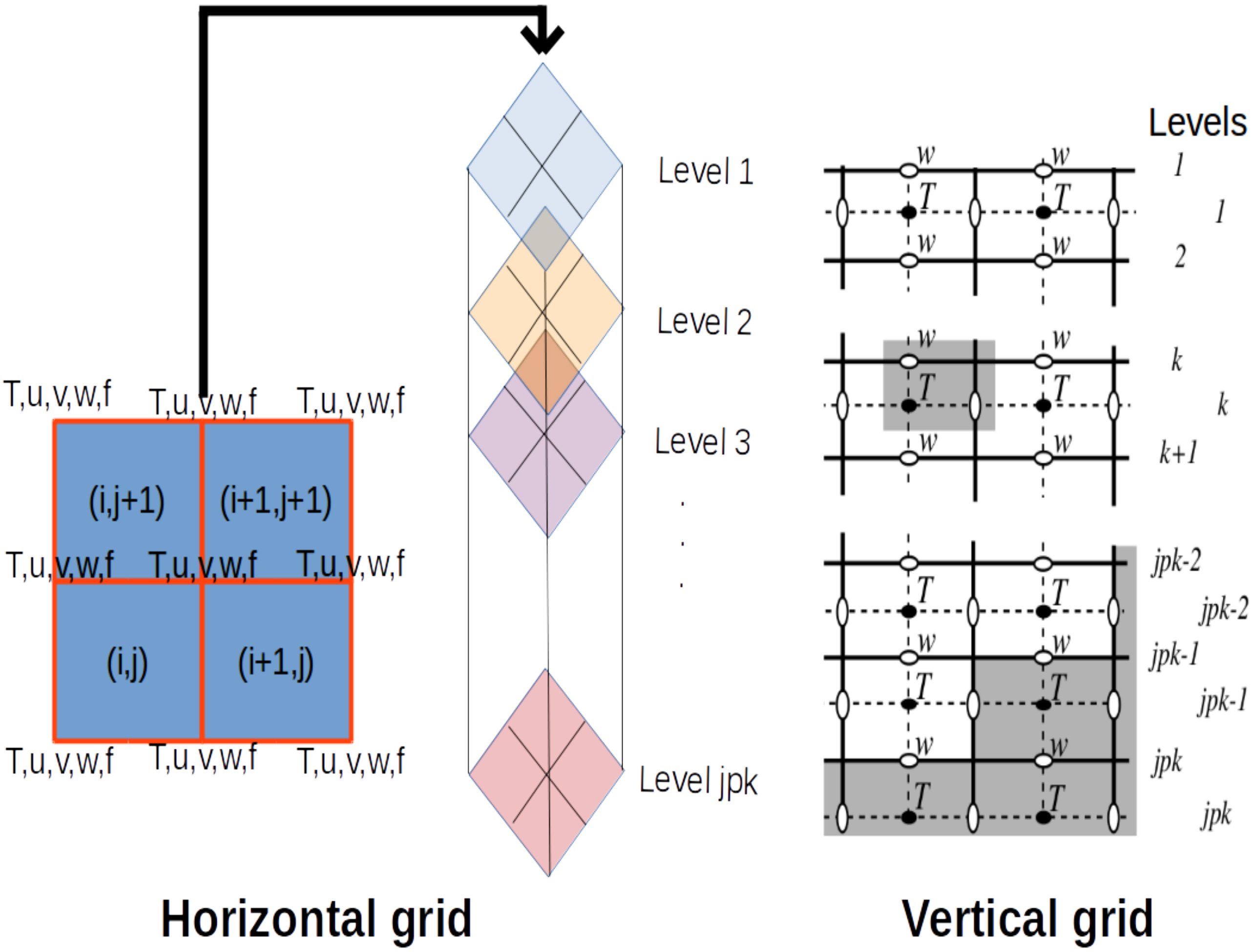

FIGURE 3.1: This figure illustrates the Arakawa A grid structure, horizontal (left) and vertical (right), used for both the C1D_PAPA (Reffray et al., 2015) and SAZ1D configurations.[1] The horizontal grid is composed of nine identical columns. One-dimensionality is enforced by setting horizontal gradients to zero implying scalar and vector quantities per horizontal level are constant. k and jpk are the vertical indexes denoting the $k_{th}$ and bottom vertical level.[2] i and j denote horizontal indexes in $\hat{\imath}$ and $\hat{\jmath}$ directions respectively. $T$ represents scalar quantities where salinity, temperature, density and pressure is defined.[3] $u, v, w$ are velocity components and f is the Coriolis parameter. Adapted from the NEMO manual (Madec, 2008).

one-dimensional models and 151 vertical levels may be physically achievable in the near future due to the rapid advancement in technology.

After determining the number of vertical levels, the vertical spacing between levels must be distributed. Determining the spacing between levels is extremely important for resolving near surface processes. It is favourable to have tight spacing in the vicinity where the physics needs to be resolved accurately. The ocean surface is the area of focus in this study invoking a need for tight spacing in the upper section of the grid.

The technique used for the distribution of vertical spacing between levels (Weisstein, 2017) involves

---

[1] This is actually the vertical staggered Arakawa C grid layout used in NEMO. Solid and dashed lines represent separate grids. k and jpk are indexes denoting the $k_{th}$ and last vertical level in the vertical. The $w$ grid is not used due to the assumption $w = 0$. This implies only the $T$ vertical grid is present which is exactly the vertical Arakawa A grid structure.

[2] In this context, k represents the index for the vertical grid level and must not be confused with the turbulent kinetic energy $k$.

[3] For clarity in this study, it is only in the context of grids where $T$ represents tracer quantities, otherwise it is temperature.

using a modified hyperbolic tangent curve $\left(\tanh(z) \equiv \frac{\sinh}{\cosh} = \frac{e^z - e^{-z}}{e^z + e^{-z}}\right)$. The hyperbolic tangent function is scaled and translated to fit the bathymetry, number of vertical levels and distribute the spacing accordingly. The modified hyperbolic tangent for 75 vertical levels with a bathymetry of 4200 $\mathrm{m}$ is shown in Fig. 3.2 as an example. The valuable property of the modified hyperbolic function and its first derivative being smooth and containing no abrupt discontinuities or kinks is leveraged. Another property of the modified hyperbolic tangent ensures tight spaced levels near the surface and increasing spacing descending deeper into the water column. Near the bottom, the spacing becomes uniform due to the asymptotic nature of the hyperbolic tangent. The spacing near the bottom is coarse because this study does not focus on sediment dynamics or geothermal fluxes which have an insignificant effect near the surface. This distribution of spacing between levels better resolves the finer details of downward convection of momentum and energy at the ocean-atmosphere interface. Other functions can be used for the vertical spacing but the distribution formulation (see Eqns. 3.4 and 3.5 below) would need to change. The hyperbolic tangent spacing was used since NEMO has this distribution available.

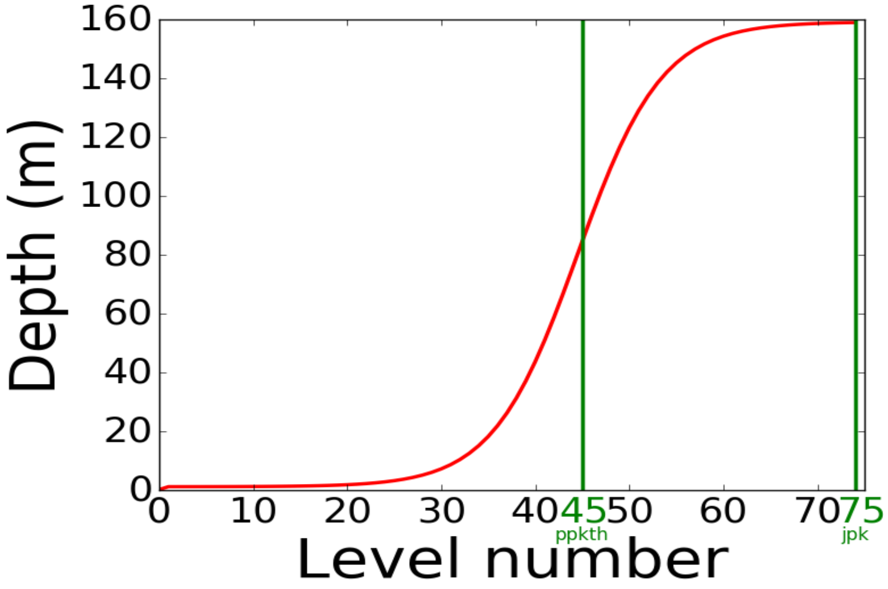

FIGURE 3.2: The modified hyperbolic tangent function plotted using Eqns. 3.4 and 3.5 with 75 vertical levels and bathymetry of 4200 $\mathrm{m}$. The modified hyperbolic tangent is utilised because there are no abrupt discontinuities or kinks are present. The minimum spacing is 1 $\mathrm{m}$ between upper levels and gradually increases descending to the bottom. The fastest rate of increase (point of concavity) is found at $ppkth$ and the bottom vertical level is at $jpk$.

The equations governing the modified hyperbolic tangent function are specified by five parameters, namely *jpk*, *ppacr*, *ppkth*, *ppdzmin* and *pphmax* respectively (Madec, 2008). *jpk* is the number of vertical levels (refer to Fig. 3.2), *ppacr* is a stretching factor (larger values imply smaller stretching), *ppkth* is the level at which maximum rate of stretching occurs, i.e. the point of inflection, *ppdzmin* is the minimum allowable spacing in the upper layer and *pphmax* is the bathymetry at the location, i.e. 4200 $\mathrm{m}$ for the NP. Three intermediate quantities are needed before obtaining the distribution of vertical spacings, namely *za0*, *za1* and *zsur* and are given by

$$za1 = \frac{\left[\frac{ppdzmin - pphmax}{jpk - 1}\right]}{\left[\tanh\left[\frac{1 - ppkth}{ppacr}\right] - (jpk - 1)\ln\left[\cosh\left[\frac{jpk - ppkth}{ppacr}\right]\right] - \ln\left[\cosh\left[\frac{1 - ppkth}{ppacr}\right]\right]\right]}, \tag{3.1}$$

TABLE 3.1: This table displays the chosen grid parameter values for variables *jpk*, *ppacr*, *ppkth*, *ppdzmin* and *pphmax* (Eqns. 3.1-3.5). The parameters used for the NP (C1D_PAPA configuration) and SO (SAZ1D configuration) simulations are shown respectively.

| **jpk (Number of vertical levels)** | **31** | **51** | **75** | **101** | **151** |
|---|---|---|---|---|---|
| **NP (C1D_PAPA ):** | | | | | |
| **ppkth** | 18 | 27 | 45 | 53 | 69 |
| **ppacr** | 3 | 6 | 9 | 12 | 15 |
| **ppdzmin** | 1 | 1 | 1 | 1 | 1 |
| **pphmax** | 4200 | 4200 | 4200 | 4200 | 4200 |
| **SO (SAZ1D ):** | | | | | |
| **ppkth** | 16 | 28 | 50 | 70 | 97 |
| **ppacr** | 2 | 7 | 7 | 14 | 17 |
| **ppdzmin** | 1 | 1 | 1 | 1 | 1 |
| **pphmax** | 4500 | 4500 | 4500 | 4500 | 4500 |

$$za0 = ppdzmin - za1.\tanh\left[\frac{1 - ppkth}{ppacr}\right], \tag{3.2}$$

$$zsur = -za0 - za1.\ln\left[\cosh\left[\frac{1 - ppkth}{ppacr}\right]\right], \tag{3.3}$$

where $\cosh$ and $\ln$ are the hyperbolic cosine and natural logarithm functions respectively. Using Eqns. 3.1-3.3, the reference coordinate transformation, $z_0(\mathrm{k})$, containing the spacings are given by

$$z_0(\mathrm{k}) = zsur - za0.\mathrm{k} + za1.ppacr.\ln\left[\cosh\left[\frac{\mathrm{k} - ppkth}{ppacr}\right]\right], \tag{3.4}$$

and the scale factors, $e_z^0(\mathrm{k})$, are given by

$$e_z^0(\mathrm{k}) = \left| za0 + za1.\tanh\left[\frac{\mathrm{k} - ppkth}{ppacr}\right]\right|, \tag{3.5}$$

where k is the grid vertical index (refer to Fig 3.1). Note $e_z^0(\mathrm{k})$ is the analytical derivative of $z_0(\mathrm{k})$ with respect to k. The cumulative sum of $z_0(\mathrm{k})$ yields the depth for index k. $e_z^0(\mathrm{k})$ is used in NEMO for scaling calculations. The interested reader is referred to Appendix B for technical aspects detailing the implementation of Eqns. 3.1-3.5 for the C1D_PAPA and SAZ1D configurations.

The grids consisting of different vertical levels were created from adjusting the parameters, $jpk$, $ppacr$, $ppkth$, $ppdzmin$ and $pphmax$, until a suitable vertical spacing configuration was found. A suitable configuration would distribute vertical levels that are closely spaced near the surface and gradually increases toward the bottom that fit the specified bathymetry. The parameter choices for *jpk*, *ppacr*, *ppkth*, *ppdzmin* and *pphmax* for different vertical levels for the NP and SO simulations are shown in Table 3.1.

#### 3.2.1.3 Boundary and initial conditions

Boundary and initial conditions are specified after grid construction. The ocean-atmosphere boundary condition is most significant for this study (referred to as surface forcings henceforth). It is possible to group surface forcings into three main categories, namely momentum, energy (heat) and freshwater fluxes (Li et al., 2001). Wind shear is the primary contributor to momentum flux, whereas

TABLE 3.2: This table displays the surface forcing variables and corresponding SI units. These surface forcings are used for NP (C1D_PAPA configuration) and SO (SAZ1D configuration) simulations. The 10 $\mathrm{m}$ and 2 $\mathrm{m}$ refer to the vertical distance above the mean ocean surface where measurement was acquired for the specific variable.

| **Surface Forcing Variable** | **Unit** |
|---|---|
| E-W (or i-) wind component (10 $\mathrm{m}$) | $\mathrm{m\,s^{-1}}$ |
| N-S (or j-) wind component (10 $\mathrm{m}$) | $\mathrm{m\,s^{-1}}$ |
| Downwards (incoming) longwave radiation | $\mathrm{W\,m^{-2}}$ |
| Downwards (incoming) short wave radiation | $\mathrm{W\,m^{-2}}$ |
| Air temperature (2 $\mathrm{m}$) | $\mathrm{K}$ |
| Specific humidity (2 $\mathrm{m}$) | $\%$ |
| Rain (liquid precipitation) | $\mathrm{kg\,m^{-2}\,s^{-1}}$ |
| Snow (solid precipitation) | $\mathrm{kg\,m^{-2}\,s^{-1}}$ |

radiation, air temperature and chlorophyll contribute to energy fluxes. Freshwater fluxes are mainly specified by total (solid and liquid) precipitation and specific humidity. The types of horizontal surface forcing variables are shown in Table 3.2 with corresponding SI units.

It is necessary for the surface forcing data to fit the surface level horizontal grid ($3 \times 3$ nodes, see Fig. 3.1). The data must have uniform values per time step for all nine nodes as a consequence of the one-dimensionality of the model. Due to the Arakawa A grid structure, all surface forcing values are calculated on the T grid point. The surface forcing data used in this study are explained in Section 3.4.1.

Surface forcings influence the turbulence response through specific terms in the governing equations (Eqns. 2.18-2.20). The wind stress (E-W and N-S components), for instance, has an impact on the momentum equations causing downward momentum diffusion and convection. The air temperature and short/longwave downward radiation have an impact on the temperature tracer equation (Eqn. 2.19). It must be noted that only the downwards radiation variable should be used, and not the upwards or nett radiation. This is because the albedo (radiation reflected back into the atmosphere) is already accounted for and set to $6\%$ (Reffray et al., 2015). The precipitation (snow and rain) and specific humidity forcings affect the salinity tracer equation (Eqn. 2.20). The specific humidity is used for calculating the evaporation through bulk formulae. The evaporation is needed in the salinity tracer equation (Eqn. 2.20).

The initial conditions are specified by a salinity and temperature profile. The salinity and temperature profiles must fill the entire domain ($3 \times 3 \times jpk$). The initial conditions are then modified through time by the governing equations when the simulation is left to run. The data used for the initial conditions are found in Section 3.4.3.

#### 3.2.1.4 Vertical turbulence scheme options

Among the various vertical physics that can be tested, vertical turbulence schemes representing vertical mixing is one important class. The turbulence schemes options are comprised of $k - \varepsilon$, $k - \omega$, Mellor-Yamada (M-Y), Turbulent Kinetic Energy (TKE0, TKE10 or TKE30), Generic or Pacanowski/ Philander schemes explained previously in Section 2.4. The scheme choice is selected in the NEMO configuration files before the simulation is run. Only one scheme however, may be used per simulation. Within the classes of turbulence schemes (Richardson number, GLS and TKE families), specific parameters require adjustment before any simulation is run. For Richardson number based schemes the Ekman parameters must be specified. The important TKE scheme parameters include the fraction of turbulent kinetic energy penetration below the mixed layer and type of scheme being used. The fraction of turbulent kinetic energy penetration was set to 0.05 and other parameters were left as default. Parameters for GLS schemes include surface and bottom boundary condition type, Dirichlet (fixed numerical values/non-flux allowing) or Neumann (flux allowing), stability functions and choice of scheme. The surface and bottom boundaries were Neumann, the stability function was Canuto A (Canuto et al., 2001). Reffray et al. (2015) had chosen the Canuto A stability functions and is left as a control variable in this study as the focus is on the turbulence induced structures and not on stability function sensitivity. Further technical details of vertical turbulence scheme choice and parameter settings in NEMO can be found in Appendix B.

### 3.2.2 One-dimensional configuration in the Southern Ocean (SAZ1D )

The SAZ1D configuration is an adapted version of the C1D_PAPA configuration explained in the previous section located at approximately $47°$S $4.5°$E. SAZ1D uses the same discretized governing equations (discrete version of Eqns. 2.18-2.20) as the C1D_PAPA configuration.

The overall SAZ1D configuration has an Arakawa A grid structure consisting of nine identical vertical columns in a square lattice formation (see Fig. 3.1). Regarding the horizontal grid the SAZ1D configuration has a resolution of 0.25°×0.25°. The actual horizontal resolution holds little importance due to the one-dimensionality of the model.

Converting from C1D_PAPA to the SAZ1D configuration required a change in location to the SO coordinates. Due to the location change, the bathymetry was affected. A bathymetry of 4500 $\mathrm{m}$ was obtained from the General Bathymetric Chart of the Oceans (GEBCO) (GEBCO, 2016) data set (refer to Section 3.4.2). Regarding vertical levels, the SAZ1D configuration implemented 31, 51, 75, 101 and 151 vertical levels for different simulations. The *ORCA2* vertical grid configuration was also implemented. The vertical spacing between levels are generated from Eqns. 3.4 and 3.5. The SO parameter choices for *jpk*, *ppacr*, *ppkth*, *ppdzmin* and *pphmax* are shown in Table 3.1. The SAZ1D and C1D_PAPA grid parameters differ due to dissimilar bathymetry values at the NP and SO locations. A temperature and salinity profile that matches the grid profile constitutes the initial conditions. Identical forcing function variables are employed for SAZ1D as was used for C1D_PAPA (shown in Table 3.2).

In summary, the major alterations from the C1D_PAPA configuration to the SAZ1D configuration included the location change, bathymetry specification, vertical spacing redistribution (via grid parameters), horizontal grid resolution and the specification of initial and boundary conditions. The fixed aspects include the grid structure, number of vertical levels, discretized governing equations, time period and turbulence scheme choices.

## 3.3 Simulations performed

This section describes all simulations performed in this study. The simulations were performed for the annum 15 June 2010 - 14 June 2011. All simulations were run with a time step of 360 $\mathrm{s}$. The simulations consisted of varying location (NP and SO), reanalyses (NASA, NCEP, JRA55 and ERA-Interim), vertical levels (31, 31ORCA, 51, 75, 101, 151) and turbulence schemes ($k-\varepsilon$, $k-\omega$, M-Y, Generic, TKE0, TKE10, TKE30 and Pacanowski/Philander ).

The water column simulations involved using only vertical turbulence schemes and no horizontal processes or tidal mixing. The data and various turbulence diagnostics will be explained in the sections below. In summary, before simulations were performed, surface forcing data (ERA-Interim, NASA, NCEP and JRA55) were downloaded from the relevant databases and preprocessed to create the surface forcing files. The initial conditions (temperature and salinity profiles) and chlorophyll were processed and bathymetry value for the specific location found. The SAZ1D simulation scripts were set up and run with the processed reanalysis data, chlorophyll and initial condition data. Note that the C1D_PAPA configuration was accompanied with its own set of boundary and initial condition files, used for running the NP simulations.

Fig. 3.3 displays a graph of all simulations performed in this study. Black nodes indicate that for any arrow entering it, a simulation was performed for all arrows leaving, i.e. the graph (and number of simulations) multiplies at every black node. Both NP and SO simulations are shown, i.e. the locations. Following the location change, the surface forcing data were varied. Thereafter, the number of vertical levels was changed. Finally, the turbulence schemes were varied. The outcome of each simulation led to various results, diagnostics and univariate indicators, namely temperature, salinity, density, turbulent diffusivity, turbocline, buoyancy flux, MLD, Brunt Väisälä frequency, Potential Energy Anomaly (PEA) and wind stress magnitude (last column of Fig. 3.3). These diagnostics and univariate indicators communicate the turbulence properties of the water column. The analysis will be limited to the upper water column (0-500 $\mathrm{m}$) as the focus is on the effect of surface forcing functions on the water column.

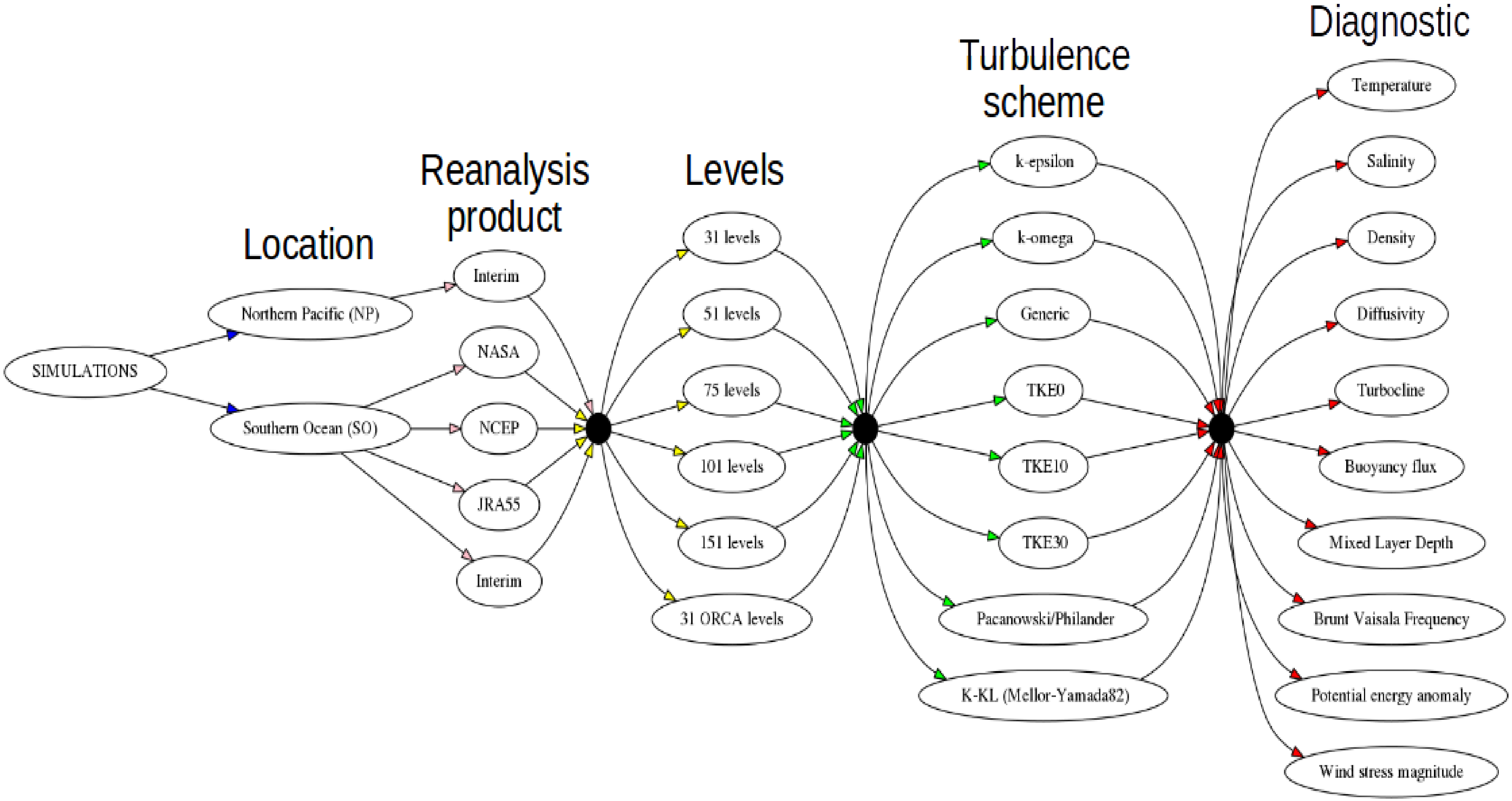

FIGURE 3.3: All simulations performed for the NP (C1D_PAPA configuration) and SO (SAZ1D configuration) locations. Black nodes indicate that for any arrow entering it, a simulation was performed for all arrows leaving, i.e. there are $5 \times 6 \times 8 = 240$ pathways (or simulations performed) leading to each diagnostic or univariate indicator. All simulations performed had a time step of 360 s.

## 3.4 Data

The research data in this study were drawn from various sources and fall into two categories. The first category is the data needed in order to perform simulations and the second category consists of validation data. Data needed for simulations consists of bathymetric data, reanalysis products, World Ocean Atlas data and chlorophyll data. Validation data consists of Conductivity, Temperature and Depth (CTD) measurements from winter cruises down to Antarctica on the *SA Agulhas II* and ARGO float (observed ocean) data. Bathymetric data are used for the specification of bathymetry values at the study locations and reanalysis data are used to supply surface forcings for SO simulations. The useful data obtained (after processing) from the various data sources are presented below.

### 3.4.1 Surface forcings (reanalysis products)

Reanalysis products provide ocean states at fixed time intervals through a data assimilation scheme and ocean-atmosphere(-land) model(s) (NCAR, 2017). Four varieties of reanalyses were chosen for this study, namely the European Centre for Medium-Range Weather Forecasts (ECMWF) ERA-Interim (Dee et al., 2011), National Aeronautics and Space Administration (NASA) (NASA, 2017), National Centers for Environmental Prediction (NCEP) (Kanamitsu et al., 2017) and Japanese Meteorological Agency (JMA) JRA55 (JRA55, 2017). They constitute the surface forcings. These reanalyses were chosen in order to determine the response of each one on the water column. A brief overview of each reanalysis is given in Table 3.3.

The full reanalyses data were obtained from the online databases and are downloadable in various formats (NetCDF and grib for instance) via the website interfaces. Technical details of the data processing method can be found in Appendix C.

The most influential surface forcings on the water column are the radiation and wind variables (see Table 3.2 for all surface forcing variables). For brevity only 2010 radiation and wind surface forcings are shown in this section.

Regarding the NP simulations, Reffray et al. (2015) had provided a set of processed ERA-Interim data used for boundary conditions. The surface forcings are displayed in Fig. 3.4.

The reanalyses data had to be processed before being used for the SO simulations. Each reanalysis had come in different horizontal grid resolutions and time intervals. The processing involved the selection of the data point with latitude and longitude closest to the SO location, which were extracted for the full annual time periods (2010 and 2011). The time subintervals varied between 1-24 $\mathrm{h}$ per surface forcing variable. These time series data were expanded to a $3 \times 3$ grid for grid compatibility with the SAZ1D configuration. The interested reader can refer to Appendix C for individual reanalysis variable names, time interval and challenges experienced during data processing.

The SO radiations and wind surface forcings used are shown in Figs. 3.5-3.8. For comparison purposes, ERA-Interim data were plotted simultaneously against the NASA, NCEP and JRA55 surface forcings (Figs. 3.6-3.8 respectively). The wind speeds vary in magnitude but follow similar trends between reanalysis products. The shortwave (solar) radiation for NCEP, JRA55 and NASA has rapid changes between high (600-800 $\mathrm{W\,m^{-2}}$) and low (5-200 $\mathrm{W\,m^{-2}}$) values, due to the intra-daily data intervals (Figs. 3.6 (c), 3.7 (c) and 3.8 (c)). This however, is not observed in the ERA-Interim data due to daily data (24 $\mathrm{h}$) intervals. The downwards longwave radiation exhibits a mild oscillation due to intra-annual variability of radiation strength.

A few challenges were encountered associated with the processing of reanalyses data to obtain the necessary boundary conditions. These challenges were duly overcome. For a detailed diagnosis and remedy of the various challenges encountered, see Appendix C.

TABLE 3.3: This table displays the reanalyses with corresponding specifications, namely period of data availability, horizontal and vertical resolutions as well as frequency of data available (in hours) depending on the specific forcing variable. These reanalyses constitute the core of surface forcings used for the SO simulations (SAZ1D configuration). All reanalyses are globally defined (NCAR, 2017).

| **Name** | **Time period of data available** | Resolution |
|---|---|---|
| ERA-Interim | January 1979 - March 2017 | 0.75°×0.75°×60 levels (24 and 3 hourly) |
| NASA | January 1979 - November 2016 | 0.5°×0.667°×72 levels (1 and 3 hourly) |
| NCEP | January 1979 - May 2017 | 2.5°×2.5°×28 levels (6 hourly) |
| JRA55 | December 1957 - January 2017 | 1.25°×1.25°×60 levels (6 hourly) |

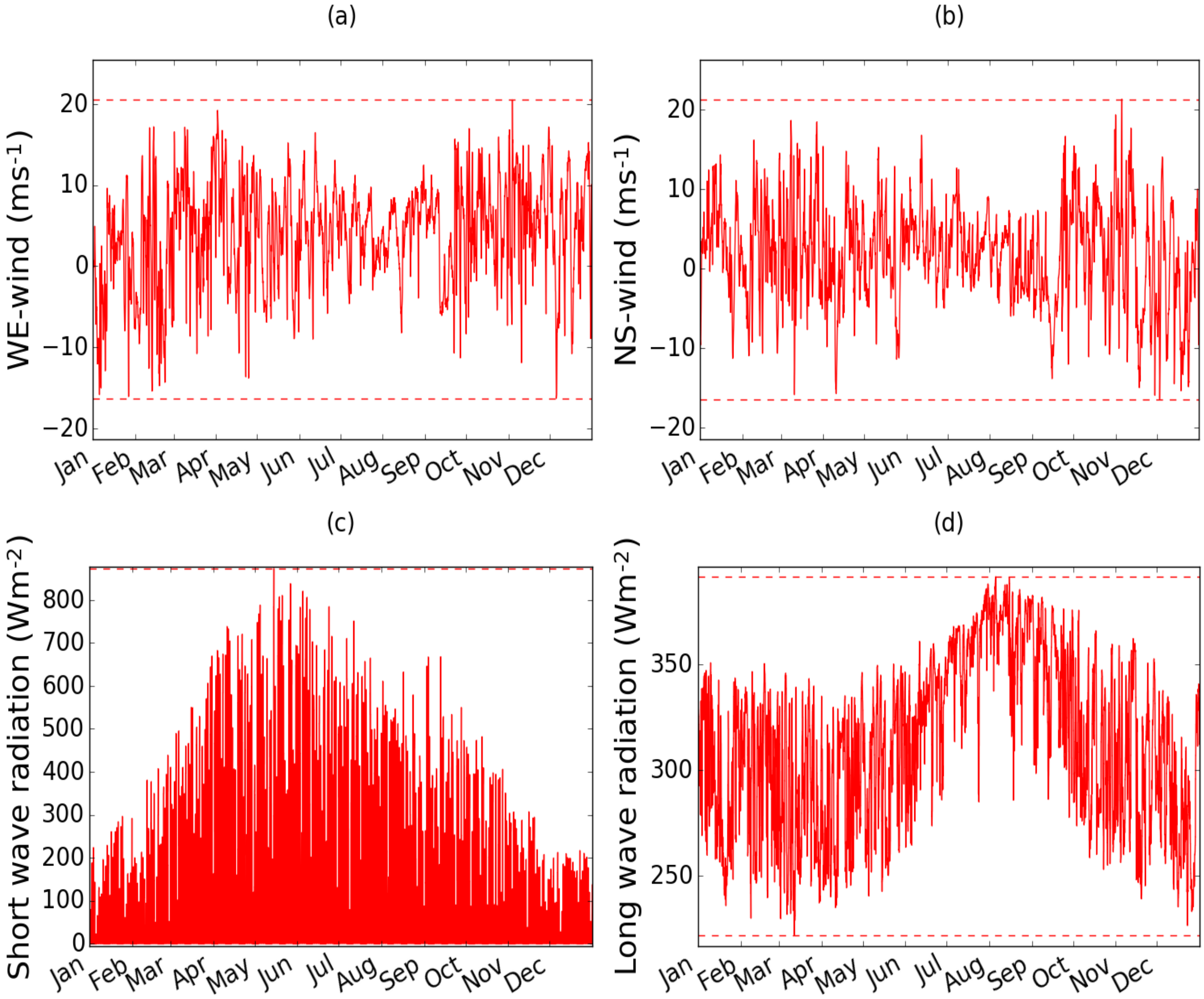

FIGURE 3.4: **ERA-Interim** (Dee et al., 2011) surface forcings used for the NP simulations (Reffray et al., 2015). Only year 2010 is shown for brevity. Horizontal lines represent maximum and minimum bounds for time series data. Shown is **(a)** East-West wind component, **(b)** North-South wind component, **(c)** shortwave radiation (note the intra-daily sharp increase and decrease in intensity due to the 1 hourly data intervals) and **(d)** downwards longwave radiation.

### 3.4.2 Bathymetric and chlorophyll data

The bathymetric data were obtained from the GEBCO (GEBCO, 2016) dataset. GEBCO bathymetry is generated via satellite radar altimetry measuring sea surface anomaly. Some advantages of this

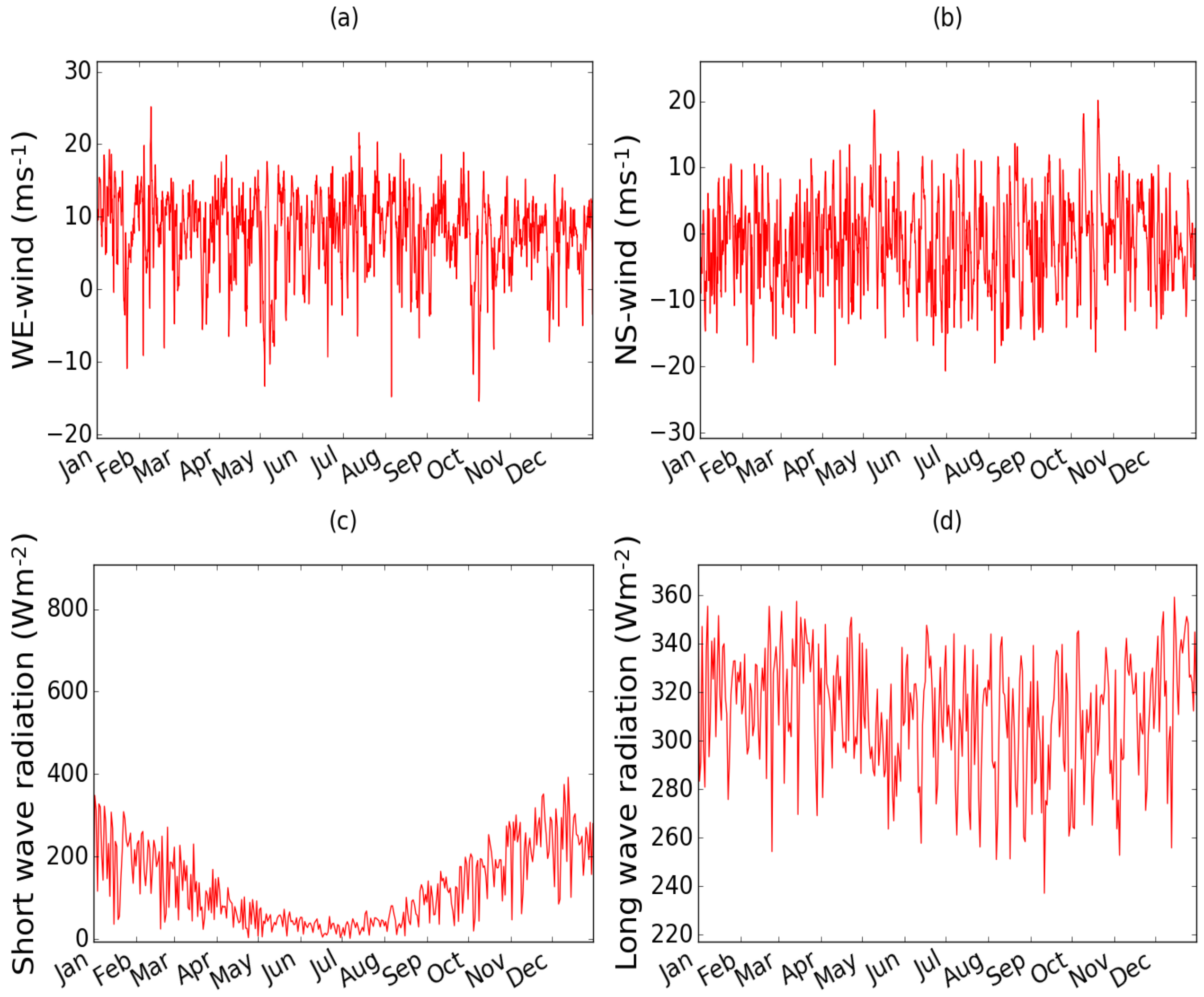

FIGURE 3.5: **ERA-Interim** (Dee et al., 2011) surface forcings used for the SO simulations. Only year 2010 is shown for brevity. Horizontal lines represent maximum and minimum bounds for time series data. Shown is **(a)** East-West wind component, **(b)** North-South wind component, **(c)** shortwave radiation and **(d)** downwards longwave radiation.

dataset are the global coverage and time for bathymetry generation (as it would have taken many years using ocean vessels to map the ocean floor). Disadvantages include ocean phenomena causing anomalies which cause false signals in the altimetry data and resolution of satellite data.

The chlorophyll data form part of the boundary forcings. The reason is due to the irradiance forcing term in the temperature tracer equation (Eqn. 2.9). The chlorophyll-A concentration provides the colour which is needed to obtain the fraction of the red, green and blue frequencies. Consequently these are used to determine how deep down (from the surface) the light penetrates before being attenuated.

Reffray et al. (2015) had obtained the NP chlorophyll data from the SeaWIFS climatological data (McClain et al., 2004). This data were supplied with the C1D_PAPA configuration. The SO chlorophyll data were acquired from the European Space agency (ESA) under the Climate Change Initiative (CCI) (CCI, 2017). The data are based on ocean colour derived from satellite imagery from various missions. Chlorophyll concentration impacts the light penetration into the water column.

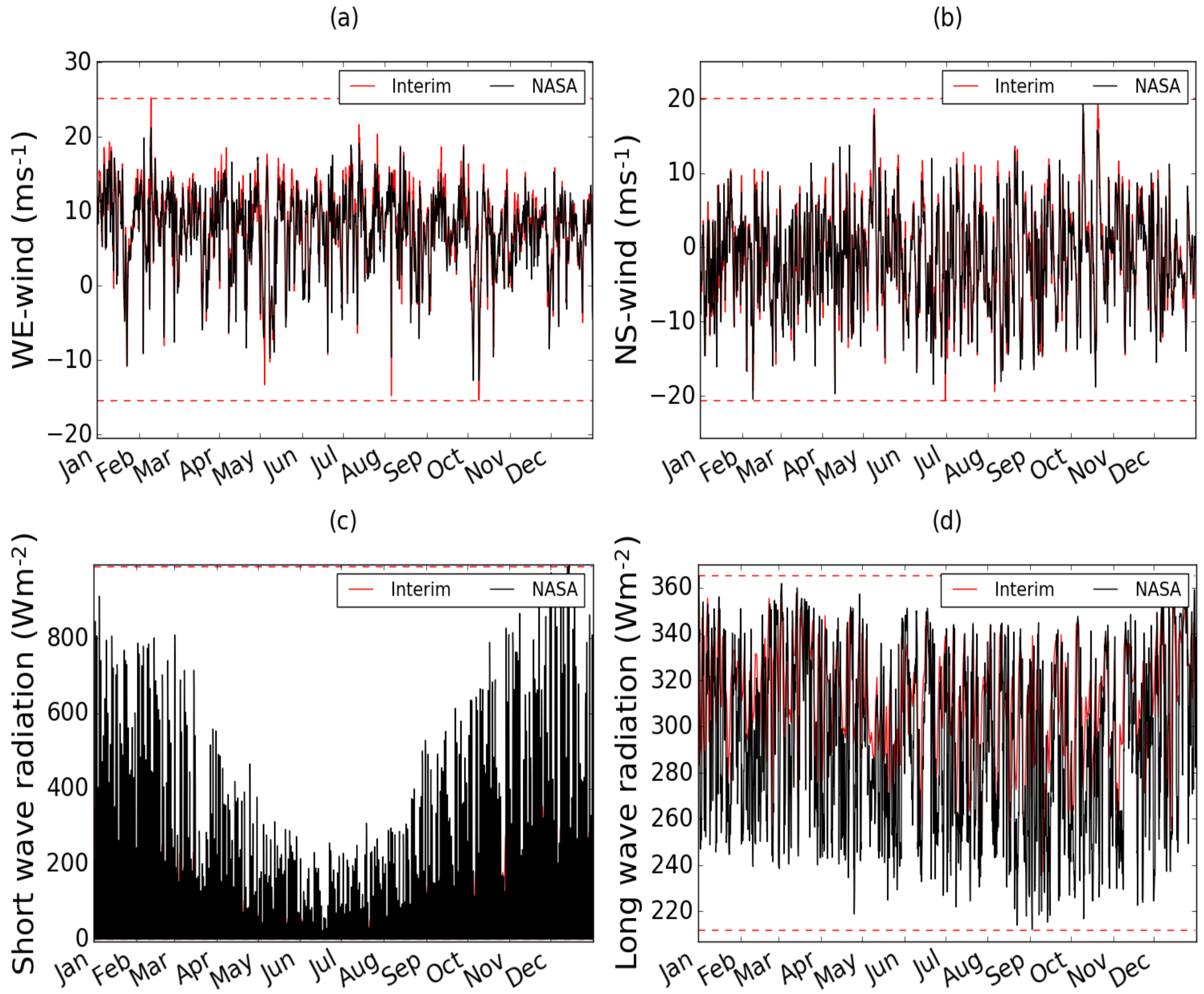

FIGURE 3.6: **NASA** (NASA, 2017) surface forcings used for the SO simulations. Only year 2010 is shown for brevity. ERA-Interim data (Fig. 3.5) are plotted simultaneously for comparison. Horizontal lines represent maximum and minimum bounds for time series data. Shown are **(a)** East-West wind component, **(b)** North-South wind component, **(c)** shortwave radiation (note the sharp increase and decrease in intensity due to intra-daily data intervals) and **(d)** downwards longwave radiation.

### 3.4.3 Initialization data (Initial conditions)

Initial conditions are composed of a depth, temperature and salinity profile. The profile must span the bathymetry at the location and match the number and position of vertical levels. The initial conditions are only needed at the $0^{th}$ time step. When the simulation is run, the new temperature and salinity calculated from the model are then used for further time steps.

Regarding the NP, Reffray et al. (2015) had used ocean station *PAPA* data (NOAA, 2016) as the initial conditions. The temperature and salinity however, could only be obtained down to 300 $\mathrm{m}$ and vertical spacing between measurements differ for temperature and salinity. For temperature and salinity values below 300 $\mathrm{m}$, Reffray et al. (2015) had made use of the World Ocean Atlas 2009 (WOA09) climatology (Levitus et al., 2013). The upper 500 $\mathrm{m}$ of the NP initial conditions are shown in Fig. 3.9. It is observed that the thermocline and halocline are approximately 70 $\mathrm{m}$ deep.

Unfortunately, no suitable mooring is located near the SO location to provide valuable temperature and salinity profile data. The temperature and salinity profile data were acquired from the World

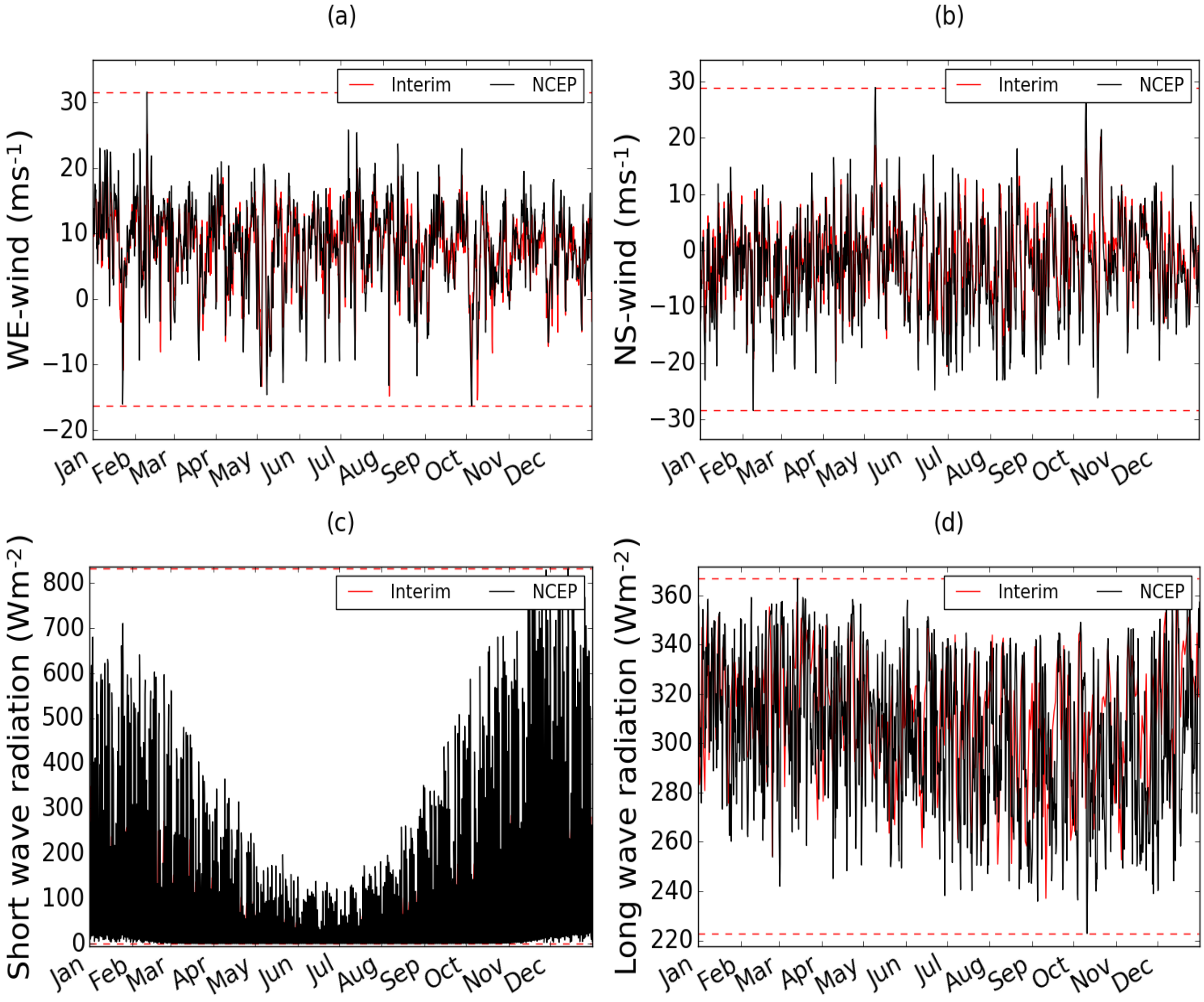

FIGURE 3.7: **NCEP** (Kanamitsu et al., 2017) surface forcings used for the SO simulations. Only year 2010 is shown for brevity. ERA-Interim data (Fig. 3.5) are plotted simultaneously for comparison. Horizontal lines represent maximum and minimum bounds for time series data. Shown are **(a)** East-West wind component, **(b)** North-South wind component, **(c)** shortwave radiation (note the sharp increase and decrease in intensity due to intra-daily data intervals) and **(d)** downwards longwave radiation.

Ocean Atlas 2013 (WOA13) (Boyer et al., 2013). A key strength of WOA13 data is that the profiles are constructed from only *in situ* data. Furthermore, there is also global coverage and is generally used by the community for initial conditions (Mishonov, 2017). Some key disadvantages include limited data for the SO, areas of inconsistent sampling could lead to spurious features and some areas may be misrepresented due to limited *in situ* observations. The upper 500 $\mathrm{m}$ salinity and temperature profile WOA13 data are shown in Fig. 3.10 for the SO location. The temperature (Fig. 3.10 (a)) is cooler (approximately 1 °C) compared to the NP temperature profile as is expected due to the cool temperatures experienced in the SAZ. The thermocline is at 100 $\mathrm{m}$, but not sharply defined as in the NP profile. The salinities (Fig. 3.10 (b)) are higher valued and the range is small (34.0-34.3 $\mathrm{PSU}$) compared to the NP salinities (32.7-34.1 $\mathrm{PSU}$). The halocline is difficult to distinguish due to the deep mixing period in winter.

The profiles for different number of vertical levels were obtained from fitting a cubic spline to the original temperature and salinity profiles (provided by Reffray et al. (2015) for NP and WOA13 profiles for SO). The temperatures and salinities corresponding to the given depths were extracted for use as the initial conditions. The technical details of the data conditioning and extraction can be

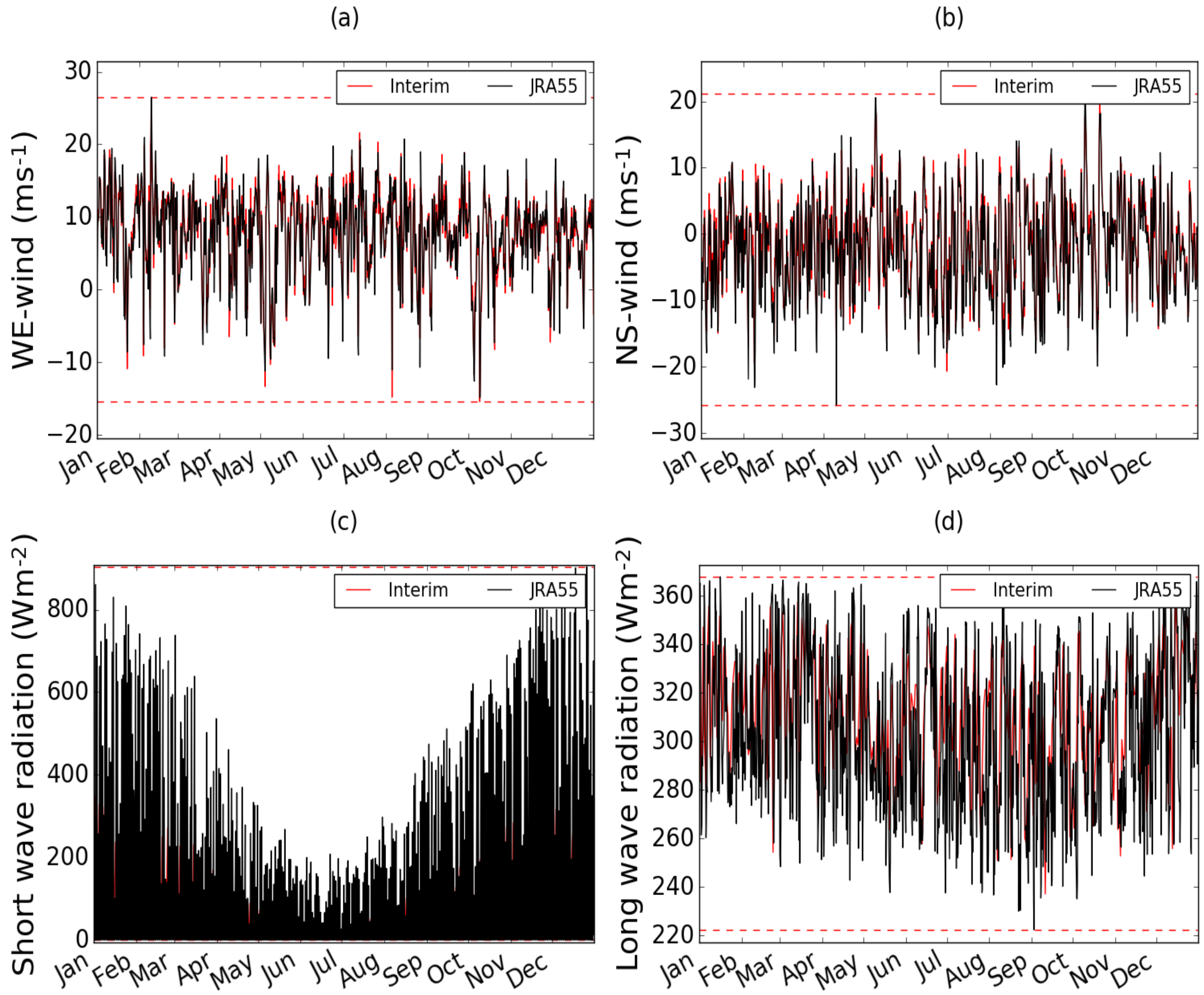

FIGURE 3.8: **JRA55** (JRA55, 2017) surface forcings used for the SO simulations. Only year 2010 is shown for brevity. ERA-Interim data (Fig. 3.5) are plotted simultaneously for comparison. Horizontal lines represent maximum and minimum bounds for time series data. Shown are **(a)** East-West wind component, **(b)** North-South wind component, **(c)** shortwave radiation (note the sharp increase and decrease in intensity due to intra-daily data intervals) and **(d)** downwards longwave radiation.

found in Appendix C.

### 3.4.4 Winter Cruise Conductivity, Temperature and Depth (CTD) validation data

The Winter Cruise is a South African initiative in cooperation with multiple local and international universities, aboard the *SA Agulhas II* (Arctic, 2017) which undertakes a journey from South Africa to the Antarctic region. The cruise is approximately two weeks in duration and normally takes place during July. Various research activities are undertaken during the cruise, in particular CTD drops with Niskin (Zee, 2017b) or GO-FLO (Zee, 2017a) bottles attached to the rosette. The winter cruise profiling CTD data (Arctic, 2017) for 2016 and 2017 are used in this study as validation of simulated temperature profiles. The data were calibrated using the International Temperature Scale (ITS) 90 standard (Preston-Thomas, 1990) which is the latest standard available for this data. Missing values were corrected for and data smoothing was applied on the up-cast dataset. This rendered the temperature and salinity profiles useful for comparison against simulation. The CTD data were collected

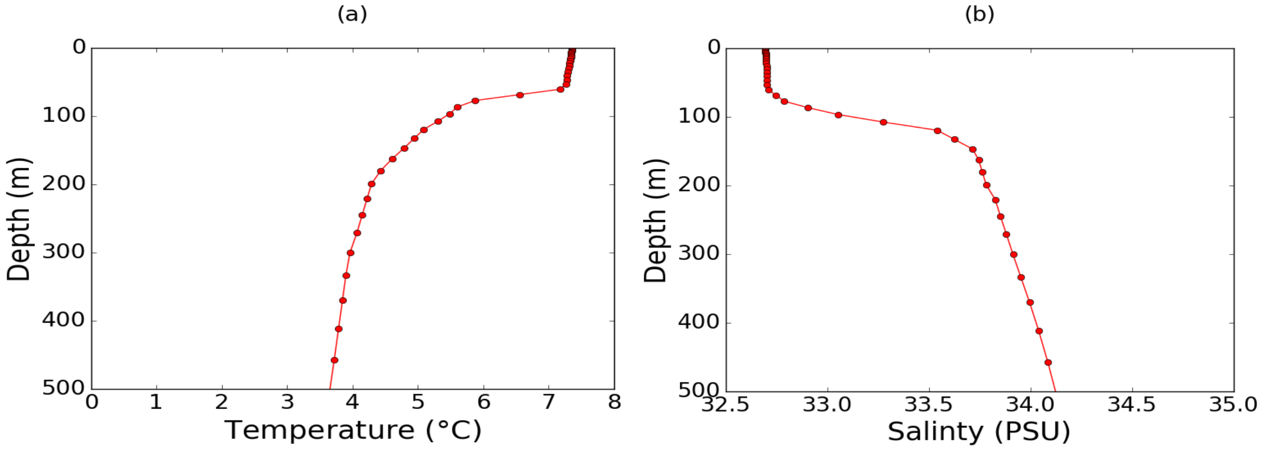

FIGURE 3.9: The upper 500 m **(a) temperature** and **(b) salinity** initial conditions for the water column located in the **NP**.

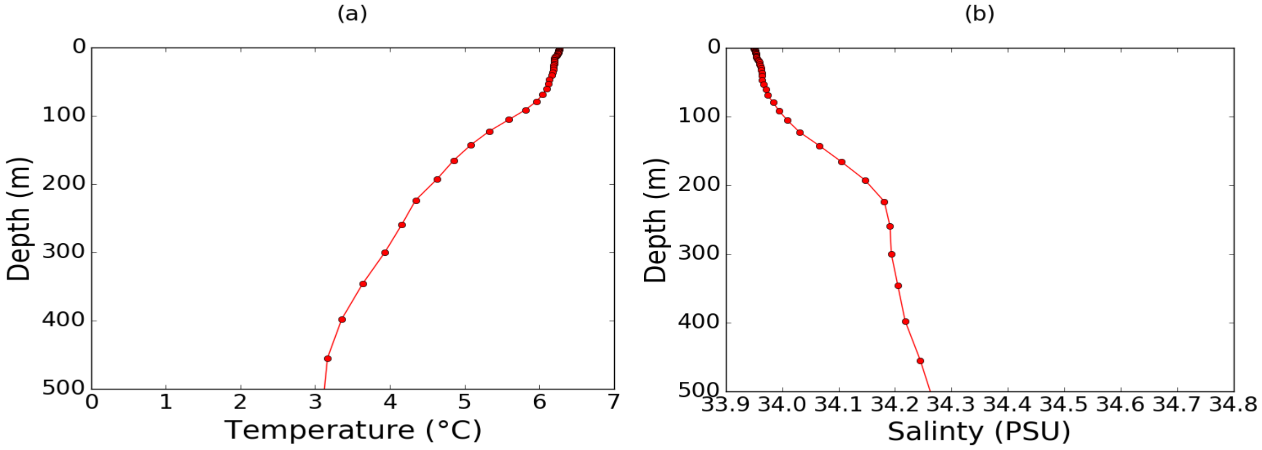

FIGURE 3.10: The upper 500 m **(a) temperature** and **(b) salinity** initial conditions for the water column located in the **SO**.

from various locations in the SO for varying depths (500-4500 m). The data were obtained from the *SA Agulhas II* data base. The 2016 and 2017 relevant data will be presented in the results (Chapter 4), plotted as comparison against the simulation output. Winter Cruise data for 2016 and 2017 are used due to the lack of data for the period of 2010 and 2011 and it is recommended to have as many sources of validation data to compare against.

### 3.4.5 Array for Real-time Geostrophic Oceanography (ARGO) float validation data

The ARGO floats (Davis, 1991; Davis et al., 2001) are various oceanographic instruments that gather profile data (temperature, salinity, pressure and many other measurements) of the upper ~1000 m of the major oceans. The initial ARGO floats were deployed in 2000 and has had an increase of deployments to the current day. The ARGO project aims at obtaining accurate, global spatio-temporal coverage of the upper ocean. ARGO floats are not constrained to major currents or shipping routes and is allowed to drift wherever the ocean may take the float. ARGO data are the leading source for model validation and data assimilation models used in reanalyses (ARGO, 2017). In acknowledgement of ARGO, "these data (ARGO, 2017) were collected and made freely available by the International Argo Program and the national programs that contribute to it.[4] The Argo Program is part of the Global

---

[4] http://www.argo.ucsd.edu and http://argo.jcommops.org

Ocean Observing System."

The ARGO temperature and salinity data were obtained from the online data base (ARGO, 2017) for a 1°×1° block around the study location (4.5°E 47°S) in the SO (see Fig. 2.4). The data are freely available for download and use. The data were extracted and processed (headers, missing values and unnecessary variables removed). The cleaned data consisted of temperature and salinity profiles spanning the surface down to 1000 $\mathrm{m}$ over various years (2009-2016), months and days. Due to the drifting nature of the ARGO floats, the float does not stay in a single position as compared to a buoy, making it difficult to obtain high temporal resolution data at a single location. Furthermore, while taking a vertical profile, horizontal oceanic processes could shift the float which implies that the data does not lie in a perfect column. Sensors may have drifted from the calibrated value leading to minor errors in temperature and salinity after raw data processing. These are a few limitations of the ARGO float data.

## 3.5 Diagnostics for the turbulent response of the water column

The temperature, salinity and density are useful for observing the turbulence response on the water column, but other natural indicators can be utilised for the same purpose. This section describes the diagnostics and univariate indicators used for determining the turbulence response and sensitivity of stratification of the water column. The diagnostics and univariate indicators include the Brunt Väisälä frequency, mixed layer depth, turbocline, wind stress and potential energy anomaly.

### 3.5.1 Brunt Väisälä frequency

Consider the following thought experiment shown in Fig. 3.11, consisting of a water parcel (green sphere) of intermediate density $\rho_{up} \lesssim \rho_i \lesssim \rho_{down}$, where $\rho_{up}$ denotes the density of the upper (red) lighter layer and $\rho_{down}$ denotes the density of the bottom (blue) denser layer. All viscous and convective effects are ignored in this experiment. The parcel, if left under the influence of gravity at the surface, will sink until the higher density layer (blue) is encountered. Three possible scenarios are possible: 1) the water parcel halts to a stop without affecting the bottom layer, 2) the parcel completely penetrates into the bottom layer or 3) the parcel does not fully penetrate into the bottom layer but indents it. The first case promotes nothing interesting. In the second case the parcel will, after penetration, accelerate upwards and then sinking again until the third case results. In the third case the parcel will perform a damped oscillatory motion (without fully penetrating into the higher density fluid), setting up a wave between the fluid layers (red and blue). The frequency of the wave is denoted by $N$ and called the Brunt Väisälä frequency. These waves are known as internal waves.

The Brunt Väisälä frequency (also known as the buoyancy frequency) characterizes the local density stratification in the ocean. A high (low) Brunt Väisälä frequency implies a large (mild or no) stratification in the water column.

In practice, the square of the Brunt Väisälä frequency is generally used and is calculated as follows

$$N^2 = -\frac{g}{\rho_0}\frac{\partial \rho}{\partial z}, \tag{3.6}$$

where $\rho$ is the density, $\rho_0 = 10^{-3}\ \mathrm{kg\,m^{-3}}$ the reference density and $g = 9.8\ \mathrm{m\,s^{-2}}$ is the gravitational acceleration. The density is required in the calculation of the Brunt Väisälä frequency. This is done using a thermodynamic equation of state (which takes into account the salinity and temperature contributions). The latest version of the Thermodynamic Equation Of State referred to as TEOS10 (TEOS, 2010) was used. A python module, *gsw* (Ådlandsvik et al., 2014), was used for the density calculation which included calculating the pressure and absolute salinity (mass fraction of salt in seawater measured in $\mathrm{g\,kg^{-1}}$) as intermediate variables. An alternative method exists for calculating

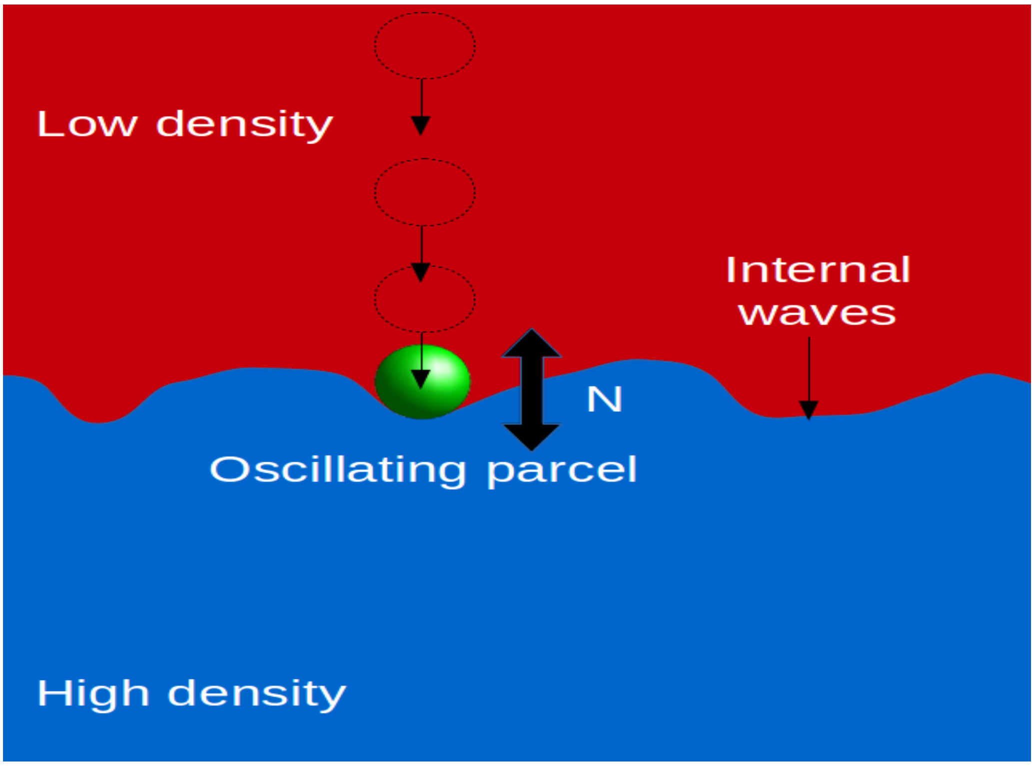

FIGURE 3.11: Thought experiment explaining the Brunt Väisälä frequency concept. A water parcel (green sphere) is left (from the surface) to sink under the influence of gravity in a stratified fluid where the upper fluid (red) is less dense than the bottom layer (blue). The resulting oscillatory motion of the water parcel sets up internal waves of frequency $N$. The frequency of oscillation ($N$) is known as the Brunt Väisälä frequency.

the Brunt Väisälä frequency which is equivalent to Eqn. 3.6 (TEOS, 2010) and is given by

$$N^2 = g\left(\alpha\frac{\partial\Theta}{\partial z} - \beta\frac{\partial S_A}{\partial z}\right), \tag{3.7}$$

where $\alpha$ is the thermal expansion coefficient, $\beta$ is the salinity contraction coefficient, $\Theta$ is the conserved temperature and $S_A$ is the absolute salinity (TEOS, 2010). The water column is stably stratified when $N^2 > 0$, i.e. $-\frac{g}{\rho_0}\frac{\partial\rho}{\partial z} > 0$ which implies that $\sqrt{-\frac{g}{\rho_0}\frac{\partial\rho}{\partial z}} = N > 0$ and $N$ is a real number. The water column is unstably stratified when $N^2 < 0$. The quantity $-\frac{g}{\rho_0}\frac{\partial\rho}{\partial z}$ is now negative and taking the square root will result in an imaginary number (or an imaginary Brunt Väisälä frequency). This condition hinders stratification and results in a production of turbulent kinetic energy in the turbulence closure scheme parameterizations reviewed in Section 2.4.

### 3.5.2 Useful univariate turbulence response indicators for the water column

Univariate indicators generally take the form of time series or profile data. They include mixed layer depth, turbocline, buoyancy flux, wind stress magnitude and potential energy anomaly. These indicators provide various insights to the turbulence response of the water column.

#### 3.5.2.1 Mixed Layer Depth (MLD)

The mixed layer is known to be the upper portion of the ocean surface (upper ∼200 m) where vertical ocean water properties are homogeneous and are dominated by turbulent flow (Helber et al., 2012). Although taken to be homogeneous, the mixed layer is actually heterogeneous in spatial distribution because time is needed for full mixing to occur. The heterogeneous nature however, is minimal because tracer values vary minimally (Smith et al., 2016). The mixed layer is composed of several layers (Woods and Barkmann, 1986). The upper mixing layer is known as the convection layer where heat is lost (or gained) to the atmosphere by latent and sensible heat. The maximum depth that the mixed layer spans is known as the MLD. The various layers of the mixed layer are shown in Fig. 3.12. Li et al. (2001) noted the importance of modelling mixed layer physics accurately, because simulations outputting incorrect sea surface temperature implies inaccurately calculated sensible and latent heat fluxes which affect the heat content (energy budget) in the upper ocean.

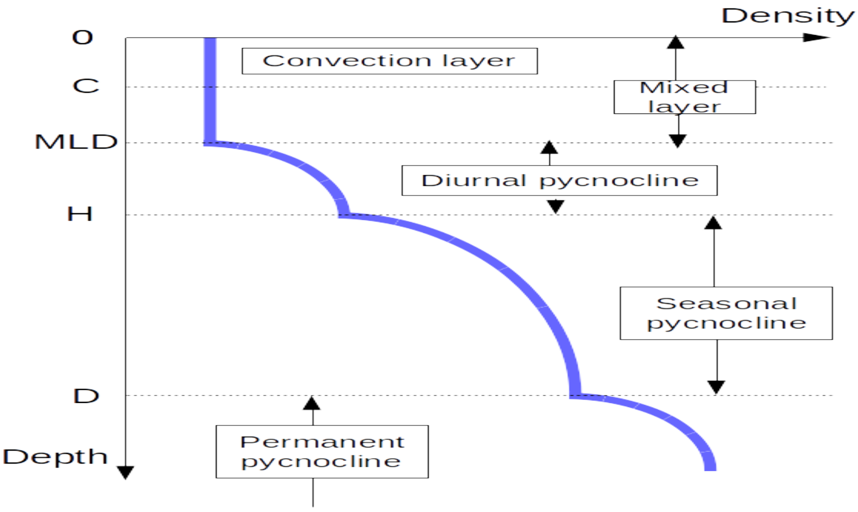

FIGURE 3.12: The different sections of the density profile in the upper ocean. The upper layer called the mixed layer consists of the convective layer and just below is the MLD. The diurnal, seasonal and permanent pycnoclines in relation to each other are also shown.

For practical (computational) purposes, the MLD can be defined by a temperature or density criterion (De Boyer-Montégut et al., 2004). This study uses a density criterion for the MLD and is defined where the change in density, $\Delta\rho = 0.01\ \mathrm{kg\,m^{-3}}$, exceeds a reference density at a shallow depth of $10\ \mathrm{m}$, i.e.

$$MLD \;=\; \text{Shallowest depth}(\rho - 0.1 < \rho(10\ \mathrm{m}) < \rho + 0.1). \tag{3.8}$$

NEMO implements Eqn. 3.8 to calculate the MLD.

In terms of turbulence, the MLD does not provide a wall (permanent barrier) to turbulent mixing as is often misinterpreted (Franks, 2015; Sutherland et al., 2013). Rather, the MLD provides an approximate separator between water of homogeneous physical properties (salinity and temperature) and the initial stratified layer.

The MLD is still a useful measure even if it does not impart full knowledge of the turbulent layer. The highest turbulent eddy diffusivity (see Section 2.4) values are found above the MLD as there is sufficient energy for overturning motion leading to turbulent mixing. This however, is better observed from the turbocline.

#### 3.5.2.2 Turbocline

The turbocline describes a turbulent separator between the upper turbulent fluid and lower quasi-laminar fluid where the turbulence is intermittent and patchy (Hinsley, 2005). Apart from a turbulent layer separator, the turbocline is also a good indicator of the depth of the convected energy and momentum from the surface (Beuvier et al., 2012). This implies the turbocline is better suited as a turbulence indicator than the MLD (as the MLD does not capture the diffusion process below the mixed layer). The diffusive stability of the water column determines the turbocline as observed by Ghosal et al. (2000), because the turbocline and diffusive nature of the water column would be misrepresented if the diffusion is unstable.

The highest diffusivities are found above the turbocline. For computational purposes NEMO uses a diffusivity criterion where the turbocline is found from the shallowest depth where the diffusivity drops below $5 \times 10^{-4}\ \mathrm{m^2\,s^{-1}}$. Note that this value is larger than O($10^{-6}\ \mathrm{m^2\,s^{-1}}$), i.e. molecular diffusivity. It is expected in the austral summer (winter) that the turbocline will shallow (deepen). A special case results when the turbocline and MLD coincide meaning the mixed layer and turbulent layer also coincide. The turbocline can then be referred to as the MLD. It must be noted that this is not true in general as the criterion used for defining the MLD and turbocline are dissimilar. Generally, the turbocline and MLD peak simultaneously except for highly diffusive scenarios, where the MLD and turbocline separate especially in the austral summer. The MLD and turbocline and are good indicators for spatial energy content as they show the depth where most of the turbulent kinetic energy is captured in the water column. In NEMO the MLD and turbocline are incorporated under the mixed layer physics.

#### 3.5.2.3 Buoyancy flux and wind stress magnitude

At the ocean-atmosphere interface, changes in buoyancy flux and wind stress in relation to past events (for example storms) determines the turbulent nature of the water column (Thorpe, 2007). The thermal and moisture fluxes (buoyancy flux components) affect the upper surface salinity and temperature of the water column. This in turn affects the density. Decreasing density (for example high precipitation event) increases the buoyancy of the upper water column. The opposite occurs for a density increase, i.e. a buoyancy decrease resulting in heavy waters. Consequently, the water column becomes convectively unstable. The overturning circulation induces turbulence that has the potential to entrain waters below and cause an overall cooling/warming in the upper water column (Steele et al., 2009).

The buoyancy flux (Gill, 1982) is given by

$$B = \frac{g\alpha Q}{C_p} + g\beta S_{surf}\left(E_f - P_f\right), \tag{3.9}$$

where $\alpha$ is the thermal expansion coefficient, $\beta$ the salinity contraction coefficient, $Q$ the upward heat flux (consisting of sensible and latent heat flux which contribute significantly), $C_p$ the specific heat capacity of water, $S_{surf}$ the surface salinity, $E_f$ the evaporation flux and $P_f$ the precipitation flux. $B$ has units of $\mathrm{m^2\,s^{-3}}$. The buoyancy flux is actually a misnomer because there is no actual flux of buoyancy, rather there are heat and moisture fluxes. The combination of these fluxes are favourably called the "fictitious" buoyancy flux (Sathiyamoorthy and Moore, 2002). It has been estimated by Cronin and Sprintall (2009) that in terms of buoyancy, a precipitation rate of $5\ \mathrm{mm\,d^{-1}}$ is roughly equivalent to $20\ \mathrm{W\,m^{-2}}$ heat flux. This shows that in areas with high rainfall, the $E_f - P_f$ term contributes significantly and possibly dominates over the heat fluxes. If the buoyancy flux has large positive amplitudes, the water column will stratify due to lighter waters at the surface laying over heavier waters below. A negative buoyancy flux however, induces a convectively unstable water column which leads to vertical mixing.

According to Gill (1982), the buoyancy flux is the main driver of the thermohaline circulation (the global energy and saline conveyor belt of the ocean), meaning that the buoyancy flux is also a strong driver of vertical processes. This implies the buoyancy flux is an important quantity to investigate as it indicates if there could be considerable deep mixing or stratification events in the water column (Sutherland et al., 2013).

The magnitude of wind stress ($|\vec{\tau}|$) is calculated at the ocean surface. The wind stress creates horizontal shear at the surface of the water column, leading to a maximum momentum flux at the surface and decreasing momentum flux with depth. This momentum flux can deepen the MLD via entrainment, set up (breaking) waves and act as catalyst to phenomenon like Langmuir circulations (Cronin and Sprintall, 2009). High magnitudes of wind stress can cause deep convection, but low magnitudes promote stratification of the water column as the thermal fluxes dominate. The wind stress introduces turbulent kinetic energy in the form of overturning cells. The buoyancy flux and Brunt Väisälä frequency (namely stratification strength) then determine the depth of these overturning cells which affects the MLD (Timmermann and Beckmann, 2004).

#### 3.5.2.4 Potential Energy Anomaly (PEA) and time derivative of PEA

Consider a highly stratified water column. In order for mixing to begin, an overturning motion must occur. This involves the conversion of kinetic energy into potential energy (because work is done on a heavier water parcel that is elevated above a lighter water parcel). This concept is naturally represented by the potential energy anomaly which was introduced by Simpson and Bowers (1981).

The potential energy anomaly (Boer et al., 2008; Holt et al., 2017) is defined by

$$\phi = \frac{1}{h} \int_{-h}^{0} z \left(\overline{\rho} - \rho\right) dz \tag{3.10}$$

where $h$ is the water column depth and $\overline{\rho}$ the column density average given by

$$\overline{\rho} = \frac{1}{h} \int_{-h}^{0} \rho dz. \tag{3.11}$$

The PEA has SI units of $\mathrm{J\,m^{-3}}$ and is useful as a stratification (or absence of stratification) indicator. The PEA is also a perfect descriptor of the effects of buoyancy flux and wind stress on the water column. PEA describes the quantity of energy required to fully mix the entire water column (per unit volume) in order to achieve homogeneity of tracers (salinity and temperature).

Burchard and Hofmeister (2008) explains that the PEA was used mainly for shallow coastal seas but it can be used for the deep ocean as there are no limitations or assumptions restricting it to only the coastal areas. The PEA has an advantage over the averaged Brunt Väisälä frequency as it takes into account the entire water column in comparison to having a work around for the local nature of the Brunt Väisälä frequency, i.e. having to set a depth limit in order to average the Brunt Väisälä frequency. The depth limit is needed to account for the high Brunt Väisälä frequencies in the upper water column structures as a deep depth limit will over average the features (due to the average having a larger denominator because of the large bathymetry of 4500 $\mathrm{m}$) rendering the averaged Brunt Väisälä frequency inferior to other turbulence diagnostics.

The time derivative of $\phi$ (denoted $\frac{d\phi}{dt}$) holds valuable insight on how adversely the PEA is affected due to wind stress and solar fluxes. $\frac{d\phi}{dt}$ also describes how quickly the thermocline is raised or lowered in the water column because it is an indicator of the rate of stratification. Large positive peaks in $\frac{d\phi}{dt}$ indicates a large injection of buoyancy which describes a fast onset of stratification. Strong negative peaks however, describe a fast onset of a deep mixing event (for example a strong storm event).

## 3.6 Summary of methods

This section has highlighted the important details of the creation of the SAZ1D configuration (based upon the C1D_PAPA configuration created by Reffray et al. (2015)) used for running simulations in the SO. The input data and validation data were described. The diagnostics which will be used to determine the turbulence response of the water column were briefly explained. All simulations performed in this study were outlined. The results will be presented in the next chapter.

# Chapter 4

# Results

## 4.1 Introduction

The previous chapter introduced the model details of the C1D_PAPA and SAZ1D configurations. Using these configurations, simulations were performed using various turbulence schemes ($k-\varepsilon$, $k-\omega$, M-Y (Mellor-Yamada or k-kl), Generic, TKE0, TKE10, TKE30 and Pacanowski/Philander), reanalyses (ERA-Interim, JRA55, NASA and NCEP) and number of vertical levels. All simulations performed are shown in Fig. 3.3. Furthermore, various turbulence univariate indicators and diagnostics were introduced in order to analyse the turbulence response of the water column.

This chapter presents the results consisting of turbulence diagnostics, correlations and various univariate indicators for the Southern Ocean (SO) simulation outputs. The analysis will be limited to the upper 300-400 $\mathrm{m}$ of the water column as the focus is on ocean upper dynamics affected by ocean-atmosphere interactions. The results presented will encompass simulations performed using 101 vertical levels due to continuous technological advancements in higher performance computing which would make 101 levels an achievable goal in the near future. Various correlations between the various reanalyses and turbulence schemes will be presented providing valuable insight.

For clarity, the diagnostics are presented in a similar order as was introduced in the methodology (Chapter 3). For brevity, a selected set of results were chosen for presentation due to the large volume of results obtained from the many simulations performed. Analysis pertaining to sets of results not displayed will be mentioned where necessary or directed to an appendix. Different aspects of results shown will have useful information for an oceanographic computational modeller interested in investigating the effect of vertical turbulence, vertical mixing sensitivity and intra-annum upper ocean dynamics on a water column.

Furthermore, an interesting characteristic regarding a warm water parcel found in the simulation output is examined in this chapter. Briefly, the warm water parcel is formed when the ocean cools from above, then cooler waters lay on top of warmer waters. In most cases turbulent mixing ensues as the denser waters sink releasing turbulent kinetic energy. In some cases however, due to strong salinity contributions the turbulent kinetic energy is not released and the cooler waters remains on top of warmer waters (which is now trapped). These entrapped warm waters can persist through an entire season depending on the location in the ocean (Steele et al., 2011; Jackson et al., 2011).

## 4.2 Assessment of water column tracers, turbulence diagnostics and correlation tables

This section presents the results pertaining to temperature, salinity, density as well as turbulence diagnostics and univariate indicators such as the Mixed Layer Depth (MLD), Brunt Väisälä frequency, turbulent diffusivity, turbocline, buoyancy flux, Potential Energy Anomaly (PEA or $\phi$), time derivative of PEA (represented as $\frac{d\phi}{dt}$) and wind stress magnitude ($|\vec{\tau}|$).

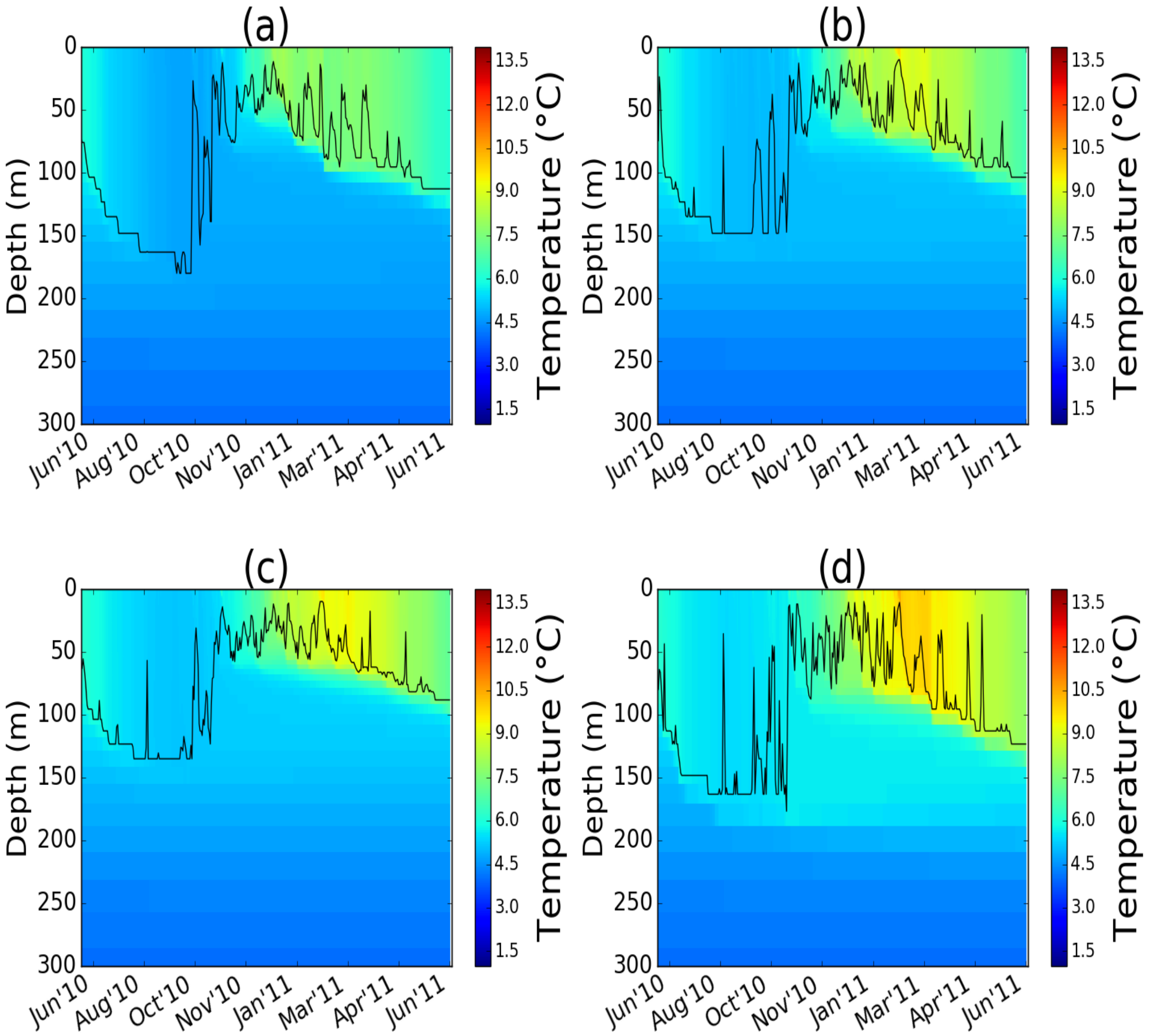

FIGURE 4.1: **Temperature** column evolution results for SO location and different reanalyses: **(a) ERA-Interim, (b) JRA55, (c) NASA and (d) NCEP** using 101 vertical levels and the $k - \varepsilon$ turbulence scheme for 15 June 2010 - 14 June 2011. The MLD (solid black line) is plotted in conjunction for comparison.

The column temperature evolution results (Fig. 4.1) were obtained using 101 vertical levels, 360 $\mathrm{s}$ as the time step and the $k - \varepsilon$ turbulence scheme. The seasons (Sloyan et al., 2010) in the SO simulations could be clearly recognised from the upper surface temperatures. July - September pertain to the austral winter (identified by deep mixing seen by homogeneous upper temperature down to 190 $\mathrm{m}$ as well as cooler water column temperatures) and January - March pertain to summer (identified by high temperature surface waters and stratification structures).

The temperature evolution results using various turbulence schemes looked similar in structure except when using the TKE30 scheme (see Appendix E). The TKE30 scheme tended to be highly diffusive and the temperature gradient at the thermocline was not distinct, i.e. the temperature was highly diffused. From Fig. 4.1, it could be observed that the temperatures differed significantly between reanalyses.

Maximum deep mixing was achieved during August for all reanalyses purely driven by the local buoyancy. During the deep mixing period (August - October) a strong stratification event had occurred. This was observed from the sudden shallowing and deepening of the MLD in the span of two days in mid-August for the NASA, NCEP and JRA55 results. This stratification anomaly was not observed in the ERA-Interim result, possibly due to the low solar and thermal forcing fluxes (Figs. 3.5 (c) and (d)) for that period. The ERA-Interim temperature result however, had the deepest MLD ($\sim$190 $\mathrm{m}$) and the NASA result had the shallowest MLD ($\sim$140 $\mathrm{m}$) during the deep mixing period in October. During the initialization of stratification (October), heat injections into the water column were present, indicated by the MLD spiking upward in the water column. The heat injections during October were the initial phase for the onset of the summer stratification of the water column. The MLD shallowed to approximately 50 $\mathrm{m}$ with large variations during the austral summer and slowly deepened heading into autumn.

Permanent stratification took effect during October for all reanalyses (NASA, NCEP, JRA55 and ERA-Interim). Consequently, the seasonal thermocline was set up and experienced a gradual deepening during the austral summer period as seen in Fig. 4.1. During the austral summer further heat injections were observed at the beginning of February and March which caused a raise in temperature of the upper 90 $\mathrm{m}$ of the water column. This effect however, was not as pronounced in the ERA-Interim result. The cooling period took effect from mid-April and the temperature in the upper 100 $\mathrm{m}$ gradually decreased. It is notable that the NCEP result showed a water column temperature approximately 0.2 °C higher during the deep mixing period compared to the other reanalyses. The lowest deep mixing temperature value of approximately 5 °C was found when using ERA-Interim data.

Fig. 4.2 displays the salinity column evolution results for all reanalyses using the $k-\varepsilon$ turbulence scheme and 101 vertical levels. The intra-annual upper 50 $\mathrm{m}$ of the water column change of salinity was very slight, varying in a band of 0.3 PSU. The results showed a minor yet persistent freshening of the water column through time. A perpetual simulation using 2010 data was run over five years to ascertain whether the freshening persistence was a permanent feature or a temporary transient artefact. It was found that seasonality was present, however, there was a constant slight freshening over the five year period of simulation. The temperature result showed seasonality and no trace of persistent cooling or heating. This implied that there was heat balance but no water balance, i.e. the fresh water influx had a noticeable effect.

The ERA-Interim salinity result (Fig. 4.2 (a)) showed the least freshening with the low salinity occurring down to 140 $\mathrm{m}$ from April onward. In contrast, the NCEP salinity result (Fig. 4.2 (d)) exhibited the most freshening with the low salinity occurring down to 150 $\mathrm{m}$ from March onward. The onset of the seasonal halocline occurred earliest (October) for the NASA result (Fig. 4.2 (c)), followed by ERA-Interim (November). The seasonal halocline developed later (December) for the JRA55 result (Fig. 4.2 (b)) and lastly for NCEP, which only occurred from January. The seasonal halocline was set up corresponding to the above mentioned months and was found at 150 $\mathrm{m}$ for ERA-Interim, JRA55 and NCEP results and 100 $\mathrm{m}$ for the NASA result respectively. The permanent halocline reached 200 $\mathrm{m}$ deep for ERA-Interim and NCEP, 170 $\mathrm{m}$ for JRA55 and 150 $\mathrm{m}$ for the NASA result.

Albeit the persistent freshening (probably due to the fresh water fluxes and not shown in this study), the seasonal dynamics were very much present. For instance, during July (for all salinity results) an increase in salinity was observed due to the breakdown of the seasonal halocline followed by the entrainment of deep waters. The deep mixing period sustained the higher saline waters in the upper water column. At the beginning of the stratification period, salinity entrainment had stopped and the seasonal halocline was set up creating a barrier for downward entrainment.

The salinity, temperature and density finer structures were visible in the profile plots shown in Figs. 4.3 and 4.4 respectively. The density was calculated using the Thermodynamic Equation Of State 2010 model (TEOS, 2010). The profiles were plotted on the day of deeper mixing (namely during early September) using the $k-\varepsilon$, TKE10 and Pacanowski/Philander schemes in conjunction with each reanalysis. The surface salinity values for all reanalyses were similar valued (33.95 PSU) and

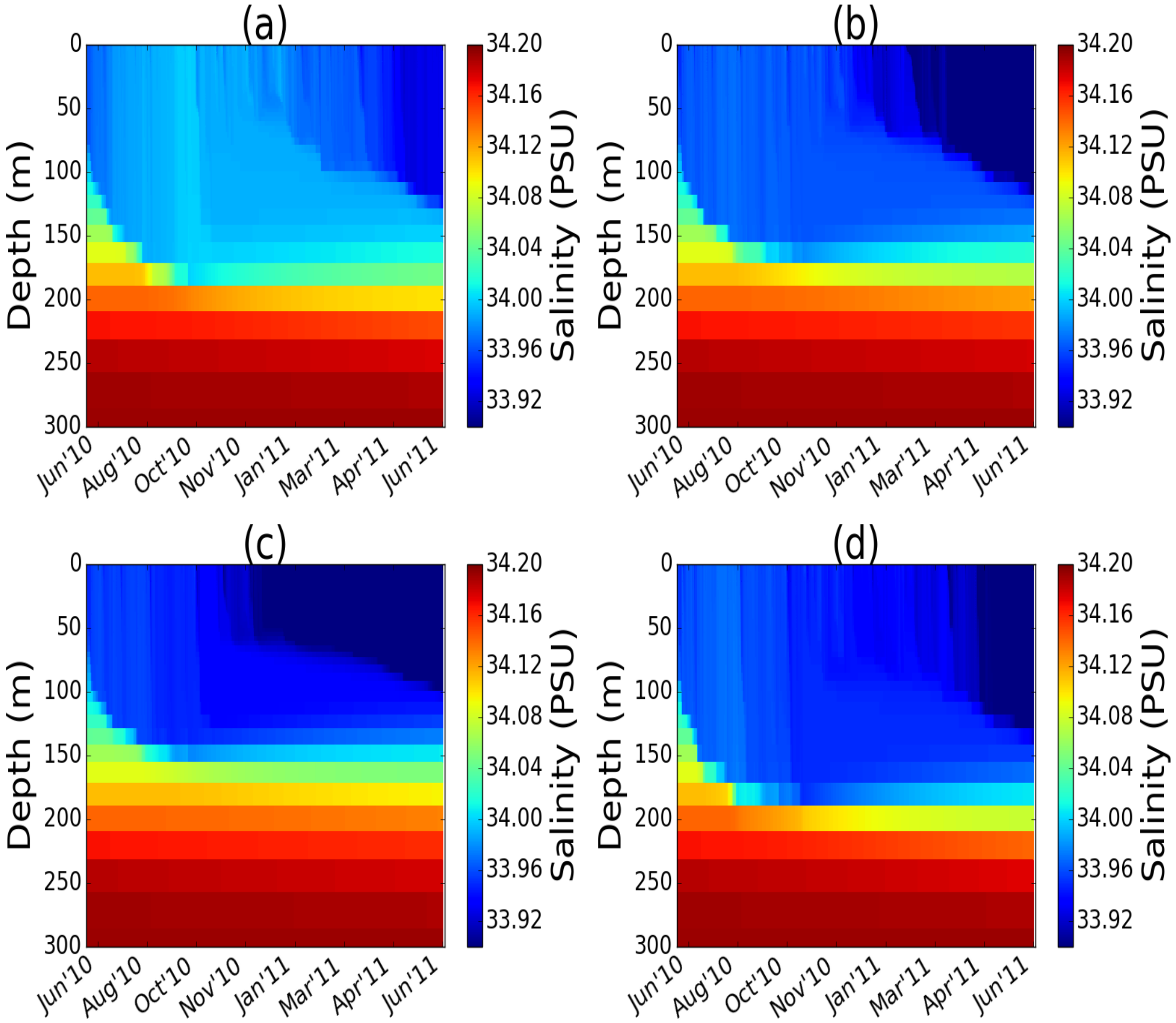

FIGURE 4.2: **Salinity** column evolution for SO location and different reanalyses products: **(a) ERA-Interim, (b) JRA55, (c) NASA and (d) NCEP** using 101 vertical levels and the $k-\varepsilon$ turbulence scheme for 15 June 2010 - 14 June 2011. Note the persistent intra-annual slight freshening of the upper 200 $\mathrm{m}$.

did not vary significantly between reanalyses. There was a reduced halocline ($\sim$100 $\mathrm{m}$) however, for the NCEP/Pacanowski/Philander result (Fig. 4.4 (c)) in comparison to the other results ($\sim$140 $\mathrm{m}$). The density profiles remained relatively constant down to the MLD, thereafter gradually increased. The beginning of the gradual density increase showed the location of the permanent pycnocline (100-140 $\mathrm{m}$ for the various reanalyses). The densities were similar in trend and value for all profiles displayed during this period.

Upon closer inspection of the temperature profiles in Figs. 4.3 and 4.4, it was observed that a pocket of warm water was entrapped below cooler waters in certain instances. This was not easily noticeable from the column time series plots in Fig. 4.1, but is clearly visible in the temperature profiles. The warm parcel could clearly be observed at approximately 140 $\mathrm{m}$ deep as a warm bulge in the temperature profiles and was present in the NASA, ERA-Interim and JRA55 results but generally not in the NCEP results. The warm water parcel was absent in the ERA-Interim, JRA55 and NCEP results in conjunction with the $k-\varepsilon$ turbulence scheme as well as NCEP in conjunction with the TKE10 scheme. The warm water parcel was only manifest in the results when using NCEP in conjunction with the Pacanowski/Philander turbulence scheme. This was possibly due to the elevated temperature values found when using NCEP (low spatial resolution data) as compared to the other reanalyses or the strong wind stress (Fig. 4.12 (d)) which may have induced stronger vertical mixing making it unfavourable for warm parcel entrapment.

It seems the inducing mechanism for this warm parcel had a link with the breakdown of the summer stratification which is now explained. Prior to the deep mixing period in July (see Fig. 4.1), the upper 150 $\mathrm{m}$ of the water column consisted of warm water. The initial stages of the cooling period deepened the mixed layer and the summer stratification was destroyed. It appeared that the cooling did not have an effect down to 150 $\mathrm{m}$ and warm water from the previous summer time was captured just below the mixed layer. This warm water was a past impression of the previous season. After the deep mixing period, the upper 150 $\mathrm{m}$ began to undergo stratification. Excessive temperatures (in relation to NASA, ERA-Interim and JRA55) however, remained down to 150 $\mathrm{m}$ for the NCEP result. In some cases (Table 4.1), it seemed deep mixing was unable to entrain deep enough during the initial cooling period due to the warm water parcel acting as a barrier.

The warm parcel presented itself for specific combinations of reanalysis and turbulence schemes shown in Table 4.1 (shown at the end of this chapter). The warm parcel persisted because entrainment could not occur above or below the warm parcel (namely the potential energy was not converted into turbulent kinetic energy). The entrapped warm parcel between cooler waters however, was not detectable in the density profiles due to the hydrostatic stability nature of the water column. One would have expected an anomaly or change in signal around 150 $\mathrm{m}$ in the density profile due to the warm water parcel, but this did not happen. This implied that in this case, salinity played a large role in the density stabilization because an increase in salinity was found where the warm parcel was observed leading to the density stabilization.

In general, it was found that using the Pacanowski/Philander turbulence scheme enhanced the warm water parcel in the temperature profiles, i.e. a larger warm parcel was observed possibly due to the lack of time evolution equations governing the transfer of turbulent kinetic energy and its dissipation. The presence of the warm water parcel was searched for during the deep mixing period (September), beginning of stratification period (October) and the beginning of deep mixing period (April) and is shown in Table 4.1 for all simulations performed using 101 vertical levels. This gave an indication of how long the warm water parcel persisted for the different combinations on turbulence schemes and reanalyses. The warm parcel appeared in all simulations performed with exception of a few cases. For NASA, a warm water parcel was always produced for any combination of turbulence scheme without exception. NCEP did not produce a warm water parcel, except when using the Pacanowski/Philander scheme. This was possibly due to the algebraic nature of the turbulence scheme, i.e. lack of a prognostic equation for turbulent kinetic energy and dissipation of turbulent kinetic energy. JRA55 and ERA-Interim in conjunction with the $k - \varepsilon$ turbulence scheme did not produce a warm parcel. In a few cases, the warm water parcel persisted for more than half a year, especially for the TKE10, TKE30 and Pacanowski/Philander turbulence schemes in conjunction with ERA-Interim and JRA55 reanalyses. The $k - \varepsilon$ scheme in conjunction with the reanalyses had produced only one warm parcel result ($k - \varepsilon$/NASA combination) as compared to the other turbulence schemes producing warm parcels for more than one reanalysis. This suggested that the $k - \varepsilon$ turbulence scheme could possibly be a better turbulence scheme option than the other schemes.

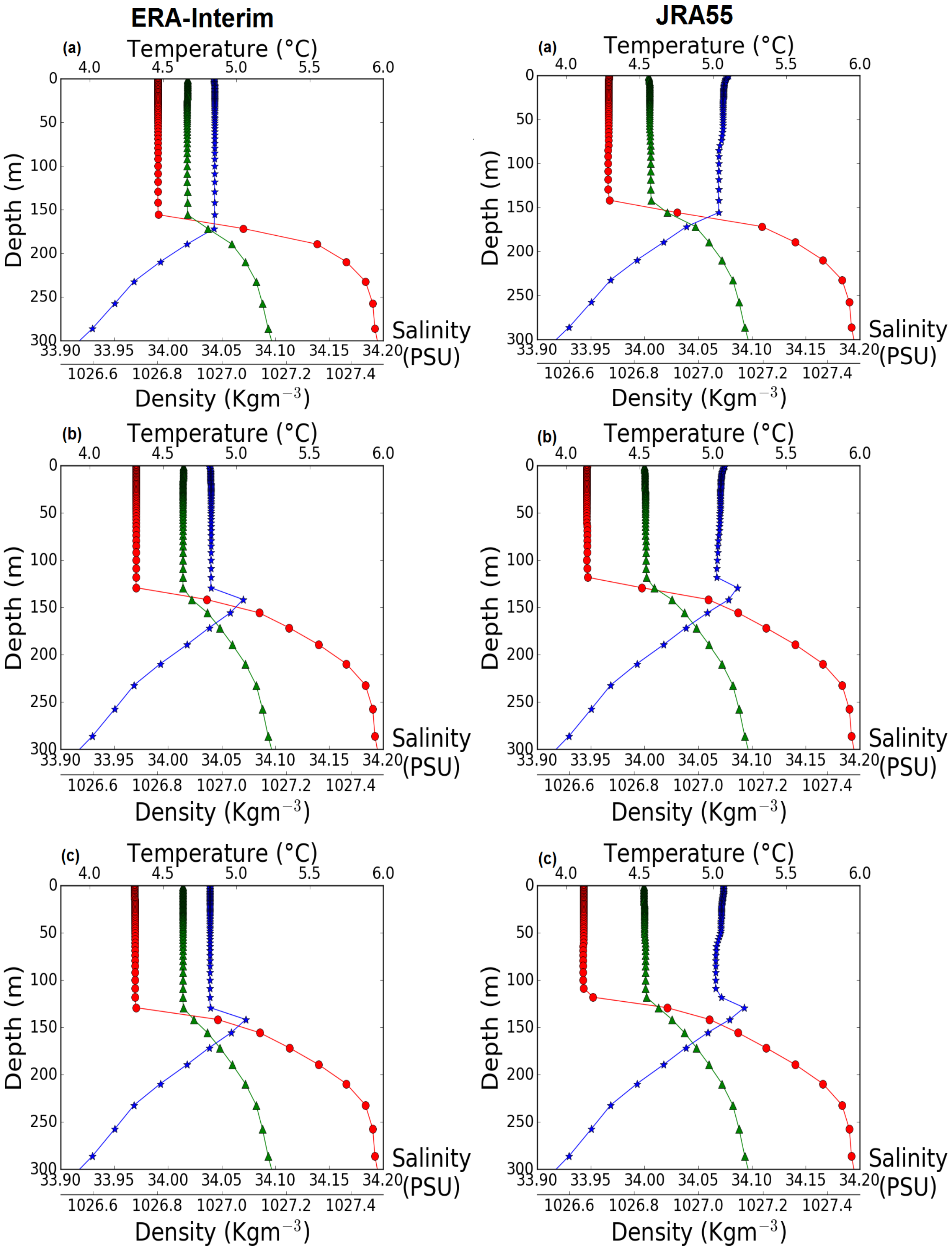

FIGURE 4.3: The column **temperature, salinity and density profiles** for **ERA-Interim** and **JRA55** using 101 vertical levels and (a) $k-\varepsilon$, (b) TKE10 and (c) the Pacanowski/Philander schemes for the SO respectively. These profiles were plotted for a day during deeper mixing in September. The warm water parcel can be observed at approximately 140 $\mathrm{m}$ deep. The key to all graphs is given by: ●-● salinity, ▲-▲ density and ★-★ temperature. Note that the salinity axis is above the density axis for all plots.

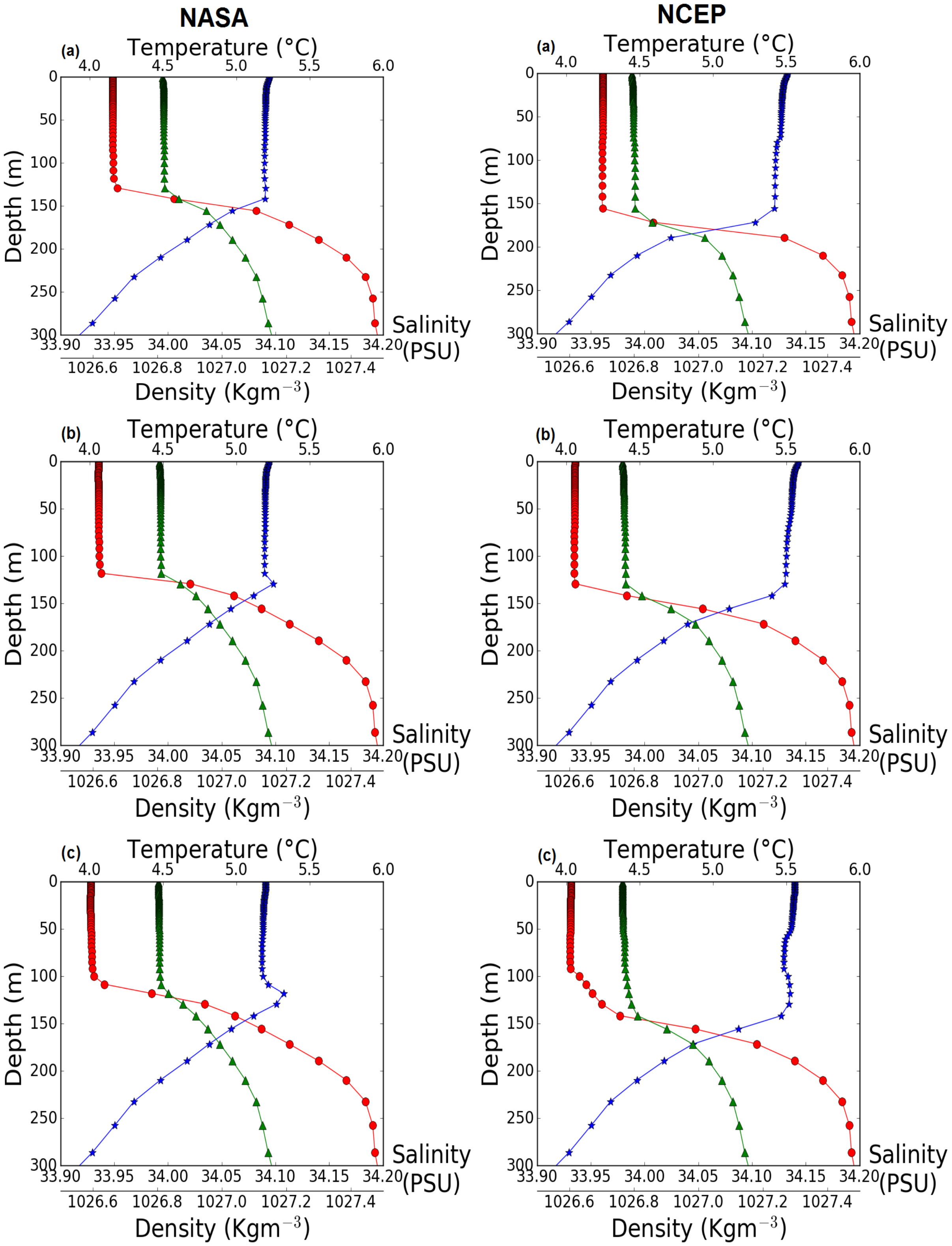

FIGURE 4.4: Continuation of Fig. 4.3 illustrating the SO column **temperature, salinity and density profiles** for **NASA** and **NCEP** using 101 vertical levels and the (a) $k-\varepsilon$, (b) TKE10 and (c) the Pacanowski/Philander schemes respectively. These profiles were plotted for a day during deeper mixing in September. The warm water parcel can be clearly observed at approximately 140 $\mathrm{m}$. The key to all graphs is given by: ●-● salinity, ▲-▲ density and ★-★ temperature. Note that the salinity axis is above the density axis for all plots.

## 4.3 Simulation output validation against ARGO observed data and the early stratification

Fig. 4.5 shows the simulated data compared to the ARGO float data and Winter Cruise (WC_CTD ) temperature profile data for June/July/August. The WC_CTD data were measured from the greater SAZ region (see Section 3.4.4). Fig. 4.6 shows the November ARGO temperature profiles. These profiles were chosen to investigate the austral winter deep mixing season and the austral spring water column dynamics respectively. The sensitivity to the various turbulence schemes and reanalyses are presented later in this chapter. For Figs. 4.5 and 4.7 in this section, the ERA-Interim and Pacanowski/Philander turbulence scheme combination was used as a representative for the various reanalyses and turbulence schemes.

The June/July/August ARGO profiles all exhibited full mixing (namely no stratification of the upper water column). The mixing was found down to approximately 110 $\mathrm{m}$ deep. The WC_CTD data also show full upper column mixing and was found down to approximately 150 $\mathrm{m}$ deep. Note that the near surface WC_CTD data for 2016 was noisy and probably was due to the CTD apparatus swinging or adjusting to the cooler water temperatures upon being submerged.

The simulation output was mixed down to approximately 130 $\mathrm{m}$. This showed that the model was able to correctly simulate deep mixing in accordance with the season as compared to the validation data (ARGO and WC_CTD ). The simulation MLD's were comparable to the ARGO and WC_CTD data. The simulation MLD's however, were not exactly the same as the ARGO and WC_CTD MLD's and the upper mixed column temperature was dissimilar by at least 1 $^{\circ}\mathrm{C}$ in comparison to the validation data. This was mainly due to the various locations (within a $1^{\circ}\times1^{\circ}$ box surrounding the study location for ARGO profiles, see Section 3.4.5) and years of the validation data. Below the mixed layer at $\sim$180 $\mathrm{m}$, the simulation profiles followed the validation data closely with exception of the 2016 WC_CTD and June 2011 ARGO profiles.

The ARGO and WC_CTD profiles showed the presence of a warm water parcel entrapped below the upper mixed layer (with exception of the June and July 2011 ARGO profiles). This was strong evidence that the warm water feature found in the simulation profiles did exist in reality and are not a model defect or numerical error issue. The WC_CTD profiles exhibited a warm parcel at approximately 180-200 $\mathrm{m}$ whereas the warm parcels in the ARGO profiles were found roughly at 140 $\mathrm{m}$ and 180 $\mathrm{m}$ respectively. The simulation profiles had a warm parcel at $\sim$140 $\mathrm{m}$ deep which was considerably shallow compared to the WC_CTD profiles. The varying depths of the warm water parcel could have suggested that this was an intermittent phenomenon only occurring under specific conditions where the potential energy of the parcel cannot be released into turbulent kinetic energy. The 2016 ARGO profile data showed two warm bulges in the upper water column.

The spring upper column dynamics could be examined using the November ARGO profiles which are shown in Fig. 4.6. The data obtained were from the same ARGO float and the profiles were recorded two days apart (20 and 22 November respectively). On 20 November, the MLD extended down to 100 $\mathrm{m}$ with an approximate temperature jump of 1.5 $^{\circ}\mathrm{C}$ at the thermocline (namely transitional layer). On 22 November, the MLD remained at 100 $\mathrm{m}$, however, the temperature jump at the transitional layer was approximately 0.5 $^{\circ}\mathrm{C}$. The temperature of the water column (close to the vicinity where the 20 November profile was obtained) had cooled by $\sim$1 $^{\circ}\mathrm{C}$. This decrease in temperature was probably due to a storm event drawing energy from the water column, consequently cooling it.

Despite the cooling, the selected November ARGO profiles still had a well mixed upper water column. Fig. 4.6 also shows simulation temperatures plotted for the various reanalyses using the $k-\varepsilon$, TKE10 and Pacanowski/Philander turbulence schemes. It was noticeable that all upper column simulation profiles during November were already stratified as compared to the November ARGO profiles which showed no signs of stratification. This suggested that the simulations have stratified approximately one month earlier. The simulation profiles showed evidence of initial stratification during October (see Fig. 4.1 and Section 4.4). This showed that the model struggled to correctly capture the spring water column dynamics. This did not imply that the model was entirely wrong. It suggested that the model only failed to capture the stratification dynamics during November in this case. Due to limited ARGO data in the region for November, it was impossible to ascertain whether the model always stratified early. The upper 100 m temperatures tended to be lower than the ARGO profile data with exception of the NCEP result (Fig. 4.6 (d)) which tended to follow the 20 November ARGO temperature profile. The simulation temperatures below 150 m followed the 20 November ARGO temperature profile with minimal deviation.

It was interesting to note that there were warm water parcels captured below cooler waters in the November ARGO profiles. This suggested possible further evidence of the entrapment of the warm water parcel feature. After a cooling of the upper water column (from 20 to 22 November), the warm parcel had somewhat diminished and the transitional layer had a narrower temperature gap (from $\sim 1.3$ °C to 0.5 °C).

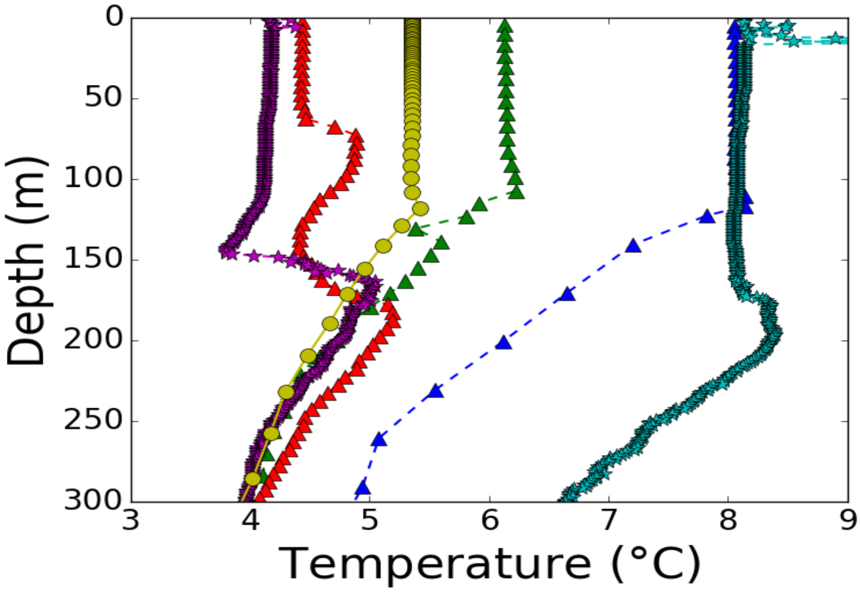

FIGURE 4.5: ARGO temperature profiles and simulated temperature profiles for June/July/August. The NEMO simulation had 101 vertical levels and are plotted for ERA-Interim and Pacanowski/Philander turbulence scheme. The legend is given by ▲-▲ ARGO 2011-06-25, ▲-▲ ARGO 2011-07-25, ▲-▲ ARGO 2016-08-20, ★-★ WC_CTD 2016-07-18, ★-★ WC_CTD 2017-07-01 and ●-● NEMO July ERA-Interim/PP.

The Brunt Väisälä frequencies, for the upper 300 m of the water column, were computed for the ARGO profiles as well as the ERA-Interim and Pacanowski/Philander scheme combination. These are shown in Fig. 4.7. The June and July (Fig. 4.7 (a)) ARGO Brunt Väisälä frequency profiles showed a well defined permanent pycnocline at ∼130 m. The August profile (Fig. 4.5 (a)) had two peaks in the column profile due to the two warm bulges found at ∼60 m and ∼170 m. The simulation was able to obtain a comparable position for the permanent pycnocline compared to the June and July ARGO profiles. The magnitude of Brunt Väisälä frequency however, was underestimated by approximately $1.5\times10^{-4}\ \mathrm{s}^{-1}$. The simulated Brunt Väisälä frequency overestimated (with exception of the August ARGO profile) the ARGO Brunt Väisälä frequencies between 150-200 m. The November Brunt Väisälä frequency profiles (Fig. 4.7 (b)) showed two peaks that coincided at their respective depths (∼80 m and ∼150 m). The larger peak at a shallower depth indicated the permanent pycnocline whereas the flatter peak at a deeper depth indicated the warm parcel presence. The simulation had also shown two peaks. Due to the model showing an earlier stratification however, the larger peak at shallower depth was the seasonal pycnocline and the flattened peak was where the warm parcel was found (see temperature profiles in Fig. 4.5). The seasonal pycnocline was shallower than the ARGO permanent pycnocline by ~30 $\mathrm{m}$. Furthermore, the model simulated the area of warm parcel (~150 $\mathrm{m}$) satisfactorily.

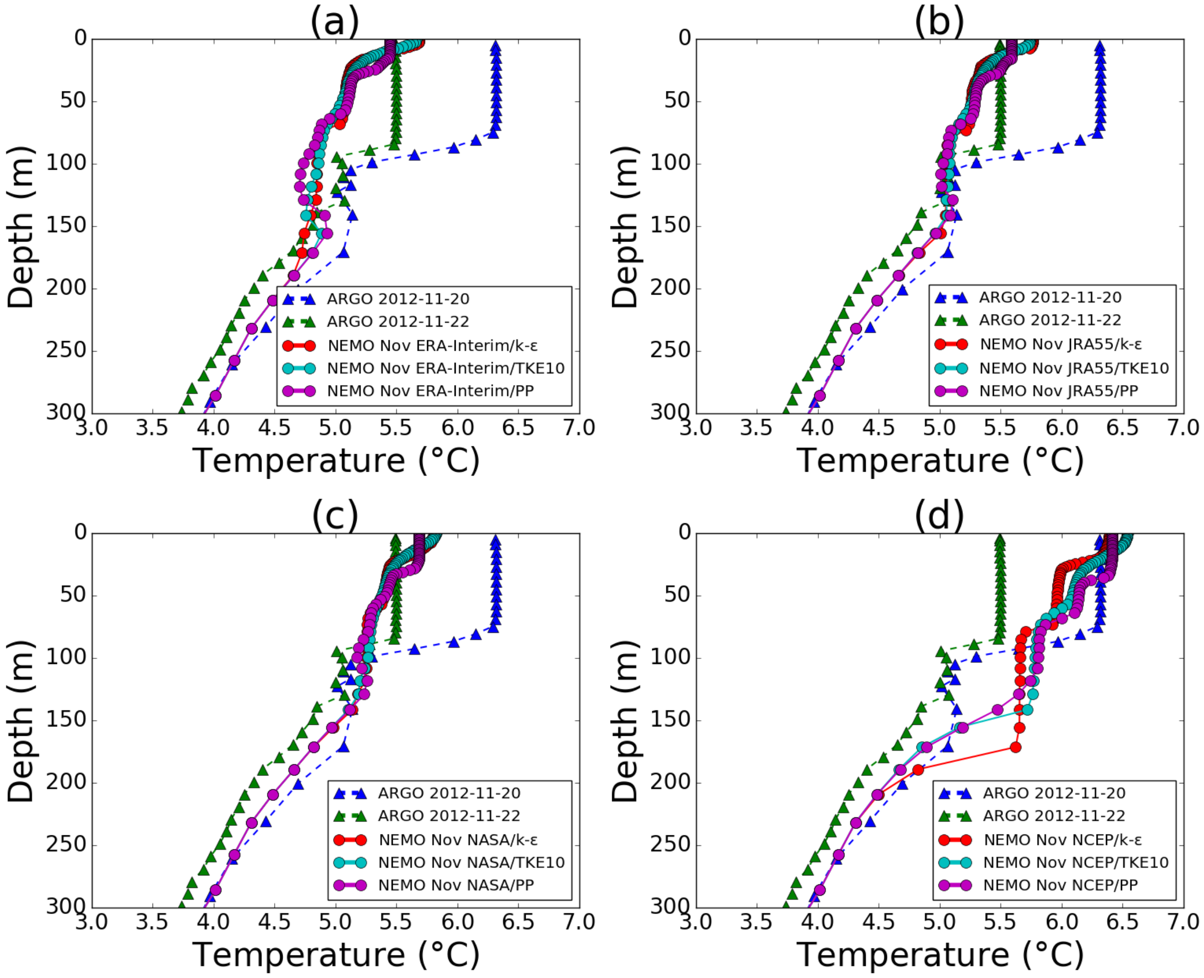

FIGURE 4.6: ARGO temperature profiles and simulated temperature profiles for November. Simulations used 101 vertical levels and are plotted for **(a) ERA-Interim**, **(b) JRA55**, **(c) NASA** and **(d) NCEP** for the $k-\varepsilon$, TKE10 and Pacanowski/Philander turbulence schemes.

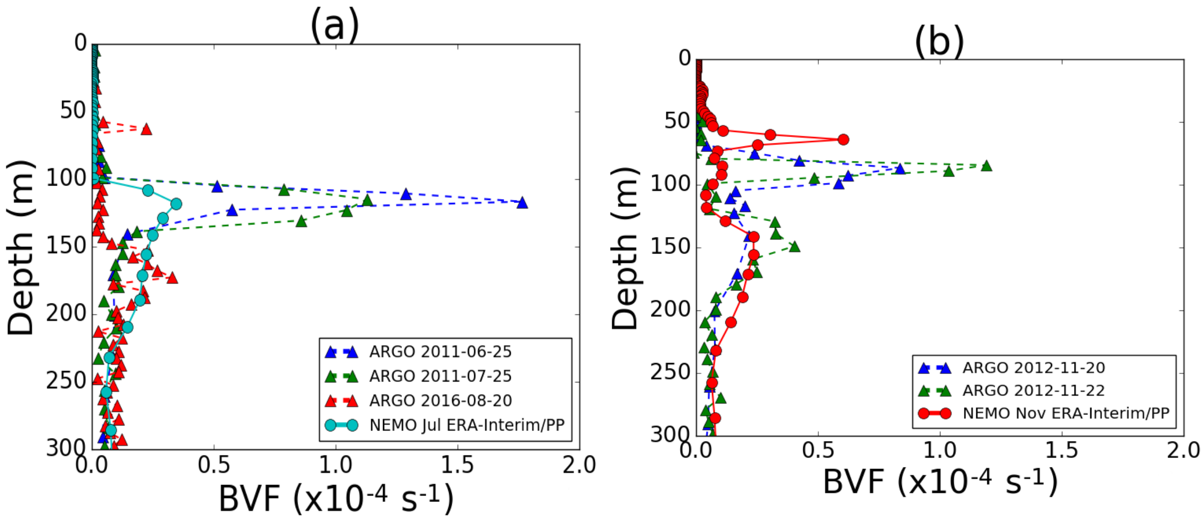

FIGURE 4.7: ARGO and NEMO simulation (ERA-Interim and Pacanowski/Philander turbulence scheme combination) Brunt Väisälä frequency profiles for **(a) June/July/August** and **(b) November**. Simulation used 101 vertical levels and time step of 360 s.

## 4.4 Brunt Väisälä frequency as an indicator to track the water column stratification

In order to ascertain whether the start of stratification was October for simulation output, the evolution of Brunt Väisälä frequency was computed as it is a natural indicator of local stratification strength. The water column stratification structure was observed from the Brunt Väisälä frequency plots shown in Fig. 4.8. They were computed using Eqn. 3.6 via the potential density which in turn was computed using the temperature and salinity results. Brunt Väisälä frequencies from simulations of JRA55 data (chosen as an example to represent the other reanalyses as they have similar trends and Brunt Väisälä frequencies) in conjunction with the $k - \varepsilon$, TKE10 and Pacanowski/Philander schemes are shown. During the deep mixing period the upper water column ($\sim$120 m) had low frequencies indicating the absence of strong stratification. Higher frequencies were found during the austral summer implied the onset of strong stratification events. The high frequency band (red area at $\sim$60 m in Fig. 4.8) indicated the seasonal pycnocline. The permanent onset of the seasonal pycnocline occurred during October and underwent a descent further through the season. The high frequency band at approximately 150 m was known as the permanent pycnocline. The permanent and seasonal pycnoclines slowly merged during the stratification breakdown.

At the austral spring onset, multiple strong stratification events occurred which initiated the formation of the seasonal pycnocline. The seasonal pycnocline was formed at $\sim$60 m (October) and slowly descended to $\sim$100 m from October to June leading into the austral autumn. The descending trend implied the stratification began to erode and slowly diminished allowing deeper mixing events. The one month early stratification tended to force an early onset of the seasonal pycnocline due to the hydrostatic assumption (see Subsection 2.3.1) in ocean models which inhibits mixing if there is a stable density profile. Larger Brunt Väisälä frequencies implied larger energy was required for initiating the overturning motion (the motion of lifting heavy waters upon lighter waters) within the water column (especially at the seasonal and permanent pycnoclines) and consequently, the turbulent layer shallowed.

During the formation of the seasonal pycnocline, there were 'pockets' of stratification that resembled bulges upon the pycnocline as it was formed during October to early December. These 'pockets' were due to stratification events resulting from positive buoyancy injections (explained in Subsection 4.6).

This suggested that the seasonal pycnocline provided a barrier in this aspect, as the buoyancy effects transmitted downward from the ocean surface could not penetrate below the seasonal pycnocline. The pycnocline also inhibited momentum transfer between oceanic layers of inhomogeneous properties and suppressed the turbulence (although internal waves may have been present at ocean layer interfaces in reality and is parameterized because it is not part of the model). This had the implication of diminished turbulence during the austral summer as compared to the winter season.

The result obtained using the Pacanowski/Philander scheme (Fig. 4.8 (c)) displayed a sudden deepening of the seasonal pycnocline during March and eventually merged with the permanent pycnocline. The complete merging however, was not seen in Figs. 4.8 (a) and (b) and occurred after the end of the time period (June). The pycnoclines had merged earlier (April) when using the Pacanowski/Philander scheme. The column averaged Brunt Väisälä frequency, down to 300 m, was plotted on the same Brunt Väisälä plot for comparison of the frequency density throughout the time period. During August a sudden stratification event was detected by the strong signal in the average Brunt Väisälä frequency curve when using the $k - \varepsilon$ and TKE10 turbulence schemes. The stratification event was still present when using the Pacanowski/Philander scheme, however, a weaker signal was found compared to the other turbulence schemes. This mid-winter stratification event in August (Fig. 4.8), persisted for a single day and deep mixing commenced thereafter. The average Brunt Väisälä frequency peaked during mid-December and beginning of February (for all turbulence schemes), indicating that these were the periods of strongest stratification in the water column.

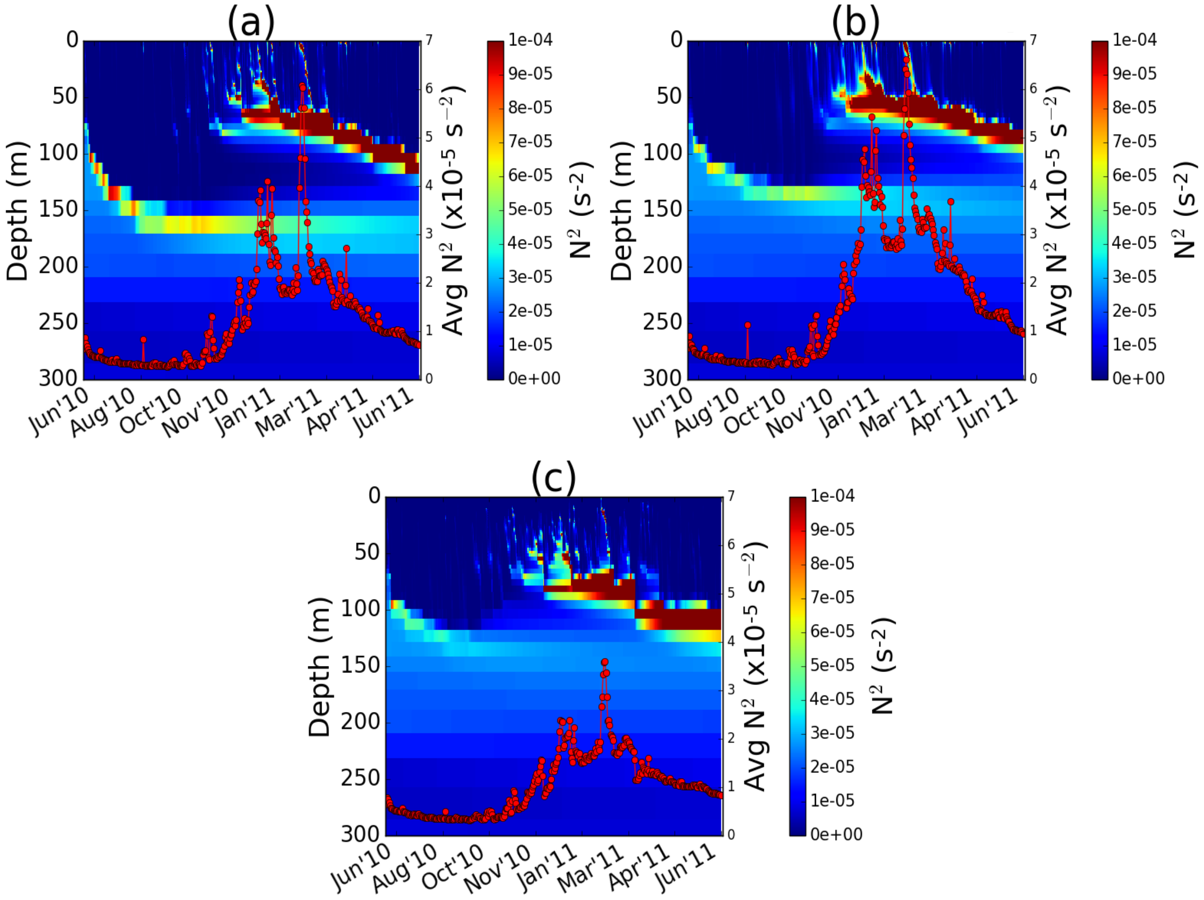

FIGURE 4.8: **Brunt Väisälä frequency** (15 June 2010 - 14 June 2011) using JRA55 data, 101 vertical levels for the **(a) $k - \varepsilon$, (b) TKE10 and (c) Pacanowski/Philander** turbulence schemes respectively. The column averaged Brunt Väisälä frequency for the upper 300 m (red curve) is also plotted for comparison.

## 4.5 Turbulent diffusivity, turbocline and MLD analysis

The turbulent eddy diffusivity (see Section 2.4) is one of the prognostic model variables that indicates the localised turbulence strength within the water column. This diagnostic helped to indicate when the action of high turbulence diminished in the upper water column which led to stratification. Fig. 4.10 shows the evolution of diffusivity, MLD and turbocline results plotted for the $k-\varepsilon$, TKE10, Pacanowski/Philander and TKE30 turbulence schemes respectively. The JRA55 results were chosen as a representative amongst the various reanalyses. Diffusivities below $1\times10^{-4}\ \mathrm{m^2\,s^{-1}}$ were masked to highlight the turbocline and MLD behaviour. High diffusivities (O($10^2\ \mathrm{m^2\,s^{-1}}$)) were found down to 150 m during deeper mixing which indicated that the convective adjustment parameterization was initiated which allowed for deep penetration of turbulence during the austral winter. During summer, high diffusivities were contained within the upper 50 m of the water column due to the seasonal pycnocline acting as a convective barrier against turbulent kinetic energy penetration. Note that using the Pacanowski/Philander scheme resulted in diffusivities with an order of magnitude larger compared to other turbulence schemes possibly due to the lack of prognostic equations governing the evolution of turbulent kinetic energy and dissipation of turbulent kinetic energy.

Stratification occurred during October due to the containment of the high diffusivities from ∼150 m to ∼50 m. During the stratification period, high diffusivities were bounded by the seasonal pycnocline (see Brunt Väisälä frequency results in Fig. 4.8). The pycnocline acted as a barrier that inhibited the entrainment of deeper waters resulting from turbulence. This ensured that the turbulent layer shallowed during the stratification period. During the descent of the seasonal pycnocline (or stratification erosion), up until it merged with the permanent pycnocline, turbulence began to dominate leading to higher diffusivities penetrating deeper into the water column.

The turbocline (see Subsection 3.5.2.2) is the depth indicating the interface between turbulent fluid above from quasi-laminar fluid below. In general, the turbocline and MLD spiked simultaneously because a stratifying (destratification) event shallowed (deepened) both the MLD and turbulent layer simultaneously. The turbocline however, exhibited a higher sensitivity to the water column turbulent state as compared to the MLD. This was because the turbulent layer was more volatile to slight changes in column state and obtained signal where sometimes the MLD was without variation. This was especially observed during the deep mixing period, where sudden stratification events occurred that were not found in the MLD signal. For example, the stratification event during August for NASA, NCEP and JRA55 was easily observed as a sudden shallowing in the turbocline. Nonetheless, the MLD did not shallow. This event seemed strange but was consistent with the prescribed surface buoyancy fluxes (Figs. 3.5-3.8) where the wind speeds were effectively $0\ \mathrm{m\,s^{-1}}$ allowing the solar and thermal fluxes to dominate on that day creating a significant stratification. The shallowest MLD and turbocline depths occurred during mid-December and beginning of February. These periods suppressed the turbulence within the water column. As the stratification broke down from March onward, the MLD and turbocline deepened. This was known as the austral autumn descent of the MLD and turbocline.

A comparison of MLD's and turboclines (Fig. 4.9) between turbulence schemes indicated that using $k-\varepsilon$ and the Generic schemes provided the deepest MLD for all reanalyses. Similarly for the turboclines, the $k-\varepsilon$ and Generic schemes provided the deepest turboclines for ERA-Interim and NCEP. The Generic scheme produced the deepest turboclines for JRA55 and NASA. The shallowest turboclines and MLD's were all under 20 m for any combination of reanalyses and turbulence schemes. This meant that the turbulent and mixed layer was in the band of 15-190 m throughout the simulation period.

When using the TKE30 scheme shown in Fig. 4.10 (d), the results tended to exhibit higher diffusivity due to the deeper injection of turbulent kinetic energy (30 m below the MLD). Consequently,

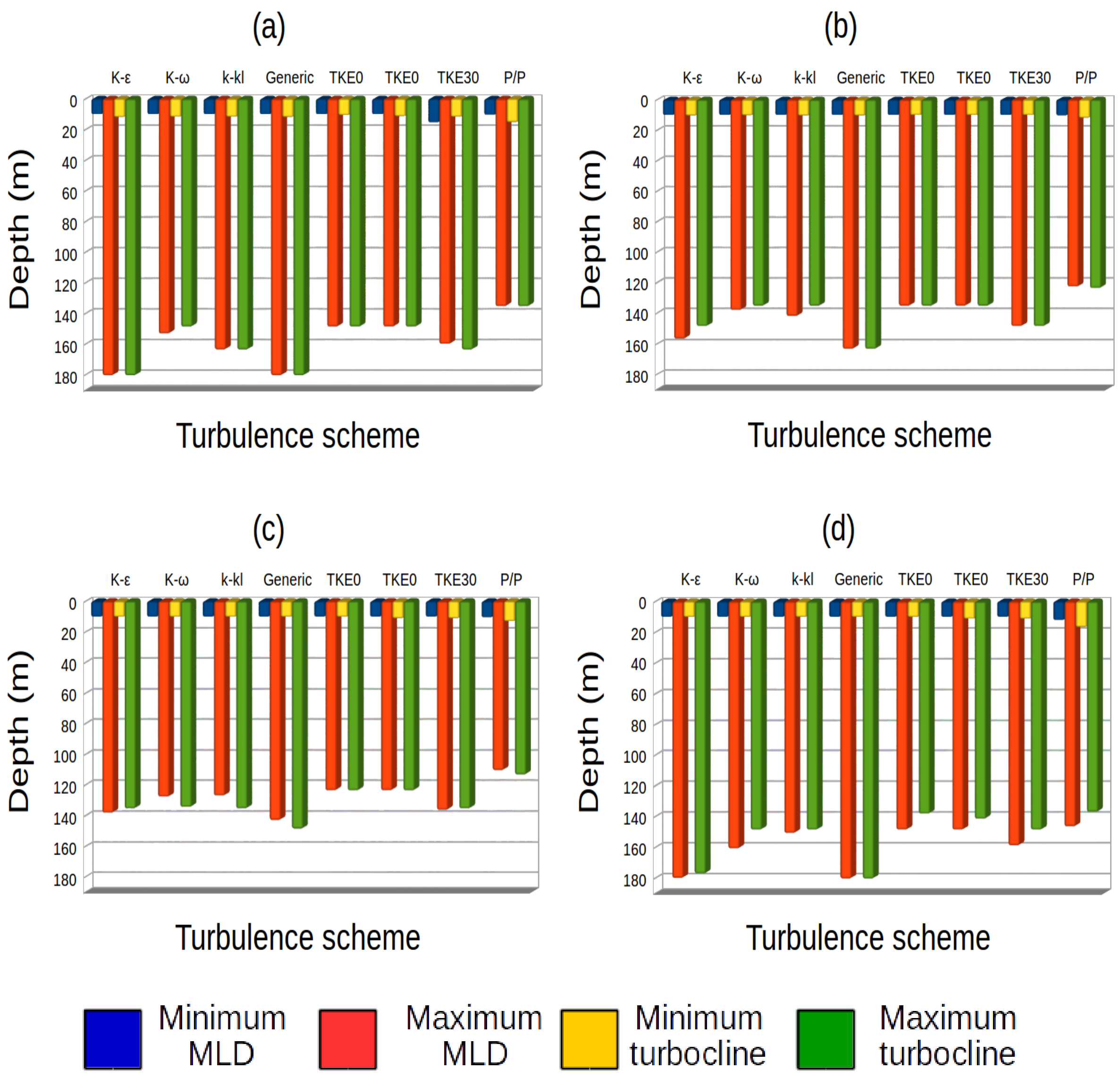

FIGURE 4.9: Comparison of deepest and shallowest **MLD's** and **turboclines** for the various turbulence schemes and reanalyses: **(a) ERA-Interim**, **(b) JRA55**, **(c) NASA** and **(d) NCEP**. The values were found for the period June 2010 - June 2011 for simulations using 101 vertical levels.

deeper mixing was induced and the thermoclines were not sharp (namely not well defined). As austral spring stratification events occurred, turbulence immediately below $50\ \mathrm{m}$ was sustained and not suppressed (compared to other schemes), consequently deepening the turbocline. The MLD on the other hand remained shallow due to the density criterion used in its calculation. This implied that the turbocline and MLD separated during the austral spring/summer. They had rejoined during the austral autumn.

Turbulent diffusivity leakage below the turbocline was present in all turbulent diffusivity results. The leakage (having approximate values close to $1 \times 10^{-4}\ \mathrm{m}^2\,\mathrm{s}^{-1}$) showed areas where turbulence was still present. This leakage was acceptable due to the model having a numerical turbulent diffusivity threshold used in calculating the turbocline which allowed weak turbulent behaviour to have occurred directly below the turbocline.

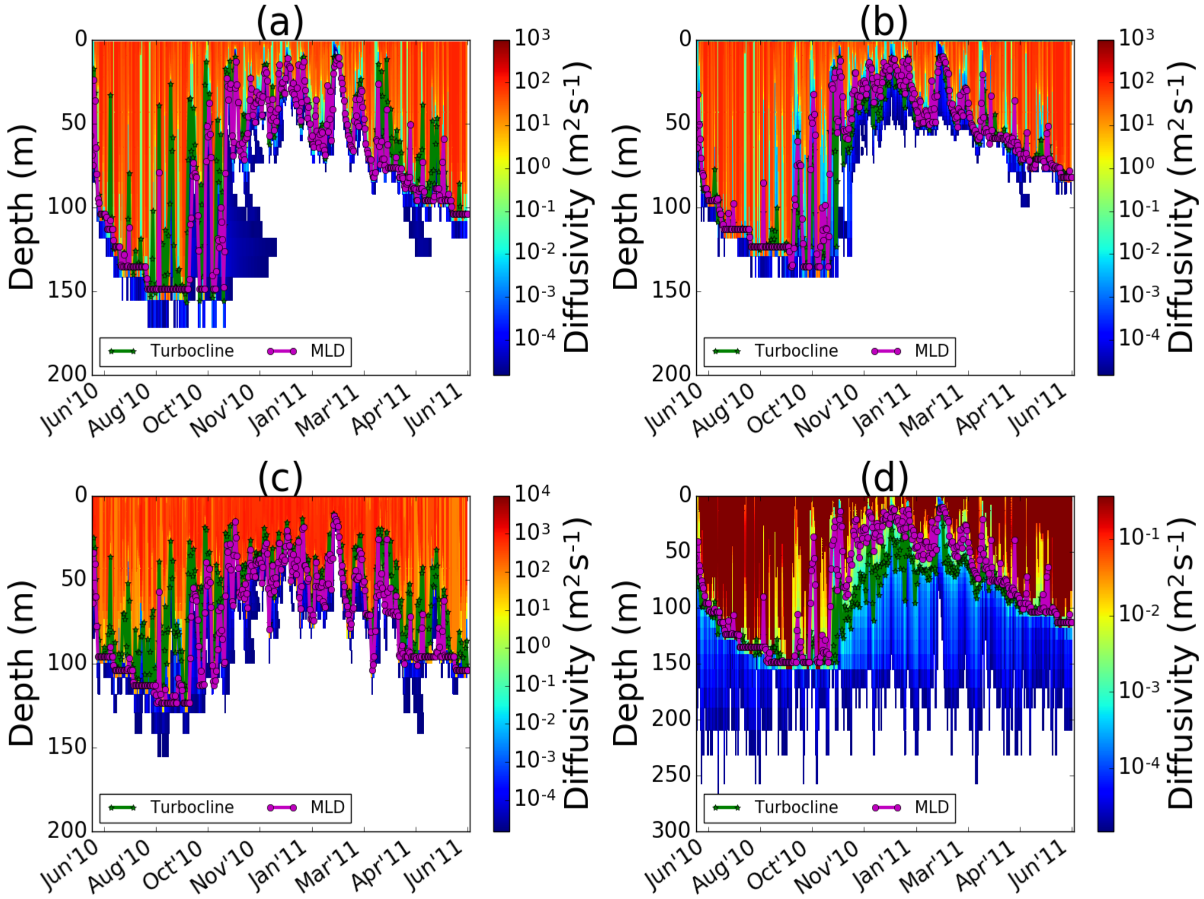

FIGURE 4.10: **Turbulent diffusivity, turbocline and MLD** for JRA55, 101 vertical levels and using the **(a) $k-\varepsilon$, (b) TKE10, (c) Pacanowski/Philander and (d) TKE30** turbulence schemes respectively. White space consist of turbulent diffusivities below the threshold of $1.5 \times 10^{-5}$ m$^2$ s$^{-1}$.

## 4.6 Buoyancy flux, wind stress magnitude and potential energy anomaly (PEA)

The buoyancy flux and wind stress magnitude (calculated using Eqns. 3.9 and 3.5.2.3 respectively) are shown in Figs. 4.11 and 4.12 respectively. The average Brunt Väisälä frequency was plotted for comparison as well as the weekly running mean of buoyancy flux and wind stress to filter synoptic (large scale) events to better observe the trends. The zero horizontal line and change from positive to negative vertical lines plotted over the buoyancy flux was to aid the analyses. They were plotted for all reanalyses in conjunction with the $k - \varepsilon$ turbulence scheme (used as the representative amongst all the schemes). Every peak in the buoyancy flux and wind magnitude indicated a physical event (high/low precipitation, solar radiation influx or storm event) which influenced the upper water column accordingly.

During the austral winter, the buoyancy flux was generally negative which was indicative of surface cooling. Small positive peaks were present during this season which had the effect of mildly suppressing the deep mixing (mild stratification). The downward momentum entrainment due to deep mixing slightly increased the density of the upper waters (namely shifted mass upward) which in turn raised the centre of mass of the water column. The large positive buoyancy fluxes in summer lead to the strong stratification of the upper layers of the water column shown earlier. The stratification implied a downward shift of the centre of mass in the water column due to the lighter waters present in the upper layers. The buoyancy flux started to decrease during February, allowing the beginning of stratification erosion by wind stress to dominate.

The buoyancy flux and wind stress magnitude worked in conjunction which could be observed using the averaged Brunt Väisälä frequency. This was especially seen during September where the buoyancy flux was positively increasing (implying a stratification), however, the averaged Brunt Väisälä frequency was still decreasing (namely deep mixing was persisting). This suppression of the stratification indicated the presence of the wind stress which dominated during this period leading to deep mixing even though there was a positive increasing buoyancy flux.

Low values of wind stress indicated weak or no wind which were favourable for stratification (in combination with a strong positive buoyancy flux) as there was little momentum injection contributing to turbulent mixing. In contrast, a strong wind stress implied large impartation of momentum into the water column providing favourable conditions for deep mixing especially in conjunction with a negative buoyancy flux. This could have however, been dampened if strong stratification was present (large dominating positive buoyancy flux).

All buoyancy fluxes in Fig. 4.11 followed a similar annual trend and showed a gradual increase from the end of winter up to summer and slowly decreased thereafter. There appeared to have been no general trend between the wind stress magnitude for the various reanalyses as the values varied considerably (Fig. 4.12). The ERA-Interim wind stress magnitude displayed a succession of storm events during the austral winter as well as a very strong storm event during the summer. The other reanalysis also displayed a succession of storm events during the austral winter. NCEP however, had larger storm events (compared to the other reanalyses) throughout the year. For summer storm events (January - March), the average Brunt Väisälä frequency showed a decrease which was consistent with mixing involved during a storm.

During September and October the wind stress (which drove the deep mixing) was contending against an increasing positive buoyancy flux (which drove stratification). For the early stratification (see Section 4.3) to have occurred the buoyancy flux had to have dominated the wind stress. Fig. 4.11 shows the buoyancy flux increasing during September while the average Brunt Väisälä flux remains small. This was a possible reason for the early stratification.

The PEA (see Subsection 3.5.2.4) describes the amount of energy needed to fully mix the water column in order to obtain homogeneous tracer (salinity and temperature) values throughout the water column. The PEA (or $\phi$) results are shown in Fig. 4.13 and plotted for the various reanalyses using the $k-\varepsilon$ turbulence scheme. They followed similar general trends, i.e. the seasonality was present. The average Brunt Väisälä frequency (upper 300 $\mathrm{m}$) was plotted for comparison as well as the change from positive to negative vertical lines that appeared in the buoyancy flux plots (Fig. 4.11). The PEA was a great descriptor for the buoyancy flux and wind stress magnitude as it could be computed from the salinity and temperature simulation data (in conjunction with TEOS10 to calculate the density). It was observed that both PEA and Brunt Väisälä frequency increased during the stratification period and were at a minimum during the deep mixing period which conformed to the seasonal cycle. Low PEA were found during winter due to deep mixing (turbulence) homogenizing the upper water column, whereas energy needed for full column mixing increased during summer due to the various upper stratified layers.

The NCEP result (Fig. 4.13 (d)) indicated the largest PEA (21 $\mathrm{kJ\,m^{-3}}$) as compared to the other reanalyses suggesting that higher energy was needed in general to enable full column mixing during summer even though the wind stress (Fig. 4.12 (d)) was stronger than the other reanalyses. This was due to the larger fluxes from the forcing functions (Fig. 3.7). The lowest PEA during winter (12 $\mathrm{kJ\,m^{-3}}$) resulted using ERA-Interim data, implying that the least energy was needed to enable full column mixing as compared to the other reanalyses. This was due to the low solar fluxes as shown in the ERA-Interim surface forcings (Fig. 3.5).

The PEA had an increase of $0.6\times10^4 \pm 0.2\times10^4$ $\mathrm{J\,m^{-3}}$ from the austral winter (deep mixing) to the summer (strong stratification). The wind stress had a considerable effect on the PEA as a significant drop in PEA, due to a strong storm event, was observed during February for ERA-Interim and March for NCEP. The storm events were observed in the wind stress results in Figs. 4.12 (a) and (d) respectively corresponding to the same time as the drop in PEA. The drop in the PEA signal for JRA55 and NASA were also present. The storm events for these reanalyses however, was not as pronounced as compared to NCEP and ERA-Interim. The PEA was impacted by the storm event with implications of an overall decrease in the energy needed to sustain the stratification, i.e. turbulent mixing dominated. Seasonality was present in all PEA results (for all simulations) however, the PEA value at the beginning of simulation (15 June 2010) did not correspond to the value at end of simulation (14 June 2011) for most cases. The PEA at the end of simulation was always larger compared to at the beginning of simulation value which implied that there was a gain in potential energy in the system. This suggested that turbulence may have been lost (due to turbulent kinetic energy being converted into potential energy) or that energy was not conserved in the system and there was an external source (namely possibly the thermal and solar fluxes) that influenced the PEA. Another possible reason could have been the drift in salinity (slight persistent freshening) that influenced the density calculation.

The time derivative of PEA or $\dfrac{d\phi}{dt}$ held further insight about the PEA curves as it indicates the rate of change of PEA, i.e. how fast stratification onset or destruction occurred due to the buoyancy flux and wind stress. Fig. 4.14 shows the $\dfrac{d\phi}{dt}$ results for the various reanalysis in conjunction with the $k-\varepsilon$ turbulence scheme. All results (including results not displayed for other simulations) $\frac{d\phi}{dt}$ were generally bounded between -200 and 200 $\mathrm{J\,m^{-3}\,s^{-1}}$ with a few exceptions. $\dfrac{d\phi}{dt}$ spiked negative below -200 $\mathrm{J\,m^{-3}\,s^{-1}}$ for the ERA-Interim, JRA55 and NCEP reanalyses due to the strong storm events experienced at this time. These down spikes indicated the severity of the sudden decrease seen in the PEA results due to the storm events. This was a clear indication that storm events had a significant affect on tracer evolution and could be captured in a one-dimensional model.

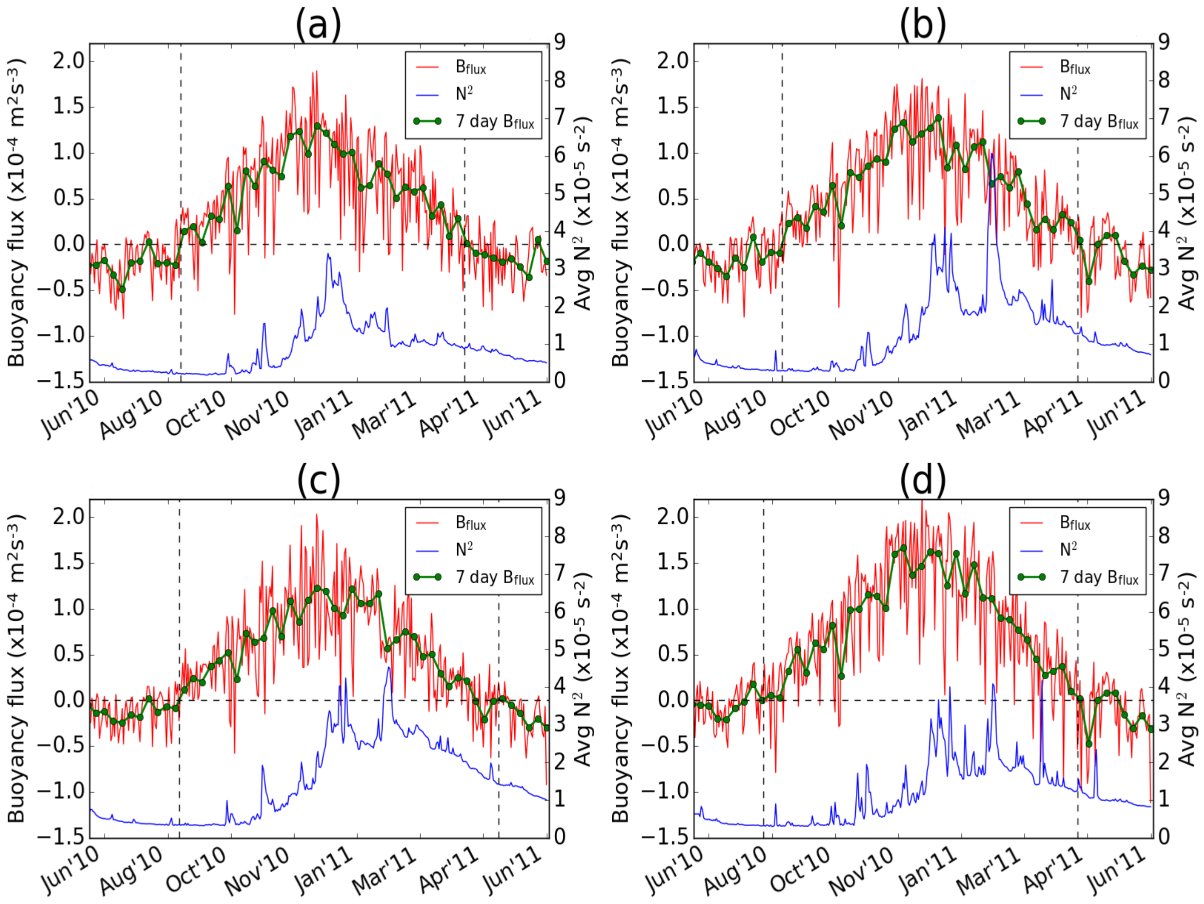

FIGURE 4.11: **Buoyancy flux** (calculated using Eqn. 3.9) for $k - \varepsilon$ and 101 vertical levels. The Brunt Väisälä frequency averaged down to 300 m is plotted for comparison. Simulations were run for 15 June 2010 - 14 June 2011 using **(a) ERA-Interim, (b) JRA55, (c) NASA and (d) NCEP** data respectively.

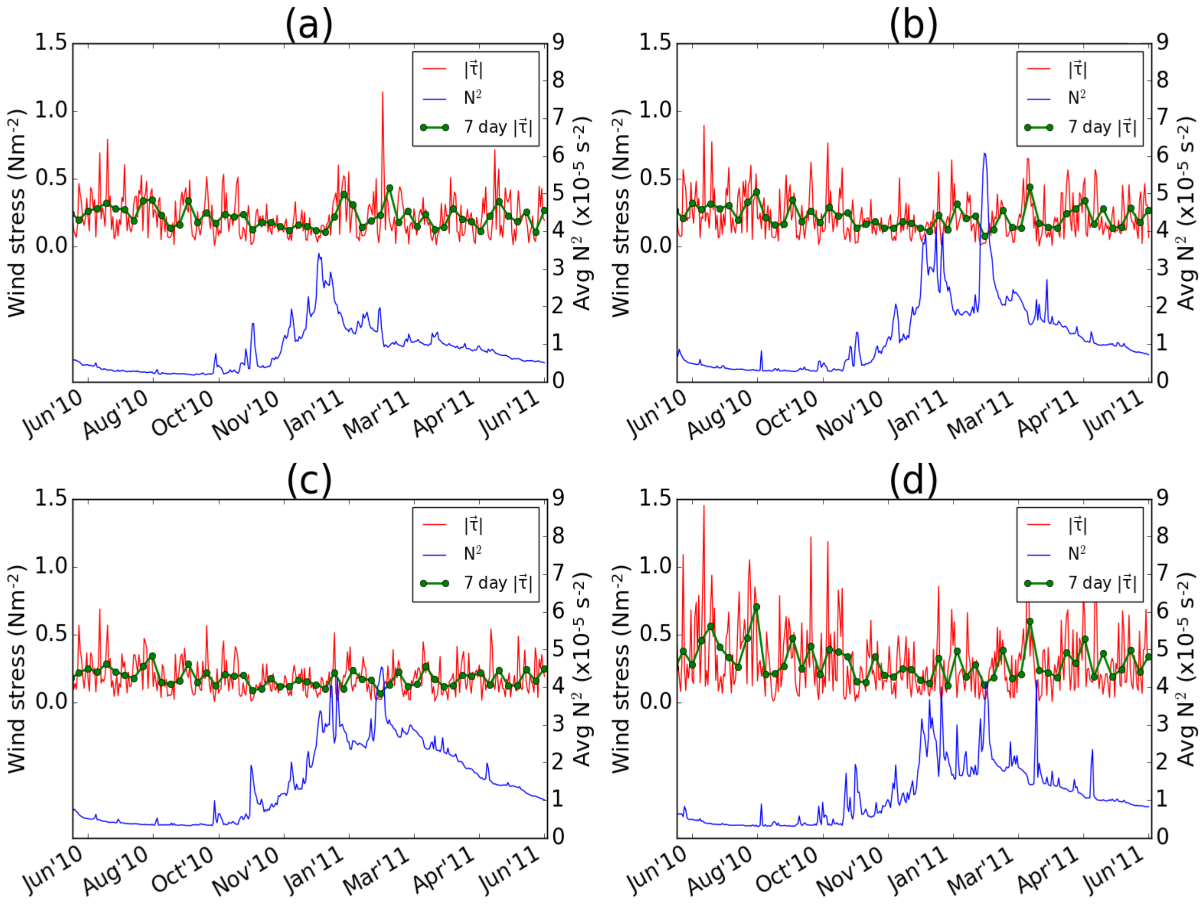

FIGURE 4.12: **Wind stress magnitude** for $k-\varepsilon$ and 101 vertical levels. The Brunt Väisälä frequency averaged down to 300 m is plotted for comparison. The simulations were run for 15 June 2010 - 14 June 2011 using **(a) ERA-Interim, (b) JRA55, (c) NASA and (d) NCEP** data respectively.

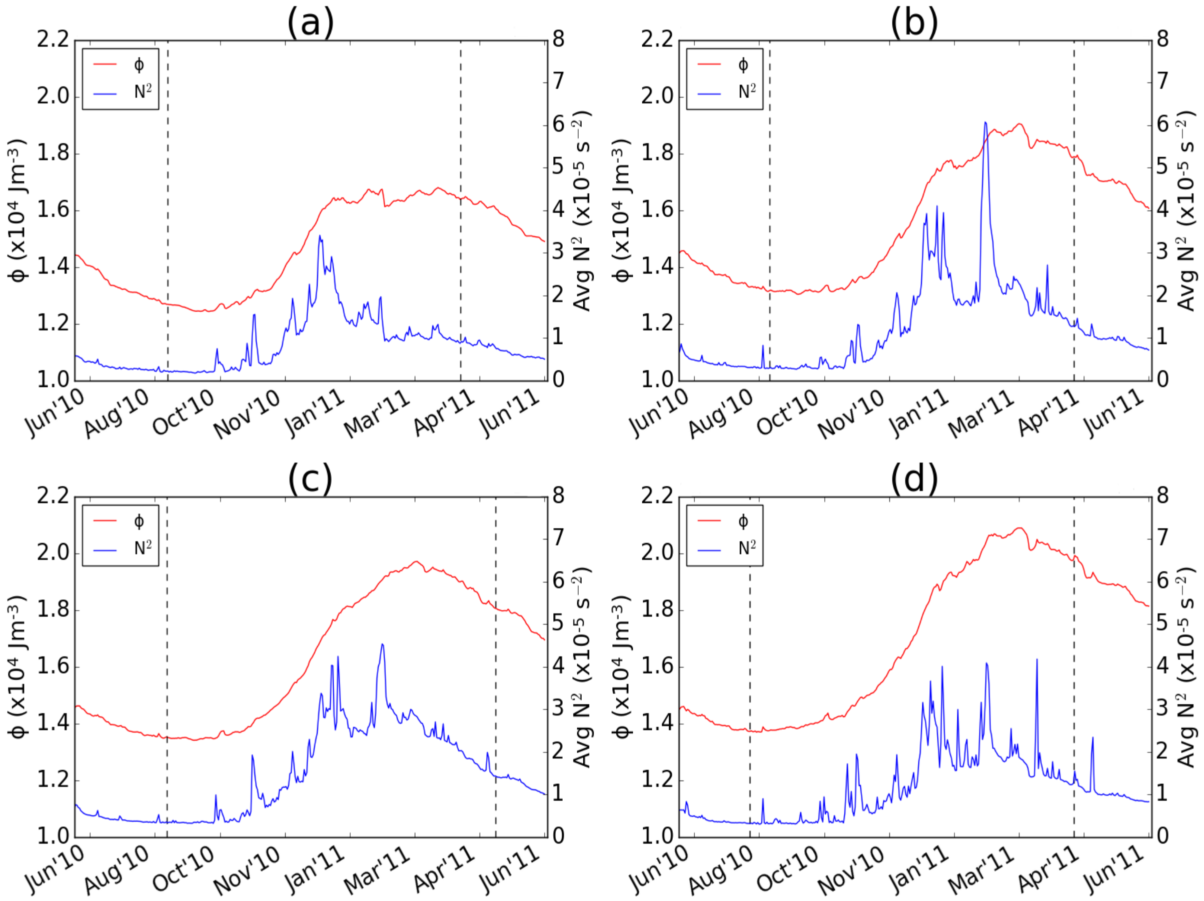

FIGURE 4.13: The **PEA** (calculated using Eqn. 3.10) for $k - \varepsilon$ and 101 vertical levels. The Brunt Väisälä frequency averaged down to 300 $\mathrm{m}$ is plotted for comparison. Simulations were performed for 15 June 2010 - 14 June 2011 using **(a) ERA-Interim, (b) JRA55, (c) NASA and (d) NCEP** data respectively. Vertical lines indicate the change of buoyancy flux from positive to negative according to Fig. 4.11.

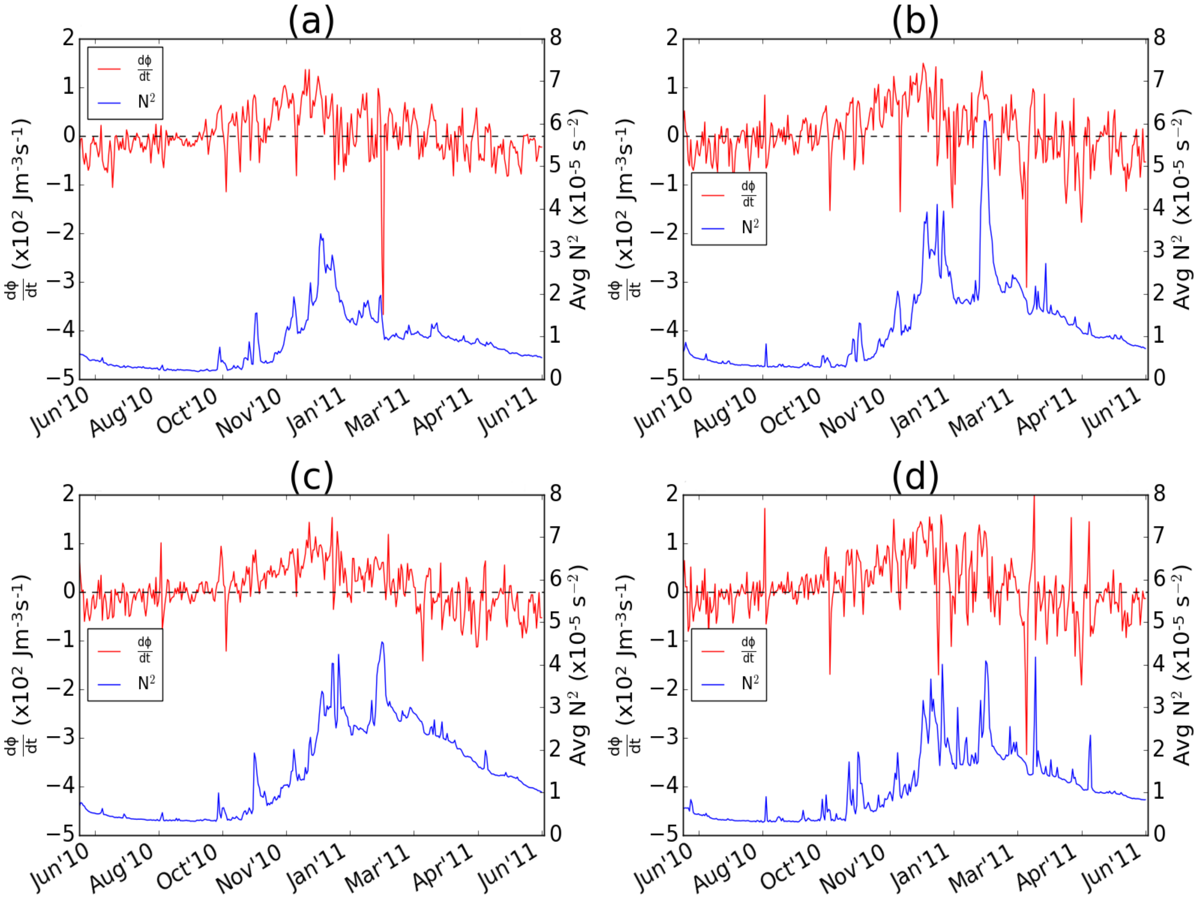

FIGURE 4.14: The time evolution of PEA or $\frac{\mathbf{d}\phi}{\mathbf{dt}}$ for $k-\varepsilon$ and 101 vertical levels. The Brunt Väisälä frequency averaged down to 300 $\mathrm{m}$ is plotted for comparison. Simulations were performed for 15 June 2010 - 14 June 2011 using **(a) ERA-Interim, (b) JRA55, (c) NASA and (d) NCEP** data respectively.

## 4.7 Analysis concerning the role of turbulence schemes and reanalyses

The correlations between the reanalyses for the various turbulence diagnostics and univariate indicators were used to display similarities and trends through the many simulations performed.[1] All correlations were computed using turbulence univariate indicators time series (15 June 2010 - 14 June 2011) unless stated otherwise. Three types of correlations using the diagnostics and univariate indicators were performed, namely (1) correlations between a single turbulence scheme and reanalysis combinations (Table 4.3), (2) correlations between a single turbulence scheme and single reanalysis (Table 4.2) and (3) correlations between a single reanalysis and turbulence scheme combinations (Tables D.1 and D.2 in Appendix D). Point (1) served to ascertain the relationship between the variability between reanalyses, (2) determined the variability of two different types of stratification measures and (3) determined the variability between turbulence schemes (not presented in this chapter due to the laborious tables but found in Appendix D, Tables D.1 and D.2.).

Regarding point (1) above, Table 4.3 displayed correlations computed for various turbulent diagnostics and univariate indicators (MLD, turbocline, Brunt Väisälä frequency, PEA and $\frac{d\phi}{dt}$). The turbocline and MLD did not correlate (low negative correlations were sometimes found) for any combination between reanalyses. No correlation was found between reanalyses for the averaged Brunt Väisälä frequency down to 300 $\mathrm{m}$ except for the JRA55/ERA-Interim which showed a low correlation. The dissimilar correlations were possibly due to the averaging operation which was necessary in order to obtain the time series data. PEA had high correlations for all combinations of reanalyses and was due to similar intra-seasonal variability. There were large $\frac{d\phi}{dt}$ correlations for the NASA/NCEP, NASA/JRA55 and NCEP/JRA55 combinations and low correlations for the other reanalysis combinations. From Table 4.3, it was clear that various reanalyses provide variable results for MLD, turbocline and average Brunt Väisälä frequency and similar results for the PEA and $\frac{d\phi}{dt}$. This suggests that the PEA was a good diagnostic to use to determine the turbulence response of the water column as it did not rely heavily on the reanalysis.

Point (2) above (Table 4.2), displayed the correlations computed between the Brunt Väisälä frequency averaged down to 300 $\mathrm{m}$ and PEA. The rationale was to correlate two indicators of stratification; one that was localized (Brunt Väisälä frequency which had to be averaged down to 300 $\mathrm{m}$ in order to create the time series) and another which incorporated the entire water column (PEA which could be computed from data and also evolve with time) and see how they compared. Due to strong intra-seasonal variability, the decision was made to separately correlate the austral winter (July - September) and summer (January - March) months. The summer correlations were generally weaker than the corresponding winter correlations with a few exceptions. The NASA/TKE0 combination had produced a higher correlation in summer than winter. The NCEP/Pacanowski/Philander combination produced high correlations for both the winter and summer. The ERA-Interim/TKE30 combination had produced poor correlations for both winter and summer. Correlations for the entire time series (namely without splitting the time series data into winter and summer partitions) are shown in Table D.3 (found in Appendix D) for the interested reader.

Regarding point (3) above, the correlations between turbulence schemes for a single reanalysis are shown in Tables D.1 and D.2 (found in Appendix D). All correlations were strong and did not fall below $R = 0.75$. This implied that for any single reanalysis, similar results were found for all turbulence diagnostics and univariate indicators. There was however, variability in the temperature and salinity results which inhibited the correlations of $R = 1$ after the diagnostics and univariate indicators were computed.

---

[1] The correlations were computed using the Pearson Correlation from the *numpy* package in Python.

TABLE 4.1: Presence of warm water parcel for the various combinations between reanalyses and turbulence schemes for 101 vertical levels. The key is given below the table.

| **Reanalysis/scheme** | $k-\varepsilon$ | $k-\omega$ | **M-Y** | **Generic** | **TKE0** | **TKE10** | **TKE30** | **P/P** |
|---|---|---|---|---|---|---|---|---|
| **ERA-Interim** | | SO | SO | S | SO | ASO | ASO | ASO |
| **JRA55** | | S | S | S | SO | SO | S | ASO |
| **NASA** | S | S | S | S | S | S | S | SO |
| **NCEP** | | | | | | | | S |

[A] Warm parcel present at start of deep mixing (April)

[S] Warm parcel present during deep mixing (September)

[O] Warm parcel present at start of stratification (October)

TABLE 4.2: Correlations ($R$) between $N^2$ and PEA for different reanalyses and turbulence schemes for 101 vertical levels results. $N^2$ was averaged down to 300 $\mathrm{m}$ to obtain the time series data. Correlations are computed for the austral winter (August - October) and summer (February - May) respectively. The key, shown in the first entry, is given below the table and applicable for all entries.

| **Reanalysis/scheme** | $k-\varepsilon$ | $k-\omega$ | **M-Y** | **Generic** | **TKE0** | **TKE10** | **TKE30** | **P/P** |
|---|---|---|---|---|---|---|---|---|
| **ERA-Interim** | L[a] N[b] | L N | L L | L N | L L | L L | N N | L N |
| **JRA55** | L N | L L | L L | L N | L L | L L | L N | H N |
| **NASA** | L L | L L | L L | L L | L H | L L | L N | H N |
| **NCEP** | L L | L L | L L | L L | L L | L L | L N | H H |

[a] $\phi$-$N^2$:Winter (July - September)

[b] $\phi$-$N^2$:Summer (January - March)

**H**-High (0.7 - 1); **L**-Low (0.3 - 0.7); **N**-No correlation (-1.0 - 0.3)

TABLE 4.3: Correlations ($R$) for turbulence univariate indicators between various reanalyses per turbulence scheme for 101 vertical levels results. All turbulence indicators correlated used time series data for 15 June 2010 - 14 June 2011. $N^2$ was averaged down to 300 $\mathrm{m}$ to obtain the time series data. The key, shown in the first entry, is given below the table and applicable for all entries.

| **Reanalysis/ Turbulence scheme** | $\boldsymbol{k-\varepsilon}$ | $\boldsymbol{k-\omega}$ | **M-Y** | **Generic** | **TKE0** | **TKE10** | **TKE30** | **P/P** |
|---|---|---|---|---|---|---|---|---|
| **NASA-NCEP** | N[a] N[b] N[c] H[d] H[e] | N N N H H | N N N H H | N N N H H | N N N H H | N N N H H | N N N H H | N N N H H |
| **NASA-JRA55** | N N N H H | N N N H H | N N N H H | N N N H H | N N N H H | N N N H H | N N N H H | N N N H H |
| **NASA-ERA-Interim** | N N N H L | N N N H L | N N N H L | N N N H L | N N N H L | N N N H L | N N N H L | N N N H L |
| **NCEP-JRA55** | N N N H H | N N N H H | N N N H H | N N N H H | N N N H H | N N N H H | N N N H H | N N N H L |
| **NCEP-ERA-Interim** | N N N H L | N N N H L | N N N H L | N N N H L | N N N H L | N N N H L | N N N H L | N N N H L |
| **JRA55-ERA-Interim** | N N L H L | N N L H L | N N L H L | N N L H L | N N N H L | N N N H L | N N L H L | N N L H L |

[a] MLD

[b] Turbocline

[c] $N^2$

[d] $\phi$

[e] $\dfrac{d\phi}{dt}$

**H**-High (0.7 - 1); **L**-Low (0.3 - 0.7); **N**-No correlation (-1.0 - 0.3)

# Chapter 5

# Summary and discussion

## 5.1 Summary of findings

This study focussed on the turbulence response from atmospheric forcing on the near surface by means of a one-dimensional water column. The analysis was done through examining and interpreting the energetics resulting from the various turbulence schemes that are available in physical ocean modelling. The results were all obtained for the annual period 15 June 2010 - 14 June 2011 in the sub-Antarctic Zone (SAZ) located exactly at 47°S, 4.5°E. The time step was chosen to be 360 $\mathrm{s}$ for all simulations.

Seasonality was present in the tracer results (temperature and salinity shown in Figs. 4.1 and 4.2 respectively) which exhibited deep mixing in the austral winter and stratification in the summer. The seasonal and permanent pycnoclines were present and were at $\sim$50 $\mathrm{m}$ and $\sim$150 $\mathrm{m}$ deep respectively. The temperature and salinity had varying results with respect to the reanalysis used. The salinity displayed a slight persistent freshening throughout the time period in focus.

Furthermore, ARGO data for June/July/August and November as well as Winter Cruise temperature profiles were compared against simulation outputs (Figs. 4.5 and 4.6 respectively) and there were three main findings. Firstly, the Mixed Layer Depths (MLD's) for the ARGO June/July/August data, Winter Cruise data and simulation outputs were comparable. This meant that the model had captured the austral winter dynamics well. Secondly, up to the month of November, the ARGO temperature profiles showed full upper column mixing (namely no stratification in the upper $\sim$100 $\mathrm{m}$). The model outputs however, had already begun to stratify during October and were well stratified during November. This showed that the model could not fully capture the austral spring upper column dynamics well and that there was a one month early stratification in the simulations. Thirdly, strong evidence of the warm parcel (at approximately 150 $\mathrm{m}$) was found in the ARGO and Winter Cruise temperature profiles. The November ARGO temperature profiles showed that the warm parcel had diminished where as the warm parcel in the model had persisted (Fig. 4.6). Furthermore, the Brunt Väisälä frequency was computed for the ARGO profiles. It was found that the austral winter ARGO and simulation Brunt Väisälä frequency profiles showed similar trends (namely permanent pycnoclines were at similar depths) although the simulation had underpredicted the ARGO Brunt Väisälä frequency.

The Brunt Väisälä frequency was computed in order to verify the early stratification in simulated data. It was found that the model did have a month early stratification (Fig. 4.8). The Brunt Väisälä frequency plots detected an odd stratification event, found during the austral winter (Fig. 4.8). The stratification event however, was only mildly present in the ERA-Interim results as compared to the other reanalyses. The stratification event was found to be consistent with the prescribed surface buoyancy fluxes.

The buoyancy flux and wind stress magnitude (Figs. 4.11 and 4.12 respectively) provided insight on the interaction of stratification and deep mixing on the water column. The turbulent diffusivity prognostic variable with MLD and turbocline (Fig. 4.10) indicated that the high turbulence areas were contained above the turbocline. The early stratification was also observed by the shallowing of the MLD and turbocline. It was found that the turbocline was more sensitive than the MLD as it had spiked for slight stratification events not detected by the MLD. The Potential Energy Anomaly (PEA) indicated a strong seasonal cycle (Fig. 4.13). Due to the salinity drift (slight persistent freshening) the end of period PEA values were higher than at the beginning of the time period, i.e. some turbulence was lost and energy conservation did not hold. A strong storm event (inferred from wind stress magnitude in Fig. 4.12) during the stratified period led to a sudden drop in PEA (also inferred from $\frac{d\phi}{dt}$ in Fig. 4.14).

The correlations computed between reanalyses for a single turbulence scheme (Table 4.3) indicated that the using different reanalyses produced varying results (namely low correlations for MLD, turbocline and average Brunt Väisälä frequency) except for the PEA and $\frac{d\phi}{dt}$ (which showed high correlations). This meant that the PEA and $\frac{d\phi}{dt}$ showed a similar response between reanalyses whereas the MLD, turbocline and average Brunt Väisälä frequency did not follow similar trends between reanalyses. Correlations computed between single reanalysis and a single turbulence scheme (Table 4.2) for the PEA and average Brunt Väisälä frequency resulted in higher correlations during winter as compared to the summer. This showed that the PEA, average Brunt Väisälä frequency and turbulent response were more consistent during the austral winter as compared to the summer. High correlations were found between turbulence schemes for a single reanalysis. This meant that similar results were obtained irrelevant of the turbulence scheme choice (shown in Appendix D, Tables D.1 and D.2 which were not presented with the results in Chapter 4).

The main findings in this study were that an early stratification had occurred in the model as compared to the ARGO temperature profile data as well as that different tracer results were obtained from simulation with the use of different reanalysis products. The sensitivity of the reanalysis choice however, was larger than for the turbulence scheme choice.

## 5.2 Discussion

It is quite interesting to see that a one-dimensional form of the primitive equations can produce results that are insightful to the vertical nature of the Southern Ocean (SO). Even though all horizontal effects (eddies, horizontal turbulence etc.) were filtered out via setting horizontal gradients to zero, the dominating seasonal and annual features such as the permanent and seasonal pycnoclines, MLD and seasonal cycle are present. It is however, essential to note that due to the many horizontal processes in the SAZ (Talley et al., 2011b), it does not suffice to think of the vertical processes as separate processes in order to achieve accurate solutions. This study shows that a Single Column Model (SCM) works well in obtaining the general behaviour of the tracer evolutions albeit a three-dimensional model would better suffice.

The one-dimensional NEMO model was chosen firstly due to its number of capabilities in various parameterization schemes and advanced numerics. Secondly due to the accessibility as it is open source software and thirdly for its one-dimensional idealized model configuration (Reffray et al., 2015). The primary advantage of this one-dimensional model is in its ability to single out vertical processes alone, i.e. creates an environment for modelling only vertical phenomenon. All horizontal processes are zeroed out and are prevented from influencing the vertical dynamics except when they are parameterized. Turbulence in general is a three-dimensional physical phenomenon. For the modelling of ocean turbulence, due to the large length scales involved in the horizontal as compared to the vertical, it is allowable (and necessary) to split the turbulence into a horizontal and vertical component. This singles out the vertical process of mixing achieved by a turbulence closure scheme parameterization.

Noticeable in the tracer results (Figs. 4.5 and 4.6), is an early stratification of approximately one month. Early stratification in ocean models is not only prevalent in one-dimensional idealized ocean models, but also appear in the full three-dimensional models (Section 2.3.1) as found by Huang et al. (2014) and Sallée et al. (2013). When the buoyancy flux (vertical dashed lines in Fig. 4.11) became positive, the average Brunt Väisälä frequency continued to decrease (namely wind stress dominated) during the austral autumn. The PEA was also decreasing indicative of deep mixing. But soon, the PEA (Fig. 4.13) as well as the average Brunt Väisälä frequency started increasing. The stratification had settled in approximately one month earlier as shown by these indicators. The early stratification may have lead to false information being passed on to the summer where the MLD and turbocline may be misrepresented (as found by Huang et al. (2014) and Sallée et al. (2013)).

There are a number of reasons that this early stratification is likely to occur. The compensation for the lag in ocean adapting to the new season might not be well accounted for in the model (by using the forcing data) is one possible reason. A further reason according to Huang et al. (2014), is that most ocean models tend to underestimate the wind stresses and overestimate the thermal and solar fluxes, implying that there is insufficient vertical mixing. This could lead to an early stratification. Another reason is due to the persistent presence of the warm water parcel trapped below cooler waters. The increasing salinity at the depth of the warm parcel strengthens the density which (entrapping it there) makes the density profile statically stable when it should have been statically unstable, leading NEMO to switch on the vertical mixing. Consequently, the conditions favour stratification as the parameterized convective mixing is not active.

The question arises on how this water parcel is formed and why it persists? Another question is why the density profile is stable and monotonously increasing even though there is a spike in temperature? During the austral summer, the warming slowly penetrates deeper into the water column stratifying the upper column and increasing the temperature. At the breaking of the stratification (during autumn), the warm waters are suddenly mixed, pushing warmer water deeper into the water column. This is likely due to the intense turbulent nature of the SO. This should increase the instability of the water column, however, the warm water remains trapped. The surface cooling convective adjustment is initiated but the warm parcel's potential energy is not released into turbulent kinetic energy. This means that the above cooler waters are not able to mix with the warmer water trapped below. This implies that the warm parcel is a impression of water from a previous season.

Temperature indeed affects the density as seen in the density profile plots (Figs. 4.3 and 4.4). But it is possible that the temperature of the warmer water was not significant enough to cause a change in density near the pycnocline. This implies the density profile remains statically stable due to the salinity contributions in the localized region. Rintoul and Trull (2001) had found that further south of the SAZ region of Australia, the stability relied more on the increase of salinity at the base of the thermocline rather than a decrease in temperature. This stopped the warm water parcel from entraining above or below the localized region preventing mixing from occurring.

This situation of the trapped warm waters implies that there is potential energy trapped within this warm parcel. If mixing were to occur, this potential energy would transform into turbulent kinetic energy. This energy however, was not released. It is likely that the momentum and energy imparted from the atmosphere-ocean interactions did not penetrate to the required depth in order to release the stored potential energy. There is a high possibility that the wind data (momentum source) failed to represent the required momentum to the necessary depth. A change of reanalyses and/or turbulence scheme may have helped with the suppression of the warm parcel, however, the stratification would still have occurred earlier than intended.

It is noteworthy to observe that when using NCEP data, no warm parcel was found except for when using the Pacanowski/Philander turbulence scheme. It is believed that due to the low resolution data and the large wind stresses (Fig. 4.12 (c)) of NCEP, the warm water parcel is suppressed. The low resolution data resulted in elevated temperature results that may have contributed in masking the effect of the warm water parcel if the wind stress had already not released all the potential energy into turbulent kinetic energy. The fact that the warm parcel was not present when using NCEP data implies that this is not a model property stemming from the turbulence closure scheme parameterizations and numerics.

Furthermore, an interesting question can be raised, namely does the warm parcel correspond to the permanent pycnocline (found at approximately 150 $\mathrm{m}$, see Section 4.4) every time? From the results presented, it seems as the permanent pycnocline is the depth above which the warm parcel is entrapped. Steele et al. (2011) and Jackson et al. (2011) had found a near surface temperature maximum (namely a warm warm water parcel) in the Canadian basin. The warm parcel was formed due to the break down of the summer time stratification which evenly distributes the heat into the upper water column. The cooling (from above) takes effect in the autumn leading to the warm water parcel trapped below. The strong salinity in this region ensures the entrapment. They had found that this warm water was always trapped near the permanent pycnocline.

One may have thought that the warm parcel would be an event over a short period of time (order of days) where diapycnal mixing would dominate in the localized region converting the stored potential energy into turbulent kinetic energy. This however, does not occur due to the column density stability and the warm parcel persists. Since internal waves are parameterized in conjunction with the TKE and GLS family of turbulence schemes, it could have helped in suppressing the warm parcel. The Pacanowski/Philander does not have the internal wave parameterization in conjunction which could suggest why it always produced a warm water parcel. The process of double diffusion (parameterized in NEMO) was implemented to see if any improvements could be observed in reducing the time in which the warm parcel persisted. The results were not useful due to seasonality being absent in both the temperature and salinity results. The warm water parcel could be due to a numerical issue or lack of a physical process not parameterized or discovered as of yet, that releases the potential energy into turbulent kinetic energy.

Though not a major point in their study, Reffray et al. (2015) had also observed a warm water parcel in their results. This was inferred from their temperature bias (simulated result subtract observed ocean data) results. The warm parcel was found entrapped beneath the MLD around 110 $\mathrm{m}$ deep. The warmer bias propagated from December 2010 throughout the boreal winter in the Northern Pacific ocean. Reffray et al. (2015) had referred to the event as the formation of a dipole within the water column.

There are other processes that may generate warm water pockets such as a warm core eddy which may have a warm pocket at $\sim$200 $\mathrm{m}$ deep (Ansorge et al., 2010). Ansorge et al. (2010) examined eddies that shed from near the Antarctic Polar Zone into the Antarctic Zone. These eddies (some of which had warm cores) were mainly generated due to the South-West Indian Ridge and not from previous seasonal waters as in the case of the entrapped warm parcel discussed before. It is possible that portions of the warm water parcels found could originate from (warm) anticyclone eddies coming from the Agulhas current (which is geographically nearby the study location, see Fig. 2.4). But probably near the end of summer the eddies would be undistinguishable from the surrounding waters due to the raised temperature of the upper water columns. It is interesting to note that Gordon and Huber (1995) had also found previous seasonal warm waters entrapped below cooler waters, however, there was a strong bathymetry dependence involved in the formation of the entrapped warm waters. The Maud rise in the Weddell sea acted as a catalyst for the entrapment of the warm waters below cooler waters (Gordon and Huber, 1995).

Section 4.3 showed that an approximate one month early stratification was found in the simulations. The model could possibly hold stratification history too strongly and this needs to be relaxed without destroying the stratification structure going into the summer. The early stratification may suggest that there is need for a new set of physics to correctly resolve this issue or an entirely different set of surface forcings.

Fig 4.5 showed the August ARGO temperature profile had two warm bulges present at ∼90 $\mathrm{m}$ and ∼200 $\mathrm{m}$ respectively. These parcels could be the presence of an unsettled warm parcel that was ruptured due to an internal wave. The possibility of two separate warm water parcels is also possible, or likely an entirely different oceanic process altogether is at work here and is beyond the scope of this study.

All salinity results (from all simulations performed) had a slow yet persistent freshening throughout the period of simulation. This had consequences for reproducing seasonality. A perpetual ten year simulation was run and the results (not shown in this study) indicated the persistent freshening continued into the further years. An attempt to remedy the problem was carried out using Newtonian dampening (numerical tool in NEMO). Seasonality in salinity was achieved and the freshening eliminated but at the cost of excessive damping that suppressed freshwater influx and affected the temperature results. The Newtonian damping was abandoned due to not knowing the full consequences that it had on the temperature values obtained. For confirmation whether the freshening was a consequence of this study or have appeared in other studies, a perpetual simulation over five years was performed for the Northern Pacific configurations, named C1D_PAPA by Reffray et al. (2015) (see Section 3.2.1), and an intra-annual persistent slight freshening was also found. The temperature results from both of the perpetual simulations were also analysed and no persistent cooling or heating was found.

Reffray et al. (2015) had noted the persistent intra-annual freshening in their NP simulations. Consequently, they had deemed the seasonal variability of salinity unfit for their study. They computed the salinity (and temperature) bias nevertheless finding that the $k-\varepsilon$ turbulence closure scheme produced the best results.

It was deemed that if this configuration in its current state were used as a predictive tool, then one annum will be the cut off period for a single simulation before new boundary and initial conditions have to be reinstated from scratch. Simulating for more than one year and the numerical errors may overwhelm the accuracy of the results.

The Potential Energy Anomaly (PEA) was mainly used for coastal areas but can also be applied to the deep ocean. PEA is a very useful indicator in order to determine the sensitivity of wind stress and buoyancy flux anomalies (for example storms or intense solar fluxes) as well as transfers of turbulent kinetic energy. PEA can also be used as validation if the ARGO data (Figs. 4.5 and 4.6) profiles are more frequent so that the evolution can be followed better. The turbulent kinetic energy remains the largest sink of energy imparted due to atmospheric forcings especially due to wind stress (Waterman et al., 2013). Clear signs that wind stress impacts the turbulent kinetic energy production was observed in wind stress and PEA (Figs. 4.12 (a) and 4.13 (a) respectively). There is a strong storm event during February (Fig. 4.12 (a)), which imparts large surface wind stress that suddenly drops the PEA (Fig. 4.13 (a)) and is clearly seen in the time derivative of PEA (Fig. 4.14 (a)). The decrease in PEA implies the production of turbulent kinetic energy, i.e. providing a sink for the potential energy created. Table 5.1 shows PEA values for ARGO data and simulation outputs which shows that the PEA had increased from June/July/August to November (although the simulation outputs had PEA values an order of magnitude larger than the ARGO data due to the number of depth points available). Lower PEA values during November imply higher turbulent kinetic energy in the water column suggesting it is a sink for potential energy. The full impact of this indicator can be further explored in a future study.

TABLE 5.1: PEA values for ARGO data (see Section 4.3).

| | **June** | **July** | **August** | **November** |
|---|---|---|---|---|
| **Simulation PEA** ($\mathrm{J\,m^{-3}}$) | | 19238.08 | | 19366.29 |
| **ARGO data PEA** ($\mathrm{J\,m^{-3}}$) | 3624.18 | 3127.13 | 2536.92 | 3247.16/4024.41 |

The resulting turbulent diffusivities in this study, displayed in Fig. 4.10 are of order $10^{-1}\ \mathrm{m^2\,s^{-1}}$. The diffusivities for Pacanowski/Philander however, are approximately two orders of magnitude higher because high background parameter values (viscosity and diffusivity) are needed for the scheme implementation in order to achieve acceptable results (Sallée et al., 2010; Lenn and Chereskin, 2009).

Physically, diffusivities are inferred from tracer quantities however, trained experts are needed for these measurements and unfortunately very few data sets are available for validation in the SO (Frants et al., 2013). Turbulent diffusivity data found by Waterman et al. (2013), Sallée et al. (2008) and Thompson et al. (2007) yield good insight of the turbulent nature of the SAZ.

Waterman et al. (2013) had found regions in the Indian ocean sector of the SO which contained turbulent diffusivities of up to $3.4 \times 10^{-3}\ \mathrm{m^2\,s^{-1}}$. Thompson et al. (2007) on the other hand, found that turbulent diffusivities along the diapycnals in the SO can easily be three times in magnitude in relation to the background turbulent diffusivity. This implies that the turbulent diffusivity has a high spatial variability in measurements as well as being highly dynamical depending on many factors. One of these factors is bottom topography. SCM or one-dimensional models with uniform bottom topography are unable to capture the full dynamics as higher turbulence is expected over a rough topography as stressed by Thompson et al. (2007) and Garabato et al. (2004). A parameterization could hold the key to solving this problem, however, horizontal effects contribute a large component and have to be taken into account.

The turbulent diffusivity values found in this study are bounded within the values found by Waterman et al. (2013), Sallée et al. (2008) and Thompson et al. (2007), even though there is high variability for the diffusivities. The MLD and turbocline that bound the large diffusivities seems to be under predicted. For instance, Rintoul and Trull (2001) had found MLD's well below 400 $\mathrm{m}$ in the Indian sector of the SAZ during austral winter but this shallowed out to 100 $\mathrm{m}$ during the austral summer. They also found a large variability in the MLD from the Sub-Tropical Front (STF) to sub-Antarctic Front (SAF), i.e. from north to south of the SAZ. The MLD found reached down to approximately 190 $\mathrm{m}$ during the austral winter and 50 $\mathrm{m}$ during the summer.

In specific, using the TKE30 scheme tended to result in a poor stratification in the tracers. The reason was due to the large length scale which supplies large amounts of turbulent kinetic energy, which implied enhanced mixing leading to a poor formation of stratified layers. A consequence of this enhanced mixing was seen in the MLD and tubocline separation (starting from austral spring and rejoining at end of summer, shown in Fig. 4.10 (d)) leading to very distinct layers for the turbulent layer (bounded below by the turbocline) and mixed layer (bounded below by the MLD). The combining of the MLD and turbocline indicate that the TKE30 is indeed a stable numerical scheme and is consistent for the deep mixing period.

Since the 1980's, many including Pacanowski and Philander (1981) used an older version of the thermodynamic equation of state (in fact, it was linear). Since then, more accurate versions of the Thermodynamic Equation Of State (TEOS) are now available, namely TEOS10 (TEOS, 2010) which is currently used in the oceanographic field (and also in this study). The TEOS affects the density calculation which in turn is crucial for calculating the Brunt Väisälä frequency (or strength of stratification). It is important to notice that stratification is a complex process and the ocean tends to stratify during the day and destratify (homogenize) at night. The results obtained in this study contained daily output implying the diurnal stratification and destratification effects have not been analysed specifically.

The seasonal pycnocline has a Brunt Väisälä frequency (Fig. 4.8) of approximately $4 \times 10^{-4}$ $\mathrm{s}^{-2}$, the permanent pycnocline is approximately $6 \times 10^{-5}$ $\mathrm{s}^{-2}$ and the background is approximately $1 \times 10^{-5}$ $\mathrm{s}^{-2}$. Swart et al. (2015) had carried out a high resolution glider experiment in the SAZ (close to the location selected in this study) for December 2013 - February 2014 and found approximate Brunt Väisälä frequencies of $6 \times 10^{-5}$ $\mathrm{s}^{-2}$ for the seasonal pycnocline, $3 \times 10^{-5}$ $\mathrm{s}^{-2}$ for the permanent pycnocline and $1 \times 10^{-5}$ $\mathrm{s}^{-2}$ for background. The background values compare well, while the permanent pycnocline in this study was twice the Brunt Väisälä frequency found by Swart et al. (2015) and lastly the seasonal pycnocline value is one magnitude higher than Swart et al. (2015). In general, Thorpe (2007) noted that the average seasonal pycnocline Brunt Väisälä frequency for global ocean is approximately $10^{-2}$ $\mathrm{s}^{-2}$. In light of the above mentioned, the model is over predicting the stratification. A possible reason for this is possibly due to the lack of proper internal wave dynamics and horizontal processes in the model.

The sudden stratification during winter (late August in Figs. 4.8 (a) and (b)) was also reported by Sallée et al. (2008), who used the 2006 JRA25 (predecessor to JRA55) set of forcing functions for their simulations. They had found no reason for the sudden stratification, however, they found that the stratification event is consistent with the forcing functions used, i.e. an increase in solar fluxes on the day.

### 5.2.1 The role of reanalyses and turbulence closure schemes

The various reanalyses proved to be the driver for large variations in the tracer results. Reanalyses have passed through 'generations' of advancement. First generation reanalyses had the resolution to resolve synoptic-scale processes and features. NCEP is still a first generation reanalysis, even though it has been significantly improved from the previous versions (Kanamitsu et al., 2017). The low correlations found between reanalyses and a single turbulence scheme for the MLD, turbocline and average Brunt Väisälä frequency, shown in Table 4.3, indicates that tracer results from simulations are different when using different reanalyses. There is a risk that the choice of an inappropriate reanalysis, may lead to inadequate results not anticipated by the user. It is essential that the assumptions, limitations, advantages and disadvantages of the reanalysis be firstly understood before its use in simulations. It is preferable that more than one reanalysis be used if possible and a comparison of results carried out. It is a major outcome of this study that using various turbulence schemes resulted in less variable tracer results compared to a change in reanalysis data.

Timmermann and Beckmann (2004), using a combination of NCEP and ERA-Interim data, found that both the M-Y (Mellor-Yamada or k-kl) and Pacanowski/Philander schemes resulted in underestimating the upper mixing for a stable stratification in the Weddell sea. The Pacanowski/Philander scheme performed better in their study. They found sporadically high turbulent diffusivities leading to static instabilities and negative Brunt Väisälä frequencies whereas in this study only positive values were found, i.e. the water column was convectively stable. In another study using a SCM in the Persian Gulf, Namin et al. (2017) carried out a comparison between the $k - \varepsilon$, $k - \omega$ and Pacanowski/Philander schemes. They had found the GLS schemes performed better than the

Pacanowski/Philander scheme, i.e. the $k-\omega$ and M-Y schemes produced the best result in comparison to observation. Also noteworthy in other parts of the ocean, such as the *Juan de Fuca* strait, sensitivity studies had been done by Soontiens and Allen (2017) involving the GLS closure schemes ($k-\varepsilon$, $k-\omega$ and M-Y). They found that the $k-\varepsilon$ scheme compared better than the $k-\omega$ scheme. It was also reported that the M-Y scheme could not be implemented due to model instability issues. For the NP, Reffray et al. (2015) had implemented a SCM and found that the $k-\varepsilon$ scheme produced the best results as compared to observation using *PAPA* data (NOAA, 2016) for their chosen location. The above four studies discussed, suggest there is not a single correct vertical turbulence scheme that is applicable for global scale simulations but that a single scheme possibly would work well for smaller regional scales.

It remains a challenging task to understand the full mechanisms of turbulent phenomenon. Generally, the high turbulence areas are at the interface between two layers of homogeneous fluid. Initially shear instabilities develop leading to convective rolls (due to heavy waters being carried over lighter waters). These instabilities decay via viscous and diffusive dissipation as well as production of potential energy (later released as turbulent kinetic energy) which then lead to a fully turbulent state (Gregg, 1987).

It was a crucial turning point when it was discovered that turbulence was found in patches over various spatio-temporal scales and did not act over a continuous sheet (Gregg, 1987). This implied turbulence exists over a broad range of spatio-temporal scales that could potentially imply turbulence modelling at specific regions requires more advanced methods needed to resolve turbulence at variable scales. Following this trend, Namin et al. (2017) suggests using various turbulence schemes at various locations which could possibly provide better results regarding the turbulence response. For the application of this idea, one-dimensional models are ideal as they can be employed with minimal cost and time constraints. A similar concept to using different turbulence schemes at various locations is the idea of running models with patchy mixing. This was carried out by Jochum (2009) and it was found that patchy mixing produced different results compared to homogeneous mixing.

Currently, turbulence closure schemes are the best option to take into account vertical mixing. Turbulence schemes are more developed and better simulate the vertical mixing than any other vertical mixing techniques (Gaspar, 1988). Serious challenges remain however, for validation of turbulence measurements in the oceans compared to simulation due to various reasons, namely only one component (for example z direction) of the Reynolds stresses are measured by oceanographic instruments (suggesting a theory not advanced enough to extract all three components at once), sparse data and high levels of noise in the signal (Gregg, 1987). Not only turbulence diagnostics falls trap to poor data, for instance, precipitation measurements feeding into reanalyses products are poor due to the measurement process. An underlying problem, which Badin et al. (2013) and Garabato et al. (2004) confirmed, is that the SO is undersampled (especially in the Pacific sector) leading to a lack of understanding of the processes involved within the SO and its bad representation in numerical models. Consequently, confirming the current globally averaged turbulent diffusivity of O($10^{-4}\ \mathrm{m}^2\,\mathrm{s}^{-1}$) (and many other measures) is difficult due to undersampling (Garabato et al., 2004).

It is not only in undersampling and inaccurate measurements where problems lie. Soontiens and Allen (2017) highlighted the fact that finding errors in simulations using an ocean modelling program is challenging as there are many sources. Some include forcing functions, initial conditions, model parameters and various numerical errors. The relevant contribution of each type of error is difficult to establish. As an example on parameter choice in this study, from a range of stability functions, the Canuto A functions (Canuto et al., 2001) were used because the literature pointed out that these stability functions would yield the best results. It was decided to employ the same stability function for all simulations, i.e. Canuto A was a control parameter and the sensitivity of this choice was not assessed.

A better (mathematical) understanding for various turbulence inducing mechanisms is needed. For instance, diapycnal turbulent mixing and surface buoyancy fluxes are the main drivers of the overturning circulations in the SO. The extent however, of which process dominates is still unknown (Badin et al., 2013). Many, including Thompson et al. (2007), suggested that better understanding of diapycnal mixing is needed before accurate solutions can be obtained in simulations. Diapycnal mixing is a leading factor in the stability of ocean stratification according to Frants et al. (2013). Another process where turbulence was enhanced and sustained in the upper 1000 m due to wind generated waves and bottom topography in the Indian ocean sector of the SO was found by Waterman et al. (2013). They also found that within the ocean interior, turbulent dissipation is governed by the breaking of internal waves. According to Monin et al. (1978) this is an efficient mechanism for turbulence induction. This further supports the promotion of understanding the physical mechanisms involved which can consequently aid the measurement and validation process. Various other interesting theories have emerged, for instance the theory that turbulence persists in the absence of breaking waves by Walsh et al. (2017). Although these theories are somewhat controversial, in the future they may hold the key to better understanding the physical mechanisms involved in turbulence generation.

# Chapter 6

# Conclusion

This study presented the various results, turbulence diagnostics and univariate indicators found from modelling a one-dimensional water column using the Nucleus for the European Modelling of the Ocean (NEMO) for a location in the Southern Ocean (SO). After being simulated using various turbulence schemes and reanalyses, the water column annual temperature/salinity evolution profiles and various energetics were analysed. A warm water parcel was found entrapped at approximately 150 $\mathrm{m}$ deep due to the erosion of stratification from the previous austral summer season distributing upper column heat deeper down. The warm water parcel did not mix after the cooling convective adjustment was turned on, upon the onset of the cooling period (austral autumn) and the warm water remained entrapped. The Brunt Väisälä frequency gave insight on the stratification process for the various turbulence schemes and the water column turbulence response. The PEA and $\frac{d\phi}{dt}$ indicated the strength of stratification onset and were good descriptors between reanalyses. The PEA was found to correlate well between reanalyses as compared to the Mixed Layer Depth (MLD), turbocline and average Brunt Väisälä frequency indicators which were poor (given a single turbulence scheme). This meant that the PEA was a near invariant measure that was a good descriptor of the prescribed buoyancy fluxes and was used to determine mixing sensitivity information of the water column. The early stratification showed that there could have been a possible erroneous transfer of stratification information from austral spring to the summer, due to the fact that the austral spring obtained an early stratification (see Section 4.3) which probably transferred the wrong stratification signal into the summer period.

It was found that each reanalysis produced different tracer results for any single turbulence scheme. The tracer results did vary when using various turbulence schemes for a single reanalysis product, but not as much as for the reanalysis choice. Furthermore, strong evidences were presented for the warm parcel existence using the available scattered ARGO and Winter Cruise validation data. The mechanism of why the potential energy of the warm water parcel was not released into turbulent kinetic energy remains unknown and was possibly due to the lack of a physical process(es) not parameterized.

The literature review (Chapter 2), methodology (Chapter 3) and findings (Chapter 4) had fulfilled the first research objective (Section 1.2), which was to understand the role of turbulence schemes and their implementation in conjunction with one-dimensional ocean models. The methodology (Chapter 3) and findings (Chapter 4) had outlined the process of setting up and running simulations as well as computing the various energetics, turbulence diagnostics and univariate indicators for the SO location chosen in this study, thereby fulfilling the second research objective of implementing the one-dimensional ocean model (following the work done by Reffray et al. (2015)). The resulting energetics and tracer results were analysed in Chapter 4 and discussed in Chapter 5, satisfying the third and forth research objectives which entailed analysing the resulting simulation output via various energetics and turbulence diagnostics as well as determining the relevant portions where the upper water column dynamics were well captured. From using the ARGO and Winter Cruise validation data (Chapter 4), it was found that the model had captured the austral winter dynamics well. The spring time dynamics however, showed an early stratification whereas the validation data showed a well mixed upper water column. The discussion in Chapter 5, had also highlighted many other aspects of the results obtained and presented in Chapter 4.

The underlying important points addressed in this study were understanding the implications, advantages and disadvantages of using the various reanalyses and turbulence closure scheme parameterizations (Chapters 2, 4 and 5). An outcome of this study points towards needing a better understanding of the physical turbulence inducing mechanisms for ocean modelling. The validation data in the SO are sparse as the SO is severely undersampled (although much interest has been shown in SO sampling in recent years) and available data has large error when *in situ* measurements are collected due to various ocean conditions at the time of measurement, such as stormy conditions (Badin et al., 2013; Garabato et al., 2004).

In reality, ocean phenomenon in the mesoscale and sub-mesoscale regimes are three-dimensional processes. This study had singled out only the vertical processes for simulation in the SAZ region. Due to the strong horizontal influences in the SAZ, it does not suffice to think of vertical oceanic processes as separate processes. This study however, showed that a Single Column Model (SCM) works well in obtaining the general behaviour of the tracer (temperature and salinity) evolutions (especially during the austral winter) even though a three-dimensional model would better suffice.

This study has contributed to expanding on the work done by Reffray et al. (2015), by implementing their the one-dimensional NEMO model to a location in the SO and determining the sensitivity and turbulence response, which has not been done previously. This study further provided a bridge for the beginner to acquaint themselves with turbulence modelling and expert tips in analysing the sensitivity and turbulence response of a SCM.

## 6.1 Study implications

This study provided the basis to enter the study of turbulence schemes, their implementation and underlying physics (Chapter 2) to the beginner pursuing oceanographic modelling using numerical software, especially the NEMO model. This study also had implications that a reanalysis product should be chosen with care as the results obtained using various reanalyses differed. The number of vertical grid levels choice (Chapter 3) had an important implication on resolving the atmosphere-ocean interactions and how the prescribed buoyancy fluxes affected the upper water column. This study also had an impact on suggesting the best turbulence scheme choice possible for the chosen SO location (Chapter 5).

## 6.2 Future research

There are many available opportunities to expand on this study and a few suggestions are presented below.

1. There are various turbulence schemes that are not incorporated into NEMO. These include YSU, QNSE and various others (Optis and Monahan, 2017). There is scope to incorporate these turbulence schemes into NEMO and include them in the analyses. There are also turbulence schemes that NEMO contains but were not tested in this study (e.g. K-Profile Parameterization turbulence scheme) and can be included in the analyses.
2. There is scope to test the sensitivity when the shifting the simulation starting time, i.e. starting during the austral summer (stratification period). The stratification should kick in immediately and the remainder of the year should be comparably similar to the results obtained in this study (Chapter 4).

3. It remains a challenge with choosing the correct initialization parameters (stability functions, thresholds parameters etc.) for the implementation of a turbulence scheme as the effect each parameter will have on the results are not clear prior to simulation. Soontiens and Allen (2017) has also expressed this view as they have encountered this problem during their research. More effort can be diverted to parameter selection optimization.

4. The warm water parcel persisted too long in the simulations as compared to the ARGO data. There is possibly an entire section of physics or a parameterization missing which would be needed to capture the true dynamics of the warm parcel. A further influence could be the strength of stratification of the model as the simulated ocean may keep a stronger history of stratification than in reality, but this needs further testing. The horizontal extent for which the warm parcel is found is also unknown due to using a one-dimensional model. This can be explored using a three-dimensional model.

5. Looking at the results obtained for the buoyancy flux in Fig. 4.11 (with average Brunt Väisälä frequency plotted for comparison), it could be speculated that (especially during austral spring/ summer) there was approximately a two day lag between the buoyancy flux and the average Brunt Väisälä frequency peaks. The buoyancy flux had peaked first, consequently leading to the average Brunt Väisälä frequency peaking. This suggested that the stratification onset occurred after a buoyancy injection, i.e. the buoyancy flux effects had to propagate from surface into the water column before stratification was ’felt’. A further study can be performed to determine the validity of this speculation.

6. There are a multitude of techniques in Computational Fluid Dynamics (CFD) that have been modified and adapted to model problems not specific to oceanography. The Geophysical Fluid Dynamics (GFD) domain unfortunately, have not seen fast advancement as CFD, according to Tang and Wu (2010). They proposed that if it were possible to use the advanced methods in CFD to model problems in GFD, then more accurate results could be obtained than what GFD could presently produce. An attempt was made by Tang and Wu (2010) to model coastal systems however, an ocean model would require other techniques for modelling the various parameterizations and turbulence closure schemes involved.

7. Although many lab experiments were set up to test and verify various turbulence inducing mechanisms, much work remains in fully understanding the underlying physics of vertical oceanic processes. Many generation (and destruction) of turbulence inducing mechanisms such as shear instabilities and convective overturning, were found through lab visualizations (Kato and Phillips, 1969; Thorpe, 1973) but the coupling between the various mechanisms still remain unclear.

# Appendix A

# Derivation of the mass balance equations for the Primitive equations

## A.1 Mass balance equation derivation

This appendix presents the derivation of the mass balance equations used to govern the density property of the fluid in focus. Due to the ocean being an incompressible fluid, the incompressibility constraint (forming part of the primitive equations, (Griffies and Adcroft, 2013; Adcroft et al., 2016)) is further derived below.

Consider the mass element having dimensions $\delta x \times \delta y \times \delta z$, shown in Fig. A.1.

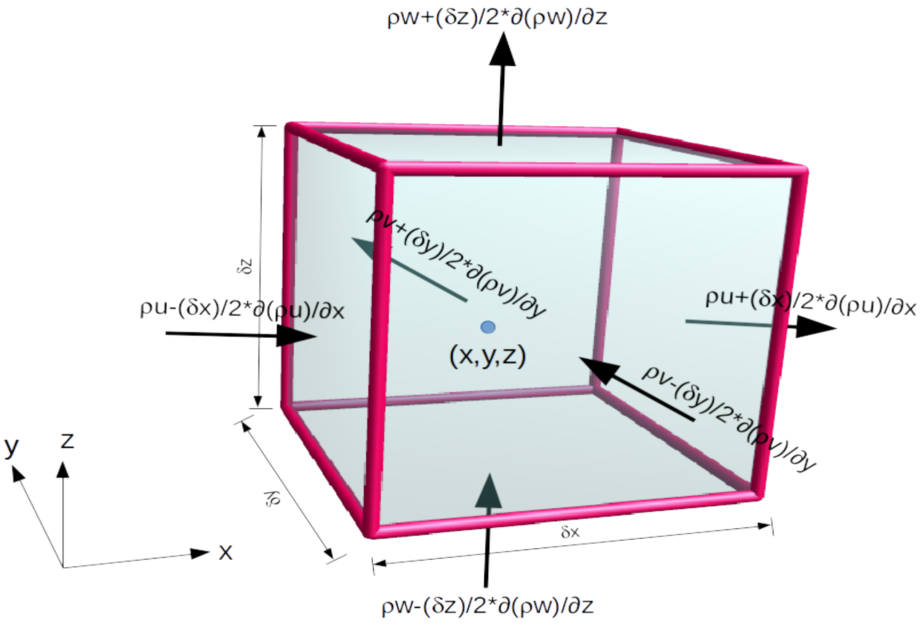

FIGURE A.1: Mass element depicting the mass flux at each face of the element. All flux terms are constructed in relation to the centre of the mass element (x,y,z) and density ($\rho$).

The basic Law of Conservation of Mass states the following:

**Rate of change of mass within element**

**=**

**Net rate of flow of mass through the faces of the element**

By rearrangement of the density equation, the mass can be made the subject of the formula:

$$m = \rho V \tag{A.1}$$

where V is the volume and $\rho$ the density of the element.

The volume of the element is simply $V = \delta x \delta y \delta z$. Using equation A.1, the mass can be written as

$$m = \rho \delta x \delta y \delta z \tag{A.2}$$

The rate of change of mass inside the element is defined by

$$\frac{\partial m}{\partial t} = \frac{\partial(\rho \delta x \delta y \delta z)}{\partial t} = \frac{\partial \rho}{\partial t} \delta x \delta y \delta z \tag{A.3}$$

The Net rate of mass flux is the sum of all individual contributions through each faces multiplied by the face area (refer to Fig. A.1)

$$\begin{aligned}
&\left(\rho u - \frac{1}{2}\frac{\partial \rho u}{\partial x}\delta x\right)\delta y \delta z - \left(\rho u + \frac{1}{2}\frac{\partial \rho u}{\partial x}\delta x\right)\delta y \delta z && \text{(A.4)}\\
&+\left(\rho v - \frac{1}{2}\frac{\partial \rho v}{\partial y}\delta y\right)\delta x \delta z - \left(\rho v + \frac{1}{2}\frac{\partial \rho v}{\partial y}\delta y\right)\delta x \delta z && \text{(A.5)}\\
&+\left(\rho w - \frac{1}{2}\frac{\partial \rho w}{\partial z}\delta z\right)\delta x \delta y - \left(\rho w + \frac{1}{2}\frac{\partial \rho w}{\partial z}\delta z\right)\delta x \delta y && \text{(A.6)}\\
&= -\left(\frac{\partial \rho u}{\partial x} + \frac{\partial \rho v}{\partial y} + \frac{\partial \rho w}{\partial z}\right)\delta x \delta y \delta z && \text{(A.7)}
\end{aligned}$$

Equating Eqns. A.3 and A.4 results in the mass balance equation

$$\frac{\partial \rho}{\partial t} + \nabla \cdot (\rho \vec{U}) = 0 \tag{A.8}$$

For deriving the incompressibility constraint, the ocean is considered to be an incompressible fluid. This assumption implies the density is constant and time and space independent giving

$$\begin{aligned}
\rho \nabla \cdot (\vec{U}) &= 0 && \text{(A.9)}\\
\implies \nabla \cdot (\vec{U}) &= 0 && \text{(A.10)}
\end{aligned}$$

Equation A.9 is known as the incompressibility constraint. This constraint has an important consequence. Rearranging equation A.9 leads to

$$\frac{\partial u}{\partial x} + \frac{\partial v}{\partial y} = -\frac{\partial w}{\partial z} \tag{A.11}$$

Assuming horizontal gradients are zero implies $\frac{\partial u}{\partial x} + \frac{\partial v}{\partial y} = 0$. This forces $\frac{\partial w}{\partial z} = 0$. Consequently this implies the vertical velocity $w$ is a constant. This constant is arbitrary and can be set to 0 for convenience. The NEMO model output W file (refer to variable *vovecrtz* in Table B.1) shows this.

# Appendix B

# Operation of NEMO and C1D_PAPA

## B.1 Introduction

This appendix describes the process of getting NEMO to run. It also describes the various settings needed for running each turbulence scheme. All NEMO script snippets from the *namelist* file can be found from the NEMO ocean program (Madec, 2008).

## B.2 How to install and setup the C1D_PAPA case for NEMO

This section briefly covers the installation procedure of NEMO and the setup of the configuration used by Reffray et al. (2015).

The NEMO model as well as other supporting tools are available for download from their svn server.[1] Supporting software is needed before simulations can be performed, namely *hdf5* and *NetCDF*, Fortran and C++ compilers. Depending on the case, *XIOS* may also have to be installed prior simulations. For the C1D_PAPA case, *XIOS* is not necessary.

After downloading the NEMO trunk (main folder containing all core model codes), the architecture has to be specified. The architecture is specified in the *ARCH* folder within the *arch-***.fcm* file. My system is Ubuntu 16.04 LTS leading to my *arch* file taking on the following format

```
%NCDF_HOME           /usr
%HDF5_HOME           /usr
%NCDF_INC            -I%NCDF_HOME/include -I%HDF5_HOME/include
%NCDF_LIB            -L%NCDF_HOME/lib -L%HDF5_HOME/lib -lnetcdff -lnetcdf
%CPP              cpp
%FC              gfortran
%FCFLAGS             -fdefault-real-8 -O3 -funroll-all-loops -fcray-pointer
%FFLAGS              %FCFLAGS
%LD                  %FC
%LDFLAGS             -lstdc++
%FPPFLAGS            -P  -traditional
%AR                  ar
%ARFLAGS             rs
%MK                  make
%USER_INC             %NCDF_INC
%USER_LIB             %NCDF_LIB
%CC                  cc
%CFLAGS              -O0
```

The tricky bit is locating the correct header files for *NetCDF*, *hdf5* and the Fortran and C++ compilers. In some cases the **FPPFLAGS** may have to use the **-P** flag to ignore header file comments as different

---

[1] The details are documented on their website:
https://forge.ipsl.jussieu.fr/nemo/wiki/Users/ModelInstall#a1.ExtracttheNEMOcode

versions of header files have various initial comments that could cause an error while the case is compiled in NEMO.

The configurations are found in the *CONFIG* folder. The C1D_PAPA case is present in this folder. Before a case can be run, it has to be compiled on the specific architecture. There is a *makenemo* script provided for this. The following command can be executed in the terminal opened in the *CONFIG* folder

$$./makenemo\ -m\ architecture\_file\ -r\ reference\_case\ -n\ config\_name\ -j8\ >\&log\_filename \tag{B.1}$$

Before compilation the specified keys must be selected in the *cpp_***.fcm* file. To avoid errors the keys key_c1d and key_nosignedzero should always appear when running the 1-D simulations. The vertical mixing scheme key is also inserted in this file which takes the form

```
 bld::tool::fppkeys key_c1d key_zdfric key_nosignedzero
```

The *namelist_cfg* file (found in the *EXP00* folder) must also be filled in with the correct parameters, module selection and variable values. The important sections are shown below

```
!!>>>>>>>>>>>>>>>>>>>>>>>>>>>>>>>>>>>>>>>>>>>>>>>>>>>>>>>>>>>>>>>>>>>>>>>
!! NEMO/OPA  : 1D configuration based on Kato-Philipps exp.
!!>>>>>>>>>>>>>>>>>>>>>>>>>>>>>>>>>>>>>>>>>>>>>>>>>>>>>>>>>>>>>>>>>>>>>>>
!------------------------------------------------------------------------
&namrun        !   parameters of the run
!------------------------------------------------------------------------
  cn_exp      =  "SO1011"   !  experience name
  nn_it000    =        1   !  first time step
  nn_itend    =    135600   !  last  time step
  nn_date0    =   20100615 !  date at nit_0000
  nn_leapy    =        1   !  Leap year calendar (1) or not (0)
  nn_stock    =    87600 ! frequency of creation of a restart file
  nn_write    =    240   !  frequency of write in the output file
/
!------------------------------------------------------------------------
&namcfg !parameters of the configuration, original number of levels is 75
!------------------------------------------------------------------------
cp_cfg = "SO" ! name of the configuration
jp_cfg = 1 ! resolution of the configuration
jpidta = 3 ! 1st lateral dimension ( >= jpi ) = 30*jp_cfg+2
jpjdta = 3 ! 2nd    "         "    ( >= jpj ) = 20*jp_cfg+2
jpkdta = 31 ! number of levels      ( >= jpk )
jpiglo = 3 ! 1st dimension of global domain --> i  = jpidta
jpjglo = 3 ! 2nd    -                  -    --> j  = jpjdta
jpizoom = 1 ! left bottom (i,j) indices of the zoom
jpjzoom = 1 ! in data domain indices
jperio = 0 ! lateral cond. type (between 0 and 6)
/
!------------------------------------------------------------------------
&namdom        !   space and time domain (bathymetry, mesh, timestep)
!------------------------------------------------------------------------
nn_bathy = 0 !compute (=0) or read (=1) the bathymetry file
rn_bathy = 4500. !value of the bathymetry.
nn_msh = 0 !create (=1) a mesh file or not (=0)
rn_rdt = 360. !time step for the dynamics (and tracer if nn_acc=0)
rn_rdtmin = 360. !minimum time step on tracers (used if nn_acc=1)
```

```
rn_rdtmax = 360. !maximum time step on tracers (used if nn_acc=1)
jphgr_msh = 1 !type of horizontal mesh
ppglam0 = 4.25 !longitude of first raw and column T-point
ppgphi0 = -47.25 !latitude  of first raw and column T-point
ppe1_deg = 0.25 !zonal      grid-spacing (degrees)
ppe2_deg = 0.25 !meridional grid-spacing (degrees)
ppe1_m = 999999.0 !zonal      grid-spacing (degrees)
ppe2_m = 999999.0 !meridional grid-spacing (degrees)
ppsur = 999999.0 !ORCA r4, r2 and r05 coefficients
ppa0 = 999999.0 !(default coefficients)
ppa1 = 999999.0
ppkth = 16.0
ppacr = 2.0
ppdzmin = 1.0 !Minimum vertical spacing
pphmax = 4500.0 !Maximum depth
ldbletanh = .false.
ppa2 = 100.7609285000000 !Double tanh function parameters
ppkth2 = 48.02989372000000
ppacr2 = 13.00000000000
/
!------------------------------------------------------------------------
&namc1d        !   1D configuration options                  ("key_c1d")
!------------------------------------------------------------------------
ln_c1d_locpt=.false. !Localization of 1D config: grid(T) or point(F)
/
!------------------------------------------------------------------------
&namtsd    !   data : Temperature  & Salinity
!------------------------------------------------------------------------
sn_tem =’init_PAPASTATION’,-12,’votemper’,.false.,.true.,’yearly’,’’,’’,’’
sn_sal =’init_PAPASTATION’,-12,’vosaline’,.false.,.true.,’yearly’,’’,’’,’’
cn_dir = ’./’ !root directory for the location of the runoff files
ln_tsd_init = .true. !Initialisation of ocean T&S with T&S input data
ln_tsd_tradmp = .false. !damping of ocean T&S toward T&S input data
/
!------------------------------------------------------------------------
&namsbc        !   Surface Boundary Condition (surface module)
!------------------------------------------------------------------------
nn_fsbc = 1 !frequency of surface boundary condition computation
            !(also = the frequency of sea-ice model call)
nn_ice = 0 !=0 no ice boundary condition
ln_rnf=.false.!runoffs                             (T => fill namsbc_rnf)
ln_ssr=.false.!Sea Surface Restoring on T and/or S(T => fill namsbc_ssr)
nn_fwb = 0 !FreshWater Budget: =0 unchecked
/
!------------------------------------------------------------------------
&namsbc_core   !   namsbc_core  CORE bulk formulae
!------------------------------------------------------------------------
sn_wndi = ’Uwind’,3,’Uwind’,.true.,.false.,’yearly’,’’,’’,’’
sn_wndj = ’Vwind’,3,’Vwind’,.true.,.false.,’yearly’,’’,’’,’’
sn_qsr = ’swrad’,24,’swrad’,.false.,.false.,’yearly’,’’,’’,’’
sn_qlw = ’lwrad’,24,’lwrad’,.false.,.false.,’yearly’,’’,’’,’’
sn_tair = ’temp2m’,3,’temp2m’,.true.,.false.,’yearly’,’’,’’,’’
sn_humi = ’spechumid’,3,’spechumid’,.true.,.false.,’yearly’,’’,’’,’’
```

```
sn_prec = 'rain',24,'rain',.false.,.false.,'yearly','','',''
sn_snow = 'snow',24,'snow',.false.,.false.,'yearly','','',''
rn_zqt = 2. !air temperature/humidity referenced at 2m (T)
/
!-----------------------------------------------------------------------
&namtra_qsr    !   penetrative solar radiation
!-----------------------------------------------------------------------
sn_chl = 'chlorophyll',-1,'chloro',.true.,.true.,'yearly','','',''
/
!-----------------------------------------------------------------------
&namsbc_ssr    !   surface boundary condition : sea surface restoring
!-----------------------------------------------------------------------
nn_sssr = 0 !add a damping term in the surface freshwater flux (=2)
rn_deds = -27.7 !magnitude of the damping on salinity   [mm/day]
ln_sssr_bnd = .false. !flag to bound erp term (associated with nn_sssr=2)
/
!-----------------------------------------------------------------------
&nameos        !   ocean physical parameters
!-----------------------------------------------------------------------
nn_eos = 0 !type of equation of state and Brunt-Vaisala frequency
                                 !  =-1, TEOS-10
                                 !  = 0, EOS-80
                                 !  = 1, S-EOS   (simplified eos)
ln_useCT = .false. !use surface CT converted in Pot. Temp.
/
!-----------------------------------------------------------------------
&namtra_dmp    !   tracer: T & S newtonian damping
!-----------------------------------------------------------------------
ln_tradmp   =  .false.  !  add a damping termn (T) or not (F)
/
!-----------------------------------------------------------------------
&namzdf        !   vertical physics
!-----------------------------------------------------------------------
ln_zdfevd   = .true. !enhanced vertical diffusion (evd) (T) or not (F)
/
!-----------------------------------------------------------------------
&namzdf_ric!richardson number dependent vertical diffusion("key_zdfric")
!-----------------------------------------------------------------------
rn_avmri = 100.e-4 !maximum value of the vertical viscosity /no change
rn_alp = 5. !coefficient of the parameterization  /no change
nn_ric = 2 !coefficient of the parameterization  /no change
rn_ekmfc = 7.0 !orig  Factor in the Ekman depth Equation
rn_mldmin = 1.0 !minimum allowable mixed-layer depth estimate (m)
rn_mldmax = 1000.0 !maximum allowable mixed-layer depth estimate (m)
rn_wtmix = 10.0 !vertical eddy viscosity coeff [m2/s] in the mixed-layer
rn_wvmix = 10.0 !vertical eddy diffusion coeff [m2/s] in the mixed-layer
ln_mldw = .true. !Flag to use or not the mized layer depth param.
/
!-----------------------------------------------------------------------
&namzdf_tke!turbulent eddy kinetic dependent vertical diffusion("key_zdftke")
!-----------------------------------------------------------------------
rn_ediff = 0.1 !coef. for vertical eddy coef. (avt=rn_ediff*mxl*sqrt(e))
rn_ediss = 0.7 !coef. of the Kolmogoroff dissipation
```

```
rn_ebb = 67.83 !coef. of tke surface input(=67.83 when ln_mxl0=T)
rn_emin = 1.e-6 !minimum value of tke [m2/s2]
rn_emin0 = 1.e-4 !surface minimum value of tke [m2/s2]
rn_bshear = 1.e-20 !background shear (>0) currently a numerical threshold
nn_mxl= 2!mixing length:=0 bounded by the distance to surface and bottom
                !=1 bounded by the local vertical scale factor
                !=2 first vertical derivative of mixing length bounded by 1
                !=3 as =2 with distinct disspipative an mixing length scale
nn_pdl = 1 !Pr function of Ri(=1, avt=pdl(Ri)*avm) or not (=0, avt=avm)
ln_mxl0 = .true. !surface mixing length scale = F(wind stress) (T) or (F)
rn_mxl0 = 0.04 !surface  buoyancy lenght scale minimum value
ln_lc = .true. !Langmuir cell parameterisation (Axell 2002)
rn_lc = 0.15 !coef. associated to Langmuir cells
nn_etau = 1 !TKE penetration below ML due to internal+intertial waves
                !=0 no penetration
                !=1 add a tke source below the ML
                !=2 add a tke source just at the base of the ML
                !=3 as = 1 applied on HF part of the stress("key_oasis3")
rn_efr = 0 !TKE surface fraction penetrating below ML (nn_etau=1 or 2)
nn_htau = 0 !type of exponential decrease of tke penetration below the ML
                !=0  constant 10 m length scale
                !=1  0.5m at equator to 30m poleward of 40 deg
/
!-----------------------------------------------------------------------
&namzdf_gls       !   GLS vertical diffusion      ("key_zdfgls")
!-----------------------------------------------------------------------
rn_emin      = 1.e-7 !minimum value of e   [m2/s2]
rn_epsmin    = 1.e-12!minimum value of eps [m2/s3]
ln_length_lim= .true.!dissipation rate limit for stable stratification
rn_clim_galp = 0.267 !galperin limit
ln_sigpsi    = .true.!Burchard 2001 mods on psi schmidt number in wb case
rn_crban     = 100.  !Craig and Banner 1994 constant for wb tke flux
rn_charn     = 70000.!Charnock constant for wb induced roughness length
rn_hsro      =  0.02 !Minimum surface roughness
rn_frac_hs   = 1.3 !Fraction of wave height as roughness (if nn_z0_met=2)
nn_z0_met    = 2 !Method for surface roughness computation (0/1/2)
nn_bc_surf   = 1 !surface condition (0/1=Dir/Neum)
nn_bc_bot    = 1 !bottom condition (0/1=Dir/Neum)
nn_stab_func = 2 !stability function (0=Galp,1= KC94,2=CanutoA,3=CanutoB)
nn_clos      = 3 !predefined closure type(0=MY82, 1=k-eps, 2=k-w, 3=Gen)
/
```

After compiling, the folder contains the *BLD*, *EXP00*, *MY_SRC* and *WORK* folders as well as the *readme* file. The executable is found in the *EXP00* folder. For enabling a 1-D simulation, the boundary and initial condition data files are needed in the folder. The *readme* file contains the template for the script needed for running the case. The general format of the *readme* file looks as follows

```
## =====================================================================
## Path
## =====================================================================
# path of NEMO trunk
MAINPATH=$HOME
# PATH for the initial condition file
DIR_ARCHI_INIT=$MAINPATH/NEMOGCM/CONFIG/SO_lev31_gls_test/EXP00/1011_nasa
```

```
# PATH for the forcing input files
DIR_ARCHI_FORC=${DIR_ARCHI_INIT}
## ==================================================================
## =======  Nothing to be changed bellow this line  ====================
## ==================================================================
mkdir rundir
cd rundir
## ==================================================================
## file needed for the run
## ==================================================================
cp ${MAINPATH}/NEMOGCM/CONFIG/SHARED/namelist_ref .
cp ../*.xml          .
cp ../namelist_cfg     .
cp ../opa            .
## ==================================================================
## Atmospherical forcings
## ==================================================================
## all nc files located here
ln -s ${DIR_ARCHI_FORC}/*.nc .
./opa
```

The paths to the NEMO trunk, forcing files and initial conditions must be specified. The grid files and physics module paths are already supplied. The ./opa is the command for running the simulation.

Due to the large volumes of simulations needed to run, a script folder generating the *readme* file and various cases was created. The script file for running the specific cases for a certain number of levels and reanalysis product (which runs the case for each turbulence scheme) takes the form

```
#This script runs all gls, richardson(pacanowski/philander) and TKE schemes
# make the variables needed: (Fill these in)
tkeORglsORric="gls"  # choices: tke, gls, ric
levels="31" # choices: 31, 31orca, 51, 75, 101, 151
# data packs:
datapack="1011_interim" #choices:interim,1011_jra55,1011_nasa,1011_ncep
#folder names
compilefolder="SO_lev31_gls_test"#the directory name of the compiled folder
# ric params (leave the default if not using)
ekmanfactor="7.0" #default "7.0"
ekmanviscosity="10.0" #default: "10.0"
ekmandiffusivity="10.0" #default: "10.0"
#forcing variables time frequency
timefreq_var1="3" #(Uwind)
timefreq_var2="3" #(Vwind)
timefreq_var3="24" #(swrad)
timefreq_var4="24" #(lwrad)
timefreq_var5="3" #(temp2m)
timefreq_var6="3" #(spechumid)
timefreq_var7="24" #(rain)
timefreq_var8="24" #(snow)

## A guide on the time frequency for the different data sets:
# 1011_interim: 3,3,24,24,3,3,24,24
# 1011_jra55: 6,6,6,6,6,6,6,6
# 1011_nasa: 3,3,3,3,3,3,3,3
```

```
# 1011_ncep: 6,6,6,6,6,6,6,6

# paths and static variables
# used in this file to create,copy,run certain files
trunk_orig=$HOME/Documents/script_files_for_running_cases
# call the loops script to run all the cases:
. /$trunk_orig/1011_loops.sh
```

The output is dumped into the *rundir* directory. The following section describes the output data structure.

## B.3 Output data structure

After the simulation is run, the output files can be found in the *rundir* folder. Symbolic links are formed to the grid, initial condition, surface forcings, executable and *namelist* files. The *ocean.output* file contains a summary of all details of the simulation (model details, parameters, errors etc.). Five data files are outputted from NEMO.

### B.3.1 Output files

The NEMO configurations used in this study had the following output files:

1. PAPA_1d_20100615_20110614_grid_T.nc

2. PAPA_1d_20100615_20110614_grid_U.nc

3. PAPA_1d_20100615_20110614_grid_V.nc

4. PAPA_1d_20100615_20110614_grid_W.nc

5. PAPA_00087600_restart.nc

Files 1-4 will be referred to as the *T,U,V,W* files respectively and contain the out put for tracers and u, v, w directions respectively. The *restart* file contains data for a simulation to start from that time step and state forwards in a different simulation. Table B.1-B.2 shows the output variables names and descriptions for the *T,U,V,W* files.

In the salinity (*vosaline*) and temperature (*votemper*) outputs from NEMO the seabed value of the water column is always 0. The reason is due to the staggered Arakawa grid. The seabed grid point is embedded into the 'ground' and is always set to 0. For plotting and calculation purposes cropping out the zero values was sufficient.

TABLE B.1: This table displays the different variables and their descriptions for the T and W output files from NEMO.

| **T file** | | **W file** | |
|---|---|---|---|
| **Variable** | **Description** (and unit) | **Variable** | **Description** (and unit) |
| nav_lon | Longitude (°) | nav_lon | Longitude (°) |
| nav_lat | Latitude (°) | nav_lat | Latitude (°) |
| deptht | Vertical depth values (m) | depthw | Vertical depth values (m) |
| time_counter | Time from the first to the last time step (s) | time_counter | Time from the first to the last time step (s) |
| time_counter_bnds | Time bands/sections (s) | time_counter_bnds | Time bands/sections (s) |
| votemper | Temperature (°C) | vovecrtz | The vertical velocity ($\mathrm{m\,s^{-1}}$) |
| vosaline | Salinity (PSU) | votkeavt | The vertical eddy diffusivity ($\mathrm{m^2\,s^{-1}}$) |
| sosstsst | Sea surface temperature (°C) | votkeavm | The vertical eddy viscosity ($\mathrm{m^2\,s^{-1}}$) |
| sosaline | Sea surface salinity (PSU) | | |
| sossheig | Sea surface height (m) | | |
| sowaflup | Net upward water flux ($\mathrm{kg\,m^{-2}\,s^{-1}}$) | | |
| sorunoff | River runoff ($\mathrm{kg\,m^{-2}\,s^{-1}}$) | | |
| sosfldow | Downward salt flux (PSU$\mathrm{m^{-2}\,s^{-1}}$) | | |
| sosst_cd | Concentration/Dilution term on temperature ($\mathrm{kg\,^{\circ}C\,m^{-2}\,s^{-1}}$) | | |
| sosss_cd | Concentration/Dilution term on salinity (PSU$\mathrm{kg\,m^{-2}\,s^{-1}}$) | | |
| sohefldo | Net downward heat flux ($\mathrm{W\,m^{-2}}$) | | |
| soshfldo | Shortwave radiation ($\mathrm{W\,m^{-2}}$) | | |
| somixhgt | Turbocline depth (m) | | |
| somxl010 | Mixed layer depth 0.01 (m) | | |
| soicecov | Ice fraction (scaled value between [0,1]) | | |
| sowindsp | Wind speed at 10m ($\mathrm{m\,s^{-1}}$) | | |
| sohefldp | Surface heat flux: Damping ($\mathrm{W\,m^{-2}}$) | | |
| sowafldp | Surface water flux: Damping ($\mathrm{kg\,m^{-2}\,s^{-1}}$) | | |
| sosafldp | Surface salt flux: Damping ($\mathrm{kg\,m^{-2}\,s^{-1}}$) | | |
| sobowlin | Bowl index (W-point) | | |

TABLE B.2: This table shows the different variables and their descriptions from the *V* and *W* output files from NEMO.

| **U file** | | **V file** | |
|---|---|---|---|
| **Variable** | **Description** (and unit) | **Variable** | **Description** (and unit) |
| nav_lon | Longitude (°) | nav_lon | Longitude (°) |
| nav_lat | Latitude (°) | nav_lat | Latitude (°) |
| depthu | Vertical depth values (m) | depthv | Vertical depth values (m) |
| time_counter | Time from the first to the last time step (s) | time_counter | Time from the first to the last time step (s) |
| time_counter_bnds | Time bands/sections (s) | time_counter_bnds | Time bands/sections (s) |
| vozocrtx | Zonal current ($\mathrm{m\,s^{-1}}$) | vomecrty | Meridional current ($\mathrm{m\,s^{-1}}$) |
| sozotaux | Wind stress along i(or x)-axis ($\mathrm{N\,m^{-2}}$) | sozotauy | Wind stress along j(or y)-axis ($\mathrm{N\,m^{-2}}$) |

## B.4 The grid parameters in NEMO

Refer to Section 3.2.1.2 with Eqns. 3.4 and 3.5. The coefficients $h_{sur}$, $h_0$, $h_1$ and $h_{th}$ correspond to the variables *ppsur*, *ppa0*, *ppa1* and *ppkth* in the NEMO configuration *namelist* file. These coefficients need not be specified directly and can be recalculated through four other variables, namely *ppacr* = $h_{cr}$, *ppkth* = $h_{th}$, *ppdzmin* and *pphmax*. These four variables are specified for determining the vertical grid structure. The *ppacr* variable is a stretching factor for the hyperbolic tangent. A larger *ppacr* implies a smaller stretching of the hyperbolic tangent and vice versa. *ppkth* is the level where maximum stretching occurs, i.e. the inflection point. This level is normally found around half or two thirds of the maximum number of levels. *ppdzmin* is the minimum spacing for the first level near the surface. *pphmax* is the maximum depth of the water column (4200 $\mathrm{m}$ for C1D_PAPA and 4500 $\mathrm{m}$ for SAZ1D configurations respectively). The subroutine in NEMO carrying out all calculations in determining vertical spacing and depths for the grid is found in file *domzgr.F90*. This subroutine was converted into *Python* code for handling the NetCDF files and testing and finding the best hyperbolic tangent function needed for the various levels (31, 51, 75, 101 and 151) chosen for the simulations in this study.

## B.5 Initial and boundary conditions

The initial conditions are stored in a file named

1. init_PAPASTATION.nc

The boundary conditions are specified by the files

1. chlorophyll.nc
2. Uwind_y2010.nc
3. Vwind_y2010.nc
4. swrad_y2010.nc
5. lwrad_y2010.nc
6. rain_y2010.nc

7. snow_y2010.nc
8. spechumid_y2010.nc
9. temp2m_y2010.nc
10. Uwind_y2011.nc
11. Vwind_y2011.nc
12. swrad_y2011.nc
13. lwrad_y2011.nc
14. rain_y2011.nc
15. snow_y2011.nc
16. spechumid_y2011.nc
17. temp2m_y2011.nc

The boundary condition files must have annual data. NEMO then uses the simulation begin date and selects it from the data. If annual data is not provided, NEMO is confused and will select the start date from the data given to it as if annual data was provided. The initial condition file (1) contains the temperature and salinity profiles corresponding to the specified number of vertical levels chosen. The boundary conditions contain the surface forcing data necessary for the atmospheric interaction on the ocean surface. The variables contained within the initial condition and boundary files are displayed in Tables B.3 and B.4.

For all simulations, the surface forcing files can be used without modification. The initial condition file however, (1) needs modification because the temperature and salinity profiles need to conform to the number of vertical levels due to spacing between levels for various simulations. The new depth and spacing values is calculated using the subroutine found file *domzgr.F90* in the NEMO code. This subroutine was converted into *Python* code and the suitable parameters (*ppacr*, *ppkth*, *ppdzmin* and *pphmaz* [Section 3.2.1.2]) were chosen to produce a suitable hyperbolic tangent curve for the required number of vertical levels. Firstly, these parameters were inserted into the configuration *namelist* file (*namelist_cfg*) in NEMO to compile the simulations. Secondly, these new depths are then written to a NetCDF file needed for running the simulation. The new depths are used to gather the corresponding

TABLE B.3: This table shows the various variables and their descriptions from the *chlorophyll.nc* (1) boundary file and *init_PAPASTATION.nc* (4) initial condition file used for the C1D_PAPA and SAZ1D cases in NEMO.

| **File name: chlorophyll.nc** | | **File Name: init_PAPASTATION.nc** | |
|---|---|---|---|
| **Variable** | **Description (and unit)** | **Variable** | **Description (and unit)** |
| CHLA | Chlorophyll a concentrations ($\mu g\,L^{-1}$) | longitude | Longitude (°) |
| MONTH_REG | Month index (None) | latitude | Latitude (°) |
| XAXIS | Degrees East (°) | deptht | Vertical depth values (m) |
| YAXIS | Degrees North (°) | time_counter | Time from the first to the last time step (s) |
| | | votemper | Vertical temperature profile (°C) |
| | | vovecrtz | Vertical salinity profile (PSU) |

TABLE B.4: This table shows the various variables and descriptions for the 2010 and 2011 forcing files (2-17) used for the C1D_PAPA and SAZ1D configurations in NEMO.

| Variable | Description (unit) | Variable | Description (unit) |
|---|---|---|---|
| **All Files** | | **All Files** | |
| lon | Longitude (°) | lon | Longitude (°) |
| lat | Latitude (°) | lat | Latitude (°) |
| time | Hours since 1 January 2010 (h) | time | Hours since 1 January 2011 (h) |
| **File Name: Uwind_y2010.nc** | | **File Name: Uwind_y2011.nc** | |
| Uwind | West-East 10 m wind velocity component ($\mathrm{m\,s^{-1}}$) | Uwind | West-East 10 m wind velocity component ($\mathrm{m\,s^{-1}}$) |
| **File Name: Vwind_y2010.nc** | | **File Name: Vwind_y2011.nc** | |
| Vwind | South-North 10 m wind velocity component ($\mathrm{m\,s^{-1}}$) | Vwind | South-North 10 m wind velocity component ($\mathrm{m\,s^{-1}}$) |
| **File Name: swrad_y2010.nc** | | **File Name: swrad_y2011.nc** | |
| swrad | Shortwave radiation ($\mathrm{W\,m^{-2}}$) | swrad | Shortwave radiation ($\mathrm{W\,m^{-2}}$) |
| **File Name: lwrad_y2010.nc** | | **File Name: lwrad_y2011.nc** | |
| lwrad | Longwave radiation ($\mathrm{W\,m^{-2}}$) | lwrad | Longwave radiation ($\mathrm{W\,m^{-2}}$) |
| **File Name: rain_y2010.nc** | | **File Name: rain_y2011.nc** | |
| rain | Total liquid precipitation ($\mathrm{kg\,m^{-2}\,s^{-1}}$) | rain | Total liquid precipitation ($\mathrm{kg\,m^{-2}\,s^{-1}}$) |
| **File Name: snow_y2010.nc** | | **File Name: snow_y2011.nc** | |
| snow | Total solid precipitation ($\mathrm{kg\,m^{-2}\,s^{-1}}$) | snow | Total solid precipitation ($\mathrm{kg\,m^{-2}\,s^{-1}}$) |
| **File Name: spechumid_y2010.nc** | | **File Name: spechumid_y2011.nc** | |
| spechumid | Specific humidity (%) | spechumid | Specific humidity (%) |
| **File Name: temp2m_y2010.nc** | | **File Name: temp2m_y2011.nc** | |
| temp2m | Air temperature at 2 m (K) | temp2m | Air temperature at 2 m (K) |

interpolated (using splines) temperature and salinity values (from WOA (Boyer et al., 2013)) for each depth. These temperature and salinity values are appended to the NetCDF file containing he depths forming the initial condition file (*init_PAPASTATION.nc*). Note that if the vertical mixing scheme is changed then a new NetCDF file does not have to be recreated.

## B.6 Turbulence scheme implementations

### B.6.1 Choosing a vertical turbulence scheme

Refer to Section 2.4 for the details of the turbulence schemes used in the study. All turbulence schemes discussed in Section 2.4 are available in NEMO. NEMO uses keys (key word in code indicating that module should be used) for choosing the specific turbulence scheme code. They include the Richardson based scheme (key_zdfric), KPP scheme (key_zdfkpp), TKE scheme (key_zdftke), the GLS schemes (key_zdfgls) and other tidal or diffusive mixing options. NEMO stipulates that one scheme must be used per simulation, i.e. one key. For a specific turbulence scheme to be chosen, the case must first be compiled with the correct key for that turbulence category. After compilation, the specific turbulence scheme may be chosen in the *namelist* file. The case can then be run using the compiled executable. The selection of the Pacanowski/Philander scheme followed by the TKE and GLS family of schemes are discussed below.

### B.6.2 Pacanowski/Philander scheme implementation in NEMO

As stated previously in Section 2.4.1, the implementation of the Pacanowski/Philander scheme in NEMO is under a different name, i.e. it falls part of the Richardson number based vertical physics schemes. The part of *namelist* file concerning the Pacanowski/Philander scheme parameters is shown below

```
!-----------------------------------------------------------------------
&namzdf_ric !richardson number dependent vertical diffusion("key_zdfric" )
!-----------------------------------------------------------------------
rn_avmri = 100.e-4 !maximum value of the vertical viscosity /no change
rn_alp = 5. !coefficient of the parameterization  /no change
nn_ric = 2 !coefficient of the parameterization  /no change
rn_ekmfc = 7.0 !Factor in the Ekman depth Equation
rn_mldmin= 1.0 !min allowable mixed-layer depth estimate(m)/no change
rn_mldmax= 1000.0 !max allowable mixed-layer depth estimate(m)/no change
rn_wtmix = 10.0 !vertical eddy viscosity coeff [m2/s] in the mixed-layer
rn_wvmix = 10.0 !vertical eddy diffusion coeff [m2/s] in the mixed-layer
ln_mldw =.true. !Flag to use mixed layer depth param./no change
/
```

The parameters *rn_ekmfc* (factor in the Ekman depth equation), *rn_wtmix* (vertical viscosity coefficient) and *rn_wvmix* (vertical eddy diffusivity coefficient) need adjustment for use in obtaining results using the Pacanowski/Philander scheme. The key_zdfric key has to be activated in the *cpp_***.fcm* file. A further option in the *namelist* file, namely the enhanced vertical diffusion, had to be set to true. This was found under the namzdf (vertical physics) *ln_zdfevd* variable. The parameters linking to $\alpha$, $\nu_0$ and n (Eqns. 2.24 and 2.23) are *rn_alp*, *rn_avmri* and *rn_ric* respectively, shown in the *namelist* file snippet above.

The Pacanowski/Philander scheme implementation in NEMO uses the Ekman equations to obtain the current velocities. The horizontal eddy velocity values are used in the calculation of the vertical sheers terms as found in the denominator of Richardson number (Eqn. 2.22). The Ekman parameters have to be chosen within reasonable bounds for the Pacanowski/Philander scheme to produce reasonable results. It is limited in a sense because, very high diffusivities (of order $10^4\ \mathrm{m^2\,s^{-1}}$) are needed for attaining best results (Sallée et al., 2010). Another major limiting factor resides on the Ekman depth factor. This factor is very sensitive in the order of $10^{-1}$ and has an overpowering effect stronger than the viscosity and diffusivity coefficients which is undesirable. The viscosity value was obtained from (Lenn and Chereskin, 2009), being in the order of $10^2 - 10^3)\ \mathrm{cm}^2\,\mathrm{s}^{-1}$.

### B.6.3 TKE schemes implementation

The TKE scheme implementation is done by activating the *key_zdftke* key in the *cpp_***.fcm* file. Furthermore the following section in the *namelist* file must be setup

```
!-----------------------------------------------------------------------
&namzdf_tke!turbulent eddy kinetic dependent vertical diffusion("key_zdftke")
!-----------------------------------------------------------------------
rn_ediff = 0.1 !coef. for vertical eddy coef. (avt=rn_ediff*mxl*sqrt(e) )
rn_ediss = 0.7 !coef. of the Kolmogoroff dissipation
rn_ebb = 67.83 !coef. of tke surface input(=67.83 when ln_mxl0=T)
rn_emin = 1.e-6 !minimum value of tke [m2/s2]
rn_emin0 = 1.e-4 !surface minimum value of tke [m2/s2]
rn_bshear=1.e-20 !background shear(>0) currently a numerical threshold
nn_mxl=2 !mixing length:=0 bounded by distance to surface and bottom
!=1 bounded by the local vertical scale factor
!=2 first vertical derivative of mixing length bounded by 1
!=3 as =2 with distinct disspipative an mixing length scale
nn_pdl = 1 !Pr function of Ri(=1, avt=pdl(Ri)*avm) or not (=0, avt=avm)
ln_mxl0=.true. !surface mixing length scale =F(wind stress)(T) or (F)
rn_mxl0 = 0.04 !surface  buoyancy lenght scale minimum value
ln_lc = .true. !Langmuir cell parameterisation (Axell 2002)
rn_lc = 0.15 !coef. associated to Langmuir cells
nn_etau = 1 !TKE penetration below ML due to internal+intertial waves
!=0 no penetration
!=1 add a tke source below the ML
!=2 add a tke source just at the base of the ML
!=3 as = 1 applied on HF part of the stress("key_oasis3")
rn_efr=0.05 !TKE surface fraction penetrating below ML (nn_etau=1 or 2)
nn_htau=0 !type of exponential decrease of tke penetration below the ML
!=0  constant 10 m length scale
!=1  0.5m at equator to 30m poleward of 40 deg
/
```

The TKE0 scheme is chosen by setting *rn_efr* and *nn_htau* to 0. The TKE10 scheme is chosen by setting *rn_efr* to 0.05 and *nn_htau* to 0. Lastly, the TKE30 is chosen by setting *rn_efr* to 0.05 and *nn_htau* to 1.

### B.6.4 GLS schemes implementation

The GLS scheme implementation is done by activating the *key_zdfgls* key in the *cpp_***.fcm* file. Furthermore the following section in the *namelist* file must be setup

```
!-----------------------------------------------------------------------
&namzdf_gls       !   GLS vertical diffusion      ("key_zdfgls")
!-----------------------------------------------------------------------
rn_emin      = 1.e-7 !minimum value of e   [m2/s2]
rn_epsmin    = 1.e-12!minimum value of eps [m2/s3]
ln_length_lim= .true.!dissipation rate limit for stable stratification
rn_clim_galp = 0.267 !galperin limit
ln_sigpsi    = .true.!Burchard 2001 mods on psi schmidt number in wb case
```

```
rn_crban     = 100.  !Craig and Banner 1994 constant for wb tke flux
rn_charn     = 70000.!Charnock constant for wb induced roughness length
rn_hsro      =  0.02 !Minimum surface roughness
rn_frac_hs   = 1.3 !Fraction of wave height as roughness (if nn_z0_met=2)
nn_z0_met    = 2 !Method for surface roughness computation (0/1/2)
nn_bc_surf   = 1 !surface condition (0/1=Dir/Neum)
nn_bc_bot    = 1 !bottom condition (0/1=Dir/Neum)
nn_stab_func = 2 !stability function (0=Galp,1= KC94,2=CanutoA,3=CanutoB)
nn_clos      = 3 !predefined closure type(0=MY82, 1=k-eps, 2=k-w, 3=Gen)
/
```

The M-Y (Mellor-Yamada or k-kl), $k - \varepsilon$, $k - \omega$ or Genric scheme is selected by setting *nn_clos* to 0, 1, 2 or 3 respectively. The model constants are coded into a generic framework that is easily selects the constants for the chosen scheme.

## B.7 How to run the climatology

The climatology is run for an extended period of years using data from a specific year. The aim is to observe if seasonality is present. The climatology can also pick up if there is a slow heating (or cooling) in temperature and a freshening (or saline increase) in the salinity results.

For the climatology implementation, the climatology flag must be set to true for all surface forcing variables (chlorophyll, air temperature, specific humidity, wind speed, solar radiation, thermal radiation, snow and precipitation) where it is being read from the *namelist* file.

Due to the use of one specific year data, the leap year time counter must be set to 0 otherwise NEMO will attempt to read an extra day for the leap year leading to an error.

The climatology also requires the data file names to exclude all year conventions or an error is thrown, i.e. file names should not carry the suffix $*_y2010.nc$ for example where * indicates the file name.

## B.8 Conclusion

This Appendix outline the installation of NEMO. Furthermore the technical details of how to setup the C1D_PAPA and SAZ1D configurations in NEMO were outlined. The output files and variables were shown where to be found. A brief overview was given on the boundary and initial condition files and variables needed for operating the configurations. The process of changing the family of turbulence schemes and the individual turbulence schemes were given. Lastly, the importance and process of running the climatology was outlined.

# Appendix C

# Data processing particulars

This appendix outlines from where and how the boundary (surface forcings) and initial data was acquired. The surface forcings consisted of chlorophyll data as well as various reanalysis data. The initial condition data were acquired from World Ocean Atlas (WOA) (Boyer et al., 2013). Furthermore, this appendix deals with the steps taken to process the reanalysis and WOA data to a usable form for simulation input for the C1D_PAPA and SAZ1D configurations. The scripts, code and supporting files created for processing the data are provided in this Appendix. All NEMO script snippets from the *namelist* file can be found from the NEMO ocean program (Madec, 2008).

## C.1 Forcing functions and chlorophyll data acquisition and processing

The following subsections describe the source of reanalysis (JRA55, NASA, ERA-Interim and NCEP) and chlorophyll data. The processing particulars are also outlined.

### C.1.1 Reanalysis data source and variable selection

The reanalysis data was download from their respective databases via a web interface in various formats (NetCDF, GRB etc.).[1] A list of the file names (category of data or field name) and corresponding variables used are give in Tables C.1 and C.2. Below each table is a list of incorrect variables initially used in the simulations. It was later found that due to incorrect units and sea level surface readings the variables (data) had to be discarded and the correct data was found.

Note that the data had to consist of a full 2010 dataset as well as a 2011 full dataset. Initially, due to the time period in focus (15 June 2010 - 14 June 2011) a single dataset was created specifically for these dates, however, NEMO misinterpreted the data as a yearly dataset for 2010, leading to the simulation starting near 1 January 2011. The results displayed a false seasonal phase shift where summer appeared in winter and vice versa. It was found out that separate yearly datasets were needed for the input, i.e. a 2010 yearly dataset and a 2011 yearly dataset was needed (even though the excess dates data went unused) due to NEMO's set up.

### C.1.2 Chlorophyll data acquisition

The chlorophyll data was obtained from the ESA CCI dataset (CCI, 2017) via a file ftp.[2]

---

[1] The website interface to NASA data is https://disc.sci.gsfc.nasa.gov/daac-bin/FTPSubset.pl. NCEP data can be found at https://rda.ucar.edu/datasets/ds091.0/. JRA55 data is downloadable through the interface, but a user needs to register with the database found at http://jra.kishou.go.jp/JRA-55/index_en.html. ERA-Interim data is found at https://www.ecmwf.int/en/research/climate-reanalysis/era-interim. All sites last visited 1 August 2017.

[2] Chlorophyll data was acquired from ftp://ftp.rsg.pml.ac.uk/occci-v3.0/geographic/netcdf/monthly/chlor_a/2013/. Last visited 1 August 2017.

### C.1.3 Data processing particulars

All data was processed using *Ubuntu* scripts in conjunction with *CDO* operators and file management.[3] Scripts were created for year 2010 and 2011 separately due to name changes in data files. The scripts are shown at the end of this subsection for reference to the method of data processing.

The initial step in processing the data was to convert the data to a format used by NEMO, i.e. NetCDF format. NCEP, ERA-Interim and NASA data can be obtained in NetCDF format, however, JRA55 comes in grb (binary) format. This format must be converted to NetCDF and was done using the following script format (only snow variable shown):

```
# converts the binary format to netcdf format
echo "copying:"
for filename in anl_snow125.*; do
    cdo -f nc4 copy $filename $filename.nc4
done
echo "merging:"
cdo mergetime *.nc4 allmerged.nc
echo "Done. file allmerged.nc is the result"
```

The following step involved the selection (extraction) of the specific variable in focus. It must be noted that initially a few incorrect variables were selected. For instance, the nett radiation was used which giving incorrect results (especially in the case of NASA data). The problem was that NEMO calculates the albedo (ocean surface light reflection) but the nett fluxes have already calculated albedo implying albedo is calculated twice when running simulations. This was solved by using NASA chemistry grids (coarser)containing the correct variables, i.e. downwards radiation fluxes.

Following the variable selection, the closest latitude and longitude to 4.5°E -47°S must be selected. This is done using panoply[4] or nco[5] to view the longitudes and latitudes. The resulting time series data is now ready for interpolation onto the NEMO grid format. This is done with the aid of *station-SAZ.txt* needed for specifying the bounds of longitude and latitude and number of horizontal grid points for the SO simulations and is given below

```
# gridID SAZ: meridional
#
gridtype  = lonlat
gridsize  = 9
xname     = lon
xlongname = longitude
xunits    = degrees_east
yname     = lat
ylongname = latitude
yunits    = degrees_north
xsize     = 3
ysize     = 3
xfirst    = 4.25
xinc      = 0.25
yfirst    = -47.25
yinc      = 0.25
```

The operation effectively takes a single data point in the time series and copies itself nine times to fit onto a $3 \times 3$ grid. Conversions to the correct unit was done where necessary. Finally the name

---

[3] https://code.mpimet.mpg.de/projects/cdo/

[4] https://github.com/panoplyio

[5] **http://nco.sourceforge.net/**.

of the file was changed to a common name that simplified the automation process of running many simulations.

Chlorophyll data was obtained in NetCDF format with correct units and needed no preprocessing other than extraction of the chlorophyll variable and interpolation onto the NEMO simulation grid.

The script to process and extract the NASA data (2010) is given below:

```
#!/bin/sh
# this script processes NASA data
### put the merged files here (yearly data)
FNAME="rawdata/surf/allmerged.nc"
FNAMEchm="rawdata/chmsurf/allmerged.nc"

# lonlat for ordinary ocean surface diagnostics grid and chemistry grid.
# lonlats were found closest to 4.5E -47S using panoply
LONLAT="4,4.5,-47.5,-47"
LONLATchm="4.5,5.5,-47.5,-46.5"


###ocean surf fvariables: wind, precip

cdo select,name=U10M $FNAME temp.nc
cdo -R sellonlatbox,$LONLAT temp.nc tmp.nc
rm temp.nc
cdo enlarge,stationSAZ.txt tmp.nc NASA.nc
rm tmp.nc
cdo chname,U10M,Uwind NASA.nc dataPack/Uwind_y2010.nc
rm NASA.nc

cdo select,name=V10M $FNAME temp.nc
cdo -R sellonlatbox,$LONLAT temp.nc tmp.nc
rm temp.nc
cdo enlarge,stationSAZ.txt tmp.nc NASA.nc
rm tmp.nc
cdo chname,V10M,Vwind NASA.nc dataPack/Vwind_y2010.nc
rm NASA.nc

cdo select,name=RAINOCN $FNAME temp.nc
cdo -R sellonlatbox,$LONLAT temp.nc tmp.nc
rm temp.nc
cdo enlarge,stationSAZ.txt tmp.nc NASA1.nc
rm tmp.nc
cdo chname,RAINOCN,rain NASA1.nc dataPack/rain_y2010.nc
rm NASA1.nc

cdo select,name=PRECSNOOCN $FNAME temp.nc
cdo -R sellonlatbox,$LONLAT temp.nc tmp.nc
rm temp.nc
cdo enlarge,stationSAZ.txt tmp.nc NASA1.nc
rm tmp.nc
cdo chname,PRECSNOOCN,snow NASA1.nc dataPack/snow_y2010.nc
rm NASA1.nc
```

```
###chem surf fvariables: T,Q radiation

cdo select,name=T2M $FNAMEchm temp.nc
cdo -R sellonlatbox,$LONLATchm temp.nc tmp.nc
rm temp.nc
cdo enlarge,stationSAZ.txt tmp.nc NASA.nc
rm tmp.nc
cdo chname,T2M,temp2m NASA.nc dataPack/temp2m_y2010.nc
rm NASA.nc

cdo select,name=QV2M $FNAMEchm temp.nc
cdo -R sellonlatbox,$LONLATchm temp.nc tmp.nc
rm temp.nc
cdo enlarge,stationSAZ.txt tmp.nc NASA.nc
rm tmp.nc
cdo chname,QV2M,spechumid NASA.nc dataPack/spechumid_y2010.nc
rm NASA.nc

cdo select,name=SWGDWN $FNAMEchm temp.nc
cdo -R sellonlatbox,$LONLATchm temp.nc tmp.nc
rm temp.nc
cdo enlarge,stationSAZ.txt tmp.nc NASA.nc
rm tmp.nc
cdo chname,SWGDWN,swrad NASA.nc dataPack/swrad_y2010.nc
rm NASA.nc

cdo select,name=LWGDWN $FNAMEchm temp.nc
cdo -R sellonlatbox,$LONLATchm temp.nc tmp.nc
rm temp.nc
cdo enlarge,stationSAZ.txt tmp.nc NASA.nc
rm tmp.nc
cdo chname,LWGDWN,lwrad NASA.nc dataPack/lwrad_y2010.nc
rm NASA.nc
```

The script to process and extract the NCEP (2010) data is given below:

```
#!/bin/sh
# this script processes NCEP data
### yearly data here
FNAME="rawdata/allmerged.nc"

#Lon/lat are selected closest to:4.5E -47S for NCEP(found using panoply)
LONLAT="5.5,5.7,-46.7,-46.5"


### wind are at levels 10m
cdo select,name=U_GRD_98_HTGL $FNAME temp.nc
cdo -R sellonlatbox,$LONLAT temp.nc test.nc
rm temp.nc
cdo enlarge,stationSAZ.txt test.nc NCEP.nc
rm test.nc
cdo chname,U_GRD_98_HTGL,Uwind NCEP.nc dataPack/Uwind_y2010.nc
rm NCEP.nc
```

```
cdo select,name=V_GRD_98_HTGL $FNAME temp.nc
cdo -R sellonlatbox,$LONLAT temp.nc test.nc
rm temp.nc
cdo enlarge,stationSAZ.txt test.nc NCEP.nc
rm test.nc
cdo chname,V_GRD_98_HTGL,Vwind NCEP.nc dataPack/Vwind_y2010.nc
rm NCEP.nc

### use this temp as it is at level = 2m
cdo select,name=TMP_98_HTGL $FNAME temp.nc
cdo -R sellonlatbox,$LONLAT temp.nc test.nc
rm temp.nc
cdo enlarge,stationSAZ.txt test.nc NCEP.nc
rm test.nc
cdo chname,TMP_98_HTGL,temp2m NCEP.nc dataPack/temp2m_y2010.nc
rm NCEP.nc

cdo select,name=PRATE_98_SFC_ave6h $FNAME temp.nc
cdo -R sellonlatbox,$LONLAT temp.nc test.nc
rm temp.nc
cdo enlarge,stationSAZ.txt test.nc NCEP.nc
rm test.nc
cdo chname,PRATE_98_SFC_ave6h,rain NCEP.nc dataPack/rain_y2010.nc
rm NCEP.nc

cdo select,name=SPFH_98_HTGL $FNAME temp.nc
cdo -R sellonlatbox,$LONLAT temp.nc test.nc
rm temp.nc
cdo enlarge,stationSAZ.txt test.nc NCEP.nc
rm test.nc
cdo chname,SPFH_98_HTGL,spechumid NCEP.nc dataPack/spechumid_y2010.nc
rm NCEP.nc

cdo select,name=SRWEQ_98_SFC_ave6h $FNAME temp.nc
cdo -R sellonlatbox,$LONLAT temp.nc test.nc
rm temp.nc
cdo enlarge,stationSAZ.txt test.nc NCEP.nc
rm test.nc
cdo chname,SRWEQ_98_SFC_ave6h,snow NCEP.nc dataPack/snow_y2010.nc
rm NCEP.nc

cdo select,name=DSWRF_98_SFC_ave6h $FNAME temp.nc
cdo -R sellonlatbox,$LONLAT temp.nc test.nc
rm temp.nc
cdo enlarge,stationSAZ.txt test.nc NCEP.nc
rm test.nc
cdo chname,DSWRF_98_SFC_ave6h,swrad NCEP.nc dataPack/swrad_y2010.nc
rm NCEP.nc

cdo select,name=DLWRF_98_SFC_ave6h $FNAME temp.nc
cdo -R sellonlatbox,$LONLAT temp.nc test.nc
rm temp.nc
```

```
cdo enlarge,stationSAZ.txt test.nc NCEP.nc
rm test.nc
cdo chname,DLWRF_98_SFC_ave6h,lwrad NCEP.nc dataPack/lwrad_y2010.nc
rm NCEP.nc
```

The script to process and extract the JRA55 (2010) data is given below:

```
#!/bin/sh
### This script processes JRA55 data
FNAME="allmerged.nc"

# the lon lat that is closest to 4.5E -47S (found using panoply)
LONLAT="4.0,6.0,-47.6,-47.4"

# rad125(phy2m files): rain, snow, radx2

cdo select,name=tpratsfc rawdata/rad125x2/$FNAME temp.nc
cdo -R sellonlatbox,$LONLAT temp.nc test.nc
rm temp.nc
cdo enlarge,stationSAZ.txt test.nc JRA55.nc
rm test.nc
# convert the mm/day to mm/s. Data is in mm/day => x(1)/(24x60x60)
cdo mulc,0.000011574074074074073 JRA55.nc conv.nc
cdo chname,tpratsfc,rain conv.nc dataPack/rain_y2010.nc
rm conv.nc
rm JRA55.nc

cdo select,name=srweqsfc rawdata/rad125x2/$FNAME temp.nc
cdo -R sellonlatbox,$LONLAT temp.nc test.nc
rm temp.nc
cdo enlarge,stationSAZ.txt test.nc JRA55.nc
rm test.nc
# convert the mm/day to m/s. Data is in mm/day => x(1)/(24x60x60)
cdo mulc,0.000011574074074074073 JRA55.nc conv.nc
cdo chname,srweqsfc,snow conv.nc dataPack/snow_y2010.nc
rm conv.nc
rm JRA55.nc

cdo select,name=dswrf rawdata/rad125x2/$FNAME temp.nc
cdo -R sellonlatbox,$LONLAT temp.nc test.nc
rm temp.nc
cdo enlarge,stationSAZ.txt test.nc JRA55.nc
rm test.nc
cdo chname,dswrf,swrad JRA55.nc dataPack/swrad_y2010.nc
rm JRA55.nc

cdo select,name=dlwrf rawdata/rad125x2/$FNAME temp.nc
cdo -R sellonlatbox,$LONLAT temp.nc test.nc
rm temp.nc
cdo enlarge,stationSAZ.txt test.nc JRA55.nc
rm test.nc
cdo chname,dlwrf,lwrad JRA55.nc dataPack/lwrad_y2010.nc
rm JRA55.nc
```

```
# tuvq125(surf files): t,u,v,q

cdo select,name=u rawdata/tuvq125/$FNAME temp.nc
cdo -R sellonlatbox,$LONLAT temp.nc test.nc
rm temp.nc
cdo enlarge,stationSAZ.txt test.nc JRA55.nc
rm test.nc
#average out the height dim
ncwa -a height_2 JRA55.nc train.nc
cdo chname,u,Uwind train.nc dataPack/Uwind_y2010.nc
rm train.nc
rm JRA55.nc

cdo select,name=v rawdata/tuvq125/$FNAME temp.nc
cdo -R sellonlatbox,$LONLAT temp.nc test.nc
rm temp.nc
cdo enlarge,stationSAZ.txt test.nc JRA55.nc
rm test.nc
#average out the height
ncwa -a height_2 JRA55.nc train.nc
cdo chname,v,Vwind train.nc dataPack/Vwind_y2010.nc
rm train.nc
rm JRA55.nc

cdo select,name=t rawdata/tuvq125/$FNAME temp.nc
cdo -R sellonlatbox,$LONLAT temp.nc test.nc
rm temp.nc
cdo enlarge,stationSAZ.txt test.nc JRA55.nc
rm test.nc
# average out height
ncwa -a height JRA55.nc train.nc
cdo chname,t,temp2m train.nc dataPack/temp2m_y2010.nc
rm train.nc
rm JRA55.nc

cdo select,name=q rawdata/tuvq125/$FNAME temp.nc
cdo -R sellonlatbox,$LONLAT temp.nc test.nc
rm temp.nc
cdo enlarge,stationSAZ.txt test.nc JRA55.nc
rm test.nc
# average the height
ncwa -a height JRA55.nc train.nc
cdo chname,q,spechumid train.nc dataPack/spechumid_y2010.nc
rm train.nc
rm JRA55.nc
```

## C.2 Temperature and salinity profile data (initial conditions) acquisition and processing

The temperature and salinity profiles needed for the initial conditions were obtained from World Ocean Atlas (WOA) data.[6]

---

[6] The website interface to WOA data is https://www.nodc.noaa.gov/OC5/woa13/ Last visited 1 August 2017.

### C.2.1 Initial condition processing details

The processing of the WOA data was constrained to the number of vertical levels of the grid. The vertical levels were fixed at 31, 51, 75, 101 or 151 with various spacing between levels. NEMO has a subroutine to achieve this. This subroutine (NEMO/OPA_SRC/DOM/*domzgr.F90*) was converted to *Python* code for finding the required parameters. The code is shown below

```
def zgrid(jpk=75,ppsur=-3958.951371276829,
    ppa0=103.9530096000000,ppa1=2.415951269000000,ppkth=15.3510137,
    ppacr=7.0,ppdzmin=np.nan,pphmax=np.nan,ldbletanh=1,ppa2=100.7609285,
    ppkth2=48.02989372,ppacr2=13.0):
#--------------------------------------------------------------
#ROUTINE zgr_z:
# Purpose: Set model level depths and resulting vertical scale factors.
# Method: z-coordinate system. Model level depths is defined from
#         an analytical function where derivative gives scale factors.
#         Both depth and scale factors only depend on k.
#                w-level: gdepw_1d = gdep(k)
#                         e3w_1d(k)= dk(gdep)(k)  = e3(k)
#                t-level: gdept_1d = gdep(k+0.5)
#                         e3t_1d(k)= dk(gdep)(k+0.5)=e3(k+0.5)
#   Reference :Marti,Madec&Delecluse,1992,JGR,97,No8,12,763-12,766.
#  --------------------------------------------------------------
    # initialize
    gdept_1d = np.empty((jpk, 1));
    gdept_1d[:] = np.NAN
    e3t_1d = gdept_1d;
    gdepw_1d = gdept_1d;
    e3w_1d = gdept_1d;
    zkth = ppkth;
    zacr = ppacr; # amount of stretching
    zdzmin = ppdzmin;
    zhmax = pphmax;
    zkth2 = ppkth2;
    zacr2 = ppacr2;  # optional double tanh parameters
    jpkm1 = jpk - 1;

    # If ppa1 and ppa0 and ppsur are equal to np.NAN
    #  za0, za1, zsur are computed from ppdzmin , pphmax, ppkth, ppacr
    if (np.isnan(ppa1) and np.isnan(ppa0) and np.isnan(ppsur)):
        za1=(ppdzmin-pphmax/float(jpkm1))/(math.tanh((1-ppkth)/ppacr)
            -ppacr/float(jpk-1)*(math.log(math.cosh((jpk-ppkth)/ppacr))
            -math.log(math.cosh((1-ppkth)/ppacr))));
        za0= ppdzmin - za1 * math.tanh((1 - ppkth) / ppacr);
        zsur=-za0-za1*ppacr*math.log(math.cosh((1-ppkth)/ppacr));
    else:
        za1 = ppa1;
        za0 = ppa0;
        zsur = ppsur; # z at surface
        za2 = ppa2;  # optional (ldbletanh=T) double tanh parameter
    print(’    zgr_z   : Reference vertical z-coordinates’)
    print(’    ~~~~~~~’)
    if (ppkth == 0):
        print("      Uniform grid with "+ str(jpk-1)+" layers")
```

```
        print("      Total depth    :" + str(zhmax))
        print("      Layer thickness:" + str(zhmax / (jpk - 1)))
    else:
        if (ppa1 == 0 and ppa0 == 0 and ppsur == 0):
            print("         zsur, za0, za1 computed from ")
            print("                 zdzmin = " + str(zdzmin))
            print("                 zhmax  = " + str(zhmax))
        print(’           Value of coefficients for vertical mesh:’)
        print([’                 zsur = ’, str(zsur)])
        print([’                 za0  = ’, str(za0)])
        print([’                 za1  = ’, str(za1)])
        print([’                 zkth = ’, str(zkth)])
        print([’                 zacr = ’, str(zacr)])
        if (ldbletanh):
            print(" (Double tanh    za2  = " + str(za2))
            print("  parameters)    zkth2= " + str(zkth2))
            print("                 zacr2= " + str(zacr2))
    # Reference z-coordinate(depth-scale factor at T- and W-points)
    #  ======================
    if (ppkth == 0):  # uniform vertical grid
        za1 = zhmax / float(jpk - 1);
        for jk in range(0, jpk):
            zw = float(jk);
            zt = float(jk) + 0.5;
            gdepw_1d[jk] = (zw - 1) * za1;
            gdept_1d[jk] = (zt - 1) * za1;
            e3w_1d[jk] = za1;
            e3t_1d[jk] = za1;
    else:  # Madec & Imbard 1996 function
        if (not ldbletanh):
            for jk in range(0, jpk):
                zw = float(jk);
                zt = float(jk) + 0.5;
                gdepw_1d[jk]=(zsur+za0*zw+za1*zacr*
                             math.log(math.cosh((zw-zkth)/zacr)));
                gdept_1d[jk]=(zsur+za0*zt+za1*zacr*
                             math.log(math.cosh((zt-zkth)/zacr)));
                e3w_1d[jk] = za0 + za1 * math.tanh((zw - zkth) / zacr);
                e3t_1d[jk] = za0 + za1 * math.tanh((zt - zkth) / zacr);
        else:
            for jk in range(0, jpk):
                zw = float(jk);
                zt = float(jk) + 0.5;
                # Double tanh function
                gdepw_1d[jk]=(zsur+za0*zw+za1*zacr*
                              math.log(math.cosh((zw-zkth)/zacr))+
                              za2*zacr2*math.log(math.cosh((zw-zkth2)/
                              zacr2)));
                gdept_1d[jk]=(zsur+za0*zt+za1*zacr*
                             math.log(math.cosh((zt-zkth)/zacr))+za2*
                             zacr2*math.log(math.cosh((zt-zkth2)/
                             zacr2)));
                e3w_1d[jk]=za0+za1*math.tanh((zw-zkth)/zacr)+za2*
```

```
                    math.tanh((zw-zkth2)/zacr2);
            e3t_1d[jk]=za0+za1*math.tanh((zt-zkth)/zacr)+za2*
                    math.tanh((zt-zkth2)/zacr2);
        # force first w-level to be exactly at zero
        gdepw_1d[0]=5.14695644e-01;
    return [gdept_1d, e3t_1d, gdepw_1d, e3w_1d]
```

The WOA data did not match the specific grid configurations used for the NEMO simulations. The solution was to fit a (linear) spline to the WOA data and interpolate the necessary depth, salinity and temperature data suitable for the NEMO grid configurations.[7] After the temperature and salinity profiles are extracted, the profiles are copied nine times to fit the NEMO grid structure ($3 \times 3 \times number\ of\ vertical\ levels$). These new depth, temperature and salinity points were written to a NetCDF file to be used as initial conditions. Note that if the turbulence scheme or reanalysis data is changed in a simulation, then the initial conditions do not have to be recreated (given that the number of vertical levels remain constant). The *Python* code extracting the necessary data and writing the NetCDF file is given below

```
########################################################################
# Kirodh Boodhraj
# 21 November 2016
# Code purpose: This file creates temperature and salinity profiles
# needed for the SO runs
########################################################################
# import statements
from opennc import opennc
from getvar import getvar
from zgrid import zgrid
from scipy.interpolate import interp1d
from netCDF4 import Dataset as netcdffile
import numpy as np
# read in original WOA data
originalfileandprofiles = 'inputprofile/SAZL75_initial_WOA13_annual.nc'
fh_init = opennc(originalfileandprofiles,0)
init_dept = getvar(fh_init,"depth",0)
init_temp = getvar(fh_init,"temperature",0) ; init_temp = init_temp[0,:,1,1]
init_sal = getvar(fh_init,"salinity",0);init_sal = init_sal[0,:,1,1]

# append 5011 value onto data using last data point
# interpolations to lie in range (bathymetry=4500 m)
fillarray = np.arange(4100,5011)
lenfillarray = len(fillarray)
init_dept = np.append(init_dept,fillarray)
init_temp = np.append(init_temp,np.ones(lenfillarray)*init_temp[-1])
init_sal= np.append(init_sal,np.ones(lenfillarray)*init_sal[-1])

# prepare data for splining
xdata = init_dept
ydata_S = init_sal
ydata_T = init_temp
fit_temp = interp1d(xdata,ydata_T,kind='linear')
fit_sal = interp1d(xdata,ydata_S,kind='linear')
```

---

[7] https://docs.scipy.org/doc/scipy/reference/tutorial/interpolate.html

```
#get vertical spacings and depths using code from NEMO
#for 31:
#[space_t,other1,space_w,other2]=
   zgrid(31,np.nan,np.nan,np.nan,16,2,1.0,4500,0,np.nan,np.nan,np.nan)
#for 51:
#[space_t,other1,space_w,other2]=
   zgrid(51,np.nan,np.nan,np.nan,28,7,1.0,4500,0,np.nan,np.nan,np.nan)
#for 75:
#[space_t,other1,space_w,other2]=
   zgrid(75,np.nan,np.nan,np.nan,50,7,1.0,4500,0,np.nan,np.nan,np.nan)
#for 101:
#[space_t,other1,space_w,other2]=
   zgrid(101,np.nan,np.nan,np.nan,70,14,1.0,4500,0,np.nan,np.nan,np.nan)
#for 151:
#[space_t,other1,space_w,other2]=
   zgrid(151,np.nan,np.nan,np.nan,97,17,1.0,4500,0,np.nan,np.nan,np.nan)
#31 ORCA2 grid parameters
#[space_t,other1,space_w,other2]=
   zgrid(31,-4762.96,255.58,245.5813,21.43336,3,np.nan,np.nan,
   0,np.nan,np.nan,np.nan)

# cumalitive sum generating depths
cumsum = (space_t[0]).tolist()[0]
xnew=[]
xnew.append(cumsum)
for i in range(1,len(space_t)): # loop through the 2nd value and carry on
    cumsum += (space_t[i]).tolist()[0]
    xnew.append(cumsum) # append on the new depth
# ##################################
# write netcdf file
# set out temperature, salinity and depth data for new netcdf file
longitude_old = fh_init.variables["lon"][:]
latitude_old = fh_init.variables["lat"][:]
depth_old = xnew
time_old = fh_init.variables["time"][:]
temp_old = fit_temp(depth_old)
sal_old = fit_sal(depth_old)

# create file container
new_file = netcdffile('outputprofiles/init_PAPASTATION_m06d15.nc',
    "w",format="NETCDF3_64BIT")
# use original netcdf file and ncdump function to find
    dimensions and attributes
new_file.createDimension("longitude",len(longitude_old))
new_file.createDimension("latitude",len(latitude_old))
new_file.createDimension("deptht",len(depth_old))
new_file.createDimension("time_counter",None)

# create variables and attributes:
# no attributes, d is for double, f4 for float
longitude_new = new_file.createVariable("longitude","d",("longitude"))
latitude_new = new_file.createVariable("latitude","d",("latitude"))
depth_new = new_file.createVariable("deptht","d",("deptht"))
```

```
depth_new.units = "m"
depth_new.positive = "down"
depth_new.point_spacing = "uneven"
depth_new.axis = "Z"
depth_new.standard_name = "depth"
time_new = new_file.createVariable("time_counter","d",("time_counter"))
time_new.units = "days since 1950-01-01 00:00:00"
time_new.time_origin = "01-JAN-1950 00:00:00"
time_new.axis = "T"
time_new.standard_name = "time"
temp_new = new_file.createVariable("votemper","d",
    ("time_counter","deptht","latitude","longitude"))
temp_new.units = "degree celsius"
temp_new.standard_name = "Temperature"
sal_new = new_file.createVariable("vosaline","d",
    ("time_counter","deptht","latitude","longitude"))
sal_new.units = "PSU"
sal_new.standard_name = "Salinity"

# variables to fill with data
longitude_new[:] = longitude_old
latitude_new[:] = latitude_old
depth_new[:] = depth_old
time_new[:] = time_old
# write 4 dim, make 3x3 layer per depth of temp and salinity values
# for temperature:
# make 3-D array and fill with zeros according to the variables dimensions
cont_T = np.zeros((len(depth_old),len(latitude_old),len(longitude_old)))
# loop over levels and fill with temperature values
for i in range(len(depth_old)):
# levels indicated with i and [i,:,:] indicates entire 3x3 level
# .fill populates level with numpy array value needing conversion to list
# remove list by extracting first value for expansion into 3x3 layer
    cont_T[i,:,:].fill(temp_old.tolist()[i])
cont_T.resize((1,len(depth_old),3,3)) # resize the array
temp_new[:,:,:,:] = np.array(cont_T) # write the data to the nc file

# for salinity:
cont_S = np.zeros((len(depth_old),len(latitude_old),len(longitude_old)))
for i in range(len(depth_old)):
    cont_S[i,:,:].fill(sal_old.tolist()[i])
cont_S.resize((1,len(depth_old),3,3)) # resize the array
sal_new[:,:,:,:] = np.array(cont_S) # write the data to the nc file
new_file.close()
#################################
# this command made the record dimension
# ncks --mk_rec_dmn time_counter
     init_PAPASTATION_m06d15.nc init_PAPASTATION_m00d00.nc
```

## C.3 Conclusion

This appendix outlined the acquisition and processing of reanalysis, WOA and chlorophyll data. The scripts, *Python* code and supporting files were provided for reproducibility purposes. The processing methods were given in detail and challenges and solutions were highlighted.

Table C.1: This table shows the ERA-Interim and NASA reanalysis variables used for the surface forcing files. The field (category of data) and variable name is displayed for each reanalysis. The corresponding NEMO variable is shown in the first column. The unit accompanying the NEMO variable (Madec, 2008) is the variable of the reanalysis data. The bottom table indicates the erroneous variables initially used for the simulations (noticeable from the units and height above sea level for the NEMO variables in the first column). The NCEP and JRA55 reanalysis variables are shown in Table C.2.

| **NEMO variables** | **Reanalysis Products** | |
|---|---|---|
| **Forcing Variable (unit)** | **ERA-Interim** Field:Variable | **NASA** Field:Variable |
| snow ($\mathrm{kg\,m^{-2}\,s^{-1}}$) | var144:sf_sfc | tavg1_2d_ocn_Nx:PRECSNOOCN |
| precipitation ($\mathrm{kg\,m^{-2}\,s^{-1}}$) | var228:tpf_hbl | tavg1_2d_ocn_Nx:RAINOCN |
| short wave radiation ($\mathrm{W\,m^{-2}}$) | var169:ssrd_sfc | tavg3_2d_chm_Fx:SWGDWN |
| long wave radiation ($\mathrm{W\,m^{-2}}$) | var175:strd_sfc | tavg3_2d_chm_Fx:LWGDWN |
| specific humidity at $2\mathrm{m}$ ($\%$) | var133:q_hbl | tavg3_2d_chm_Fx:QV2M |
| temperature at $2\mathrm{m}$ ($\mathrm{K}$) | var167:2t_sfc | tavg3_2d_chm_Fx:T2M |
| U-wind ($\mathrm{m\,s^{-1}}$) | var165:10u_sfc | tavg1_2d_ocn_Nx:U10M |
| V-wind ($\mathrm{m\,s^{-1}}$) | var166:10v_sfc | tavg1_2d_ocn_Nx:V10M |
| | | |
| **Initial (incorrect) variables chosen** | | |
| snow ($\mathrm{kg\,m^{-2}}$) | | |
| precipitation ($\mathrm{kg\,m^{-2}}$) | | |
| nett short wave radiation ($\mathrm{W\,m^{-2}}$) | | tavg1_2d_ocn_Nx:SWGNTWTR |
| nett long wave radiation ($\mathrm{W\,m^{-2}}$) | | tavg1_2d_ocn_Nx:LWGNTWTR |
| specific humidity at $10\mathrm{m}$ ($\mathrm{kg\,kg^{-1}}$) | | tavg1_2d_ocn_Nx:QV10M |
| temperature at $10\mathrm{m}$ ($\mathrm{K}$) | | tavg1_2d_ocn_Nx:T10M |
| U-wind ($\mathrm{m\,s^{-1}}$) | | |
| V-wind ($\mathrm{m\,s^{-1}}$) | | |

TABLE C.2: This table shows the NCEP and JRA55 reanalysis variables used for the surface forcing files. The field (category of data) and variable name is displayed for each reanalysis. The corresponding NEMO variable is shown in the first column. The unit accompanying the NEMO variable (Madec, 2008) is the variable of the reanalysis data. The bottom table indicates the erroneous variables initially used for the simulations (noticeable from the units and height above sea level for the NEMO variables in the first column). The ERA-Interim and NASA reanalysis variables are shown in Table C.1.

| **NEMO variables** | **Reanalysis Products** | |
|---|---|---|
| **Forcing Variable (unit)** | **NCEP** Field:Variable | **JRA55** Field:Variable |
| snow ($\mathrm{kg\,m^{-2}\,s^{-1}}$) | flx.ft06.2010[01-12]: SRWEQ_98_SFC_ave6h | fcst_phy2m125:srweqsfc |
| precipitation ($\mathrm{kg\,m^{-2}\,s^{-1}}$) | flx.ft06.2010[01-12]: PRATE_98_SFC_ave6h | fcst_phy2m125:tpratsfc |
| short wave radiation ($\mathrm{W\,m^{-2}}$) | flx.ft06.2010[01-12]: DSWRF_98_SFC_ave6h | fcst_phy2m125:dswrf |
| long wave radiation ($\mathrm{W\,m^{-2}}$) | flx.ft06.2010[01-12]: DLWRF_98_SFC_ave6h | fcst_phy2m125:dlwrf |
| specific humidity at $2\mathrm{m}$ ($\%$) | flx.ft06.2010[01-12]: SPFH_98_HTGL | anl_surf125:q |
| temperature at $2\mathrm{m}$ ($\mathrm{K}$) | flx.ft06.2010[01-12]: TMP_98_HTGL | anl_surf125:t |
| U-wind ($\mathrm{m\,s^{-1}}$) | flx.ft06.2010[01-12]: U_GRD_98_HTGL | anl_surf125:u |
| V-wind ($\mathrm{m\,s^{-1}}$) | flx.ft06.2010[01-12]: V_GRD_98_HTGL | anl_surf125:v |
| | | |
| **Initial (incorrect) variables chosen** | | |
| snow ($\mathrm{kg\,m^{-2}}$) | flx.ft06.2010[01-12]: WEASD_98_SFC | anl_land125:sf |
| precipitation ($\mathrm{kg\,m^{-2}}$) | flx.ft06.2010[01-12]: P_WAT_98_EATM | anl_column125:pwat |
| nett short wave radiation ($\mathrm{W\,m^{-2}}$) | | |
| nett long wave radiation ($\mathrm{W\,m^{-2}}$) | | |
| specific humidity at $10\mathrm{m}$ ($\mathrm{kg\,kg^{-1}}$) | | |
| temperature at $10\mathrm{m}$ ($\mathrm{K}$) | | |
| U-wind ($\mathrm{m\,s^{-1}}$) | | |
| V-wind ($\mathrm{m\,s^{-1}}$) | | |

# Appendix D

# Supplementary correlation tables

This appendix contains tables correlations as a supplement to the results chapter (Chapter 4). The first two correlation tables contain the correlations between turbulence schemes for various turbulence indicators per reanalysis. The last table of correlations contain the correlations between turbulence schemes and reanalysis for turbulent indicators. These indicators are correlated for the annual time series.

## D.1 Correlations between all turbulence schemes for an individual reanalysis

This appendix contains correlations as a supplement to the results chapter (Chapter 4). Tables D.1 and D.2 contain the correlations between turbulence schemes for the various turbulence indicators given a single reanalysis product.

TABLE D.1: Correlations of turbulent indicators between turbulence schemes for a given reanalysis. Turbulence indicators were correlated for 15 June 2010 - 14 June 2011 for 101 vertical levels results. $N^2$ was averaged down to 300 $\mathrm{m}$. This table is continued in Table D.2. The key is displayed in the first entry and explanation given below the table and is applicable to every entry.

| **Reanalysis/ Turbulence scheme** | $\mathbf{k}-\varepsilon$/ $\mathbf{k}-\omega$ | $\mathbf{k}-\varepsilon$/ **M-Y** | $\mathbf{k}-\varepsilon$/ **Generic** | $\mathbf{k}-\varepsilon$/ **TKE0** | $\mathbf{k}-\varepsilon$/ **TKE10** | $\mathbf{k}-\varepsilon$/ **TKE30** | $\mathbf{k}-\varepsilon$/ **P/P** | $\mathbf{k}-\omega$/ **M-Y** | $\mathbf{k}-\omega$/ **Generic** | $\mathbf{k}-\omega$/ **TKE0** | $\mathbf{k}-\omega$/ **TKE10** | $\mathbf{k}-\omega$/ **TKE30** | $\mathbf{k}-\omega$/ **P/P** | **M-Y/ Generic** |
|---|---|---|---|---|---|---|---|---|---|---|---|---|---|---|
| **NASA** | 1.000[a] | 1.000 | 1.000 | 1.000 | 1.000 | 0.999 | 1.000 | 1.000 | 1.000 | 1.000 | 1.000 | 0.999 | 0.999 | 1.000 |
| | 0.999[b] | 0.997 | 1.000 | 0.995 | 0.994 | 0.983 | 0.967 | 0.999 | 0.999 | 0.998 | 0.998 | 0.977 | 0.967 | 0.997 |
| | 1.000[c] | 0.999 | 1.000 | 0.999 | 1.000 | 0.996 | 0.997 | 1.000 | 1.000 | 1.000 | 1.000 | 0.994 | 0.996 | 0.999 |
| | 0.997[d] | 0.994 | 1.000 | 0.984 | 0.984 | 0.980 | 0.859 | 0.996 | 0.997 | 0.990 | 0.990 | 0.980 | 0.839 | 0.994 |
| **NCEP** | 1.000 | 1.000 | 1.000 | 0.999 | 0.999 | 1.000 | 1.000 | 1.000 | 1.000 | 1.000 | 1.000 | 0.999 | 0.999 | 1.000 |
| | 0.997 | 0.992 | 1.000 | 0.990 | 0.989 | 0.989 | 0.961 | 0.998 | 0.997 | 0.997 | 0.996 | 0.981 | 0.972 | 0.992 |
| | 1.000 | 0.999 | 1.000 | 0.998 | 0.999 | 0.998 | 0.997 | 0.999 | 1.000 | 0.999 | 1.000 | 0.997 | 0.997 | 0.999 |
| | 0.996 | 0.991 | 1.000 | 0.976 | 0.9754 | 0.974 | 0.872 | 0.994 | 0.996 | 0.981 | 0.981 | 0.976 | 0.866 | 0.991 |
| **JRA55** | 1.000 | 1.000 | 1.000 | 0.999 | 1.000 | 0.999 | 1.000 | 1.000 | 1.000 | 1.000 | 1.000 | 0.999 | 0.999 | 1.000 |
| | 0.997 | 0.994 | 1.000 | 0.985 | 0.987 | 0.984 | 0.981 | 0.999 | 0.997 | 0.994 | 0.995 | 0.980 | 0.985 | 0.994 |
| | 1.000 | 0.999 | 1.000 | 0.998 | 0.999 | 0.995 | 0.997 | 1.000 | 1.000 | 0.999 | 1.000 | 0.993 | 0.996 | 0.999 |
| | 0.998 | 0.994 | 1.000 | 0.983 | 0.984 | 0.977 | 0.896 | 0.997 | 0.998 | 0.990 | 0.990 | 0.979 | 0.886 | 0.994 |
| **ERA-Interim** | 1.000 | 1.000 | 1.000 | 0.999 | 1.000 | 1.000 | 1.000 | 1.000 | 1.000 | 1.000 | 1.000 | 0.999 | 0.999 | 1.000 |
| | 0.998 | 0.992 | 1.000 | 0.986 | 0.985 | 0.985 | 0.974 | 0.998 | 0.997 | 0.994 | 0.993 | 0.974 | 0.980 | 0.991 |
| | 1.000 | 0.999 | 1.000 | 0.998 | 0.999 | 0.994 | 0.997 | 0.999 | 1.000 | 0.999 | 1.000 | 0.992 | 0.996 | 0.999 |
| | 0.998 | 0.996 | 1.000 | 0.989 | 0.991 | 0.975 | 0.903 | 0.998 | 0.998 | 0.992 | 0.994 | 0.975 | 0.905 | 0.996 |

[a] Buoyancy flux

[b] $N^2$

[c] $\phi$

[d] $\frac{d\phi}{dt}$

TABLE D.2: Continuation of Table D.1. Correlations of turbulent indicators between turbulence schemes for a given reanalysis. All turbulence indicators correlated used the time series for 15 June 2010 - 14 June 2011 for 101 vertical levels results. $N^2$ was averaged down to 300 $\mathrm{m}$. The key is displayed in the first entry and explanation given below the table and is applicable to every entry.

| **Reanalysis/ Turbulence scheme** | **M-Y/ TKE0** | **M-Y/ TKE10** | **M-Y/ TKE30** | **M-Y/ P/P** | **Generic/ TKE0** | **Generic/ TKE10** | **Generic/ TKE30** | **Generic/ P/P** | **TKE0/ TKE10** | **TKE0/ TKE30** | **TKE0/ P/P** | **TKE10/ TKE30** | **TKE10/ P/P** | **TKE30/ P/P** |
|---|---|---|---|---|---|---|---|---|---|---|---|---|---|---|
| **NASA** | 1.000[a] | 1.000 | 0.998 | 0.999 | 1.000 | 1.000 | 0.999 | 1.000 | 1.000 | 0.998 | 0.999 | 0.998 | 0.999 | 0.999 |
| | 0.999[b] | 0.999 | 0.972 | 0.967 | 0.995 | 0.994 | 0.984 | 0.966 | 0.999 | 0.969 | 0.962 | 0.970 | 0.964 | 0.929 |
| | 1.000[c] | 1.000 | 0.992 | 0.994 | 0.999 | 1.000 | 0.996 | 0.997 | 1.000 | 0.990 | 0.993 | 0.993 | 0.995 | 0.998 |
| | 0.997[d] | 0.997 | 0.982 | 0.854 | 0.985 | 0.985 | 0.980 | 0.858 | 0.999 | 0.979 | 0.840 | 0.982 | 0.842 | 0.839 |
| **NCEP** | 1.000 | 1.000 | 0.999 | 0.999 | 0.999 | 0.999 | 1.000 | 1.000 | 1.000 | 0.998 | 0.998 | 0.998 | 0.998 | 1.000 |
| | 0.998 | 0.998 | 0.973 | 0.977 | 0.990 | 0.989 | 0.989 | 0.960 | 0.999 | 0.976 | 0.970 | 0.977 | 0.973 | 0.930 |
| | 1.000 | 1.000 | 0.995 | 0.995 | 0.998 | 0.999 | 0.984 | 0.997 | 1.000 | 0.994 | 0.994 | 0.995 | 0.995 | 0.997 |
| | 0.993 | 0.993 | 0.985 | 0.859 | 0.976 | 0.975 | 0.975 | 0.870 | 0.998 | 0.988 | 0.827 | 0.989 | 0.834 | 0.827 |
| **JRA55** | 1.000 | 1.000 | 0.998 | 0.999 | 0.999 | 1.000 | 0.999 | 1.000 | 1.000 | 0.997 | 0.998 | 0.998 | 0.999 | 1.000 |
| | 0.997 | 0.997 | 0.974 | 0.984 | 0.985 | 0.986 | 0.984 | 0.980 | 0.998 | 0.965 | 0.975 | 0.974 | 0.980 | 0.963 |
| | 1.000 | 1.000 | 0.991 | 0.994 | 0.998 | 0.999 | 0.995 | 0.997 | 1.000 | 0.988 | 0.992 | 0.991 | 0.994 | 0.997 |
| | 0.996 | 0.996 | 0.983 | 0.872 | 0.983 | 0.984 | 0.977 | 0.894 | 0.999 | 0.981 | 0.844 | 0.985 | 0.847 | 0.841 |
| **ERA-Interim** | 1.000 | 1.000 | 0.999 | 0.999 | 0.999 | 1.000 | 1.000 | 1.000 | 1.000 | 0.998 | 0.999 | 0.998 | 0.999 | 1.000 |
| | 0.998 | 0.998 | 0.962 | 0.982 | 0.985 | 0.984 | 0.985 | 0.972 | 0.998 | 0.954 | 0.977 | 0.956 | 0.979 | 0.943 |
| | 1.000 | 1.000 | 0.988 | 0.994 | 0.998 | 0.999 | 0.994 | 0.997 | 1.000 | 0.986 | 0.993 | 0.990 | 0.994 | 0.994 |
| | 0.995 | 0.997 | 0.978 | 0.896 | 0.989 | 0.991 | 0.976 | 0.902 | 0.998 | 0.969 | 0.881 | 0.979 | 0.880 | 0.860 |

[a] Buoyancy flux

[b] $N^2$

[c] $\phi$

[d] $\frac{d\phi}{dt}$

## D.2 Correlations between turbulence schemes and reanalysis for various turbulence indicators

TABLE D.3: Correlations for various reanalysis versus turbulence schemes for turbulence indicators. Turbulent indicators used time series data computed for period 15 June 2010 - 14 June 2011 for 101 vertical levels results. $N^2$ was averaged down to 300 $\mathrm{m}$. The key is displayed in the first entry and explanation given below the table and is applicable to every entry.

| **Reanalysis/scheme** | **k $-\,\varepsilon$** | **k $-\,\omega$** | **M-Y** | **Generic** | **TKE0** | **TKE10** | **TKE30** | **P/P** |
|---|---|---|---|---|---|---|---|---|
| **ERA-Interim** | 0.939[a]<br>0.740[b] | 0.945†‡<br>0.776 | 0.933†‡<br>0.807 | 0.941†<br>0.736 | 0.964†‡<br>0.814 | 0.952∗ † ‡<br>0.824 | 0.856∗ † ‡<br>0.653 | 0.867∗ † ‡<br>0.803 |
| **JRA55** | 0.900<br>0.608 | 0.897†<br>0.664 | 0.897†<br>0.672 | 0.894†<br>0.606 | 0.920†‡<br>0.696 | 0.952†‡<br>0.709 | 0.868†<br>0.612 | 0.838∗ † ‡<br>0.649 |
| **NASA** | 0.911†<br>0.854 | 0.906†<br>0.872 | 0.906†<br>0.880 | 0.907†<br>0.852 | 0.938†<br>0.888 | 0.958†<br>0.887 | 0.879†<br>0.751 | 0.836†‡<br>0.910 |
| **NCEP** | 0.882<br>0.759 | 0.879<br>0.800 | 0.886<br>0.825 | 0.879<br>0.755 | 0.898<br>0.835 | 0.922<br>0.838 | 0.864<br>0.704 | 0.880†<br>0.856 |

[a] MLD-Turbocline

[b] $\phi$-$N^2$

* Warm parcel present at start of deep mixing (1 April 2011)

† Warm parcel present during deep mixing (1 September 2011)

‡ Warm parcel present at start of stratification (1 November 2011)

# Appendix E

# Supplementary temperature and salinity results

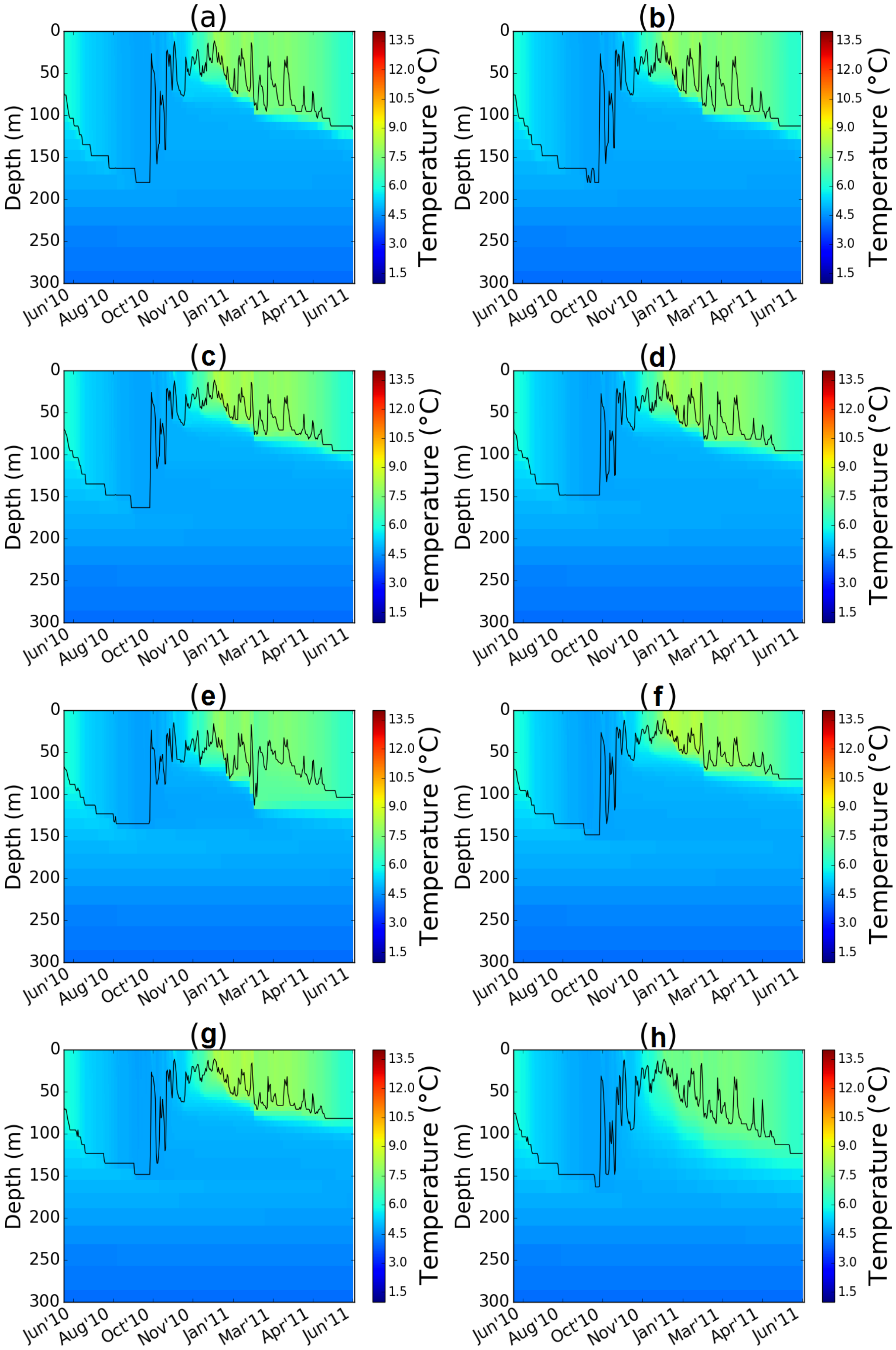

FIGURE E.1: The **temperature** column evolution results for ERA-Interim using (a) Generic, (b) $k-\varepsilon$, (c) M-Y, (d) $k-\omega$, (e) Pacanowski/Philander , (f) TKE0, (g) TKE10 and (h) TKE30. Simulations were performed for 15 June 2010 - 14 June 2011 using 101 vertical levels.

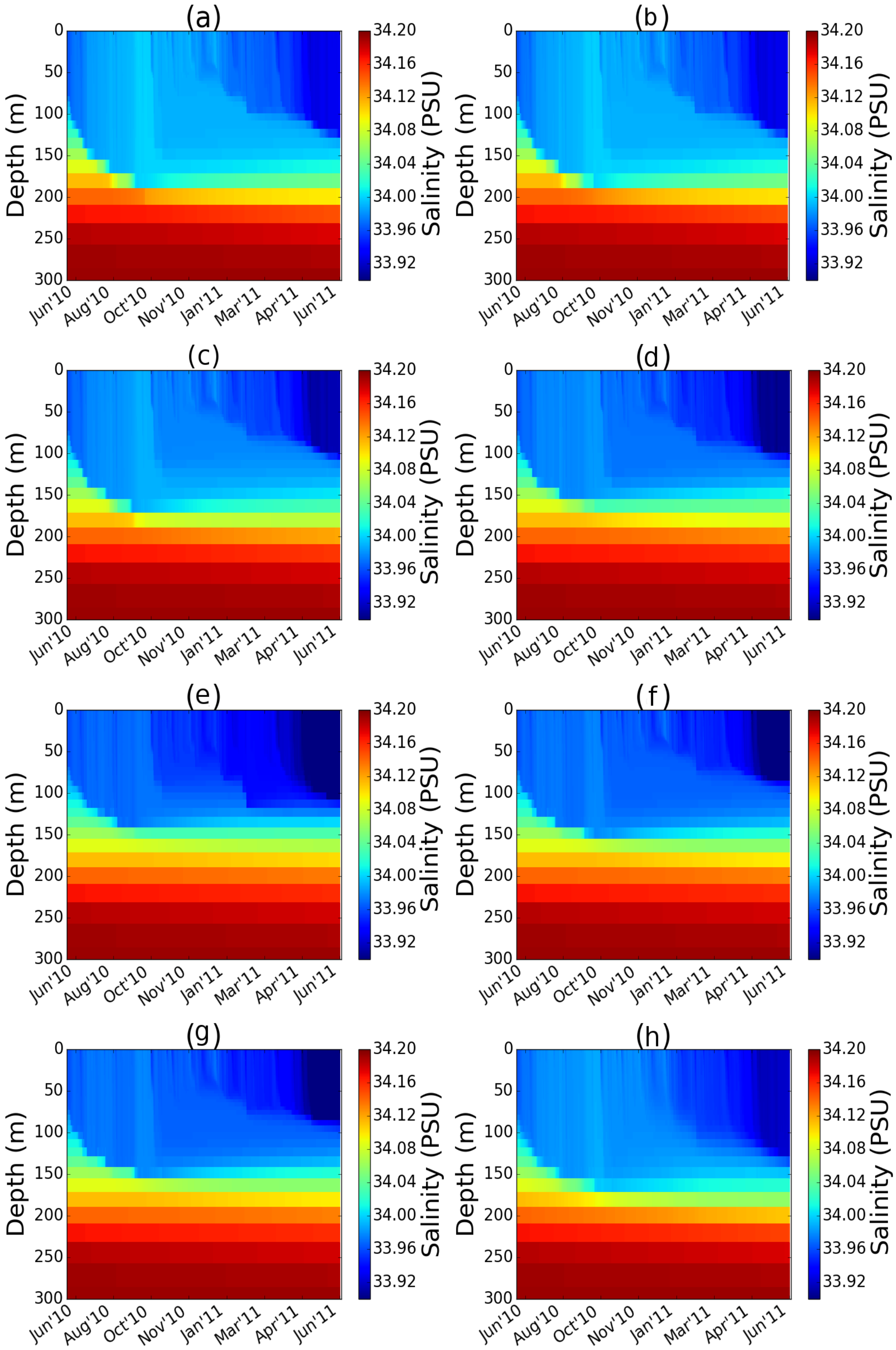

FIGURE E.2: The **salinity** column evolution results for ERA-Interim using (a) Generic, (b) $k - \varepsilon$, (c) M-Y, (d) $k - \omega$, (e) Pacanowski/Philander , (f) TKE0, (g) TKE10 and (h) TKE30.. Simulations were performed for 15 June 2010 - 14 June 2011 using 101 vertical levels.

# Bibliography

Ådlandsvik, B., E. Firing, and F. Fernandes (2014). *Gibbs SeaWater Oceanographic Package of TEOS-10*. Last visited on 29 March 2017. URL: `https://pypi.python.org/pypi/gsw/`.

Adcroft, A., J.-M. Campin, S. Dutkiewicz, C. Evangelinos, G. Ferreira D. Forget, B. Fox-Kemper, P. Heimbach, C. Hill, E. Hill, H. Hill, M. Jahn O. Losch, J. Marshall, G. Maze, D. Menemenlis, and A. Molod (2016). *MITgcm User Manual*. Last visited on 4 October 2016. pp 60. MIT Department of EAPS. URL: `http://mitgcm.org/public/r2_manual/latest/online_documents/manual.pdf`.

Allison, L. C., H. L. Johnson, D. P. Marshall, and D. R. Munday (2010). "Where do winds drive the Antarctic Circumpolar Current?" In: *Geophysical Research Letters* 37.12. DOI: `10.1029/2010GL043355`. URL: `http://dx.doi.org/10.1029/2010GL043355`.

Ansorge, I. J., E. A. Pakhomov, S. Kaehler, J. R. E. Lutjeharms, and J. V. Durgadoo (2010). "Physical and biological coupling in eddies in the lee of the South-West Indian Ridge". In: *Polar Biology* 33.6, pp. 747–759. DOI: `10.1007/s00300-009-0752-9`.

Arakawa, A. and V. R. Lamb (1977). "Computational design of the basic dynamical processes of the UCLA general circulation model". In: *Methods in Computational Physics* 17, pp. 173–265.

Arctic, Aker (2017). *S. A. Agulhas II*. Last visited on 20 September 2017. Aker Arctic The Ice Technology Partner. URL: `https://akerarctic.fi/en/references/built/s-agulhas-ii`.

ARGO (2017). *Argo float data and metadata from Global Data Assembly Centre (Argo GDAC)*. Last visited on 20 September 2017. SEANOE. URL: `http://doi.org/10.17882/42182`.

Badin, G., R. G. Williams, Z. Jing, and L. Wu (2013). "Water Mass Transformations in the Southern Ocean Diagnosed from Observations: Contrasting Effects of Air-Sea Fluxes and Diapycnal Mixing". In: *Journal of Physical Oceanography* 43.7, pp. 1472–1484. DOI: `10.1175/JPO-D-12-0216.1`.

Bernard, B., G. Madec, T. Penduff, J.-M. Molines, A.-M. Treguier, J. Le Sommer, A. Beckmann, A. Biastoch, C. Böning, J. Dengg, C. Derval, E. Durand, S. Gulev, E. Remy, C. Talandier, S. Theetten, M. Maltrud, J. McClean, and B. De Cuevas (2006). "Impact of partial steps and momentum advection schemes in a global ocean circulation model at eddy-permitting resolution". In: *Ocean Dynamics* 56.5, pp. 543–567. DOI: `10.1007/s10236-006-0082-1`.

Beuvier, J., C. L. Brossier, K. Béranger, T. Arsouze, R. Bourdallé-Badie, C. Deltel, Y. Drillet, P. Drobinski, N. Ferry, F. Lyard, F. Sevault, and S. Somot (2012). "MED12, oceanic component for the modeling of the regional Mediterranean Earth System". In: *Mercator Ocean Quarterly Newsletter*.

Biastoch, A., C. W. Böning, and J. R. E. Lutjeharms (2008). "Agulhas leakage dynamics affects decadal variability in Atlantic overturning circulation". In: *Nature* 456, p. 489. URL: `http://dx.doi.org/10.1038/nature07426`.

Blanke, B. and P. Delecluse (1993). "Variability of the Tropical Atlantic Ocean Simulated by a General Circulation Model with Two Different Mixed-Layer Physics". In: *Journal of Physical Oceanography* 23.7, pp. 1363–1388. DOI: `10.1175/1520-0485(1993)023<1363:VOTTAO>2.0.CO;2`.

Boer, G. J. de, J. D. Pietrzak, and J. C. Winterwerp (2008). "Using the potential energy anomaly equation to investigate tidal straining and advection of stratification in a region of freshwater influence". In: *Ocean Modelling* 22.1-2, pp. 1–11. DOI: `http://doi.org/10.1016/j.ocemod.2007.12.003`.

Boyer, T.P., J. I. Antonov, O. K. Baranova, C. L. Coleman, H. E. Garcia, A. I. Grodsky, D. R. Johnson, R. A. Locarnini, A. V. Mishonov, T. D. O'Brien, C. R. Paver, J. R. Reagan, D. Seidov, I. V. Smolyar, M. M. Zweng, S. Levitus, and A. Mishonov (2013). "World Ocean Database 2013". In: *NOAA Atlas NESDIS Technical Edition Silver Spring, MD*, p. 209. DOI: `http://doi.org/10.7289/V5NZ85MT`.

Bryan, K. (1969). “A numerical method for the study of the circulation of the world ocean”. In: *Journal of Computational Physics* 4.3, pp. 347–376. DOI: `10.1016/0021-9991(69)90004-7`.

Burchard, H. and K. Bolding (2001). “Comparative Analysis of Four Second-Moment Turbulence Closure Models for the Oceanic Mixed Layer”. In: *Journal of Physical Oceanography* 31.8, pp. 1943–1968. DOI: `10.1175/1520-0485(2001)031<1943:CAOFSM>2.0.CO;2`.

Burchard, H. and R. Hofmeister (2008). “A dynamic equation for the potential energy anomaly for analysing mixing and stratification in estuaries and coastal seas”. In: *Estuarine, Coastal and Shelf Science* 77.4, pp. 679–687. DOI: `https://doi.org/10.1016/j.ecss.2007.10.025`.

Canuto, V. M., A. Howard, Y. Cheng, and M. S. Dubovikov (2001). “Ocean Turbulence. Part I: One-Point Closure Model-Momentum and Heat Vertical Diffusivities”. In: *Journal of Physical Oceanography* 31.6, pp. 1413–1426. DOI: `10.1175/1520-0485(2001)031<1413:OTPIOP>2.0.CO;2`.

CCI, ESA (2017). *Ocean Colour CCI*. Last visited on 8 February 2017. European Space Agency. URL: `http://www.esa-oceancolour-cci.org/?q=project`.

CeCILL (2017). *Cea Cnrs Inria Logiciel Libre License, version 2.1 (CECILL-2.1)*. Last visited on 23 October 2017. CEA, CNRS and INRIA. URL: `https://opensource.org/licenses/CECILL-2.1`.

COMSOL (2017). *The Boussinesq Approximation*. Last visited on 15 June 2017. COMSOL. URL: `https://www.comsol.com/multiphysics/boussinesq-approximation`.

Cronin, M. F. and J. Sprintall (2009). “Wind and buoyancy-forced upper ocean”. In: *Elements of Physical Oceanography: A derivative of the Encyclopedia of Ocean Sciences*, pp. 237–245.

Cummins, P. F. (1991). “The deep water stratification of ocean general circulation models”. In: *Atmosphere-Ocean* 29.3, pp. 563–575. DOI: `10.1080/07055900.1991.9649417`.

Davis, R. E. (1991). “Observing the general circulation with floats”. In: *Deep Sea Research Part A. Oceanographic Research Papers* 38.1, pp. 531–571. ISSN: 0198-0149. DOI: `https://doi.org/10.1016/S0198-0149(12)80023-9`.

Davis, R. E., J. T. Sherman, and J. Dufour (2001). “Profiling ALACEs and Other Advances in Autonomous Subsurface Floats”. In: *Journal of Atmospheric and Oceanic Technology* 18.6, pp. 982–993. DOI: `10.1175/1520-0426(2001)018<0982:PAAOAI>2.0.CO;2`.

De Boyer-Montégut, C., G. Madec, A. S. Fischer, A. Lazar, and D. Iudicone (2004). “Mixed layer depth over the global ocean: An examination of profile data and a profile-based climatology”. In: *Journal of Geophysical Research: Oceans* 109.12. DOI: `10.1029/2004JC002378`.

Dee, D. P., S. M. Uppala, A. J. Simmons, P. Berrisford, P. Poli, S. Kobayashi, U. Andrae, M. A. Balmaseda, G. Balsamo, P. Bauer, P. Bechtold, A. C. M. Beljaars, L. van de Berg, J. Bidlot, N. Bormann, C. Delsol, R. Dragani, M. Fuentes, A. J. Geer, L. Haimberger, S. B. Healy, H. Hersbach, E. V. Hólm, L. Isaksen, P. Kållberg, M. Köhler, M. Matricardi, A. P. McNally, B. M. Monge-Sanz, J.-J. Morcrette, B.-K. Park, C. Peubey, P. de Rosnay, C. Tavolato, J.-N. Thépaut, and F. Vitart (2011). “The ERA-Interim reanalysis: configuration and performance of the data assimilation system.” In: *Quarterly Journal of the Royal Meteorological Society* 137, pp. 553–597. DOI: `10.1002/qj.828`.

Dutay, J.-C, J. L. Bullister, S. C. Doney, J. C. Orr, R. Najjar, K. Caldeira, J.-M. Campin, H. Drange, M. Follows, Y. Gao, N. Gruber, M. W. Hecht, A. Ishida, F. Joos, K. Lindsay, G. Madec, E. Maier-Reimer, J. C. Marshall, R. J. Matear, P. Monfray, A. Mouchet, G.-K. Plattner, J. Sarmiento, R. Schlitzer, R. Slater, I. J. Totterdell, M.-F Weirig, Y. Yamanaka, and A. Yool (2002). “Evaluation of ocean model ventilation with CFC-11: comparison of 13 global ocean models”. In: *Ocean Modelling* 4.2, pp. 89–120. DOI: `http://dx.doi.org/10.1016/S1463-5003(01)00013-0`.

Foken, T. (2006). “50 Years of the Monin-Obukhov Similarity Theory”. In: *Boundary-Layer Meteorology* 119.3, pp. 431–447. ISSN: 1573-1472. DOI: `10.1007/s10546-006-9048-6`. URL: `https://doi.org/10.1007/s10546-006-9048-6`.

Franks, P. J. S. (2015). “Has Sverdrup’s critical depth hypothesis been tested? Mixed layers vs. turbulent layers”. In: *ICES Journal of Marine Science* 72.6, p. 1897. DOI: `10.1093/icesjms/fsu175`.

Frants, M., G. M. Damerell, S. T. Gille, K. J. Heywood, J. MacKinnon, and J. Sprintall (2013). “An Assessment of Density-Based Finescale Methods for Estimating Diapycnal Diffusivity in the Southern Ocean”. In: *Journal of Atmospheric and Oceanic Technology* 30.11, pp. 2647–2661. DOI: `10.1175/JTECH-D-12-00241.1`.

Garabato, A. C. N., K. L. Polzin, B. A. King, K. J. Heywood, and M. Visbeck (2004). "Widespread Intense Turbulent Mixing in the Southern Ocean". In: *Science* 303.5655, pp. 210–213. ISSN: 0036-8075. DOI: 10.1126/science.1090929.

Garabato, A. C. N., K. L. Polzin, R. Ferrari, J. D. Zika, and A. Forryan (2016). "A Microscale View of Mixing and Overturning across the Antarctic Circumpolar Current". In: *Journal of Physical Oceanography* 46.1, pp. 233–254. DOI: 10.1175/JPO-D-15-0025.1.

Gaspar, P. (1988). "Modeling the Seasonal Cycle of the Upper Ocean". In: *Journal of Physical Oceanography* 18.2, pp. 161–180. DOI: 10.1175/1520-0485(1988)018<0161:MTSCOT>2.0.CO;2.

GEBCO (2016). *General Bathymetric Chart of the Oceans*. Last visited on 18 April 2017. British Oceanographic Data Centre. URL: http://www.gebco.net/.

Gehlen, M., R. Barciela, L. Bertino, P. Brasseur, M. Butenschön, F. Chai, A. Crise, Y. Drillet, D. Ford, D. Lavoie, P. Lehodey, C. Perruche, A. Samuelsen, and E. Simon (2015). "Building the capacity for forecasting marine biogeochemistry and ecosystems: recent advances and future developments". In: *Journal of Operational Oceanography* 8.1, pp. 168–187. DOI: 10.1080/1755876X.2015.1022350.

Gent, P. R. and J. C. Mcwilliams (1990). "Isopycnal Mixing in Ocean Circulation Models". In: *Journal of Physical Oceanography* 20.1, pp. 150–155. DOI: 10.1175/1520-0485(1990)020<0150:IMIOCM>2.0.CO;2.

Gent, Peter R. (2011). "The Gent-McWilliams parameterization: 20/20 hindsight". In: *Ocean Modelling* 39.1, pp. 2–9. DOI: 10.1016/j.ocemod.2010.08.002.

GFDL (2016). *MOM*. Last visited on 3 October 2016. Geophysical Fluid Dynamics Laboratory. URL: https://www.gfdl.noaa.gov/mom-ocean-model/.

— (2017). *Ocean Mixing*. Last visited on 8 April 2017. Geophysical Fluid Dynamics Laboratory. URL: https://www.gfdl.noaa.gov/mom-ocean-model/.

Ghosal, S., M. Rogers, and A. Wray (2000). "The turbulent life of phytoplankton". In: *Center for Turbulence Research Proceeding of the Summer Program*, pp. 31–45.

Gill, A. E. (1982). *Chapter Two - Transfer of Properties between Atmosphere and Ocean*. Ed. by W. L. Donn. Vol. 30. Academic Press, pp. 19–38. DOI: https://doi.org/10.1016/S0074-6142(08)60027-3.

Gordon, A. L. and B. A. Huber (1995). "Warm Weddell Deep Water west of Maud Rise". In: *Journal of Geophysical Research: Oceans* 100.C7, pp. 13747–13753. DOI: 10.1029/95JC01361.

Gregg, M. C. (1987). "Diapycnal mixing in the thermocline: A review". In: *Journal of Geophysical Research: Oceans* 92.C5, pp. 5249–5286. ISSN: 2156-2202. DOI: 10.1029/JC092iC05p05249.

Griffies, S. M. and A. J. Adcroft (2013). "Formulating the Equations of Ocean Models". In: *Ocean Modeling in an Eddying Regime*. American Geophysical Union, pp. 281–317. ISBN: 9781118666432. DOI: 10.1029/177GM18.

Helber, R. W., A. B. Kara, J. G. Richman, M. R. Carnes, C. N. Barron, H. E. Hurlburt, and T. Boyer (2012). "Temperature versus salinity gradients below the ocean mixed layer". In: *Journal of Geophysical Research: Oceans* 117.C5. DOI: 10.1029/2011JC007382.

Hibiya, T., M. Nagasawa, and Y. Niwa (2002). "Nonlinear energy transfer within the oceanic internal wave spectrum at mid and high latitudes". In: *Journal of Geophysical Research: Oceans* 107.C11. 3207, pp. 1–8. ISSN: 2156-2202. DOI: 10.1029/2001JC001210.

Hinsley, W. R. (2005). *Planktonica: A system for doing biological oceanography by computer*. University of London.

Holt, J., P. Hyder, M. Ashworth, J. Harle, H. T. Hewitt, H. Liu, A. L. New, S. Pickles, A. Porter, and E. Popova (2017). "Prospects for improving the representation of coastal and shelf seas in global ocean models". In: *Geoscientific Model Development* 10.1, p. 499.

Huang, C. J., F. Qiao, and D. Dai (2014). "Evaluating CMIP5 simulations of mixed layer depth during summer". In: *Journal of Geophysical Research: Oceans* 119.4, pp. 2568–2582. ISSN: 2169-9291. DOI: 10.1002/2013JC009535.

HYCOM (2016). *HYCOM + NCODA Global 1/12° Analysis (GLBa0.08\expt_91.2)*. Last visited on 4 October 2016. Center for Ocean-Atmospheric Prediction Studies (COAPS). URL: https://hycom.org/data/glba0pt08/expt-91pt2.

Ito, T. and J. Marshall (2008). "Control of Lower-Limb Overturning Circulation in the Southern Ocean by Diapycnal Mixing and Mesoscale Eddy Transfer". In: *Journal of Physical Oceanography* 38.12, pp. 2832–2845. DOI: `10.1175/2008JPO3878.1`.

Jackson, J. M., S. E. Allen, F. A. McLaughlin, R. A. Woodgate, and E. C. Carmack (2011). "Changes to the near-surface waters in the Canada Basin, Arctic Ocean from 1993-2009: A basin in transition". In: *Journal of Geophysical Research: Oceans* 116.C10. ISSN: 2156-2202. DOI: `10.1029/2011JC007069`.

Jochum, M. (2009). "Impact of latitudinal variations in vertical diffusivity on climate simulations". In: *Journal of Geophysical Research: Oceans* 114.C1. C01010. ISSN: 2156-2202. DOI: `10.1029/2008JC005030`.

JRA55 (2017). *Japanese 55-year Reanalysis*. Last visited on 11 February 2017. Japan Meteorological Agency (JMA). URL: `http://jra.kishou.go.jp/JRA-55/index_en.html`.

Kanamitsu, M., W. Ebisuzaki, J. Woollen, S.-K. Yang, J. J. Hnilo, M. Fiorino, and G. L. Potter (2017). "National Center for Environmental Prediction (NCEP)/DOE AMIP-II Reanalysis (R-2)". In: *Bulletin of the American Meteorological Society* 83.11. Last visited on 11 February 2017., pp. 1631–1643. DOI: `10.1175/BAMS-83-11-1631`.

Kato, H. and O. M. Phillips (1969). "On the penetration of a turbulent layer into stratified fluid". In: *Journal of Fluid Mechanics* 37.04, pp. 643–655. DOI: `10.1017/s0022112069000784`.

Kawamura, H., H. Abe, and Y. Matsuo (1999). "DNS of turbulent heat transfer in channel flow with respect to Reynolds and Prandtl number effects". In: *International Journal of Heat and Fluid Flow* 20.3, pp. 196–207. DOI: `http://dx.doi.org/10.1016/S0142-727X(99)00014-4`.

Kolmogorov, A. N. (1941). "Dissipation of energy in locally isotropic turbulence". In: *Mathematical and Physical Sciences*. Vol. 32. 1, pp. 16–18.

Lenn, Y.-D. and T. K. Chereskin (2009). "Observations of Ekman currents in the Southern Ocean". In: *Journal of Physical Oceanography* 39.3, pp. 768–779. DOI: `http://dx.doi.org/10.1175/2008JPO3943.1`.

Leung, P.-T. and C. H. Gibson (2004). "Turbulence and fossil turbulence in oceans and lakes". In: *Chinese Journal of Oceanology and Limnology* 22.1, pp. 1–23. ISSN: 1993-5005. DOI: `10.1007/BF02842796`. URL: `https://doi.org/10.1007/BF02842796`.

Levitus, S., J. I. Antonov, O. K. Baranova, T. P. Boyer, C. L. Coleman, H. E. Garcia, A. I. Grodsky, D. R. Johnson, R. A. Locarnini, A. V. Mishonov, J. R. Reagan, C. L. Sazama, D. Seidov, I. Smolyar, E. S. Yarosh, and M. M. Zweng (2013). "The World Ocean Database". In: *Data Science Journal* 12. DOI: `http://doi.org/10.2481/dsj.WDS-041`.

Li, X., Y. Chao, J. C. McWilliams, and L.-L. Fu (2001). "A Comparison of Two Vertical-Mixing Schemes in a Pacific Ocean General Circulation Model". In: *Journal of Climate* 14.7, pp. 1377–1398. DOI: `10.1175/1520-0442(2001)014<1377:ACOTVM>2.0.CO;2`.

Lovato, T., M. Vichi, and P. Oddo (2013). "High-resolution simulations of Mediterranean Sea physical oceanography under current and scenario climate conditions: model description, assessment and scenario analysis". In: *CMCC Research Paper* 207. DOI: `http://dx.doi.org/10.2139/ssrn.2637861`.

Madec, G. (2008). *NEMO Ocean engine Manual*. Last visited on 29 September 2016. Note du Pôle de modélisation, Institut Pierre-Simon Laplace (IPSL). URL: `http://www.nemo-ocean.eu/`.

Marsland, S. J., H. Haak, J. H. Jungclaus, M. Latif, and F. Röske (2003). "The Max-Planck-Institute global ocean/sea ice model with orthogonal curvilinear coordinates". In: *Ocean Modelling* 5.2, pp. 91–127. DOI: `http://dx.doi.org/10.1016/S1463-5003(02)00015-X`.

Martin, M. J., M. Balmaseda, L. Bertino, P. Brasseur, G. Brassington, J. Cummings, Y. Fujii, D. J. Lea, J.-M. Lellouche, K. Mogensen, P. R. Oke, G. C. Smith, C.-E. Testut, G. A. Waagbø, J. Waters, and A. T. Weaver (2015). "Status and future of data assimilation in operational oceanography". In: *Journal of Operational Oceanography* 8.1, pp. 28–48. DOI: `10.1080/1755876X.2015.1022055`.

McClain, C. R., G. C. Feldman, and S. B. Hooker (2004). "An overview of the SeaWiFS project and strategies for producing a climate research quality global ocean bio-optical time series". In: *Deep Sea Research Part II: Topical Studies in Oceanography* 51.1-3. Views of Ocean Processes from the Sea-viewing Wide Field-of-view Sensor (SeaWiFS) Mission: Volume 1, pp. 5–42. DOI: `http://dx.doi.org/10.1016/j.dsr2.2003.11.001`.

McKiver, W. J., M. Vichi, T. Lovato, A. Storto, and S. Masina (2015). “Impact of increased grid resolution on global marine biogeochemistry”. In: *Journal of Marine Systems* 147, pp. 153–168. DOI: `https://doi.org/10.1016/j.jmarsys.2014.10.003`.

Mellor, G. L. and T. Yamada (1982). “Development of a turbulence closure model for geophysical fluid problems”. In: *Reviews of Geophysics* 20.4, pp. 851–875. DOI: `10.1029/RG020i004p00851`.

Mercator, Editorial team, ed. (2008). *MERCATOR Quarterly Newsletter* 31. Last visited on 4 April 2017. URL: `https://www.mercator-ocean.fr/wp-content/uploads/2015/06/lettre_31_en.pdf#page=13`.

Mishonov, A. V. (2017). *World Ocean Atlas 2013 (WOA13)*. Last visited on 22 May 2017. NCAR. URL: `https://climatedataguide.ucar.edu/climate-data/world-ocean-atlas-2013-woa13`.

Mongwe, P., N. Chang, and P. M. S. Monteiro (2016). “The seasonal cycle as a mode to diagnose biases in modelled CO2 fluxes in the Southern Ocean”. In: *Ocean Modelling* 106.C, pp. 90–103. DOI: `https://doi.org/10.1016/j.ocemod.2016.09.006`.

Monin, A. S., V. M. Kamenkovich, and V. G. Kort (1978). “Variability of the Oceans.” In: *Journal of Fluid Mechanics* 85.3, pp. 607–607. DOI: `10.1017/S0022112078210816`.

Namin, M. M., A. A. Bidokhti, and A. K. Khaniki (2017). “Estimation of turbulence parameters in a shallow sea using numerical simulation with sensitivity to vertical mixing parameterization”. In: *Indian Journal of Geo-Marine Sciences*, pp. 1788–1798.

NASA (2017). *Goddard Earth Sciences Data and Information Services Center (GES DISC)*. Last visited on 11 February 2017. National Aeronautics and Space Administration (NASA). URL: `https://disc.sci.gsfc.nasa.gov/daac-bin/FTPSubset.pl`.

Navier, C.-L. (1823). “Mémoire sur les lois du mouvement des fluides”. In: *Memoire Academic Sciences Institute of France* 6.1823, pp. 389–416.

NCAR (2017). *Atmospheric Reanalysis: Overview & Comparison Tables*. Last visited on 17 May 2017. National Center for Atmospheric Research. URL: `https://climatedataguide.ucar.edu/climate-data/atmospheric-reanalysis-overview-comparison-tables`.

NOAA (2016). *Ocean Station Papa*. Last visited on 29 September 2016. National Oceanic, Atmospheric Administration (NOAA), and United States Department of Commerce. URL: `http://www.pmel.noaa.gov/ocs/Papa`.

Oddo, P., M. Adani, N. Pinardi, C. Fratianni, M. Tonani, and D. Pettenuzzo (2009). “A nested Atlantic-Mediterranean Sea general circulation model for operational forecasting”. In: *Ocean science* 5. DOI: `http://hdl.handle.net/2122/5761`.

Optis, M. and A. Monahan (2017). “A Comparison of Equilibrium and Time-Evolving Approaches to Modeling the Wind Profile under Stable Stratification”. In: *Journal of Applied Meteorology and Climatology* 56.5, pp. 1365–1382. DOI: `10.1175/JAMC-D-16-0324.1`.

Pacanowski, R. C. and S. G. H. Philander (1981). “Parameterization of vertical mixing in numerical models of tropical oceans”. In: *Journal of Physical Oceanography* 11.11, pp. 1443–1451.

Peters, F. and C. Marrasé (2000). “Effects of turbulence on plankton: an overview of experimental evidence and some theoretical considerations”. In: *Marine Ecology Progress Series* 205, pp. 291–306. DOI: `10.3354/meps205291`.

Peters, H., M. C. Gregg, and J. M. Toole (1988). “On the parameterization of equatorial turbulence”. In: *Journal of Geophysical Research: Oceans* 93.C2, pp 1199–1218. DOI: `10.1029/JC093iC02p01199`.

Preston-Thomas, H. (1990). “The International Temperature Scale of 1990 (ITS-90)”. In: *Metrologia* 27.1, p. 3.

Reffray, G., R. Bourdalle-Badie, and C. Calone (2015). “Modelling turbulent vertical mixing sensitivity using a 1-D version of NEMO.” In: *Geoscience Model Development* 8, pp 69–86. DOI: `10.5194/gmd-8-69-2015`.

Rintoul, S. R. and T. W. Trull (2001). “Seasonal evolution of the mixed layer in the Subantarctic zone south of Australia”. In: *Journal of Geophysical Research: Oceans* 106.C12, pp. 31447–31462. ISSN: 2156-2202. DOI: `10.1029/2000JC000329`.

Robertson (2007). *Regional Ocean Modeling System (ROMS)*. Last visited on 4 October 2016. WikiROMS. URL: `https://www.myroms.org/wiki/Regional_Ocean_Modeling_System_(ROMS)`.

Rodi, W. (1987). "Examples of calculation methods for flow and mixing in stratified fluids". In: *Journal of Geophysical Research: Oceans* 92.C5, pp. 5305–5328. DOI: 10.1029/JC092iC05p05305.

Sallée, J.-B., R. Morrow, and K. Speer (2008). "Eddy heat diffusion and Subantarctic Mode Water formation". In: *Geophysical Research Letters* 35.5. L05607. ISSN: 1944-8007. DOI: 10.1029/2007GL032827.

Sallée, J.-B., K. Speer, S. Rintoul, and S. Wijffels (2010). "Southern Ocean thermocline ventilation". In: *Journal of Physical Oceanography* 40.3, pp. 509–529. DOI: http://dx.doi.org/10.1175/2009JPO4291.1.

Sallée, J.-B., E. Shuckburgh, N. Bruneau, A. J. S. Meijers, T. J. Bracegirdle, and Z. Wang (2013). "Assessment of Southern Ocean mixed-layer depths in CMIP5 models: Historical bias and forcing response". In: *Journal of Geophysical Research: Oceans* 118.4, pp. 1845–1862. ISSN: 2169-9291. DOI: 10.1002/jgrc.20157.

Sathiyamoorthy, S. and G. W. K. Moore (2002). "Buoyancy Flux at Ocean Weather Station Bravo". In: *Journal of Physical Oceanography* 32.2, pp. 458–474. DOI: 10.1175/1520-0485(2002)032<0458:BFAOWS>2.0.CO;2.

Sheen, K. L., J. A. Brearley, A. C. N. Garabato, D. A. Smeed, S. Waterman, J. R. Ledwell, M. P. Meredith, L. St. Laurent, A. M. Thurnherr, J. M. Toole, and A. J. Watson (2013). "Rates and mechanisms of turbulent dissipation and mixing in the Southern Ocean: Results from the Diapycnal and Isopycnal Mixing Experiment in the Southern Ocean (DIMES)". In: *Journal of Geophysical Research Oceans* 118.6, pp. 2774–2792. ISSN: 2169-9291.

Simpson, J. H. and D. Bowers (1981). "Models of stratification and frontal movement in shelf seas". In: *Deep Sea Research Part A. Oceanographic Research Papers* 28.7, pp. 727–738. DOI: http://dx.doi.org/10.1016/0198-0149(81)90132-1.

Sloyan, B. M., L. D. Talley, T. K. Chereskin, R. Fine, and J. Holte (2010). "Antarctic Intermediate Water and Subantarctic Mode Water Formation in the Southeast Pacific: The Role of Turbulent Mixing". In: *Journal of Physical Oceanography* 40.7, pp. 1558–1574. DOI: 10.1175/2010JPO4114.1.

Smith, K. M., P. E. Hamlington, and B. Fox-Kemper (2016). "Effects of submesoscale turbulence on ocean tracers". In: *Journal of Geophysical Research: Oceans* 121.1, pp. 908–933. DOI: 10.1002/2015JC011089.

Smith, R., P. Jones, B. Briegleb, F. Bryan, G. Danabasoglu, J. Dennis, J. Dukowicz, C. Eden, B. Fox-Kemper, P. Gent, M. Hecht, S. Jayne, M. Jochum, W. Large, K. Lindsay, M. Maltrud, N. Norton, S. Peacock, M. Vertenstein, and S. Yeager (2010). *The Parallel Ocean Program (POP): Reference Manual*. Last visited on 3 October 2016. URL: http://www.cesm.ucar.edu/models/cesm1.0/pop2/doc/sci/POPRefManual.pdf.

Soontiens, N. and S. E. Allen (2017). "Modelling sensitivities to mixing and advection in a sill-basin estuarine system". In: *Ocean Modelling* 112. DOI: http://dx.doi.org/10.1016/j.ocemod.2017.02.008.

St. Laurent, L., A. C. Naveira Garabato, J. R. Ledwell, A. M. Thurnherr, J. M. Toole, and A. J. Watson (2012). "Turbulence and Diapycnal Mixing in Drake Passage". In: *Journal of Physical Oceanography* 42.12, pp. 2143–2152. DOI: 10.1175/JPO-D-12-027.1.

Stammer, D., R. Tokmakian, A. Semtner, and C. Wunsch (1996). "How well does a $\frac{1}{4}^\circ$ global circulation model simulate large-scale oceanic observations?" In: *Journal of Geophysical Research: Oceans* 101.C11, pp. 25779–25811. DOI: 10.1029/96JC01754.

Steele, J. H., S. A. Thorpe, and K. K. Turekian (2009). *Elements of Physical Oceanography: A derivative of the Encyclopedia of Ocean Sciences*. Elsevier Science. ISBN: 9780123757210.

Steele, M., W. Ermold, and J. Zhang (2011). "Modeling the formation and fate of the near-surface temperature maximum in the Canadian Basin of the Arctic Ocean". In: *Journal of Geophysical Research: Oceans* 116.C11. ISSN: 2156-2202. DOI: 10.1029/2010JC006803.

Sutherland, G., B. Ward, and K. H. Christensen (2013). "Wave-turbulence scaling in the ocean mixed layer". In: *Ocean Science* 9.4, p. 597. DOI: 10.5194/os-9-597-2013.

Swart, S., S. J. Thomalla, and P. M. S. Monteiro (2015). "The seasonal cycle of mixed layer dynamics and phytoplankton biomass in the Sub-Antarctic Zone: A high-resolution glider experiment". In:

*Journal of Marine Systems* 147, pp. 103–115. DOI: `https://doi.org/10.1016/j.jmarsys.2014.06.002`.

Talley, L. D., G. L. Pickard, W. J. Emery, and J. H. Swift (2011a). "Chapter 13 - Southern Ocean". In: *Descriptive Physical Oceanography (Sixth Edition)*. Ed. by L. D. Talley, G. L. Pickard, W. J. E., and J. H. Swift. Sixth Edition. Boston: Academic Press, pp. 437–471. ISBN: 978-0-7506-4552-2. DOI: `http://dx.doi.org/10.1016/B978-0-7506-4552-2.10013-7`.

— (2011b). *Descriptive Physical Oceanography: An Introduction*. 6th ed. ELSEVIER.

Tang, H. S. and X. G. Wu (2010). "CFD and GFD Hybrid Approach for Simulation of Multi-Scale Coastal Ocean Flow". In: *International Congress on Environmental Modelling and Software*. Vol. 454. International Congress on Environmental Modelling and Software.

TEOS (2010). *The international thermodynamic equation of seawater - 2010: Calculation and use of thermodynamic properties*. Vol. 56. IOC, SCOR, IAPSO, Intergovernmental Oceanographic Commission, Manuals, and Guides.

Thompson, A. F., S. T. Gille, J. A. MacKinnon, and J. Sprintall (2007). "Spatial and Temporal Patterns of Small-Scale Mixing in Drake Passage". In: *Journal of Physical Oceanography* 37.3, pp. 572–592. DOI: `10.1175/JPO3021.1`.

Thorpe, S. A. (1973). "Experiments on instability and turbulence in a stratified shear flow". In: *Journal of Fluid Mechanics* 61.4, pp. 731–751. DOI: `10.1017/S0022112073000911`.

— (2007). *An Introduction to Ocean Turbulence*. Cambridge University Press. ISBN: 9781139467810.

Timmermann, R. and A. Beckmann (2004). "Parameterization of vertical mixing in the Weddell Sea". In: *Ocean Modelling* 6.1, pp. 83–100. ISSN: 1463-5003. DOI: `http://dx.doi.org/10.1016/S1463-5003(02)00061-6`.

Tominaga, Y. and T. Stathopoulos (2007). "Turbulent Schmidt numbers for CFD analysis with various types of flowfield". In: *Atmospheric Environment* 41.37, pp. 8091–8099. DOI: `http://dx.doi.org/10.1016/j.atmosenv.2007.06.054`.

Tonani, M., M. Balmaseda, L. Bertino, E. Blockley, G. Brassington, F. Davidson, Y. Drillet, P. Hogan, T. Kuragano, T. Lee, A. Mehra, F. Paranathara, C. A. S. TaTanajura, and H. Wang (2015). "Status and future of global and regional ocean prediction systems". In: *Journal of Operational Oceanography* 8.sup2, s201–s220. DOI: `10.1080/1755876X.2015.1049892`.

Turner, J. S. (1973). *Buoyancy effects in fluids*. Cambridge University Press.

Umlauf, L. and H. Burchard (2003). "A generic length-scale equation for geophysical turbulence models". In: *Journal of Marine Research* 61.2, pp. 235–265. DOI: `10.1357/002224003322005087`.

Versteeg, H. K. and W. Malalasekera (2007). *An Introduction to Computational Fluid Dynamics: The Finite Volume Method*. Pearson Education Limited. ISBN: 9780131274983.

Walsh, K., P. Govekar, A. V. Babanin, M. Ghantous, P. Spence, and E. Scoccimarro (2017). "The effect on simulated ocean climate of a parameterization of unbroken wave-induced mixing incorporated into the k-epsilon mixing scheme". In: *Journal of Advances in Modeling Earth Systems* 9.2, pp. 735–758. ISSN: 1942-2466. DOI: `10.1002/2016MS000707`.

Warner, J. C., C. R. Sherwood, H. G. Arango, and R. P. Signell (2005). "Performance of four turbulence closure models implemented using a generic length scale method". In: *Ocean Modelling* 8.1, pp. 81–113. ISSN: 1463-5003. DOI: `https://doi.org/10.1016/j.ocemod.2003.12.003`.

Waterman, S., A. C. N. Garabato, and K. L. Polzin (2013). "Internal Waves and Turbulence in the Antarctic Circumpolar Current". In: *Journal of Physical Oceanography* 43.2, pp. 259–282. DOI: `10.1175/JPO-D-11-0194.1`.

Weisstein, E. W. (2017). *Hyperbolic Tangent*. Last visited on 17 April 2017. MathWorld-A Wolfram Web Resource. URL: `http://mathworld.wolfram.com/HyperbolicTangent.html`.

Wilcox, D. C. (1988). "Reassessment of the scale-determining equation for advanced turbulence models". In: *AIAA Journal* 26.11, pp. 1299–1310. DOI: `10.2514/3.10041`.

Woods, J. D. and W. Barkmann (1986). "The response of the upper ocean to solar heating. I: The mixed layer". In: *Quarterly Journal of the Royal Meteorological Society* 112.471, pp. 1–27. DOI: `10.1002/qj.49711247102`.

Zee, Vlaams Instituut voor de (2017a). *GO-FLO bottle*. Last visited on 17 September 2017. Flanders Marine Institute. URL: `http://www.vliz.be/en/go-flobottle`.

Zee, Vlaams Instituut voor de (2017b). *Niskin Bottle*. Last visited on 17 September 2017. Flanders Marine institute. URL: `http://www.vliz.be/en/Niskinbottle`.